AN ABSTRACT OF THE DISSERTATION OF

Cheng Chen for the degree of Doctor of Philosophy in Chemistry presented on August 27, 2020.

Title: Dynamics and Design of Green Fluorescent Protein-Inspired Superphotoacids and Red-Emitting Fluorophores with Transient Absorption and Femtosecond Stimulated Raman Spectroscopy

Abstract approved:

_____

Chong Fang

In the past decades, femtosecond stimulated Raman spectroscopy (FSRS) has been gaining tremendous popularity in fundamental sciences stemming from chemistry to biology. It is capable of capturing both equilibrium and non-equilibrium structural information across a broad range of timescales with simultaneously high temporal and spectral resolutions. Femtosecond transient absorption spectroscopy (fs-TA) acts as a powerful partner technique that complements the dynamics analysis and guides the resonance selection for FSRS pulses. In this dissertation, two bodies of work on the excited-state dynamics and design strategies of the green fluorescent protein (GFP) chromophore-based superphotoacids and red-emitting fluorophores studied by FSRS and TA are presented.

First, FSRS and fs-TA were implemented to dissect the ultrafast excited-state proton transfer (ESPT) dynamics of superphotoacids in aqueous and nonaqueous solutions. The superphotoacids were derived from the synthetic GFP chromophore, namely, *p*-hydroxybenzylidiene-dimethylimidazolinone or *p*-HBDI. By strategic conformational locking and multi-site halogenation, *p*-HBDI was transformed from a dim weak photoacid to a bright superphotoacid. The locking enables a three-order increase of

magnitude in fluorescence quantum yield from 10^{-4} to 10^{-1} while the halogenation remarkably elevates the photoacidity characterized by the excited-state pK_a or pK_a* (asterisk denotes excited state) value which is lowered from ~2.1 of p-HBDI to negative values of the derived superphotoacids. FSRS and fs-TA results showed that the ESPT dynamics of these superphotoacids in protic organic solvents such as methanol (an inert proton acceptor) are inhomogeneous. Three pathways including direct, solvent reorientation-controlled, and rotational diffusion-controlled ESPT are coexisting within the excited-state lifetime. Through a systematic comparison of different photoacids, new design principles of tuning photoacidity was proposed. Besides, a comparison between locked and unlocked halogenated superphotoacids of similar strengths was made. They exhibit drastically different ESPT dynamics and thus highlight the importance of structure-activity relationship of functional molecules.

Second, ground- and excited-state FSRS in conjunction with quantum calculations allows a deep understanding of the emission mechanism in GFP chromophore and its derivatives. A unique "double-donor-one-acceptor" red-shifting strategy thereby was proposed based on the GFP chromophore and we showed that this strategy can be generalized to other fluorophore scaffolds. Excited-state intramolecular charge transfer (ICT) was extensively proven to be able to red-shift emission wavelength by stabilizing the excited state. The presence of excited-state ICT in GFP chromophore and its derivatives were both experimentally and theoretically demonstrated with site precision by FSRS and quantum calculations, respectively. Moreover, a "double-donor" structure that incorporates another electron-donating group (EDG) to the *ortho* site of the $-OH/O^-$ group of p-HBDI was discovered to destabilize the ground state. In synergy with the "one-acceptor" that lowers excited-state energy through ICT, the emission energy gap could be lowered to a remarkable extent. The red emission wavelength is highly desired in biological imaging due to the resultant small background noise and has drawn lots of attention in the design of imaging probes. The "double-donor-one-acceptor" strategy is advantageous in that it does not require large π-conjugation extension and hence provides space for further chemical engineering for other wanted imaging properties such as high FQY.

Dynamics and Design of Green Fluorescent Protein-Inspired Superphotoacids and
Red-Emitting Fluorophores with Transient Absorption and Femtosecond Stimulated
Raman Spectroscopy

by
Cheng Chen

A DISSERTATION

submitted to

Oregon State University

in partial fulfillment of
the requirements for the
degree of

Doctor of Philosophy

Presented August 27, 2020
Commencement June 2021

Doctor of Philosophy dissertation of Cheng Chen presented on August 27, 2020

APPROVED:

_____

Major Professor, representing Chemistry

_____

Head of the Department of Chemistry

_____

Dean of the Graduate School

I understand that my dissertation will become part of the permanent collection of Oregon State University libraries. My signature below authorizes release of my dissertation to any reader upon request.

_____

Cheng Chen, Author

ACKNOWLEDGEMENTS

This journey in pursuit of the PhD degree has had so many meanings to me that I shall treasure the experiences and memories in my life. Over these years, I have been able to accumulate lots of knowledge and experience and be productive in research, which I believe will profoundly benefit my future career. I have also had a wonderful life here at Corvallis with many memorable moments. These would not be possible without the kindness and support of so many great people for which I am truly grateful.

First and foremost, I would like to thank my advisor, Dr. Chong Fang, who brought me into the femtosecond photochemistry field which I fell in love with and then advised me to be an experienced researcher with his expertise, who treated me not only as a student but also a close friend and selflessly shared his working experience with me, who offered me incredible space and freedom to express and realize my research ideas, who always prioritized my efforted work and provided me timely feedbacks to motivate me forward, who gave me the best trust I could ever ask for. I am deeply thankful for his mentorship and friendship.

I would like to thank our former postdoctoral research associate, Dr. Weimin Liu, who is currently a research professor at ShanghaiTech University in China for the great help and advice in my early PhD life. He initiated my interest in research so I could constantly keep full curiosity for the research. His expertise in ultrafast optics got me through the initial struggle with theory, experiments, data analysis such that I could be on the right track. His constant encouragement has also kept me motivated and excited about research along the way.

I would like to thank my committee member, Dr. Wei Kong, who taught me most of the graduate P-Chem courses and offered me lots of her experience and advice on courses and research. Her rigorous and strict attitude toward science and research has always been what I was after over these years. I would also like to thank Dr. Yun-Shik

Lee, Dr. Paul Blakemore, and Dr. Weihong Qiu for their kindness and support to serve on my committee.

I would like to thank all the lab mates I have worked with: Dr. Liangdong Zhu, Dr. Longteng Tang, Dr. Yanli Wang, Dr. Breland Oscar, Liang Wang, Sean Tachibana, Miles Taylor, Taylor Krueger, Sean Boulanger. Not only did they offer great help and discussions but also they made the sometimes tedious lab life joyful with so many delightful moments. I would also like to thank the other chemistry colleagues at OSU I received help from for their generosity and kindness.

I would like to thank all of our collaborators. In particular, Dr. Mikhail Baranov at Russian Academy of Sciences and Pirogov Russian National Research Medical University has been synthesizing and providing us the samples of GFP derivatives that constituted my many projects and always given timely feedbacks on project progress. It has been a great pleasure to collaborate with him and his team.

I would like to thank the Department of Chemistry at OSU for offering me tremendous amounts of assistantships and resources including teaching assistantships, research fellowships, and awards. Without these abundant supports, I would not be able to complete the PhD degree with the achievement in teaching and research experience.

I would like to thank all my friends here at Corvallis. The conversations and gatherings with them have been a great complement and adjustment to my long demanding research life and brought me so much happiness. I cannot imagine what life I would be living without them. I enjoyed every single moment that we were making and having meals, playing card games, hiking in the forest and on the mountain, working out in the gym, etc. I am deeply grateful for all these precious friendships and the wonderful moments they brought to me.

CONTRIBUTION OF AUTHORS

First, Dr. Chong Fang has contributed to the design and final execution for all projects presented in this dissertation.

Dr. Liangdong Zhu has contributed to the conduction of some fs-TA and FSRS experiments for the projects in Chapter 3, 4, 5, 6, and 7. Dr. Weimin Liu has contributed to the conduction of some fs-TA and FSRS experiments for the projects in Chapter 3 (Section 3.3) and 4.

Dr. Mikhail Baranov, Dr. Ilia Yampolsky, Dr. Kyril Solntsev and their teams have contributed to the chemical synthesis and some steady-state measurements for projects in Chapter 4, 5, 6, and 7.

Dr. Longteng Tang has contributed to the theoretical calculations and discussions for the project in Chapter 5. Dr. Yanli Wang has contributed to the theoretical calculations and discussions for the project in Chapter 4.

Dr. Breland Oscar has contributed to the data processing and manuscript writing for the project in Chapter 3 (Section 3.3).

Sean Boulanger has contributed to some steady-state measurements for the project in Chapter 6.

TABLE OF CONTENTS

LIST OF FIGURES

LIST OF FIGURES (Continued)

LIST OF TABLES

Chapter 1 Introduction

1.1 Excited-state proton transfer (ESPT) and photoacids

Proton transfer or acid-base reactions are the most fundamental events in many chemical and biological processes.[1-12] Among these, excited-state proton transfer (ESPT) triggered by photoexcitation has drawn the most scientific attention.[13-35] Ever since the discovery of ESPT phenomenon 90 years ago by Weber,[36] it has been the subject of extensive experimental and theoretical research across a broad range of disciplines due to its central roles to a myriad of life and energy conversion processes as well as many other chemical applications. For instance, photosynthesis in green plants converts the solar energy to chemical energy and then fuels the animals or organisms on the Earth. The key process in Photosystem II is photoinduced proton-coupled electron transfer, one kind of ESPT.[7] In view of the growing fuel and energy crisis, investigations of ESPT in photosynthesis meets the quest for the new sustainable energy sources and thus has stimulated tremendous interest in the chemistry and material science fields. Another example is the green fluorescent protein (GFP) that revolutionized molecular and cellular biology for decades.[10,37,38] The functioning of GFP lies in the three-residue chromophore that undergoes ESPT in response to ultraviolet light irradiation.[25,26,39-43] The unique protein environment renders the ESPT process highly energy-conserving and hence bright green emission in the deprotonated form. This makes GFP an excellent fluorescence marker for biological imaging with a desirable high fluorescence quantum yield and large Stokes shift. Its discovery and

investigations have also inspired a broad library of fluorescent proteins with various functions and imaging applications in optogenetics.[44-46]

Chemically, the cores of these chemical and biological machines are molecules capable of undergoing photoinduced proton dissociation and transferring the proton to the nearby environment. They are typically termed as photoacids, which combine two important components, i.e., "photo" and "acid". The "photo" highlights the photoinduced process and "acid" indicates the acid nature. Therefore, photoacids are molecules, typically aromatic, that are weak acids in the electronic ground state but of increased acidity by many orders of magnitude in the electronic excited states.[16-18,20,22,26,47-51] Similar to the ground state acidity characterized by the pK_a value where K_a denotes the acid dissociation reaction constant, the excited state acidity or photoacidity can be quantified by the pK_a* value. The lower the pK_a* value, the higher strength of the photoacidity. Some representative photoacids include naphthol and its derivatives,[20,26,48] pyranine (8-hydroxypyrene-1,3,6-trisulfonate or HPTS) and its derivatives,[18,52] cyanine-based photoacids.[21,22,53,54] Before the advent of modern ultrafast spectroscopy that sheds light on the ultrafast ESPT events down to femtoseconds, the ESPT process had been typically described by the Eigen-Weller model with a two-step reaction mechanism as shown in Figure 1.1.[6,14,55] The first step involves an initial small-scale proton transfer into a contact ion-pair (CIP). The second step is the diffusion-controlled further proton separation into free ions.

$$\text{ROH*} \xrightleftharpoons[k_r]{k_{PT}} \underset{\text{(CIP)}}{\text{RO}^-\text{*}\cdots\text{H}^+} \xrightarrow{k_d} \text{RO}^-\text{*} + \text{H}^+$$

$$\text{h}\nu \updownarrow \qquad\qquad \downarrow \qquad\qquad \downarrow$$

$$\text{ROH} \longleftarrow \text{RO}^-\cdots\text{H} \longleftarrow \text{RO}^- + \text{H}^+$$
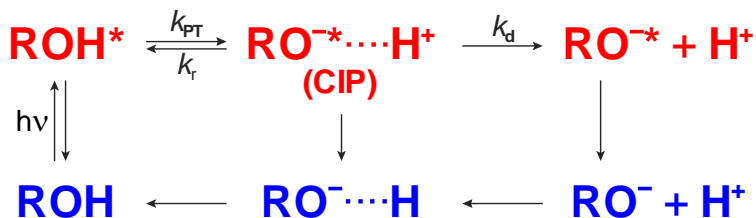
Figure 1.1. Eigen-Weller model for excited-state proton transfer. The labels k_{PT}, k_r, and k_d denote rate constants of the intrinsic proton transfer, proton recombination, and diffusion-controlled proton dissociation, respectively.

It appears that this model only works well for weak- and moderate-strength photoacids. It fails to describe the ESPT dynamics for even stronger photoacids, or superphotoacids defined as those with rather negative pK_a* values. In these cases, solvent orientation becomes a rate-limiting step for the actual proton transfer.[16,19,23,47] Some extremely strong photoacids such as the cyanine dye QCy9 have been reported to undergo ultrafast ESPT that even goes beyond the solvent-control limit,[54] indicating that the ESPT is essentially barrierless and the exact origin, however, remain elusive. These different ESPT behaviors have been shown to be correlated with the strengths of photoacids while solvent motions also play an important role in determining the ESPT dynamics (see below).

1.1.1 Strengths of photoacids

Similar to the ground-state acidity characterized by the pK_a value, the photoacidity can be measured by the excited-state pK_a or pK_a* value despite that the electronic excited state is non-equilibrium, going beyond thermodynamics considerations at equilibrium.

However, the pK_a^* values correlate well with the photoacidity and have qualitatively accounted for ESPT rates for most photoacids. Notably, it is difficult to extract the pK_a^* directly from experiment due to the none-quilibrium nature of the excited state, but one can estimate it by Förster equation (see below, based on ground- and excited-state theromodynamics) using steady-state absorption or emission wavelengths.[56,57]

$$pK_a^* = pK_a - \frac{\Delta\Delta G°}{RT\ln 10} \approx pK_a - \frac{hc}{k_B T\ln 10}(\frac{1}{\lambda_{HA}} - \frac{1}{\lambda_{A^-}})$$

where λ_{HA} and λ_{A^-} are the absorption or emission wavelengths of the acid and its conjugate base, and $\Delta\Delta G°$ is the difference in $\Delta G°$ between ground and excited states. On this basis, Huppert and coworkers classified photoacids investigated so far into four regimes by their strengths.[16]

The first regime (Regime I) is categorized as the weak photoacids with pK_a^* values above zero. They can only undergo ESPT to water but no other protic organic solvents such as alcohols. The ESPT rate k_{PT} is highly dependent upon the pK_a^* value and typically slower than 5×10^{10} s^{-1} ($\tau_{PT} > 20$ ps). One example in this regime is pyranine (Figure 1.2a), a well-investigated photoacid, that has an EPST time of ~100 ps.[29]
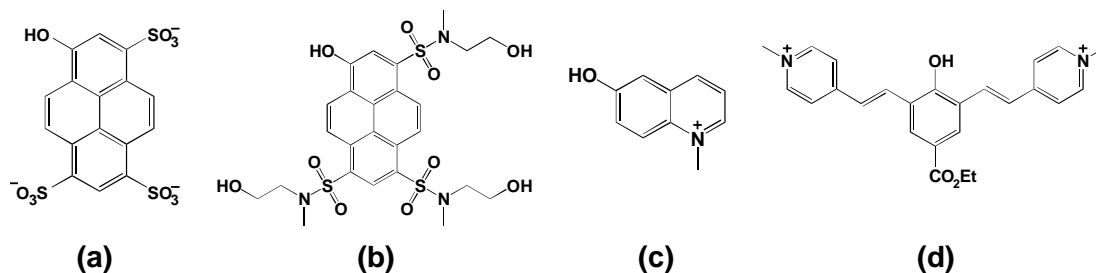
Figure 1.2. Representative photoacids in Regimes I-IV. The a-d correspond to the Regime I-IV accordingly.

The second regime (Regime II) includes the stronger photoacids with pK_a^* values in the range of $-4 < pK_a^* < 0$. The ESPT time constant is faster than 20 ps. These photoacids can not only transfer a proton to water but also to alcohols and other protic solvents. The ESPT capability in alcohols benefits from the extremely long excited state lifetimes of these photoacids such that ESPT could occur at a very slow rate within the lifetime. Some pyranine derivatives[18] belong to this category (Figure 1.2b).

The third regime (Regime III) represents photoacids that can undergo ultrafast ESPT such that solvent orientation becomes a significant rate-limiting step, which can thus be defined as superphotoacids. This is because the solvent molecules, especially those surrounding the photoacid molecule, need to reorganize their orientations to adapt to the new dipole moment of the photoacid induced by the photoexcitation and rebuild the hydrogen-bond (H-bond) chains for actual proton transfer. Though the driving force of ESPT is large, the solvent orientation time is rather slow and weakly dependent on the photoacid property, thereby giving rise to the slower "apparent" ESPT rate. One example of this class is *N*-methyl-6-hydroxyquinolinium (NM6HQ$^+$)[19] as shown in Figure 1.2c, the ESPT rate of which well follows the long-time components of the solvation correlation function of water, methanol and ethanol.

The last regime (Regime IV) is categorized by the strongest superphotoacids with pK_a^* < -7. In this regime, the ESPT rate is no longer dictated by the solvent orientation and is almost identical for solvents like water, methanol and ethanol. To date, only one photoacid in this regime has been reported, i.e., QCy9 (Figure 1.2d). The ESPT time

constant is ~ 100 fs, irrespective of the solvents (water, methanol and ethanol).[22] The origin for its superphotoacidity remains elusive despite a few proposed mechanisms.

1.1.2   Roles of solvent and excited-state lifetime on ESPT

According to the aforementioned classifications of photoacids, it is evident that ESPT dynamics are strongly dependent on photoacidity and H-bonding interactions between the solute and solvent. Weak photoacids usually undergo ESPT only in aqueous solution while stronger photoacids or superphotoacids with a negative pK_a* can transfer a proton not only to water but also to nonaqueous solvents including certain protic and basic solvents.[19,47,55] Therefore, some researchers have invoked a more general ESPT model. The ESPT reaction can be understood along two coordinates: the proton transfer coordinate and the solvent coordinate.[16,58] The first coordinate is determined by the intrinsic photoacidity that dictates the proton transfer rate and the second coordinate is determined by the solvent whose orientational motions to minimize the dipolar interaction between the photoacid and solvent upon photoexcitation give rise to a reaction barrier. The "apparent" ESPT rate is exhibited by whichever coordinate is slower. The rate-limiting solvent-orientation time is usually close to its longitudinal relaxation time rather than Debye relaxation time.[19,59] It indicates that the local H-bonding environment is likely most important for actual proton transfer from the solvated chromophore molecule. Provided that the local solvent orientation time constants for common protic solvents are on the timescales of a few to tens of picosecond (e.g., water is 1-2 ps, methanol is 5-10 ps), weak and moderate photoacids

(Regime I and II) show no limit by solvent orientation due to their slower intrinsic ESPT rate. In contrast, photoacids in Regime III have faster intrinsic ESPT rates than solvent-orientation and thus exhibit the solvent-limited ESPT rates.

Besides the solvent, the excited state lifetime also plays an important role in ESPT. In essence, the competition between ESPT and other decay pathways including fluorescence determines the excited-state dynamics. It is reasonable to imagine that the ESPT would be absent if the excited-state population decays through a more efficient pathway. One such example is the synthetic GFP chromophore, i.e., *p*-HBDI, in aqueous solution. GFP is known to undergo ESPT in protein matrix that generates the bright green emission of the deprotonated form.[39] Outside the protein pocket, however, *p*-HBDI loses the ESPT capability due to the much more efficient isomerization-induced nonradiative decay (see more in later sections).[41] For Regime II photoacid (Figure 2d), it is noted that the ESPT rate is very slow in methanol (~2.5 ns) and ethanol (~3.5 ns). This is favored by the even longer radiative lifetime (> 6 ns) that allows the relatively faster ESPT pathway.[16,18] Furthermore, how would a shorter lifetime (shorter than solvent orientation) influence the ESPT dynamics for Regime III photoacids (solvent-limited)? This remains an intriguing question as no systematic research has shed light on it. One may speculate that the ESPT does not occur because the solvent reorientation would be truncated by the faster population deactivation of the photoacid.[24,30] Regardless, many questions concerning ESPT dynamics in solutions are still not settled and demanding further investigations with capabilities to elucidate the coupled electronic and atomic motions in real time.[9]

1.2 Green fluorescent protein chromophore in protein *versus* in solution

As the iconic symbol of fluorescent proteins (FPs), the green fluorescent protein discovered in jellyfish *Aequorea victoria* has revolutionized the molecular and cellular biology for decades. It has inspired an enormous amount of fluorescent proteins used for varieties of imaging and sensing applications, and also stimulated the development of organic imaging probes. There are pros and cons in both areas but regardless, the design of new molecular sensors or machines demands the mechanistic understanding of the structure-environment (protein matrix)-activity relationships. In comparison to organic chromophores in solutions, the environment plays a more profound role in the properties of FPs.[60-63] This has caused the drastic difference between the GFP chromophore in protein matrix and in solution in the aspects of electronic transitions, ESPT, and fluorescence performance.

1.2.1   Absorption and emission

Structurally, *p*-HBDI is the chromophore core of wild-type (wt)GFP protein that is autocatalytically formed by three residues: Serine 65, Tyrosine 66, and Glycine 67 (SYG). However, the synthetic *p*-HBDI are significantly blue-shifted in absorption and emission of both protonated and deprotonated forms with respect to those inside wtGFP.[30,39,64] Table 1.1 summaries the absorption and emission data of *p*-HBDI and wtGFP. It is noted that both absorption and emission of *p*-HBDI is blue-shifted in the presence of solvent with respect to those in gas phase.[64] And the gas-phase absorption wavelengths are similar to wtGFP in protein pocket. It indicates that the absorption characteristics of wtGFP is mainly a result of the intrinsic properties of the

chromophore core, and the environment that the chromophore experiences is closer to vacuum despite the presence of residues and water molecules interacting with the chromophore.[65]

Table 1.1. Absorption and emission wavelength of wtGFP and *p*-HBDI.

	neutral abs. (nm)	neutral em. (nm)	anionic abs. (nm)	anionic em. (nm)
wtGFP	398	460	477	508
p-HBDI in water	370	448	425	494
p-HBDI *in vacuo*	406	–	479	–

1.2.2   ESPT

Another large difference between wtGFP and *p*-HBDI is the ESPT capability. The wtGFP is known for ESPT to produce the bright deprotonated emission in response to UV irradiation, while *p*-HBDI is not capable of ESPT even in aqueous solution. The ESPT mechanism of wtGFP has been reported to occur along the chromophore-W22-S205-E222 H-bonding chain with the aid of crystal structure (Figure 1.3).[25] The ESPT time constant was found to be ~5 ps involving multiple proton motions through the proton transfer wire. The absence of ESPT for *p*-HBDI in aqueous solution cannot be explained by the weak photoacidity alone. Using Förster equation, the pK_a* of *p*-HBDI ($pK_a = 8.5$)[66] is estimated to be ~2.6 by averaging the pK_a* values calculated from

absorption and emission data in Table 1.1. Since the wtGFP is not titratable across a wide pH range (while maintaining the protein integrity), no pK_a value has been obtained.[67] However, based on the absorption profile and considering the relative magnitudes of extinction coefficients of the protonated and deprotonated forms, the pK_a of wtGFP should be around 6−6.5.[38,39] Using the absorption and emission wavelengths in Table 1.1, the pK_a* of wtGFP at room temperature is thus estimated to be in the range of −0.6 < pK_a* < −0.1 (see Figure 1.2a). Therefore, p-HBDI can be classified as a weak photoacid in Regime I. The wtGFP is in Regime II and the 5-ps ESPT time constant agrees with the definition of ESPT rate in this regime.
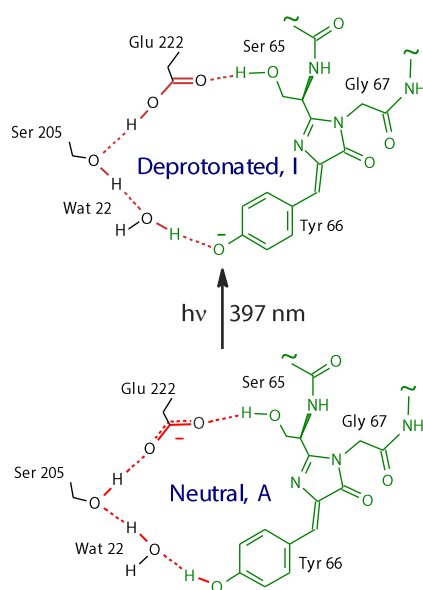
Figure 1.3. ESPT mechanism inside the wtGFP chromophore pocket. Adapted with permission from Ref. [25]. Copyright 2009 Macmillan Publishers Limited.

Note that a conformationally locked p-HBDI, namely p-HOBDI-BF$_2$ (note that p-HOBDI is equivalent to p-HBDI, just the former term emphasizes the phenolic hydroxyl group), is able to undergo ESPT in aqueous solution with a pK_a* of 0.6,[68] which is also a weak Regime I photoacid. The conformational locking does not significantly lower the pK_a* with respect to p-HBDI but makes the chromophore highly fluorescent with a long radiative lifetime. This comparison suggests that the short excited-state lifetime of p-HBDI is the main cause for the loss of ESPT capability in solution. The p-HBDI is known as a nonfluorescent molecule with the fluorescence lifetime shorter than 1 ps in most solvents due to the efficient nonradiative decay pathways induced by bridge-twisting motions.[41] The conformational locking in p-HOBDI-BF$_2$ suppresses these decay pathways and hence makes the chromophore highly fluorescent. The ESPT time constant of p-HOBDI-BF$_2$ in aqueous solution was measured to be 450 ps. So theoretically the intrinsic ESPT time constant of p-HBDI should be longer than 450 ps due to its higher pK_a* value than p-HOBDI-BF$_2$.

1.2.3 Fluorescence quantum yield

One of the superior properties of wtGFP is the high fluorescence quantum yield (FQY~0.79). This arises from the unique protein environment that constrains the bridge twisting motions of the chromophore in contrast to the facile twisting motions of p-HBDI in solution. As a result, the FQY of p-HBDI is on the order of 10^{-4}, which is lower by three orders of magnitude than wtGFP. This highlights the importance of environment on chromophore properties particularly in proteins. The exact origin of

the decay mechanism of *p*-HBDI, however, has not been addressed and remains a debatable scientific problem. Two mechanisms were previously proposed: one-bond flip (C=C torsion) and hula-twist (concerted C=C and C-C torsion). The one-bond flip mechanism is more favored due to the agreement with experiments and calculations.[42,43,69-72] The hula-twist mechanism has been generally denied by calculations because of a high energy cost along this reaction coordinate.[40,41,43,73]

1.3 Fluorescence imaging

Fluorescence imaging is one type of imaging technique that uses fluorescence to visualize biological processes such as disease diagnosis in living organisms.[74] It has been one of the most prevalent biological imaging methods with significant developments in recent decades. Ever since the discovery of GFP and its applications in imaging, a great variety of fluorescent proteins (FPs) has been developed.[44-46,75,76] In parallel, organic dyes have also drawn increased attention due to their many advantages in comparison to FPs.[77-86] In either case, an ideal fluorescence probe should possess a number of crucial properties for practical use. As physical chemists and spectroscopists, we are more interested in their photophysical and photochemical properties. The few desirable properties include long emission wavelength, large Stokes shift, and high FQY or brightness. Some other important considerations such as photostability, pH stability, and toxicity/phototoxicity[44] will not be discussed here for simplicity and focus. These photophysical properties are correlated with the imaging sensitivity and signal-to-noise ratio. For instance, long emission wavelengths can

greatly reduce the background noise from the autofluorescence of tissues and improve the tissue penetration depth. High brightness can lower the requirement of the dose of excitation light and hence minimize the phototoxic effect.

1.3.1 Fluorescent proteins

Inspired by the applications of wtGFP in imaging, many fluorescent proteins (FPs) have been developed over the past few decades. Nowadays, one can find a whole palette of FPs emitting different colors across the visible region. Meanwhile, many FPs have been used to generate biosensors for the detection of biological analytes such as ions or other biomolecules.[87-92] Among these, red fluorescent proteins (RFPs) and RFP-based biosensors have drawn special attention due to the reduced autofluorescence, deeper tissue penetration, and minimal absorption at longer imaging wavelengths.[45,46,75] Despite the intensive efforts on RFPs and RFPs-based biosensors, some challenges in terms of synthesis and application are still present and so far the choice of RFPs remains limited.[93] Therefore, versatile approaches of developing RFPs with enhanced properties are still in demand.

1.3.2 Organic fluorophores

Compared to FPs, the smaller organic fluorophores have several advantages such as high selectivity and sensitivity, low cost, ease of synthesis, etc. Due to the simplicity in synthesis and relatively easier structure-activity relationships, organic dyes that have

been created for bioimaging are countless to date. Red and near-infrared dyes have been the focus of many works for better signal-to-noise ratio in practice.[78,80,94] Unfortunately, many of these efforts are still trial-and-error which lacks efficiency and causes a waste of resources to a great extent.[95] Most efforts have based the red-shifting strategy on extending the π-conjugation over the chromophore framework. The resultant large molecular size has brought other issues that hinders the bioimaging applications such as the fluorescence loss due to the long-chain design.[78] Above all, a comprehensive mechanistic understanding of relationships between fluorophore structure and dynamics with respect to absorption, emission, and FQY has not been there yet.[96-102] Cross-discipline collaborations remain highly in demand to reach this goal for efficient and effective design of the next-generation organic bioprobes.

1.4 References

[1]   Agmon, N. The Grotthuss mechanism. *Chem. Phys. Lett.* **1995**, *244*, 456-462.

[2]   Thämer, M.; De Marco, L.; Ramasesha, K.; Mandal, A.; Tokmakoff, A. Ultrafast 2D IR spectroscopy of the excess proton in liquid water. *Science* **2015**, *350*, 78-82.

[3]   Wolke, C. T.; Fournier, J. A.; Dzugan, L. C.; Fagiani, M. R.; Odbadrakh, T. T.; Knorke, H.; Jordan, K. D.; McCoy, A. B.; Asmis, K. R.; Johnson, M. A. Spectroscopic snapshots of the proton-transfer mechanism in water. *Science* **2016**, *354*, 1131-1135.

[4]   Yuan, R.; Napoli, J. A.; Yan, C.; Marsalek, O.; Markland, T. E.; Fayer, M. D. Tracking Aqueous Proton Transfer by Two-Dimensional Infrared Spectroscopy and ab Initio Molecular Dynamics Simulations. *ACS Cent. Sci.* **2019**, *5*, 1269-1277.

[5]   Huynh, M. H. V.; Meyer, T. J. Proton-Coupled Electron Transfer. *Chem. Rev.* **2007**, *107*, 5004-5064.

[6]   Eigen, M. Proton Transfer, Acid-Base Catalysis, and Enzymatic Hydrolysis. Part I: ELEMENTARY PROCESSES. *Angew. Chem. Int. Ed.* **1964**, *3*, 1-19.

[7]   Gagliardi, C. J.; Westlake, B. C.; Kent, C. A.; Paul, J. J.; Papanikolas, J. M.; Meyer, T. J. Integrating proton coupled electron transfer (PCET) and excited states. *Coord. Chem. Rev.* **2010**, *254*, 2459-2471.

[8]   Odella, E.; Mora, S. J.; Wadsworth, B. L.; Huynh, M. T.; Goings, J. J.; Liddell, P. A.; Groy, T. L.; Gervaldo, M.; Sereno, L. E.; Gust, D.; Moore, T. A.; Moore, G. F.; Hammes-Schiffer, S.; Moore, A. L. Controlling Proton-Coupled Electron Transfer in Bioinspired Artificial Photosynthetic Relays. *J. Am. Chem. Soc.* **2018**, *140*, 15450-15460.

[9]   Odella, E.; Wadsworth, B. L.; Mora, S. J.; Goings, J. J.; Huynh, M. T.; Gust, D.; Moore, T. A.; Moore, G. F.; Hammes-Schiffer, S.; Moore, A. L. Proton-Coupled Electron Transfer Drives Long-Range Proton Translocation in Bioinspired Systems. *J. Am. Chem. Soc.* **2019**, *141*, 14057-14061.

[10]   Tsien, R. Y. THE GREEN FLUORESCENT PROTEIN. *Annu. Rev. Biochem* **1998**, *67*, 509-544.

[11]   Tutol, J. N.; Peng, W.; Dodani, S. C. Discovery and Characterization of a Naturally Occurring, Turn-On Yellow Fluorescent Protein Sensor for Chloride. *Biochemistry* **2019**, *58*, 31-35.

[12]   Kumpulainen, T.; Lang, B.; Rosspeintner, A.; Vauthey, E. Ultrafast Elementary Photochemical Processes of Organic Molecules in Liquid Solution. *Chem. Rev.* **2017**, *117*, 10826-10939.

[13] Agmon, N. Elementary Steps in Excited-State Proton Transfer. *J. Phys. Chem. A* **2005**, *109*, 13-35.

[14] Pines, E.; Huppert, D.; Agmon, N. Geminate recombination in excited-state proton-transfer reactions: Numerical solution of the Debye–Smoluchowski equation with backreaction and comparison with experimental results. *J. Chem. Phys.* **1988**, *88*, 5620-5630.

[15] Mohammed, O. F.; Pines, D.; Dreyer, J.; Pines, E.; Nibbering, E. T. J. Sequential Proton Transfer Through Water Bridges in Acid-Base Reactions. *Science* **2005**, *310*, 83-86.

[16] Simkovitch, R.; Shomer, S.; Gepshtein, R.; Huppert, D. How Fast Can a Proton-Transfer Reaction Be beyond the Solvent-Control Limit? *J. Phys. Chem. B* **2015**, *119*, 2253-2262.

[17] Tolbert, L. M.; Solntsev, K. M. Excited-State Proton Transfer: From Constrained Systems to "Super" Photoacids to Superfast Proton Transfer. *Acc. Chem. Res.* **2002**, *35*, 19-27.

[18] Finkler, B.; Spies, C.; Vester, M.; Walte, F.; Omlor, K.; Riemann, I.; Zimmer, M.; Stracke, F.; Gerhards, M.; Jung, G. Highly photostable "super"-photoacids for ultrasensitive fluorescence spectroscopy. *Photochem. Photobiol. Sci.* **2014**, *13*, 548-562.

[19] Pérez-Lustres, J. L.; Rodriguez-Prieto, F.; Mosquera, M.; Senyushkina, T. A.; Ernsting, N. P.; Kovalenko, S. A. Ultrafast Proton Transfer to Solvent: Molecularity and Intermediates from Solvation- and Diffusion-Controlled Regimes. *J. Am. Chem. Soc.* **2007**, *129*, 5408-5418.

[20] Huppert, D.; Tolbert, L. M.; Linares-Samaniego, S. Ultrafast Excited-State Proton Transfer from Cyano-Substituted 2-Naphthols. *J. Phys. Chem. A* **1997**, *101*, 4602-4605.

[21] Presiado, I.; Karton-Lifshin, N.; Erez, Y.; Gepshtein, R.; Shabat, D.; Huppert, D. Ultrafast Proton Transfer of Three Novel Quinone Cyanine Photoacids. *J. Phys. Chem. A* **2012**, *116*, 7353-7363.

[22] Simkovitch, R.; Karton-Lifshin, N.; Shomer, S.; Shabat, D.; Huppert, D. Ultrafast Excited-State Proton Transfer to the Solvent Occurs on a Hundred-Femtosecond Time-Scale. *J. Phys. Chem. A* **2013**, *117*, 3405-3413.

[23] Chen, C.; Liu, W.; Baranov, M. S.; Baleeva, N. S.; Yampolsky, I. V.; Zhu, L.; Wang, Y.; Shamir, A.; Solntsev, K. M.; Fang, C. Unveiling Structural Motions of a Highly Fluorescent Superphotoacid by Locking and Fluorinating the GFP Chromophore in Solution. *J. Phys. Chem. Lett.* **2017**, *8*, 5921-5928.

[24] Chen, C.; Zhu, L.; Boulanger, S. A.; Baleeva, N. S.; Myasnyanko, I. N.; Baranov, M. S.; Fang, C. Ultrafast excited-state proton transfer dynamics in dihalogenated non-fluorescent and fluorescent GFP chromophores. *J. Chem. Phys.* **2020**, *152*, 021101.

[25] Fang, C.; Frontiera, R. R.; Tran, R.; Mathies, R. A. Mapping GFP Structure Evolution During Proton Transfer with Femtosecond Raman Spectroscopy. *Nature* **2009**, *462*, 200-204.

[26] Carmeli, I.; Huppert, D.; Tolbert, L. M.; Haubrich, J. E. Ultrafast excited-state proton transfer from dicyano-naphthol. *Chem. Phys. Lett.* **1996**, *260*, 109-114.

[27] Driscoll, E. W.; Hunt, J. R.; Dawlaty, J. M. Proton Capture Dynamics in Quinoline Photobases: Substituent Effect and Involvement of Triplet States. *J. Phys. Chem. A* **2017**, *121*, 7099-7107.

[28] Sheng, W.; Nairat, M.; Pawlaczyk, P. D.; Mroczka, E.; Farris, B.; Pines, E.; Geiger, J. H.; Borhan, B.; Dantus, M. Ultrafast Dynamics of a "Super" Photobase. *Angew. Chem. Int. Ed.* **2018**, *57*, 14742-14746.

[29] Liu, W.; Wang, Y.; Tang, L.; Oscar, B. G.; Zhu, L.; Fang, C. Panoramic portrait of primary molecular events preceding excited state proton transfer in water. *Chem. Sci.* **2016**, *7*, 5484-5494.

[30] Laptenok, S. P.; Conyard, J.; Page, P. C. B.; Chan, Y.; You, M.; Jaffrey, S. R.; Meech, S. R. Photoacid behaviour in a fluorinated green fluorescent protein chromophore: ultrafast formation of anion and zwitterion states. *Chem. Sci.* **2016**, *7*, 5747-5752.

[31] Gajst, O.; Green, O.; Simkovitch, R.; Shabat, D.; Huppert, D. The photoacidity of phenol chloro benzoate cyanine picolinium salt photoacid in alkanols. *J. Photochem. Photobiol. A: Chem.* **2018**, *353*, 546-556.

[32] Borgis, D.; Hynes, J. T. Curve Crossing Formulation for Proton Transfer Reactions in Solution. *J. Phys. Chem.* **1996**, *100*, 1118-1128.

[33] Goyal, P.; Hammes-Schiffer, S. Tuning the Ultrafast Dynamics of Photoinduced Proton-Coupled Electron Transfer in Energy Conversion Processes. *ACS Energy Lett.* **2017**, *2*, 512-519.

[34] Horke, D. A.; Watts, H. M.; Smith, A. D.; Jager, E.; Springate, E.; Alexander, O.; Cacho, C.; Chapman, R. T.; Minns, R. S. Hydrogen Bonds in Excited State Proton Transfer. *Phys. Rev. Lett.* **2016**, *117*, 163002.

[35] Oscar, B. G.; Liu, W.; Zhao, Y.; Tang, L.; Wang, Y.; Campbell, R. E.; Fang, C. Excited-State Structural Dynamics of a Dual-Emission Calmodulin-Green Fluorescent Protein Sensor for Calcium Ion Imaging. *Proc. Natl. Acad. Sci. U. S. A.* **2014**, *111*, 10191-10196.

[36] Weber, K. The Close Relationship of Fluorescence Obliteration to the Inhibition of Photochemical Reactions. *Z. Phys. Chem., Abt. B* **1931**, *15*, 18-44.

[37] Zimmer, M. Green Fluorescent Protein (GFP): Applications, Structure, and Related Photophysical Behavior. *Chem. Rev.* **2002**, *102*, 759-782.

[38] Kneen, M.; Farinas, J.; Li, Y.; Verkman, A. S. Green Fluorescent Protein as a Noninvasive Intracellular pH Indicator. *Biophys. J.* **1998**, *74*, 1591-1599.

[39] Chattoraj, M.; King, B. A.; Bublitz, G. U.; Boxer, S. G. Ultra-fast excited state dynamics in green fluorescent protein: multiple states and proton transfer. *Proc. Natl. Acad. Sci. U.S.A.* **1996**, *93*, 8362-8367.

[40] Weber, W.; Helms, V.; McCammon, J. A.; Langhoff, P. W. Shedding light on the dark and weakly fluorescent states of green fluorescent proteins. *Proc. Natl. Acad. Sci. U.S.A.* **1999**, *96*, 6177-6182.

[41] Mandal, D.; Tahara, T.; Meech, S. R. Excited-State Dynamics in the Green Fluorescent Protein Chromophore. *J. Phys. Chem. B* **2004**, *108*, 1102-1108.

[42] Martin, M. E.; Negri, F.; Olivucci, M. Origin, Nature, and Fate of the Fluorescent State of the Green Fluorescent Protein Chromophore at the CASPT2//CASSCF Resolution. *J. Am. Chem. Soc.* **2004**, *126*, 5452-5464.

[43] Svendsen, A.; Kiefer, H. V.; Pedersen, H. B.; Bochenkova, A. V.; Andersen, L. H. Origin of the Intrinsic Fluorescence of the Green Fluorescent Protein. *J. Am. Chem. Soc.* **2017**, *139*, 8766-8771.

[44] Chudakov, D. M.; Matz, M. V.; Lukyanov, S.; Lukyanov, K. A. Fluorescent Proteins and Their Applications in Imaging Living Cells and Tissues. *Physiol. Rev.* **2010**, *90*, 1103-1163.

[45] Dedecker, P.; De Schryver, F. C.; Hofkens, J. Fluorescent Proteins: Shine on, You Crazy Diamond. *J. Am. Chem. Soc.* **2013**, *135*, 2387-2402.

[46] Adam, V.; Berardozzi, R.; Byrdin, M.; Bourgeois, D. Phototransformable fluorescent proteins: Future challenges. *Curr. Opin. Chem. Biol.* **2014**, *20*, 92-102.

[47] Chen, C.; Zhu, L.; Baranov, M. S.; Tang, L.; Baleeva, N. S.; Smirnov, A. Y.; Yampolsky, I. V.; Solntsev, K. M.; Fang, C. Photoinduced Proton Transfer of GFP-Inspired Fluorescent Superphotoacids: Principles and Design. *J. Phys. Chem. B* **2019**, *123*, 3804-3821.

[48] Tolbert, L. M.; Haubrich, J. E. Enhanced photoacidities of cyanonaphthols. *J. Am. Chem. Soc.* **1990**, *112*, 8163-8165.

[49] Tolbert, L. M.; Haubrich, J. E. Photoexcited Proton Transfer from Enhanced Photoacids. *J. Am. Chem. Soc.* **1994**, *116*, 10593-10600.

[50] Simkovitch, R.; Shomer, S.; Gepshtein, R.; Roth, M. E.; Shabat, D.; Huppert, D. Comparison of the rate of excited-state proton transfer from photoacids to alcohols and water. *J. Photochem. Photobiol. A: Chem.* **2014**, *277*, 90-101.

[51] Agmon, N.; Rettig, W.; Groth, C. Electronic Determinants of Photoacidity in Cyanonaphthols. *J. Am. Chem. Soc.* **2002**, *124*, 1089-1096.

[52] Liu, W.; Han, F.; Smith, C.; Fang, C. Ultrafast Conformational Dynamics of Pyranine during Excited State Proton Transfer in Aqueous Solution Revealed by Femtosecond Stimulated Raman Spectroscopy. *J. Phys. Chem. B* **2012**, *116*, 10535-10550.

[53] Simkovitch, R.; Shomer, S.; Gepshtein, R.; Shabat, D.; Huppert, D. Temperature Dependence of the Excited-State Proton-Transfer Reaction of Quinone-cyanine-7. *J. Phys. Chem. A* **2013**, *117*, 3925-3934.

[54] Simkovitch, R.; Akulov, K.; Shomer, S.; Roth, M. E.; Shabat, D.; Schwartz, T.; Huppert, D. Comprehensive Study of Ultrafast Excited-State Proton Transfer in Water and D2O Providing the Missing $RO^-\cdots H^+$ Ion-Pair Fingerprint. *J. Phys. Chem. A* **2014**, *118*, 4425-4443.

[55] Kumpulainen, T.; Rosspeintner, A.; Dereka, B.; Vauthey, E. Influence of Solvent Relaxation on Ultrafast Excited-State Proton Transfer to Solvent. *J. Phys. Chem. Lett.* **2017**, *8*, 4516-4521.

[56] Fang, C.; Tang, L.; Chen, C. Unveiling coupled electronic and vibrational motions of chromophores in condensed phases. *J. Chem. Phys.* **2019**, *151*, 200901.

[57] Oltrogge, L. M.; Boxer, S. G. Short Hydrogen Bonds and Proton Delocalization in Green Fluorescent Protein (GFP). *ACS Cent. Sci.* **2015**, *1*, 148-156.

[58] Pines, E.; Magnes, B.-Z.; Lang, M. J.; Fleming, G. R. Direct measurement of intrinsic proton transfer rates in diffusion-controlled reactions. *Chem. Phys. Lett.* **1997**, *281*, 413-420.

[59] MARONCELLI, M.; MACINNIS, J.; FLEMING, G. R. Polar Solvent Dynamics and Electron-Transfer Reactions. *Science* **1989**, *243*, 1674-1681.

[60] Jayaraman, S.; Haggie, P.; Wachter, R. M.; Remington, S. J.; Verkman, A. S. Mechanism and Cellular Applications of a Green Fluorescent Protein-based Halide Sensor. *J. Biol. Chem.* **2000**, *275*, 6047-6050.

[61] Tang, L.; Wang, Y.; Zhu, L.; Kallio, K.; Remington, S. J.; Fang, C. Photoinduced proton transfer inside an engineered green fluorescent protein: a stepwise–concerted-hybrid reaction. *Phys. Chem. Chem. Phys.* **2018**, *20*, 12517-12526.

[62]   Tachibana, S. R.; Tang, L.; Zhu, L.; Liu, W.; Wang, Y.; Fang, C. Watching an Engineered Calcium Biosensor Glow: Altered Reaction Pathways before Emission. *J. Phys. Chem. B* **2018**, *122*, 11986-11995.

[63]   Lin, C.-Y.; Romei, M. G.; Oltrogge, L. M.; Mathews, I. I.; Boxer, S. G. Unified Model for Photophysical and Electro-Optical Properties of Green Fluorescent Proteins. *J. Am. Chem. Soc.* **2019**, *141*, 15250-15265.

[64]   Andersen, L. H.; Lapierre, A.; Nielsen, S. B.; Nielsen, I. B.; Pedersen, S. U.; Pedersen, U. V.; Tomita, S. Chromophores of the green fluorescent protein studied in the gas phase. *Eur. Phys. J. D* **2002**, *20*, 597-600.

[65]   Brejc, K.; Sixma, T. K.; Kitts, P. A.; Kain, S. R.; Tsien, R. Y.; Ormö, M.; Remington, S. J. Structural basis for dual excitation and photoisomerization of the *Aequorea victoria* green fluorescent protein. *Proc. Natl. Acad. Sci. U.S.A.* **1997**, *94*, 2306-2311.

[66]   Solntsev, K. M.; Poizat, O.; Dong, J.; Rehault, J.; Lou, Y.; Burda, C.; Tolbert, L. M. Meta and Para Effects in the Ultrafast Excited-State Dynamics of the Green Fluorescent Protein Chromophores. *J. Phys. Chem. B* **2008**, *112*, 2700-2711.

[67]   Bell, A. F.; He, X.; Wachter, R. M.; Tonge, P. J. Probing the Ground State Structure of the Green Fluorescent Protein Chromophore Using Raman Spectroscopy. *Biochemistry* **2000**, *39*, 4423-4431.

[68]   Baranov, M. S.; Lukyanov, K. A.; Borissova, A. O.; Shamir, J.; Kosenkov, D.; Slipchenko, L. V.; Tolbert, L. M.; Yampolsky, I. V.; Solntsev, K. M. Conformationally Locked Chromophores as Models of Excited-State Proton Transfer in Fluorescent Proteins. *J. Am. Chem. Soc.* **2012**, *134*, 6025-6032.

[69]   Yang, J.-S.; Huang, G.-J.; Liu, Y.-H.; Peng, S.-M. Photoisomerization of the green fluorescence protein chromophore and the meta- and para-amino analogues. *Chem. Commun.* **2008**, 1344-1346.

[70]   Chatterjee, T.; Lacombat, F.; Yadav, D.; Mandal, M.; Plaza, P.; Espagne, A.; Mandal, P. K. Ultrafast Dynamics of a Green Fluorescent Protein Chromophore Analogue: Competition between Excited-State Proton Transfer and Torsional Relaxation. *J. Phys. Chem. B* **2016**, *120*, 9716-9722.

[71]   Chang, J.; Romei, M. G.; Boxer, S. G. Structural Evidence of Photoisomerization Pathways in Fluorescent Proteins. *J. Am. Chem. Soc.* **2019**, *141*, 15504-15508.

[72]   Romei, M. G.; Lin, C.-Y.; Mathews, I. I.; Boxer, S. G. Electrostatic control of photoisomerization pathways in proteins. *Science* **2020**, *367*, 76-79.

[73]   Litvinenko, K. L.; Webber, N. M.; Meech, S. R. Internal Conversion in the Chromophore of the Green Fluorescent Protein: Temperature Dependence and Isoviscosity Analysis. *J. Phys. Chem. A* **2003**, *107*, 2616-2623.

[74] Qian, X.; Xu, Z. Fluorescence imaging of metal ions implicated in diseases. *Chem. Soc. Rev.* **2015**, *44*, 4487-4493.

[75] Subach, F. V.; Verkhusha, V. V. Chromophore Transformations in Red Fluorescent Proteins. *Chem. Rev.* **2012**, *112*, 4308-4327.

[76] Acharya, A.; Bogdanov, A. M.; Grigorenko, B. L.; Bravaya, K. B.; Nemukhin, A. V.; Lukyanov, K. A.; Krylov, A. I. Photoinduced Chemistry in Fluorescent Proteins: Curse or Blessing? *Chem. Rev.* **2017**, *117*, 758-795.

[77] Gonçalves, M. S. T. Fluorescent Labeling of Biomolecules with Organic Probes. *Chem. Rev.* **2009**, *109*, 190-212.

[78] Karton-Lifshin, N.; Albertazzi, L.; Bendikov, M.; Baran, P. S.; Shabat, D. "Donor–Two-Acceptor" Dye Design: A Distinct Gateway to NIR Fluorescence. *J. Am. Chem. Soc.* **2012**, *134*, 20412-20420.

[79] S., B. N.; A., M. K.; V., Y. I.; S., B. M. Bioinspired Fluorescent Dyes Based on a Conformationally Locked Chromophore of the Fluorescent Protein Kaede. *Eur. J. Org. Chem.* **2015**, *2015*, 5716-5721.

[80] Chen, W.; Xu, S.; Day, J. J.; Wang, D.; Xian, M. A General Strategy for Development of Near-Infrared Fluorescent Probes for Bioimaging. *Angew. Chem. Int. Ed.* **2017**, *56*, 16611-16615.

[81] Chen, H.-J.; Chew, C. Y.; Chang, E.-H.; Tu, Y.-W.; Wei, L.-Y.; Wu, B.-H.; Chen, C.-H.; Yang, Y.-T.; Huang, S.-C.; Chen, J.-K.; Chen, I. C.; Tan, K.-T. S-Cis Diene Conformation: A New Bathochromic Shift Strategy for Near-Infrared Fluorescence Switchable Dye and the Imaging Applications. *J. Am. Chem. Soc.* **2018**, *140*, 5224-5234.

[82] Long, L.; Huang, M.; Wang, N.; Wu, Y.; Wang, K.; Gong, A.; Zhang, Z.; Sessler, J. L. A Mitochondria-Specific Fluorescent Probe for Visualizing Endogenous Hydrogen Cyanide Fluctuations in Neurons. *J. Am. Chem. Soc.* **2018**, *140*, 1870-1875.

[83] Prioli, S.; Reinholdt, P.; Hornum, M.; Kongsted, J. Rational Design of Nile Red Analogs for Sensing in Membranes. *J. Phys. Chem. B* **2019**, *123*, 10424-10432.

[84] Tang, J.; Robichaux, M. A.; Wu, K.-L.; Pei, J.; Nguyen, N. T.; Zhou, Y.; Wensel, T. G.; Xiao, H. Single-Atom Fluorescence Switch: A General Approach toward Visible-Light-Activated Dyes for Biological Imaging. *J. Am. Chem. Soc.* **2019**, *141*, 14699-14706.

[85] Ren, X.; Zhang, F.; Luo, H.; Liao, L.; Song, X.; Chen, W. Red-emitting boron difluoride complexes with a mega-large Stokes shift and unexpectedly high fluorescence quantum yield. *Chem. Commun.* **2020**, *56*, 2159-2162.

[86] Ermakova, Y. G.; Sen, T.; Bogdanova, Y. A.; Smirnov, A. Y.; Baleeva, N. S.; Krylov, A. I.; Baranov, M. S. Pyridinium Analogues of Green Fluorescent Protein Chromophore: Fluorogenic Dyes with Large Solvent-Dependent Stokes Shift. *J. Phys. Chem. Lett.* **2018**, *9*, 1958-1963.

[87] Zhao, Y.; Araki, S.; Wu, J.; Teramoto, T.; Chang, Y.-F.; Nakano, M.; Abdelfattah, A. S.; Fujiwara, M.; Ishihara, T.; Nagai, T.; Campbell, R. E. An Expanded Palette of Genetically Encoded Ca^{2+} Indicators. *Science* **2011**, *333*, 1888-1891.

[88] Chen, Z.; Ai, H.-w. Single Fluorescent Protein-Based Indicators for Zinc Ion (Zn^{2+}). *Anal. Chem.* **2016**, *88*, 9029-9036.

[89] Marvin, J. S.; Borghuis, B. G.; Tian, L.; Cichon, J.; Harnett, M. T.; Akerboom, J.; Gordus, A.; Renninger, S. L.; Chen, T.-W.; Bargmann, C. I.; Orger, M. B.; Schreiter, E. R.; Demb, J. B.; Gan, W.-B.; Hires, S. A.; Looger, L. L. An optimized fluorescent probe for visualizing glutamate neurotransmission. *Nat. Methods* **2013**, *10*, 162-170.

[90] Tao, R.; Zhao, Y.; Chu, H.; Wang, A.; Zhu, J.; Chen, X.; Zou, Y.; Shi, M.; Liu, R.; Su, N.; Du, J.; Zhou, H.-M.; Zhu, L.; Qian, X.; Liu, H.; Loscalzo, J.; Yang, Y. Genetically encoded fluorescent sensors reveal dynamic regulation of NADPH metabolism. *Nat. Methods* **2017**, *14*, 720-728.

[91] Tantama, M.; Martínez-François, J. R.; Mongeon, R.; Yellen, G. Imaging energy status in live cells with a fluorescent biosensor of the intracellular ATP-to-ADP ratio. *Nat. Commun.* **2013**, *4*, 2550.

[92] Tutol, J. N.; Kam, H. C.; Dodani, S. C. Identification of mNeonGreen as a pH-Dependent, Turn-On Fluorescent Protein Sensor for Chloride. *ChemBioChem* **2019**, *20*, 1759-1765.

[93] Greenwald, E. C.; Mehta, S.; Zhang, J. Genetically Encoded Fluorescent Biosensors Illuminate the Spatiotemporal Regulation of Signaling Networks. *Chem. Rev.* **2018**, *118*, 11707-11794.

[94] Koide, Y.; Urano, Y.; Hanaoka, K.; Piao, W.; Kusakabe, M.; Saito, N.; Terai, T.; Okabe, T.; Nagano, T. Development of NIR Fluorescent Dyes Based on Si–rhodamine for in Vivo Imaging. *J. Am. Chem. Soc.* **2012**, *134*, 5029-5031.

[95] Yuan, L.; Lin, W.; Zheng, K.; He, L.; Huang, W. Far-red to near infrared analyte-responsive fluorescent probes based on organic fluorophore platforms for fluorescence imaging. *Chem. Soc. Rev.* **2013**, *42*, 622-661.

[96] Kim, E.; Koh, M.; Lim, B. J.; Park, S. B. Emission Wavelength Prediction of a Full-Color-Tunable Fluorescent Core Skeleton, 9-Aryl-1,2-dihydropyrrolo[3,4-b]indolizin-3-one. *J. Am. Chem. Soc.* **2011**, *133*, 6642-6649.

[97]   Hashimoto, N.; Umano, R.; Ochi, Y.; Shimahara, K.; Nakamura, J.; Mori, S.; Ohta, H.; Watanabe, Y.; Hayashi, M. Synthesis and Photophysical Properties of λ^5-Phosphinines as a Tunable Fluorophore. *J. Am. Chem. Soc.* **2018**, *140*, 2046-2049.

[98]   Jun, J. V.; Petersson, E. J.; Chenoweth, D. M. Rational Design and Facile Synthesis of a Highly Tunable Quinoline-Based Fluorescent Small-Molecule Scaffold for Live Cell Imaging. *J. Am. Chem. Soc.* **2018**, *140*, 9486-9493.

[99]   Ren, T.-B.; Xu, W.; Zhang, W.; Zhang, X.-X.; Wang, Z.-Y.; Xiang, Z.; Yuan, L.; Zhang, X.-B. A General Method To Increase Stokes Shift by Introducing Alternating Vibronic Structures. *J. Am. Chem. Soc.* **2018**, *140*, 7716-7722.

[100]   Chen, C.; Baranov, M. S.; Zhu, L.; Baleeva, N. S.; Smirnov, A. Y.; Zaitseva, S. O.; Yampolsky, I. V.; Solntsev, K. M.; Fang, C. Designing redder and brighter fluorophores by synergistic tuning of ground and excited states. *Chem. Commun.* **2019**, *55*, 2537-2540.

[101]   Chen, C.; Fang, C. Devising Efficient Red-Shifting Strategies for Bioimaging: A Generalizable Donor-Acceptor Fluorophore Prototype. *Chem. Asian. J.* **2020**, *15*, 1514-1523.

[102]   Hsu, Y.-H.; Chen, Y.-A.; Tseng, H.-W.; Zhang, Z.; Shen, J.-Y.; Chuang, W.-T.; Lin, T.-C.; Lee, C.-S.; Hung, W.-Y.; Hong, B.-C.; Liu, S.-H.; Chou, P.-T. Locked ortho- and para-Core Chromophores of Green Fluorescent Protein; Dramatic Emission Enhancement via Structural Constraint. *J. Am. Chem. Soc.* **2014**, *136*, 11805-11812.

Chapter 2 Experimental Methods and Data Analysis

"… all things are made of atoms, and that everything that living things do can be understood in terms of the jigglings and wigglings of atoms." This famous quote by the physicist Richard P. Feynman highlights the essence of chemical reactions, which is movement of electrons and nuclei. In quantum mechanics, this is described by the wavefunction of the system: $\psi = \psi_{e^-} \cdot \psi_{nuclear} = \psi_{e^-} \cdot \psi_{vib} \cdot \psi_{rot}$, where ψ_{e^-}, ψ_{vib}, ψ_{rot} represent the electronic, vibrational, rotational wavefunctions, respectively. In our laboratory, we use two complementary ultrafast spectroscopic techniques (electronic and vibrational) to provide a rather complete kinetic picture ("molecular movie") for the photosensitive molecular systems in condensed phase that undergo both electronic and nuclear motions. In this chapter, femtosecond transient absorption (electronic) and stimulated Raman (vibrational) spectroscopy are described that cover the fundamental aspects such as signal generation, spectral interpretation, data analysis, etc.

2.1 Femtosecond transient absorption spectroscopy (fs-TA)

In this section, theoretical basics and typical data analysis for femtosecond transient absorption spectroscopy (fs-TA) will be described in a concise manner. One can refer to the individual research papers for more details if needed. The fs-TA is one of the oldest but very robust time-resolved electronic techniques that can probe the electronic excited states with higher sensitivity compared to many other nonlinear

spectroscopic techniques. The experimental setup is also relatively simple as it only involves two pulses.[1] A big advantage of fs-TA is the low requirement for the selection of samples. For instance, compared to time-resolved fluorescence techniques, fs-TA does not require the samples to be fluorescent and therefore can provide more information for samples that are non-fluorescent or involve dark states.[2,3] This makes fs-TA versatile for the investigation of a great variety of molecular systems. A drawback of fs-TA is the high degree of overlap of electronic features, making the data analysis and interpretation quite difficult. For complicated systems involving diverse reaction pathways, this becomes particularly challenging.[4-6] Therefore, it is better to combine fs-TA with other techniques to provide complementary information for the system of interest. In our laboratory, the fs-TA is used as a partner technique for femtosecond stimulated Raman spectroscopy (FSRS) not only for complementary information but also for the strategic selection of resonance conditions (see below in section 2.2).

2.1.1 Basics

Briefly, one can understand fs-TA as an excited-state version of the steady-state ultraviolet/visible (UV/vis) absorption spectroscopy. But instead of starting from the electronic ground state, typically the singlet ground state (S_0), the electronic transitions including absorption/emission in fs-TA start from the excited state the molecule is excited to, typically S_1. Besides absorption, fs-TA can also probe the $S_1{\rightarrow}S_0$ emission transition. In short, UV/vis spectroscopy measures $S_0{\rightarrow}S_n$ ($n > 0$) absorption; fs-TA

typically measures $S_1 \rightarrow S_n$ (n > 1) absorption and $S_1 \rightarrow S_0$ emission. If a triplet state is involved, the fs-TA will show a purely positive band (ESA) from $T_1 \rightarrow T_n$ (n > 1).

The apparatus for fs-TA consists of two beams (Figure 2.1). A pump pulse promotes the excited-state population by exciting a portion of the sample to the target electronic excited state. The second broadband probe pulse with a time delay to the pump pulse interacts with the molecules and registers the intensity change, which is then sent into the detector. The generation of pump and probe beams can be seen in the later chapters in the experimental sections. Last, the computer processes the signal by performing the following algorithm to obtain the differential absorbance (ΔA) as a measure of fs-TA intensity (similar to the absorbance in UV/vis spectroscopy) based on the Beer-Lambert's law:

$$\Delta A\,(\lambda, \tau) = A_{ex} - A_{gr} = \left[-\log\left(\frac{I_{ex}(\lambda, \tau)}{I_0(\lambda)}\right)\right] - \left[-log\left(\frac{I_{gr}(\lambda)}{I_0(\lambda)}\right)\right] = -log\left(\frac{I_{ex}(\lambda, \tau)}{I_{gr}(\lambda)}\right)$$

where I_{ex}, I_{gr} are the probe beam intensity after passing through the sample in the presence and absence of pump excitation, respectively. I_0 is incident probe beam intensity at the same sample.
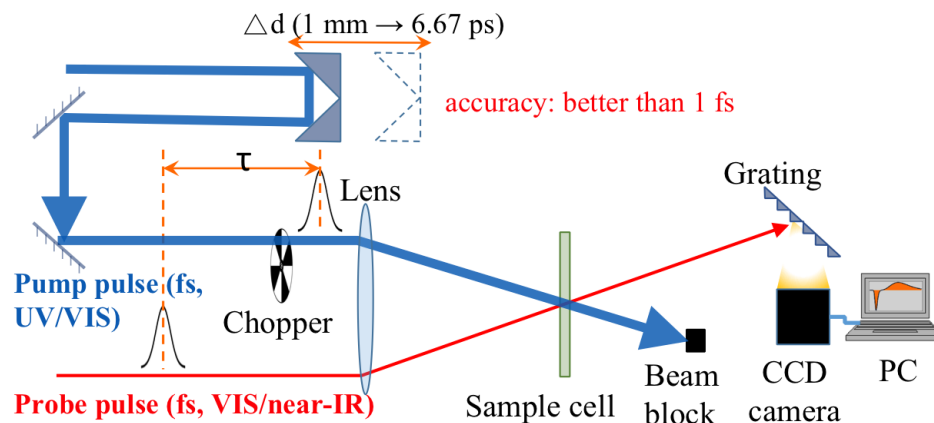
Figure 2.1. Schematic of beam geometry in fs-TA setup. The beam generation routes for pump and probe pulses are not shown.

The fs-TA signal usually arises from the following processes (Figure 2.2).

(1) Ground-state bleach (GSB). This signal is not caused by optical processes in the excited states but rather a result of the algorithm to calculate ΔA. The photoexcitation leads to the ground-state population depletion and hence less ground-state absorption. For example, assuming 10% excitation efficiency, the ΔA at ground-state absorption region is given by $(0.1A_{ex} + 0.9A_{gr}) - A_{gr} = 0.1A_{ex} - 0.1A_{gr}$. If the excited-state absorption is not present in the ground-state absorption region ($A_{ex} = 0$) or weaker than the ground-state absorption in the same region ($A_{ex} < A_{gr}$), ΔA is *negative* in magnitude. Otherwise, the ΔA will be overwhelmed by the positive ESA intensity in this spectral region.

(2) Stimulated emission (SE). The negative signal that is usually Stokes-shifted with respect to the ground state absorption is stimulated emission (SE). This is predicted by the Einstein coefficient B_{21} that occurs when the transition is

optically allowed. A photon from the probe pulse induces the emission of another photon from the molecule's excited state to ground state with exactly the same frequency and direction as the probe photon. The SE band typically has a similar profile to that of fluorescence with exceptions of dark state and nonfluorescent twisted intramolecular charge-transfer (TICT) state.[2,7] Due to the SE process-caused intensity increase, the SE signal is *negative* (see the above equation of ΔA).

(3) Excited-state absorption (ESA). This process occurs when the transitions from the excited state (usually S_1) to higher lying excited states are optically allowed. Similar to ground state absorption, the ESA signal is *positive* due to the probe intensity decrease during the light-induced absorption process. Notably, not all positive signals are ESA (see below).

(4) Ground-state absorption (GSA) by ground-state intermediates or photoproducts, either short- or long-lived. In systems involving isomerization for example, the isomerization reaction may produce short- or long-lived isomerized conformers in the ground state.[8-11] The absorption of such a product will generate a *positive* ΔA signal, which is discernible if the position is shifted from the original isomer.[12] Some molecules that can undergo facile deactivating twisting motions also show *positive* red-shifted hot ground-state absorption signal along the back-twisting coordinate on the ground-state potential energy surface.[2,5]
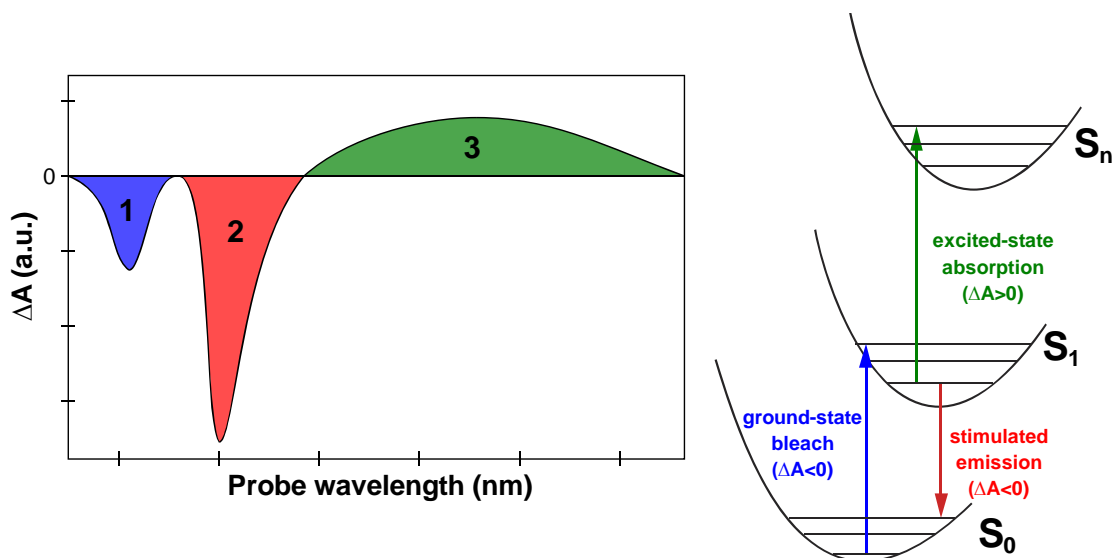
Figure 2.2. Illustration of characteristic fs-TA features (left) and corresponding optical processes by color (right). The parabolic-like curve depicts the potential energy surface and embedded lines denote the vibrational levels within the electronic states.

2.1.2 Probe-wavelength dependent analysis

The most common analysis of fs-TA spectra is to perform kinetics analysis at different wavelength regions where different reaction species are featured. One can extract the intensity data from one single wavelength or a small slice of wavelengths, and then plot them against the time delay, and fit the data based on kinetics. Due to the first-order reaction nature and presence of reversible reactions of many processes in the excited state, the dynamics can be fitted with a multiple-exponential function or dealt with by other functions otherwise. A multi-exponential function is usually given by

$$S(t) = y_0 + A_0 e^{-\frac{t-t_0}{\tau_0}} + A_1 e^{-\frac{t-t_0}{\tau_1}} + A_2 e^{-\frac{t-t_0}{\tau_2}} + \cdots$$

where A_i ($i = 0, 1, 2, ...$) is the amplitude, τ_i is the characteristic time constant, y_0 is the y-offset, and t_0 is the time zero. In a practical experiment, the actual data follow the function with convolution of the exponential decays and instrument response function (IRF, determined by the cross correlation of the pump-probe pulses). The IRF is usually approximated as a gaussian function $R(t) \sim exp\left(\frac{-(t-t_0)^2}{2\sigma^2}\right)$, where σ is the standard deviation. The observed signal is therefore fitted by

$$I(t) = \int_0^\infty R(t'-t)S(t')dt' = \sum_i \frac{1}{2} exp\left(\frac{\sigma^2}{2\tau_i^2} - \frac{t-t_0}{\tau_i}\right)\left[1 + erf\left(\frac{t - t_0 - \frac{\sigma^2}{\tau_i}}{\sqrt{2}\sigma}\right)\right]$$

where $erf\ (x)$ is the error function.[13]

2.1.3 Global and target analysis

As mentioned above, fs-TA dynamics analysis could be greatly hindered by the overlap of features from different reaction species. A simultaneous (global) analysis of the full data in both dimensions, time delay and wavelength, is required to disentangle the processes underlying the overlapped data.[13] The analysis is based on assumptions regarding the measurement process and the kinetic processes that occur after photoexcitation. Therefore, IRF and a kinetic model that connects the components of the system are considered during analysis. In our laboratory, the Glotaran program has been used to perform the global and target analysis.[14]

First, the exponential decays are still fitted with convolution with the IRF. But due to the presence of dispersion of the probe pulse, the position of IRF (i.e., t_0) can be

modeled by a polynomial. Second, the multi-dimensional data are expressed as a superposition of the characteristic spectra $\varepsilon_l(\lambda)$ of the components weighted by their concentrations $c_l(t)$:

$$\psi(t, \lambda) = \sum_{l}^{n_{comp}} c_l(t)\varepsilon_l(\lambda)$$

The $c_l(t)$ is solved from a compartmental model described by a differential equation (so the solution is given by exponentials).

$$\frac{d}{dt}c(t) = Kc(t) + j(t)$$

where the vector $c(t) = \left[c_1(t) \dots c_{n_{comp}}(t) \right]^T$ and $j(t)$ describes the concentrations of each compartment and IRF with other possible input, respectively. K is the transfer matrix that describes the compartmental model. The diagonal elements indicate the total decay of the individual compartments. The off-diagonal elements indicate the transitions between compartments from column to row. For example, the matrix element K_{32} (if it is non-zero) indicates the transition from compartment 2 (column) to compartment 3 (row).

Three different compartmental models are usually considered. (1) Parallel model. This model assumes parallel mono-exponential decays for all components and yields the so-called decay associated difference spectra (DADS). In this model, the K matrix only has non-zero diagonal elements. (2) Sequential model. This model assumes the unidirectional transition from the first to last component (i.e., $1 \rightarrow 2 \rightarrow 3 \rightarrow \dots n_{comp}$) and yields the evolutional associated difference spectra (EADS). In this model, the off-

diagonal elements $(i+1, i)$ with $i = 1, 2, .. n_{comp} - 1$ are nonzero and the last

diagonal component (n_{comp}, n_{comp}) is nonzero indicating self-decay. Note that EADS

is a linear combination of DADS and vice versa.[15] (3) A specific kinetic model. This is

also termed as target analysis. It may involve branching and a mixture of sequential

and branching for example. This model yields the species-associated difference spectra

(SADS). The K matrix varies with the kinetic model proposed.

Without a *priori* knowledge about the kinetics of the system, one can first perform the

DADS and EADS fitting to obtain a glance of the system. For most systems that

undergo consecutive excited state processes, EADS is more informative as it provides

a global view of how the system evolves. And if the system evolves sequentially, the

EADS are the true species spectra. With a *priori* knowledge about the kinetics of the

system, target analysis can also be performed to understand the kinetics. Of course, this

is not a trivial task. It requires more detailed knowledge about the system and likely

many tests of models. An important consideration in examining the model is whether

the output spectra match the assumed spectral features of each species proposed in this

model which carries distinguishable physicochemical properties of the molecular

system with a minimal number of pertinent species during modeling. [4-6,16-18]

2.2 Femtosecond stimulated Raman spectroscopy (FSRS)

In this section, theoretical basics and typical data analysis for femtosecond stimulated Raman spectroscopy (FSRS) will be briefly described. One can refer to the individual research papers for more details if needed. FSRS is a relatively new vibrational technique that has rapidly gained popularity in fundamental research since its invention back in 1990s.[3,19-27] Compared to many other time-resolved vibrational techniques, FSRS is advantageous in many aspects. For instance, FSRS can provide simultaneously high temporal and spectral resolutions due to the femtosecond actinic-picosecond Raman pump-femtosecond probe pulse (fs-ps-fs) configuration. The fs actinic-probe pulses give rise to the high temporal resolution, and the ps Raman pump with narrow bandwidth convoluted with the vibrational dephasing time determines the spectral resolution.[28,29] Another attribute of FSRS that makes FSRS stand out among various vibrational spectroscopic techniques is the resonance enhancement. It greatly improves the signal-to-noise ratio even with low sample concentrations.[4,30-35] Furthermore, FSRS is a mixed time-frequency domain technique and therefore significantly reduces the data acquisition time with respective to other time-domain techniques such as impulsive stimulated Raman, in which the all three pulses (actinic, Raman pump, and Raman probe) are of fs duration.[36,37] Also, FSRS works well for both low- and high-frequency modes while other techniques typically work best for a certain frequency region. For example, time-resolved infrared (IR) spectroscopy works best for high-frequency modes[38] while impulsive stimulated Raman spectroscopy works best for low-frequency modes.[39] The fs-ps-fs pulse train in FSRS makes it possible to track the low-frequency skeletal motions that gate and/or facilitate photochemical

reactions in the multidimensional potential energy surface through the anharmonic couplings with other vibrational motions.[21-23,40,41] These low-frequency coherences are generated by the fs actinic pump and the ps Raman pump ensures minimal interference by other coherences at early time in contrast to a fs pulse particularly in the purely time-domain technique. The capability of revealing multidimensional reaction coordinates and their couplings has drawn lots of attention in the development of many new techniques such as the two-dimensional spectroscopy including 2D electronic, 2D vibrational, and 2D electronic-vibrational techniques.[42-44]

2.2.1 Basics

FSRS is a third-order nonlinear spectroscopy and the signal is generated through the four wave-mixing process where the Raman pump (R_{pu}) and probe (R_{pr}) pulses interact with the system three times in total and the intensity is determined by the third-order polarization $P^{(3)}$ (the Raman pump interacts twice with the system).[28,29,31,45,46] In the presence and absence of the actinic pump (A_{pu}), one measures the excited- and ground-state FSRS spectra, respectively. A typical four-wave mixing process is shown in Figure 2.3. On- and off-resonance for Stokes FSRS are shown here because of the resonance enhancement effect in FSRS (which will be discussed in Chapter 3) and the former can produce much higher signal-to-noise ratio. The energy-level diagram can also be expressed by the double-sided Feynman diagram. According to the convention of Shen in stimulated Raman scattering (SRS),[47] there are eight Feynman diagrams that have the SRS output in the probe direction of the phase-match condition (see below).

Only one diagram is shown here because it is the most common process for FSRS signal generation especially for off-resonance conditions. When on-resonance, other diagrams may contribute significantly (see Chapter 3).[31,34,35,45,48,49]
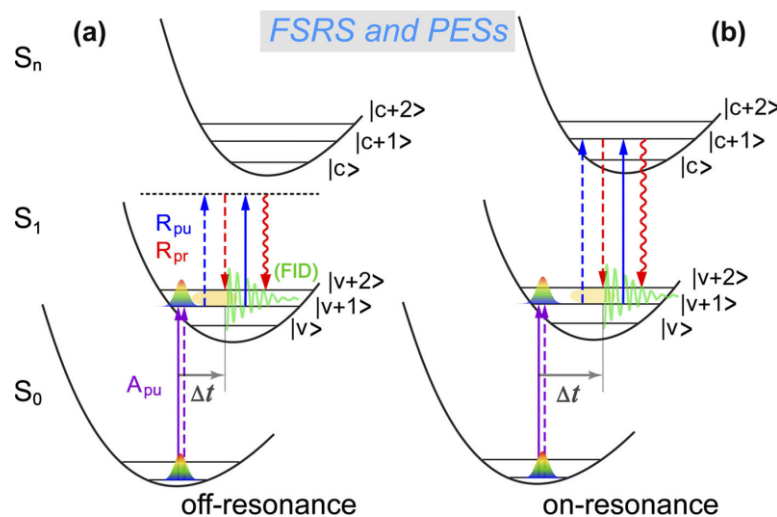
Figure 2.3. Four-wave mixing processes in excited-state FSRS under off-resonance and on-resonance conditions. The actinic pump, Raman pump, and Raman probe pulses are denoted by violet, blue, and red arrows, respectively. The solid and dashed arrows represent the light-matter interaction on the ket and bra sides of the molecular density matrix. Reproduced with permission from Ref. [46]. Copyright 2019 AIP Publishing.

The ground-state FSRS signal is obtained by spatially and temporally overlapping the Raman pump and probe pulses (Figure 2.4a).[50] Similar to the differential absorbance ΔA algorithm, Raman gain is used as the measure for FSRS intensity.[3,46,51]

$$Raman\ gain = \log\left(\frac{I}{I_0}\right) \propto a \cdot \sigma_R \cdot c \cdot I_{pu} \cdot z = \gamma,$$

where I and I_0 are the R_{pr} intensity in the presence and absence of R_{pu}, a is a constant (unit, cm$^2 \cdot$s) that contains several physical constants, σ_R is the Raman scattering cross section (unit, cm$^2 \cdot$mol^{-1}), c is the sample concentration (unit, mol$\cdot$cm^{-3}), I_{pu} is the R_{pu} intensity (unit, photons$\cdot$cm$^{-2} \cdot$s^{-1}), z is the sample pathlength (unit, cm), and the resultant Raman gain γ is unitless. Notably, when the Raman gain is small ($I \approx I_0$), $\log\left(\frac{I}{I_0}\right) \approx \frac{1}{2.303}\left(\frac{I}{I_0} - 1\right)$. So $\left(\frac{I}{I_0} - 1\right)$ is also valid to calculate the Raman gain. In the presence of A_{pu} (A_{pu} is on), the time-resolved FSRS is collected and processed in the same way as ground-state FSRS at each time delay, and then a one-to-one subtraction by the ground-state FSRS (A_{pu} is off) yields the excited-state FSRS spectrum as a function of time delay which better tracks the non-equilibrium structural dynamics.
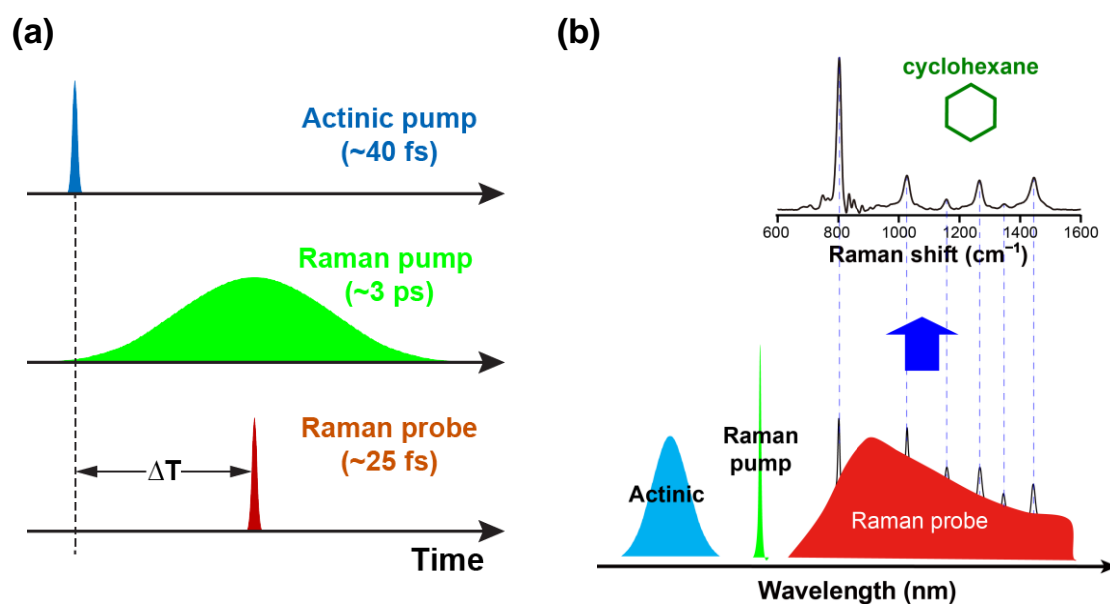
Figure 2.4. FSRS pulses in the time domain and using heterodyne detection. (a) Pulse sequence and durations of FSRS pulses. The time delay is defined by the time difference between the actinic pump and Raman pump-probe pulse pair. (b) Illustration

of the self heterodyne-detection in FSRS using cyclohexane as an example. The three incident laser pulses are illustrated in the frequency (wavelength) domain.

Experimentally, FSRS uses the heterodyne-detection along the probe direction to collect the spectrum. The vibrational signal appears on top of the probe profile and is extracted by dividing the probe field from the FSRS signal field.[28] Figure 2.4b showcases the acquisition of the FSRS spectrum of cyclohexane, a standard solvent for spectral calibration. FSRS is self-phase matched ($\vec{k}_{FSRS} = -\vec{k}_{pump} + \vec{k}_{probe} + \vec{k}_{pump} = \vec{k}_{probe}$) and the signal is collinear with the probe beam, which gives rise to eight possible Feynman diagrams (see above). Therefore, the FSRS signal is collected in the direction of the probe beam as shown in Figure 2.5.
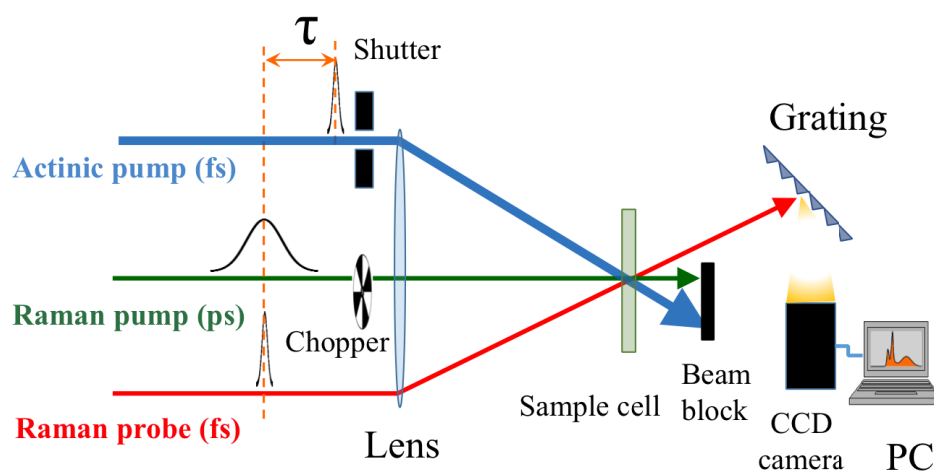
Figure 2.5. Schematic of beam geometry in FSRS. The FSRS signal is collected along the probe beam direction and registered by CCD camera after being dispersed on the ruled reflective grating.

Since resonance enhancement in FSRS greatly improves the signal-to-noise ratio that makes it versatile for a variety of systems, tunable wavelengths of FSRS pulses thus are necessary. In our laboratory, we built a tunable FSRS setup with the application of non-collinear optical parametric amplifier (NOPA) as shown in Figure 2.6.[52] The ps Raman pump wavelength is tuned through a two-stage ps NOPA system where the ps pump beam is generated by a home-built second harmonic band compressor (SHBC) and the signal beam, termed as the ps seed pusle also well, is generated from a fs-NOPA system followed by a spectral filter that selects the target wavelength. The wavelength tunability range of Raman pump is 480−720 nm by NOPA[53] in addition to 800 nm from the filtered fundamental pulse and 400 nm directly from SHBC. The actinic pump can also tuned through a fs-NOPA system with the tunability of 480−720nm. The probe beam is generated from supercontiuum white light (SCWL) by focusing a portion of the 800-nm fundamental pulse onto a 2-mm-thick sapphire crystal or a 2-mm-thick quartz cuvette filled with deionized water. To extend the probe tunability to regions around 800 nm (fundamental pulse) and 400 nm (SHG) where the incident laser residual overwhelms the SCWL, a broadband up-upconverted multicolor array (BUMA) was invented and built to obtain a background-free Raman probe (Figure 2.6).[54,55]
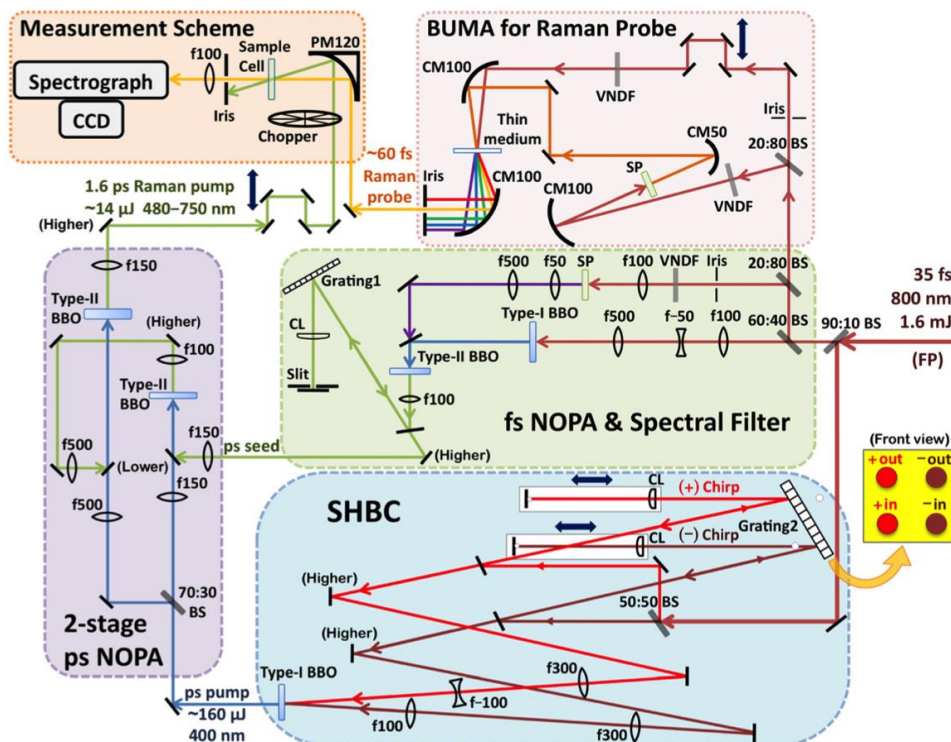
Figure 2.6. Schematic of a tunable FSRS setup. Abbreviations: NOPA (non-collinear optical parametric amplifier); SHBC (second harmonic bandwidth compressor); BUMA (broadband up-upconverted multicolor array). The compartmentalized optical setups for the generation of various laser pulses with specific wavelengths, duration, and roles in FSRS are highlighted with major optical components. Reproduced with permission from Ref. [52]. Copyright 2014 AIP Publishing LLC.

2.2.2 Data processing

FSRS data processing typically takes several steps: calibration, extraction of raw excited-state spectra, addback of ground-state spectrum, baseline subtraction, gaussian peak fitting, and dynamics fitting. This is a rigorous process that requires systematic processing of a large number of spectral datasets with consistency and reproducibility.

(1) Calibration. An organic solvent is typically used to calibrate the frequency axis. The choice of the standard is dependent upon the spectral region of interest. Cyclohexane is commonly used as its characteristic Raman bands cover a broad range from low frequency (~400 cm^{-1}) to mid-frequnecy ~1500 cm^{-1}. One can also use it to calibrate the high-frequency region (~3000 cm^{-1}). For low-frequency region below 400 cm^{-1}, one should use other standards with Raman bands in this region. For example, carbon tetrachloride (CCl_4) has multiple bands below 200 cm^{-1} and therefore provides excellent spectral precision for this region. One can also use mixed standards for even broader ranges.[55]

(2) Extraction of raw excited-state spectra. The raw excited-state spectra are obtained by subtracting the spectrum collected in the absence of A_{pu} (100% GS) from that in the presence of A_{pu} (10% ES + 90% GS) for each time delay. The resultant raw excited-state spectra contain 10% ES and 10% (−GS). The (−GS) is responsible for the ground-state bleach.

(3) Addback of ground-state spectrum. This step is to remove the ground-state bleach bands. Assuming no dispersive peaks and taking 10% (−GS) for example, one can add back 10% (+GS) to flatten the bleach peaks. This ratio may fluctuate a bit from time to time due to the experimental uncertainties. In some cases where the resonantly enhanced excited-state features dominate while the negative peaks at ground-state peak locations are comparable to the noise level, spectral addback may not be necessary and can be avoided without any noticeable effect on the spectral analysis.

(4) Baseline subtraction. The electronic background/baseline is mainly caused by the transient absorption effect and Raman-pump-induced effects on excited-state populations. Two post-processing methods of removing baselines have been commonly used. One is the manual baseline that is drawn based on certain understanding of the dataset.[4,56,57] An important criterion is that the baseline should be vibrationally featureless, meaning that the baseline should be a continuous smooth spline or spline-like curve within the range of vibrational bandwidths except for some abnormal spikes or bumps. The advantage of this method is the high degree of freedom in adjusting the baseline that can deal with anomalies and compromise the error space in automatic baseline in some occasions (see below). The drawback is the possible deviation from the true baseline caused by human input errors, i.e., subjective judgement, which has long been debated in the field.[30,56,58,59] The other one is automatic baseline generated by a polynomial/spline function. This method produces a smooth baseline with little subjective input and therefore has been adopted by many FSRS researchers.[22,32,41] However, since the true baseline is unknown, inaccurate baseline could still be generated if the underlying background cannot be described by a concave polynomial. For example, in regions of clustered bands that extend across hundreds of wavenumbers corresponding to tens of nanometers in wavelength regime, a single automatic concave baseline might be problematic because of possible convex region in TA background from vibronic couplings, crowded ESA bands, etc. In addition to these two methods, some efforts have been attempted to remove the baseline experimentally.[60,61]

Regardless, the effective and efficient baseline removal remains an active topic in FSRS and deserves further exploration.

(5) Gaussian peak fitting. Theoretically, FSRS bands are Lorentzian-type peaks but due to the inhomogeneous broadening in solution systems, gaussian-type peaks can reasonably be used to fit the vibrational bands. This step yields the intensity and center frequency for FSRS vibrational modes, while effectively removing the spectral noises for the subsequent dynamics plots and further analysis.

(6) Dynamics fitting. With information of peak intensity and center frequency, the IRF -convoluted multi-exponential fit (same as fs-TA dynamics fitting) can be performed for the observed vibrational modes. Such a vibrational-mode-dependent dynamics analysis is a staple of FSRS in tracking multiple atomic motions at once, and elucidating the multidimensional reaction coordinates following electronic excitation.

2.2.3 Intensity and frequency dynamics

The intensity and frequency dynamics are two common kinetic analyses in FSRS. Peak intensity is an extensive property of the system, i.e., subject to the quantity such as sample concentration, pulse power, and resonance condition, etc., and therefore reflects more on the content/concentration change of a specific reaction species. This is well predicted by the kinetics for which the photoreactant exhibits pure decays mono- or multi-exponentially in the presence of reversible reactions while the photoproduct and intermediate(s) are characterized by one or more rise components followed by decay

dynamics.[33,62] Notably, the mode intensity dynamics are a more reliable interpretation of a certain reaction species due to the less overlap between vibrational modes with respect to the probe-wavelength-dependent dynamics in fs-TA (see 2.1.2 above).

Compared to the peak intensity, peak frequency is an intensive property of the system, i.e., independent of the abovementioned conditions related to the quantity of the system, and therefore manifests the intrinsic processes. The frequency blueshift is usually a result of vibrational relaxation/cooling or structural changes while the frequency redshift only originates from the structural changes.[21,22,63,64] Besides, the comparison between the ground- and excited-state FSRS mode frequencies also provides valuable insights into the system concerning both electronic and nuclear structures.[65]

In either case, the mode-dependent dynamics might be observed. This is a result of the multidimensional reaction coordinates that are displayed through different vibrational modes. Thus, the obtained vibrational-mode-dependent information offers a unique analytical route to glean the multi-dimensional potential energy surface. Furthermore, the couplings between these reaction coordinates could be retrieved from the oscillatory behaviors in the observed mode intensity or frequency, revealing intrinsic couplings between an electronic transition and vibrational motion, or between characteristic vibrational motions. In essence, these couplings dictate the intricate energy transfer pathways within the target molecules.[21,22,66] This is certainly a difficult task due to the stringent experimental requirement but represents a ground-breaking research front in revealing the reaction nature at a fundamental level.

2.3 References

[1] Berera, R.; van Grondelle, R.; Kennis, J. T. M. Ultrafast transient absorption spectroscopy: principles and application to photosynthetic systems. *Photosynth. Res.* **2009**, *101*, 105-118.

[2] Tang, L.; Fang, C. Nitration of Tyrosine Channels Photoenergy through a Conical Intersection in Water. *J. Phys. Chem. B* **2019**, *123*, 4915-4928.

[3] Hall, C. R.; Conyard, J.; Heisler, I. A.; Jones, G.; Frost, J.; Browne, W. R.; Feringa, B. L.; Meech, S. R. Ultrafast Dynamics in Light-Driven Molecular Rotary Motors Probed by Femtosecond Stimulated Raman Spectroscopy. *J. Am. Chem. Soc.* **2017**, *139*, 7408-7414.

[4] Chen, C.; Liu, W.; Baranov, M. S.; Baleeva, N. S.; Yampolsky, I. V.; Zhu, L.; Wang, Y.; Shamir, A.; Solntsev, K. M.; Fang, C. Unveiling Structural Motions of a Highly Fluorescent Superphotoacid by Locking and Fluorinating the GFP Chromophore in Solution. *J. Phys. Chem. Lett.* **2017**, *8*, 5921-5928.

[5] Chen, C.; Zhu, L.; Boulanger, S. A.; Baleeva, N. S.; Myasnyanko, I. N.; Baranov, M. S.; Fang, C. Ultrafast excited-state proton transfer dynamics in dihalogenated non-fluorescent and fluorescent GFP chromophores. *J. Chem. Phys.* **2020**, *152*, 021101.

[6] Quick, M.; Dobryakov, A. L.; Ioffe, I. N.; Granovsky, A. A.; Kovalenko, S. A.; Ernsting, N. P. Perpendicular State of an Electronically Excited Stilbene: Observation by Femtosecond-Stimulated Raman Spectroscopy. *J. Phys. Chem. Lett.* **2016**, *7*, 4047-4052.

[7] Grabowski, Z. R.; Rotkiewicz, K.; Rettig, W. Structural Changes Accompanying Intramolecular Electron Transfer: Focus on Twisted Intramolecular Charge-Transfer States and Structures. *Chem. Rev.* **2003**, *103*, 3899-4032.

[8] Waldeck, D. H. Photoisomerization dynamics of stilbenes. *Chem. Rev.* **1991**, *91*, 415-436.

[9] Chatterjee, T.; Lacombat, F.; Yadav, D.; Mandal, M.; Plaza, P.; Espagne, A.; Mandal, P. K. Ultrafast Dynamics of a Green Fluorescent Protein Chromophore Analogue: Competition between Excited-State Proton Transfer and Torsional Relaxation. *J. Phys. Chem. B* **2016**, *120*, 9716-9722.

[10] Yang, J.-S.; Huang, G.-J.; Liu, Y.-H.; Peng, S.-M. Photoisomerization of the green fluorescence protein chromophore and the meta- and para-amino analogues. *Chem. Commun.* **2008**, 1344-1346.

[11] Dasgupta, J.; Frontiera, R. R.; Taylor, K. C.; Lagarias, J. C.; Mathies, R. A. Ultrafast excited-state isomerization in phytochrome revealed by femtosecond stimulated Raman spectroscopy. *Proc. Natl. Acad. Sci. U.S.A.* **2009**, *106*, 1784-1789.

[12] Mathes, T.; Ravensbergen, J.; Kloz, M.; Gleichmann, T.; Gallagher, K. D.; Woitowich, N. C.; St. Peter, R.; Kovaleva, S. E.; Stojković, E. A.; Kennis, J. T. M. Femto- to Microsecond Photodynamics of an Unusual Bacteriophytochrome. *J. Phys. Chem. Lett.* **2015**, *6*, 239-243.

[13] van Stokkum, I. H. M.; Larsen, D. S.; van Grondelle, R. Global and target analysis of time-resolved spectra. *Biochim. Biophys. Acta* **2004**, *1657*, 82-104.

[14] Snellenburg, J., J.; Laptenok, S.; Seger, R.; Mullen, K., M.; Van Stokkum, I., H.M. Glotaran: A Java-based graphical user interface for the R package TIMP. *J. Stat. Softw.* **2012**, *49*, 1-22.

[15] Toh, K. C.; Stojković, E. A.; van Stokkum, I. H. M.; Moffat, K.; Kennis, J. T. M. Fluorescence quantum yield and photochemistry of bacteriophytochrome constructs. *Phys. Chem. Chem. Phys.* **2011**, *13*, 11985-11997.

[16] Kennis, J. T. M.; Larsen, D. S.; van Stokkum, I. H. M.; Vengris, M.; van Thor, J. J.; van Grondelle, R. Uncovering the hidden ground state of green fluorescent protein. *Proc. Natl. Acad. Sci. U.S.A.* **2004**, *101*, 17988-17993.

[17] Di Donato, M.; van Wilderen, L. J. G. W.; Van Stokkum, I. H. M.; Stuart, T. C.; Kennis, J. T. M.; Hellingwerf, K. J.; van Grondelle, R.; Groot, M. L. Proton transfer events in GFP. *Phys. Chem. Chem. Phys.* **2011**, *13*, 16295-16305.

[18] Snellenburg, J. J.; Laptenok, S. P.; DeSa, R. J.; Naumov, P.; Solntsev, K. M. Excited-State Dynamics of Oxyluciferin in Firefly Luciferase. *J. Am. Chem. Soc.* **2016**, *138*, 16252-16258.

[19] Yoshizawa, M.; Hattori, Y.; Kobayashi, T. Femtosecond time-resolved resonance Raman gain spectroscopy in polydiacetylene. *Phys. Rev. B* **1994**, *49*, 13259-13262.

[20] Kukura, P.; McCamant, D. W.; Yoon, S.; Wandschneider, D. B.; Mathies, R. A. Structural Observation of the Primary Isomerization in Vision with Femtosecond-Stimulated Raman. *Science* **2005**, *310*, 1006-1009.

[21] Fang, C.; Frontiera, R. R.; Tran, R.; Mathies, R. A. Mapping GFP Structure Evolution During Proton Transfer with Femtosecond Raman Spectroscopy. *Nature* **2009**, *462*, 200-204.

[22] Hoffman, D. P.; Ellis, S. R.; Mathies, R. A. Characterization of a Conical Intersection in a Charge-Transfer Dimer with Two-Dimensional Time-Resolved Stimulated Raman Spectroscopy. *J. Phys. Chem. A* **2014**, *118*, 4955-4965.

[23] Liu, W.; Wang, Y.; Tang, L.; Oscar, B. G.; Zhu, L.; Fang, C. Panoramic portrait of primary molecular events preceding excited state proton transfer in water. *Chem. Sci.* **2016**, *7*, 5484-5494.

[24] Tang, L.; Wang, Y.; Zhu, L.; Kallio, K.; Remington, S. J.; Fang, C. Photoinduced proton transfer inside an engineered green fluorescent protein: a stepwise–concerted–hybrid reaction. *Phys. Chem. Chem. Phys.* **2018**, *20*, 12517-12526.

[25] Yoshizawa, M.; Kurosawa, M. Femtosecond time-resolved Raman spectroscopy using stimulated Raman scattering. *Phys. Rev. A* **1999**, *61*, 013808.

[26] Buhrke, D.; Hildebrandt, P. Probing Structure and Reaction Dynamics of Proteins Using Time-Resolved Resonance Raman Spectroscopy. *Chem. Rev.* **2020**, *120*, 3577-3630.

[27] Oscar, B. G.; Liu, W.; Zhao, Y.; Tang, L.; Wang, Y.; Campbell, R. E.; Fang, C. Excited-State Structural Dynamics of a Dual-Emission Calmodulin-Green Fluorescent Protein Sensor for Calcium Ion Imaging. *Proc. Natl. Acad. Sci. U. S. A.* **2014**, *111*, 10191-10196.

[28] Kukura, P.; McCamant, D. W.; Mathies, R. A. Femtosecond Stimulated Raman Spectroscopy. *Annu. Rev. Phys. Chem.* **2007**, *58*, 461-488.

[29] Lee, S.-Y.; Zhang, D.; McCamant, D. W.; Kukura, P.; Mathies, R. A. Theory of femtosecond stimulated Raman spectroscopy. *J. Chem. Phys.* **2004**, *121*, 3632-3642.

[30] Fang, C.; Tang, L.; Oscar, B. G.; Chen, C. Capturing Structural Snapshots during Photochemical Reactions with Ultrafast Raman Spectroscopy: From Materials Transformation to Biosensor Responses. *J. Phys. Chem. Lett.* **2018**, *9*, 3253-3263.

[31] Sun, Z.; Qiu, X. Q.; Lu, J.; Zhang, D. H.; Lee, S.-Y. Three-state model for femtosecond broadband stimulated Raman scattering. *J. Raman Spectrosc.* **2008**, *39*, 1568-1577.

[32] Quick, M.; Dobryakov, A. L.; Kovalenko, S. A.; Ernsting, N. P. Resonance Femtosecond-Stimulated Raman Spectroscopy without Actinic Excitation Showing Low-Frequency Vibrational Activity in the S2 State of All-Trans β-Carotene. *J. Phys. Chem. Lett.* **2015**, *6*, 1216-1220.

[33] Chen, C.; Zhu, L.; Baranov, M. S.; Tang, L.; Baleeva, N. S.; Smirnov, A. Y.; Yampolsky, I. V.; Solntsev, K. M.; Fang, C. Photoinduced Proton Transfer of GFP-Inspired Fluorescent Superphotoacids: Principles and Design. *J. Phys. Chem. B* **2019**, *123*, 3804-3821.

[34] Oscar, B. G.; Chen, C.; Liu, W.; Zhu, L.; Fang, C. Dynamic Raman Line Shapes on an Evolving Excited-State Landscape: Insights from Tunable Femtosecond Stimulated Raman Spectroscopy. *J. Phys. Chem. A* **2017**, *121*, 5428-5441.

[35] Chen, C.; Zhu, L.-d.; Fang, C. Femtosecond stimulated Raman line shapes: Dependence on resonance conditions of pump and probe pulses. *Chin. J. Chem. Phys.* **2018**, *31*, 492-502.

[36] Dhar, L.; Rogers, J. A.; Nelson, K. A. Time-resolved vibrational spectroscopy in the impulsive limit. *Chem. Rev.* **1994**, *94*, 157-193.

[37] Fujisawa, T.; Kuramochi, H.; Hosoi, H.; Takeuchi, S.; Tahara, T. Role of Coherent Low-Frequency Motion in Excited-State Proton Transfer of Green Fluorescent Protein Studied by Time-Resolved Impulsive Stimulated Raman Spectroscopy. *J. Am. Chem. Soc.* **2016**, *138*, 3942-3945.

[38] Mohammed, O. F.; Pines, D.; Dreyer, J.; Pines, E.; Nibbering, E. T. J. Sequential Proton Transfer Through Water Bridges in Acid-Base Reactions. *Science* **2005**, *310*, 83-86.

[39] Kuramochi, H.; Takeuchi, S.; Yonezawa, K.; Kamikubo, H.; Kataoka, M.; Tahara, T. Probing the Early Stages of Photoreception in Photoactive Yellow Protein with Ultrafast Time-Domain Raman Spectroscopy. *Nat. Chem.* **2017**, *9*, 660-666.

[40] Ellis, S. R.; Hoffman, D. P.; Park, M.; Mathies, R. A. Difference Bands in Time-Resolved Femtosecond Stimulated Raman Spectra of Photoexcited Intermolecular Electron Transfer from Chloronaphthalene to Tetracyanoethylene. *J. Phys. Chem. A* **2018**, *122*, 3594-3605.

[41] Taylor, M. A.; Zhu, L.; Rozanov, N. D.; Stout, K. T.; Chen, C.; Fang, C. Delayed vibrational modulation of the solvated GFP chromophore into a conical intersection. *Phys. Chem. Chem. Phys.* **2019**, *21*, 9728-9739.

[42] Hochstrasser, R. M. Two-dimensional spectroscopy at infrared and optical frequencies. *Proc. Natl. Acad. Sci. U.S.A.* **2007**, *104*, 14190-14196.

[43] Hamm, P.; Zanni, M. *Concepts and Methods of 2D Infrared Spectroscopy*; Cambridge University Press: Cambridge, 2011.

[44] Scholes, G. D.; Fleming, G. R.; Chen, L. X.; Aspuru-Guzik, A.; Buchleitner, A.; Coker, D. F.; Engel, G. S.; van Grondelle, R.; Ishizaki, A.; Jonas, D. M.; Lundeen, J. S.; McCusker, J. K.; Mukamel, S.; Ogilvie, J. P.; Olaya-Castro, A.; Ratner, M. A.; Spano, F. C.; Whaley, K. B.; Zhu, X. Using coherence to enhance function in chemical and biophysical systems. *Nature* **2017**, *543*, 647-656.

[45] Weigel, A.; Dobryakov, A.; Klaumünzer, B.; Sajadi, M.; Saalfrank, P.; Ernsting, N. P. Femtosecond Stimulated Raman Spectroscopy of Flavin after Optical Excitation. *J. Phys. Chem. B* **2011**, *115*, 3656-3680.

[46] Fang, C.; Tang, L.; Chen, C. Unveiling coupled electronic and vibrational motions of chromophores in condensed phases. *J. Chem. Phys.* **2019**, *151*, 200901.

[47] Shen, Y. R. *The principles of nonlinear optics*; J. Wiley: New York, 1984.

[48] Frontiera, R. R.; Shim, S.; Mathies, R. A. Origin of negative and dispersive features in anti-Stokes and resonance femtosecond stimulated Raman spectroscopy. *J. Chem. Phys.* **2008**, *129*, 064507.

[49] Niu, K.; Zhao, B.; Sun, Z.; Lee, S.-Y. Analysis of femtosecond stimulated Raman spectroscopy of excited-state evolution in bacteriorhodopsin. *J. Chem. Phys.* **2010**, *132*, 084510.

[50] Yoon, S.; McCamant, D. W.; Kukura, P.; Mathies, R. A.; Zhang, D.; Lee, S.-Y. Dependence of line shapes in femtosecond broadband stimulated Raman spectroscopy on pump-probe time delay. *J. Chem. Phys.* **2005**, *122*, 024505.

[51] McCamant, D. W.; Kukura, P.; Yoon, S.; Mathies, R. A. Femtosecond broadband stimulated Raman spectroscopy: Apparatus and methods. *Rev. Sci. Instrum.* **2004**, *75*, 4971-4980.

[52] Zhu, L.; Liu, W.; Fang, C. A versatile femtosecond stimulated Raman spectroscopy setup with tunable pulses in the visible to near infrared. *Appl. Phys. Lett.* **2014**, *105*, 041106.

[53] Kovalenko, S. A.; Dobryakov, A. L.; Ernsting, N. P. An efficient setup for femtosecond stimulated Raman spectroscopy. *Rev. Sci. Instrum.* **2011**, *82*, 063102.

[54] Liu, W.; Zhu, L.; Wang, L.; Fang, C. Cascaded four-wave mixing for broadband tunable laser sideband generation. *Opt. Lett.* **2013**, *38*, 1772-1774.

[55] Zhu, L.; Liu, W.; Fang, C. Tunable sideband laser from cascaded four-wave mixing in thin glass for ultra-broadband femtosecond stimulated Raman spectroscopy. *Appl. Phys. Lett.* **2013**, *103*, 061110.

[56] Tang, L.; Liu, W.; Wang, Y.; Zhao, Y.; Oscar, B. G.; Campbell, R. E.; Fang, C. Unraveling Ultrafast Photoinduced Proton Transfer Dynamics in a Fluorescent Protein Biosensor for Ca^{2+} Imaging. *Chem. Eur. J.* **2015**, *21*, 6481-6490.

[57] Tang, L.; Liu, W.; Wang, Y.; Zhu, L.; Han, F.; Fang, C. Ultrafast Structural Evolution and Chromophore Inhomogeneity inside a Green-Fluorescent-Protein-Based Ca^{2+} Biosensor. *J. Phys. Chem. Lett.* **2016**, *7*, 1225-1230.

[58] Dietze, D. R.; Mathies, R. A. Femtosecond Stimulated Raman Spectroscopy. *ChemPhysChem* **2016**, *17*, 1224-1251.

[59] Hontani, Y.; Inoue, K.; Kloz, M.; Kato, Y.; Kandori, H.; Kennis, J. T. M. The photochemistry of sodium ion pump rhodopsin observed by watermarked femto- to submillisecond stimulated Raman spectroscopy. *Phys. Chem. Chem. Phys.* **2016**, *18*, 24729-24736.

[60] Kloz, M.; Weißenborn, J.; Polívka, T.; Frank, H. A.; Kennis, J. T. M. Spectral watermarking in femtosecond stimulated Raman spectroscopy: resolving the nature of the carotenoid S* state. *Phys. Chem. Chem. Phys.* **2016**, *18*, 14619-14628.

[61] Bera, K.; Kwang, S. Y.; Cassabaum, A. A.; Rich, C. C.; Frontiera, R. R. Facile Background Discrimination in Femtosecond Stimulated Raman Spectroscopy Using a Dual-Frequency Raman Pump Technique. *J. Phys. Chem. A* **2019**, *123*, 7932-7939.

[62] Tang, L.; Zhu, L.; Wang, Y.; Fang, C. Uncovering the Hidden Excited State toward Fluorescence of an Intracellular pH Indicator. *J. Phys. Chem. Lett.* **2018**, *9*, 4969-4975.

[63] Liu, W.; Tang, L.; Oscar, B. G.; Wang, Y.; Chen, C.; Fang, C. Tracking Ultrafast Vibrational Cooling during Excited-State Proton Transfer Reaction with Anti-Stokes and Stokes Femtosecond Stimulated Raman Spectroscopy. *J. Phys. Chem. Lett.* **2017**, *8*, 997-1003.

[64] Tang, L.; Wang, Y.; Zhu, L.; Lee, C.; Fang, C. Correlated Molecular Structural Motions for Photoprotection after Deep-UV Irradiation. *J. Phys. Chem. Lett.* **2018**, *9*, 2311-2319.

[65] Chen, C.; Fang, C. Devising Efficient Red-Shifting Strategies for Bioimaging: A Generalizable Donor-Acceptor Fluorophore Prototype. *Chem. Asian. J.* **2020**, *15*, 1514-1523.

[66] Hoffman, D. P.; Mathies, R. A. Femtosecond Stimulated Raman Exposes the Role of Vibrational Coherence in Condensed-Phase Photoreactivity. *Acc. Chem. Res.* **2016**, *49*, 616-625.

Chapter 3 Resonance Enhancement and Line Shapes in

FSRS

3.1 Resonance enhancement

Ever since the discovery of Raman scattering phenomenon a century ago, the pertinent spectroscopic developments have benefited and facilitated the fundamental science in a profound manner. Its unique light-matter mechanism makes it powerful in investigating varieties of systems and complements the infrared (IR) spectroscopy in many aspects.[1] For instance, Raman spectroscopy usually works well for low- to mid-frequency region (400−1500 cm^{-1}) while IR spectroscopy often suffers from this fingerprint region containing a complicated series of vibrational peaks. This is due to the different origins of Raman and IR signals. The IR activity of a normal mode Q is determined by the magnitude of dipole moment change along the vibrational coordinate (i.e. $\partial\vec{\mu}/\partial Q$), while the Raman activity is determined by the magnitude of electric polarizability change (i.e., $\partial\bar{\bar{\alpha}}/\partial Q$) upon the vibration that leads to an induced dipole moment change (i.e., $\partial\vec{\mu}_I/\partial Q$ and $\vec{\mu}_I = \bar{\bar{\alpha}}\vec{E}$).

Traditional Raman scattering (spontaneous Raman) could be treated as a two-photon process in which an incident photon at ω_1 is absorbed and one other photon is emitted at ω_2 with a vibrational transition occurring from initial state $|i\rangle$ to final state $|f\rangle$ (Figure 3.1).[2] If the $|i\rangle$ is a lower state than $|f\rangle$, the Stokes Raman scattering signal is generated, and otherwise the anti-Stokes Raman scattering is generated. The spontaneous Raman intensity is strongly subject to the Boltzmann distribution in the

equilibrium electronic ground state for which the ground vibrational state is much more populated than other excited vibrational states. As a result, the Stokes scattering intensity is much greater than the anti-Stokes scattering. However, the cross section of spontaneous Raman scattering is very small which accounts for the weak experimental signal strength. This drawback is greatly compensated by the resonance enhancement when the incident photon energy is close to an electronic transition of the material under study.[3] The enhancement factor for spontaneous Raman could reach 10^1 to 10^5 from system to system. This greatly improves the signal-to-noise ratio and also opens up opportunities to study the vibronic couplings along different vibrational coordinates.
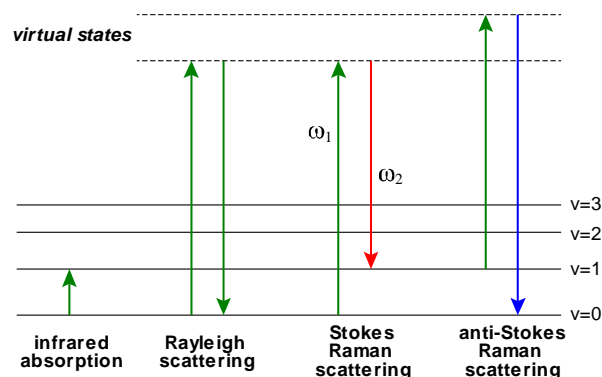
Figure 3.1. Energy-level diagram for infrared absorption, Rayleigh scattering, and Stokes & anti-Stokes Raman scattering processes.

With the advent of modern pulsed lasers, stimulated Raman spectroscopy or scattering (SRS) has been available with larger cross sections with respect to spontaneous Raman scattering and therefore becomes a much more efficient spectroscopic tool to study various materials with less stringent requirement for the sample concentration.[1,4,5] The resonance enhancement remains in SRS and has been increasingly exploited in

obtaining excited-state vibrational signals particularly in FSRS in the recent decade.[5-7]

The typical excited-state FSRS signal generation is shown in Figure 2.3 and 2.4.

Similar to the resonance with ground-state absorption transition, the excited-state

Raman modes can be enhanced by promoting the resonance between Raman pulses and

the excited-state absorption (ESA) or stimulated emission (SE) bands (Figure 3.2).
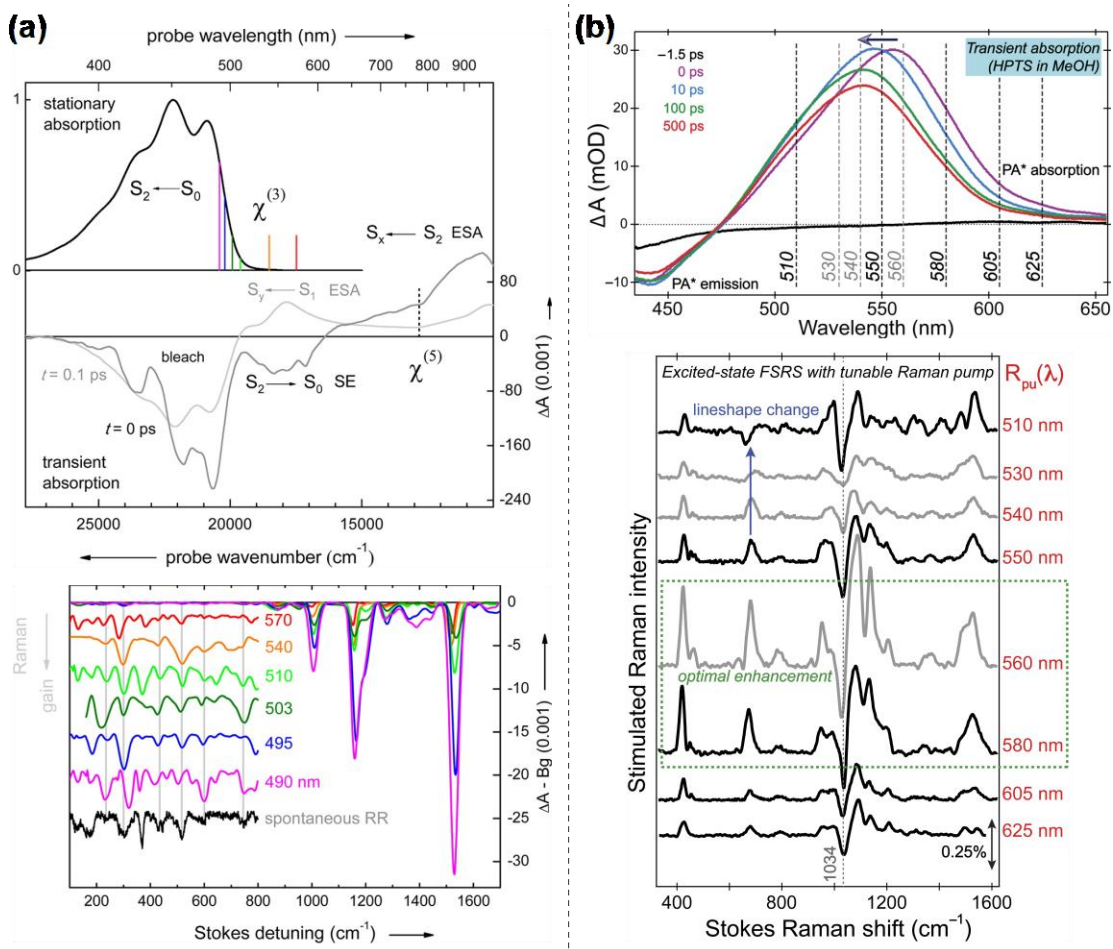
Figure 3.2. Resonance enhancement in Stokes FSRS. (a) Ground-state absorption (top)

and FSRS spectra (bottom) of β-carotene in *n*-hexane. Adapted with permission from

Ref. [8]. Copyright 2015 American Chemical Society. (b) Excited-state absorption (top)

at selected time delays and FSRS spectra (bottom) of pyranine at 500 fs in methanol.

Adapted with permission from Ref. [9]. Copyright 2017 American Chemical Society.

For β-carotene in the ground state, it is obvious that the FSRS mode intensity increases dramatically as the Raman pump is tuned into the absorption band from off-resonance at 570 nm to on-resonance at 490 nm (Figure 3.2a).[8] For pyranine in the excited state, since the ESA band blue-shifts with time, the resonance enhancement effect was investigated by examining the resonance conditions at a fixed time delay such that the ESA band is kept the same for different Raman pump wavelengths.[9] As shown in Figure 3.2b, as the Raman pump is tuned from near-off-resonance at 625 nm to on-resonance at 560 nm, the peak intensity at the same time delay of 500 fs corresponding to the ESA band with maximum at ~550 nm is greatly improved for all the observed modes. The optimal enhancement appears at 560 and 580 nm with few dispersive peaks.

Note that in the excited state, SE band can also be used to promote the resonance enhancement, but a systematic investigation on it remains underexplored despite some works that have adopted it to generate satisfactory FSRS signals without dispersive line shapes.[6,10-12] Furthermore, on-resonance FSRS can be problematic due to the undesirable dispersive line shapes. Many reports have shown that dispersive FSRS peaks are more likely to be generated when the Raman pump and probe pulses are within the absorption band (or emission) in both ground and excited states, particularly for the anti-Stokes FSRS.[9,11,13-15] This is due to the contribution of other third-order nonlinear processes such as hot luminance (HL) and inverse Raman scattering (IRS) under the same phase-matching condition (see the following sections for detail).

3.2 Ground-state FSRS line shapes*[a]*

Theoretically speaking, conventional FSRS signal is generated by a four-wave mixing process under off-resonance conditions where the vibronic transitions are mediated by a virtual state. It typically cannot achieve high signal intensity due to low transition probability between the real and virtual electronic states.[16] The low signal-to-noise ratio (SNR) may complicate data analysis to reliably retrieve accurate information. Therefore, pre- or on-resonance FSRS becomes favored by the community to achieve desirable SNR. In particular, the Raman pump (R_{pu}) wavelength in the optical regime can be tuned into an electronic band to effectively increase the transition probability (oscillator strength) in the four-wave mixing process, i.e., transition between two real vibronic states. However, dispersive features are often generated near or on resonance conditions, which could obscure the spectral analysis after data collection. This effect is more dramatic on the anti-Stokes side of the FSRS spectrum when compared to the Stokes side.[9,11,17] Therefore, it becomes important to gain a deeper understanding of the molecular origin of dispersive line shapes so they can be interpreted and made use of when necessary to streamline the FSRS data analysis.

Previous work has provided certain experimental and theoretical information on FSRS line shapes. Frontiera et al. studied the ground-state (GS) FSRS for rhodamine 6G (R6G) on both anti-Stokes and Stokes sides.[17] On the anti-Stokes side, all the Raman peaks undergo line shape progression from negative, through the oppositely phased

---

*[a]*This section is based on the publication: <u>Chen, C.; Zhu, L.; Fang, C. Femtosecond stimulated Raman line shapes: Dependence on resonance conditions of pump and probe pulses.</u> *Chin. J. Chem. Phys.* **2018**, *31*, 492-502.

dispersion, to positive-like as the R_{pu} is tuned into the absorption band. On the Stokes side, low-frequency modes evolve from positive to dispersive while high-frequency modes remain mostly positive for all the R_{pu} wavelengths. Umapathy et al. experimentally explored the line shapes for crystal violet in ultrafast Raman loss spectroscopy, shown to be equivalent to anti-Stokes FSRS,[18] and they observed the mode-dependent dispersion[15] and suggested that the wavelength-dependent Franck-Condon (FC) activity plays a crucial role in generating dispersion due to the creation of different FC states when on resonance. Lee and co-workers performed a series of simulations and represented the stimulated Raman scattering (SRS) signal by eight distinct dual time-line Feynman diagrams within the coupled wave theory framework.[14,18-23] While off-resonant in GS-FSRS,[24] the narrow Stokes gain arises from the resonance Raman scattering (RRS) term while the narrow anti-Stokes loss is caused by inverse Raman scattering (IRS). In both cases, the vibrational coherence is created in the same electronic ground state (S_0) and major contribution comes from the ground vibrational state (i.e., quantum number $v = 0$). In contrast to conventional spontaneous Raman wherein the typically weaker anti-Stokes peak intensity is subject to Boltzmann distribution, the anti-Stokes FSRS peak intensity could be larger than the Stokes side when the Raman probe (R_{pr}) wavelength is closer to an electronic transition peak.[9,15] When Raman pulses overlap with a resonant band, the stimulated Raman line shapes become nontrivial due to additional contributions from the other SRS and IRS terms.[23] Pump-probe pulse delay experiments have also been exploited to reveal the roles of Raman pump and probe in generating FSRS signals.[17,21,25]

In addition, hot luminescence (HL) pathways have been suggested to contribute to the dispersive line shapes in FSRS.[17,21] Different from the aforementioned RRS and IRS terms, the first interacting R_{pu} and R_{pr} pulses in HL processes are both excitatory and generate the vibrational coherence in a higher lying excited state (Figure 3.3, the excited-state vibrational coherence depicted by a semi-transparent red shade). The de-excitation by the picosecond R_{pu} in its second interaction after the vibrational coherence dephasing time T_2 cancels in phase with the first R_{pu} and ensures the phase-matching condition is satisfied (i.e., the FSRS signal is emitted collinearly with the R_{pr} beam). It is notable that the occurrence of HL terms to contribute narrow line shapes in FSRS requires the on-resonance condition of both pulses as the vibrational coherence has to be generated between real vibrational states in an electronic excited state population instead of a virtual state (see below for details).
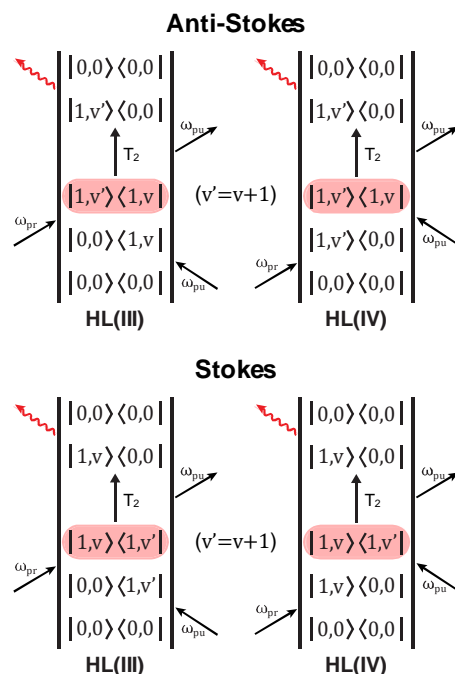
Anti-Stokes

Stokes

Figure 3.3. Double-sided Feynman diagrams of the hot luminescence (HL) terms. These processes contribute to vibrational line shapes in anti-Stokes and Stokes FSRS when on resonance. Reproduced with permission from Ref. [13]. Copyright 2018 Chinese Physical Society.

In our laboratory, we investigated the relationship between the GS-FSRS line shapes and R_{pu} and R_{pr} wavelengths. Different from previous reports,[17,26] the line shapes are also examined at shorter wavelengths resonant with the blue side of the electronic absorption band which fills a current knowledge gap. R6G in methanol is used as the model system because its absorption band (maximum at ~530 nm) lies within the wavelength tunable range (ca. 480−720 nm) of our home-built multi-stage noncollinear optical parametric amplifier (NOPA) system, which enables us to study all the resonance conditions from the red to blue side of the absorption band. Moreover, R6G

has multiple Raman peaks across the broad spectrum up to 1800 cm^{-1}, which provides rich information and internal control for line shapes. We observed that anti-Stokes FSRS is more susceptible to resonance change with respect to the Stokes side and shows line shape variation in a cyclic manner from negative through positive back to negative, mediated by the oppositely phased dispersion. The low-frequency modes ($<$1000 cm^{-1}) on the Stokes side exhibit a similar cyclic trend while the high-frequency modes remain largely unchanged throughout the Raman pump wavelength tuning. Based on these systematic experimental results in conjunction with previous FSRS studies, we provide new insights into the line shapes and develop guidelines in selecting the Raman pulse wavelengths to avoid dispersion while achieving satisfactory SNR.

3.2.1 Resonance condition

The GS-FSRS line shapes essentially correlate to the resonance conditions of R_{pu} and R_{pr} pulses with the steady-state electronic absorption band. Figure 3.3 presents the ground-state absorption (GSA) spectrum of R6G in methanol with our R_{pu} wavelengths indicated. The band maximum is at 530 nm and the shoulder peak on the blue side could be a result of vibronic progression (involving a ~1180 cm^{-1} mode). The FSRS line shapes on both Stokes and anti-Stokes sides are examined by tuning R_{pu} from off-resonance toward on-resonance, and across the GSA band to pre-resonance on the blue side. The broadband probe wavelength ranges for the spectral window are displayed by the blue and red shaded bars in Figure 1a and 1b. The associated R_{pr} experiences a similar change in resonance as the R_{pu} moves into and away from the band in the red

to blue tuning direction. As mentioned above, the information about the effect of more energetic Raman pulses on the FSRS line shape is still lacking. Through this work, the R_{pu} and R_{pr} in pre-resonance conditions with an electronic band have shown promise in tracking the ground and excited state species with sufficient SNR and nondispersive line shapes.
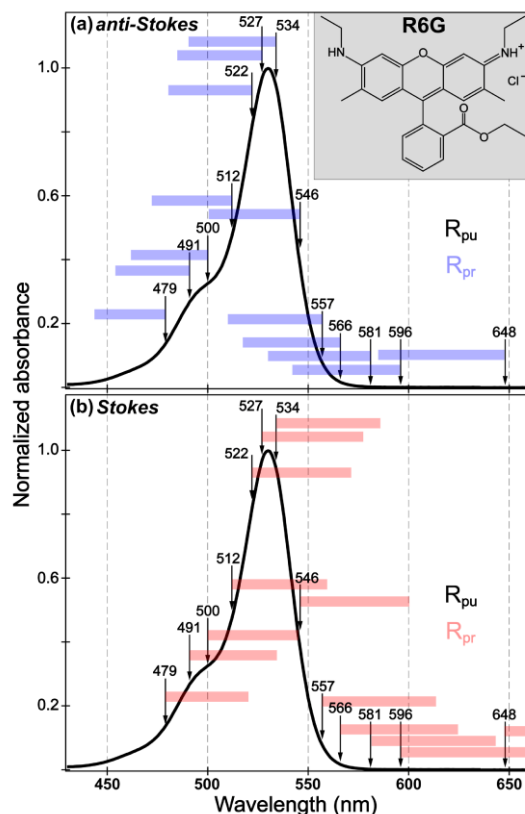
Figure 3.4. Normalized ground-state absorption spectrum of R6G in methanol with the R_{pr} wavelength range indicated for each R_{pu} wavelength. The R_{pr} range is denoted by the color-coded rectangle shaded bars in the (a) anti-Stokes and (b) Stokes region. The chemical structure of R6G is shown in the inset of (a) wherein the middle phenyl group is perpendicular to the xanthene ring to minimize steric hindrance. The probe ranges for the 596 and 648 nm R_{pu} in (b) are truncated at the red end of the wavelength axis. Reproduced with permission from Ref. [13]. Copyright 2018 Chinese Physical Society.

3.2.2 Anti-Stokes FSRS line shapes

In the ground state, both spontaneous Raman and stimulated Raman on the anti-Stokes side exhibit absorptive features under off-resonance condition. The anti-Stokes stimulated Raman can be attributed to an IRS term where probe acts as the excitatory pulse. Unlike spontaneous Raman, the anti-Stokes stimulated Raman signal is not necessarily weaker than its Stokes counterpart in spite of the inversely mirrored vibrational modes.[9,18,24,27,28] This is because: (i) R_{pr} initiates the Raman process from the most populated vibrational ground state (v=0) in IRS, (ii) the resonance of both Raman pump and probe pulses are important for the signal strength. The latter factor may explain the mode-dependent enhancement in the observed peak intensity. In this work, the 648 nm R_{pu} generates the off-resonance spectrum below 1700 cm^{-1} because all the probe photons corresponding to the Raman modes are off-resonant with the chromophore GSA band (Figure 3.4a). As R_{pu} is tuned into resonance with the GSA band from the red side, the anti-Stokes FSRS line shapes exhibit complicated changes with a clear mode dependence (Figure 3.5a). Notably, we used three sample concentrations (5, 20, and 100 μmol/L) and two R_{pu} powers (~0.4 and 2 mW) at each R_{pu} wavelength to study their effect on the FSRS peak intensity and line shape. Only the spectrum with the clearest and reproducible line shape at each R_{pu} wavelength is scaled and displayed without any baseline subtraction[9,29] for reliable comparison and retrieval of molecular information.

In the anti-Stokes FSRS (Figure 3.5a), both high- and low-frequency peaks are negative at 648 nm R_{pu} due to the off-resonant pump and probe. As R_{pu} is tuned into resonance with the GSA band, the line shape undergoes a cyclic change, i.e., negative →

dispersive → positive → oppositely phased dispersive → negative. The line shape alteration pattern for high-frequency modes is more conspicuous than low-frequency modes. For example, the 1652 and 1575 cm^{-1} modes convert back to negative features at R_{pu}=557 nm. The middle 1511, 1364, 1311, and 1183 cm^{-1} modes become negative again at a bluer R_{pu} of 546 nm. The low-frequency modes at 773 and 611 cm^{-1} do not seem to regain a negative line shape even with the bluest R_{pu} used (479 nm). The line shapes of the high-frequency modes at 479 and 491 nm R_{pu} are challenging to determine due to the extremely low SNR on a broad sloping baseline. This can be explained by the weakening of resonance conditions of R_{pu} and R_{pr}, and the deficiency of probe photons in blue wavelength region of the SCWL.[30,31] This effect occurs for the 500 and 512 nm R_{pu} as well but to a lesser extent.

What is the underlying cause for the dispersive line shapes in FSRS? The appearance of dispersion at resonance has been discussed on the basis of hot luminescence (HL) terms where a vibrational coherence is created in an electronic excited state (different from the original ground state S_0, see Figure 3.3) by the resonant R_{pu} and R_{pr} in a third-order $\chi^{(3)}$ nonlinear process.[17,22] In this case, both R_{pu} and R_{pr} are excitatory. McCamant et al. explained the dispersive line shapes observed in the ES-FSRS of bacteriorhodopsin by "Raman initiated by nonlinear emission" (RINE), which is equivalent to the HL terms for GS-FSRS in nature. The imaginary part of susceptibility $\chi^{(3)}$ can be used to account for the dispersive line shapes from RINE or HL, which are essentially a function of R_{pu}, R_{pr}, vibrational frequency, and line widths of the pertinent electronic and vibrational transitions.[9,10,22] However, the role of R_{pu} and R_{pr} has not

been discussed in detail when dispersive peaks are generated under various resonance conditions.
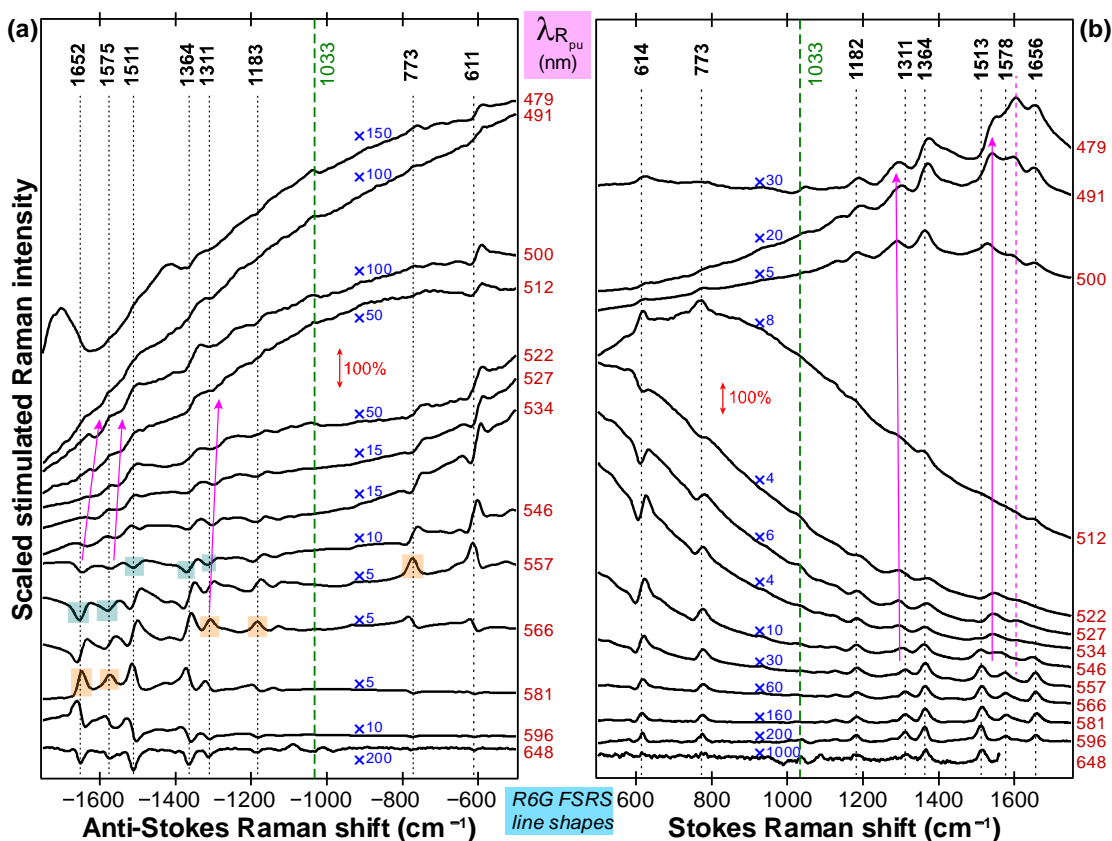
Figure 3.5. Ground-state (a) anti-Stokes and (b) Stokes FSRS spectra from $500-1750$ cm^{-1} of R6G in methanol as R_{pu} is tuned across the visible region. Major peak positions are labeled by the vertical dotted lines. The solvent peak at 1033 cm^{-1} is indicated by the green vertical dashed line. The spectra are scaled for comparison and the scaling factor is shown in blue by the corresponding spectrum. The different R_{pu} wavelengths are listed in red to the right side of the stacked spectra. Semi-transparent orange and green shades highlight some positive and negative peaks in (a). Magenta arrows denote some characteristic mode frequency redshift as R_{pu} is tuned to be bluer. Adapted with permission from Ref. [13]. Copyright 2018 Chinese Physical Society.

Since the community has long considered the resonance condition of R_{pu} to be crucial in determining the FSRS line shape and signal intensity, we aim to demonstrate that the R_{pr} is equally if not more important in determining the FSRS line shape in the $\chi^{(3)}$ process based on our systematic experimental observations. Using the framework from a previous report,[10] the imaginary part of $\chi^{(3)}$ in HL processes can be expressed by Eq.(1):

$$Im[\chi^{(3)}(\omega_2)] = A \cdot \{b\gamma_{e,n} - \Gamma_{ge}[\omega_2 - (\omega_1 \pm \omega_{n,n+1})]\} \tag{1}$$

where ω_1, ω_2, and $\omega_{n,n+1}$ are the R_{pu}, R_{pr}, and the vibrational mode frequency, respectively. $\gamma_{e,n}$ is the homogeneous line width of the vibrational transition in the excited state (e.g., S$_1$). Γ_{ge} is the homogeneous line width of the e←g electronic transition, which is the same for all the vibrational coherences generated in S$_1$. "$\pm$" marks the difference for Stokes ($-$) and anti-Stokes ($+$) frequencies. The first term A includes the Lorentzian peak at center vibrational frequency in S$_1$ and the Raman excitation profile.[32,33] The second term introduces the line shape change deviating from a Lorentzian. Specifically, $b = \omega_{ge} - \omega_2$ defines the resonance of the probe frequency corresponding to each vibrational peak. To the first approximation, the vibrational damping time $(\gamma_{e,n})^{-1}$ and electronic lifetime $(\Gamma_{ge})^{-1}$ lead to minor difference in the vibrational line widths for all the peaks when HL terms create coherences in the excited state. This highlights the importance of the remaining b factor, i.e., resonance of the mode-corresponding-probe wavelength, in determining the FSRS line shape which is corroborated by the nonsynchronous line shape change for high- and low-frequency modes in the anti-Stokes FSRS spectra (Figure 3.5a). In other words, within one FSRS spectrum, different vibrational modes cannot be considered to have the same value of

b factor especially when the R_{pr} wavelength is approaching an electronic transition gap (i.e., b → 0) and the dispersion term becomes dominant.

In Figure 3.5a, the high-frequency modes experience an "earlier" line shape change than low-frequency modes when R_{pu} is tuned from red to blue. Therefore, the resonance condition of R_{pu} alone cannot explain the different behavior of each mode at the same R_{pu} wavelength under pre- and on-resonance conditions. By inspecting the associated probe wavelengths, we note that the modes with similar line shapes correspond to similar R_{pr} wavelengths. For instance, the positive peak appears at: (i) 1575 cm^{-1} for 581 nm R_{pu}, (ii) 1183 cm^{-1} for 566 nm R_{pu}, (iii) 773 cm^{-1} for 557 nm R_{pu}. The pertinent R_{pr} wavelengths for these modes are ~532, 530, 534 nm, respectively, which are all close to the GSB peak maximum (Figure 3.4). Notably, the 1652 cm^{-1} mode at 581 nm R_{pu} shows positive line shape with a slight dispersive character, which leads us to predict that a positive-definite line shape would be generated for this mode at a R_{pu} wavelength between 581 and 596 nm (e.g., 583 nm while R_{pr}=532 nm). This can be further validated by reducing the wavelength increment of R_{pu}. Likewise, the positive-definite peak for the 1364 cm^{-1} mode will appear at a redder R_{pu} wavelength between 566 and 581 nm (e.g., 574 nm while R_{pr}=532 nm). The 1511 and 611 cm^{-1} positive-definite peaks, on the other hand, will appear at slightly bluer R_{pu} wavelengths than 581 and 557 nm, respectively, based on the phase of dispersion. It can be concluded that the same line shape will be generated at the same R_{pr} wavelength region as R_{pu} is tuned into a resonant band when HL becomes a prominent contributor. This is in accord with Eq.(1) where the R_{pr} resonance condition, measured by *b*, plays a critical role in

determining line shapes. It is interesting that a fully on-resonance R_{pr} alone does not lead to dispersive line shapes, likely because the R_{pu} is pre- or off-resonant with the electronic band (Figure 3.4a). The only exception concerns very low frequency modes where the R_{pu} and R_{pr} wavelengths are close. Moreover, the clearly broadened bandwidths of dispersive peaks also evince the generation of ES vibrational coherences due to the excitatory R_{pu} and R_{pr} pulses in HL terms. The generation of ES and GS vibrational coherences in parallel could in principle introduce further interference terms and dispersive line shapes in FSRS.[9]

As the R_{pu} wavelength is tuned further into the GSA band maximum and blue side, the peaks maintain negative line shape except for low-frequency modes. The 1364, 1311, and 1183 cm^{-1} modes appear as broadened negative peaks at close-to-GSA-maximum 534 nm and bluer R_{pu} wavelengths. These features cannot solely arise from the GS vibrational coherence via the IRS(I) pathway (Figure 3.6a) due to their broad bandwidths. The aforementioned HL terms could contribute but to a small extent. For the off-resonant R_{pu} and R_{pr} on the red side of GSA, the HL terms make marginal contributions owing to longer wavelengths than the transition gap. When on the blue side of GSA, the shorter wavelength R_{pr} is less resonant with ω_{ge} than R_{pu}, which can still stimulate transitions between S_0 and S_1 but with a lower probability caused by the reduced FC factors further away from the GSA maximum (Figure 3.4a, for the high-frequency modes above 1000 cm^{-1}). In fact, the HL signal magnitude is manifested in Eq.(1) by the factor A which is approximately proportional to FC factors at each vibronic transition wavelength.

This rationale could be supported by the dispersive modes at 773 and 611 cm^{-1}. At variance with the modes above 1000 cm^{-1}, these two modes remain dispersive as R_{pu} is tuned to blue from the GSA maximum. The 773 cm^{-1} mode line shape is obscured by weak peak intensity for R_{pu} below 512 nm, likely due to the weak FC activity of this non-symmetric mode. The distinct line shape behavior lies in different resonance conditions of the mode-dependent R_{pr} wavelength [i.e., ω_2 in Eq.(1)]. The R_{pr} photons experience better resonance for the low-frequency modes than high-frequency modes with the blue-sided R_{pu} (Figure 3.4a), indicating that the HL contribution remains appreciable in the low-frequency region. In contrast, broad negative peaks observed in the high-frequency region have minor contributions from HL terms, and much less dispersive line shapes because the R_{pu} and R_{pr} wavelengths differ by a greater extent for those modes.

Notably, peak broadening appears from 546 nm R_{pu} in the red $\rightarrow$ blue tuning direction when R_{pu} becomes strongly resonant with the GSA band. Considering the ps duration of the R_{pu} pulse, direct absorption of R_{pu} photons could allow more channels for higher-order nonlinear signaling at resonance.[6,8] The large spectral baselines in Figure 3.5a and 3.5b are indicative of the depleted GS and transient ES populations caused by R_{pu} on or near the electronic resonance.[9,29,30] A previous report by Ernsting and co-workers proposed that after a preceding photoexcitation pulse, a resonant R_{pu} could induce ES population depletion at early time before R_{pr} arrives for $\chi^{(3)}$ processes and lead to line broadening.[6] Later, the resonance FSRS without actinic excitation was demonstrated for all-trans β-carotene.[8] The broadened peaks at resonant R_{pu} wavelengths indicate the

$\chi^{(5)}$ generation of ES vibrational coherence with a shorter electronic lifetime, which can be considered as six-wave mixing in generating the FSRS signal.[34] In this scenario, R_{pu} first functions as an excitation pulse and promotes the S_1 population likely in the first half of its pulse duration (e.g., ~1 ps in our case).[6,35] The later arrival of R_{pr} initiates the Raman $\chi^{(3)}$ process in the excited state (Figure 3.6b) and gives rise to the negative signal in the anti-Stokes FSRS. Remarkably in Figure 2a, the 1652, 1575, 1511, and 1311 cm^{-1} modes all exhibit a frequency redshift as R_{pu} is tuned to the blue side. One possible reason is the photoinduced mode frequency redshift within the FC region due to electronic redistribution.[30,36] It could also imply that R_{pu} accesses high-lying vibrational levels in S_1 and consequently generates vibrational coherences with high quanta in an anharmonic potential energy surface, leading to a frequency redshift.[9,29] Furthermore, because the emission typically occurs at longer wavelengths with respect to absorption so the $\chi^{(3)}$ process on resonant with an SE band in S_1 is less likely when a more energetic R_{pu} is used. The IRS(I) process with an excitatory probe could be responsible for the observed negative features in FSRS with blue R_{pu} wavelengths (e.g., ~534 nm). The energy-level diagram representing one possible $\chi^{(5)}$ pathway is depicted in Figure 3.6b. We emphasize that the observed mode intensity and line shape consist of the contributions from all possible $\chi^{(3)}$ and higher-order nonlinear pathways, which could involve different interacting pulse sequences, overlap with an SE transition, vibrationally hot or relaxed states, and possible interference between the GS and ES vibrational coherences generated via the concurrent pathways.[9,23] We discuss the most likely pathway(s) in this work to illustrate the relevant principles for anti-Stokes FSRS line shapes which are supported by our experimental data and theoretical rationale.
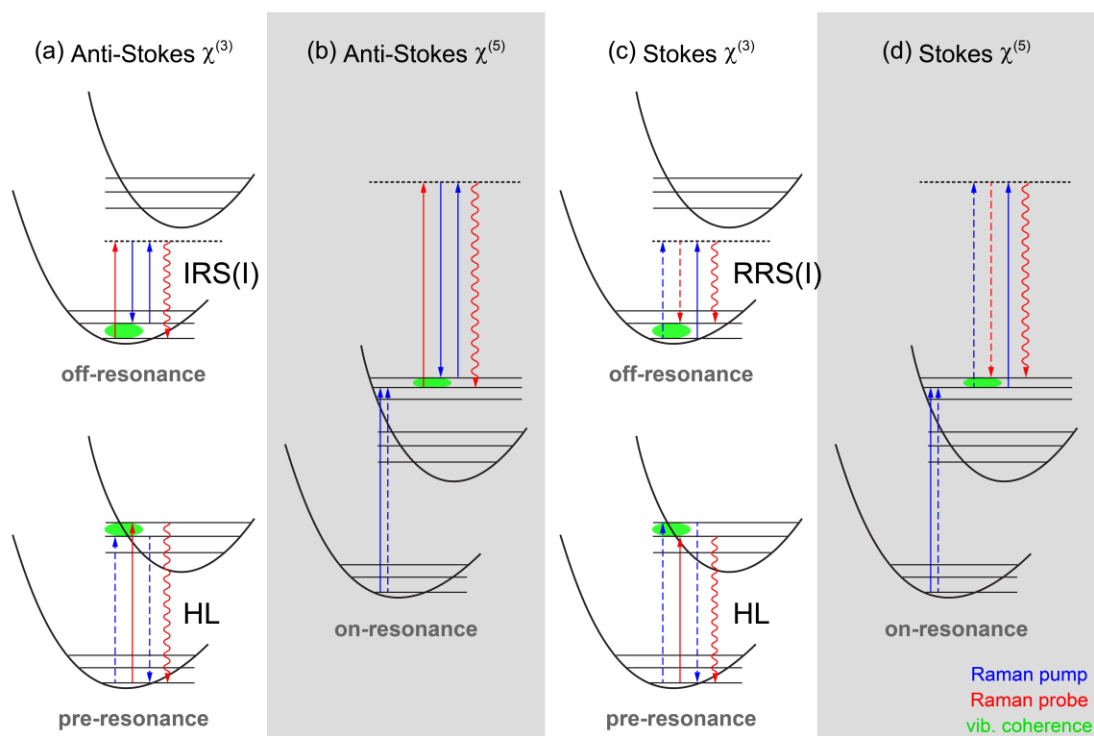
Figure 3.6. Energy-level diagrams illustrating the ground-state FSRS signal generation of R6G on the (a, b) anti-Stokes and (c, d) Stokes sides at different resonance conditions. The phase-matching condition $k_{sig} = k_{pu} + k_{pr} - k_{pu}$ of Raman pump (blue) and probe (red) pulses is satisfied. Solid and dash arrows represent the light-matter interactions/dipole couplings on the ket and bra sides of the molecular density matrix in the double-sided Feynman diagrams, respectively. The interaction proceeds from left to right in time. The green ellipse highlights the vibrational coherence generated in the electronic ground state (S_0) or excited state (e.g., S_1). For proof of principle, one representative HL and $\chi^{(5)}$ term is shown for the pre- and on-resonance condition. Reproduced with permission from Ref. [13]. Copyright 2018 Chinese Physical Society.

3.2.3 Stokes FSRS line shapes

The FSRS spectra on the Stokes side show different and less complicated line shape changes, implying a variation in nonlinear contributions. In Figure 3.5b, dispersive peaks are identified in the low-frequency region while positive peaks persist for high-frequency modes above 1000 cm^{-1} across the R_{pu} tuning range. At off- and pre-resonant R_{pu} wavelengths of 648, 596, and 581 nm, Stokes FSRS exhibits clear positive peaks generated by the RRS(I) term (Figure 3.6c). As R_{pu} is tuned into resonance, low and high-frequency modes start to differ. The dispersion of 614 and 773 cm^{-1} modes could be ascribed to the HL contribution because the corresponding R_{pr} wavelengths are more resonant than the high-frequency modes with the same R_{pu}. The 614 cm^{-1} mode exhibits an "earlier" line shape change (i.e., from absorptive to dispersive) relative to the 773 cm^{-1} mode as R_{pu} is tuned toward the blue side (Figure 3.5b), which is consistent with the anti-Stokes side (Figure 3.5a) and further highlights the important role of R_{pr} in determining line shapes in HL processes.[9,11] As R_{pu} is tuned from the GSA maximum to blue side (≤ 512 nm), these two modes regain positive line shape but show a broadened peak width. We attribute it to the $\chi^{(5)}$ contribution where R_{pu} excites some GS populations, followed by a $\chi^{(3)}$ process in the ES (Figure 3.6d).

For high-frequency modes above 1000 cm^{-1}, in sharp contrast to the anti-Stokes side, no dispersive line shapes are observed before R_{pu} is tuned into resonance. This result arises from different resonance conditions of R_{pr} on the Stokes and anti-Stokes sides. With red-sided R_{pu}, the anti-Stokes R_{pr} photons can be on-resonance with the GSA band while the Stokes photons remain off-resonant, leading to small contribution from HL terms on the Stokes side. It is conceivable that dispersive line shapes could appear when

R_{pu} is tuned to shorter wavelength until the mode-associated R_{pr} photons go into resonance, which cannot be easily observed in the Stokes spectra unless the R_{pu} and R_{pr} achieve comparable resonance conditions. Consequently, all the high- frequency modes show peak broadening but not significantly dispersive line shapes. Moreover, the 1656, 1578, 1513, and 1311 cm^{-1} modes red shift in center frequency, reminiscent of the anti-Stokes side. This key observation implies that the $\chi^{(5)}$ contribution becomes significant with these R_{pu} wavelengths and a transient ES population is involved (Figure 3.6d). Therefore, the absence of dispersion for high frequency modes in the Stokes FSRS lies in the fact that $\chi^{(5)}$ contributions become dominant over HL terms when the less energetic R_{pr} approaches resonance, while R_{pu} "overshoots" to the blue side (Figure. 3.4b) and has excessive energy for electronic excitation. In contrast, the more energetic R_{pr} on the anti-Stokes side gets into resonance before R_{pu} goes from pre- to on-resonance with the GSA band (Figure 3.4a). This intrinsic difference in pulse resonance conditions between the Stokes and anti-Stokes FSRS governs the peculiar line shape behaviors.

Moreover, the 1656, 1578, and 1513 cm^{-1} modes exhibit some intriguing changes from the 534 nm to 479 nm R_{pu} (Figure 3.5b). The 1656 cm^{-1} mode red shifts to ~1600 cm^{-1} with 534 nm to 522 nm R_{pu} and reappears with 512 nm to 479 nm R_{pu}, essentially showing the competition between different contributions under certain resonance conditions. The red-shifted feature could be assigned to a $\chi^{(5)}$ signal with minor HL contribution involving ES vibrational coherences while the unshifted, narrower peak mainly arises from the RRS(I) term involving GS vibrational coherences. The red shift

and frequency gap of the two peaks also indicate large anharmonicity of the 1656 cm^{-1} mode which could involve vibrationally hot states after electronic excitation by a bluer R_{pu}. For comparison, the 1578 and 1513 cm^{-1} modes only exhibit red-shifted peaks in FSRS with bluer R_{pu} wavelengths, and the latter mode shows very weak peak intensity as it red-shifts. The same phenomenon is also observed in the anti-Stokes spectra (Figure 3.5a), indicating the weak FC activity of this particular mode at blue wavelengths during the course of multidimensional vibronic transitions[9,32,37] of a photoexcited molecule in solution.

3.2.4 Competition between different nonlinear pathways

We have experimentally elucidated that the resonance conditions of both Raman pump and probe pulses are key players responsible for the FSRS line shapes. The Stokes and anti-Stokes spectra have distinct line shape behaviors particularly under pre- (quasi-) and on-resonance conditions. The stimulated Raman scattering has been addressed as a third-order nonlinear effect, thereby leading to various contributions caused by different pulse sequences of the picosecond R_{pu} and femtosecond R_{pr}. When these incident laser pulses approach resonance with the electronic band, the FSRS signal is complicated by more pathways involving the generation of vibrational coherences in different electronic states. In conjunction with relevant literature, our experiments provide further insights into the FSRS line shapes and intrinsic competition between possible pathways under the vibrational-mode-dependent resonance conditions. With an off-resonance R_{pu}, off-resonance $\chi^{(3)}$ processes such as RRS(I) and IRS(I) contribute

dominantly to sharp positive and negative line shapes in the Stokes and anti-Stokes FSRS, respectively (Figure 3.6a and 3.6c), because other resonant $\chi^{(3)}$ as well as $\chi^{(5)}$ processes are not favored without notable resonance. However, when R_{pu} becomes pre- or on-resonant with an electronic band, competing pathways become significant with a strong dependence of the mode-dependent R_{pr} resonance as the following: (i) HL terms with ES vibrational coherences which lead to the apparent mode dispersion line shapes (Figure 3.3), and/or (ii) the IRS(I) or RRS(I) with both ES population and vibrational coherences which lead to mode broadening and a discernible frequency redshift.

When R_{pu} is pre-resonant on the red side of GSA band, Stokes and anti-Stokes spectra show distinct line shapes due to different resonance conditions of R_{pr}. In anti-Stokes FSRS (Figure 3.5a), we observe circular line shape changes of the high-frequency modes when R_{pu} is tuned from 648 nm to 557 nm, strongly suggesting that the resonant R_{pr} favors HL terms over the resonant IRS(I) process. In contrast, weaker resonance of R_{pr} in Stokes FSRS leads to minor contribution from HL while the main contributor RRS(I) is evinced by narrow, positive, high-frequency peaks with R_{pu} from 596 nm to 557 nm (Figure 3.5b). Meanwhile, the low-frequency modes actually become more dispersive which indicates that HL contribution increases with better resonance of R_{pr}. This direct comparison between multiple vibrational modes under identical experimental conditions (Figure 3.5a and 3.5b) further confirms that R_{pr} is crucial in determining the FSRS line shapes from the HL terms.

When R_{pu} approaches full resonance, higher-order nonlinear pathways become appreciable as confirmed by the broadened and red-shifted peaks with R_{pu} at 534, 527, and 522 nm. Different line shapes in high- and low- frequency regions reveal the competition between HL and $\chi^{(5)}$ pathways in addition to the IRS(I) and RRS(I) terms. Since the high-frequency modes correspond to less resonant R_{pr}, the HL contributions diminish, while prominent $\chi^{(5)}$ processes generate positive and negative peaks on the Stokes and anti-Stokes sides, respectively. However, for the low-frequency modes, the R_{pr} achieves comparable resonance with R_{pu}, so the HL pathways still make notable contributions and lead to dispersive line shapes. Furthermore, we observed that the 614 and 773 cm^{-1} modes in Stokes FSRS at 522 nm R_{pu} exhibit different line shapes with different R_{pu} powers. This peculiar power dependence may suggest that the pertinent $\chi^{(3)}$ and $\chi^{(5)}$ processes, i.e., HL and RRS(I) in Figure 3.6c and 3.6d, strongly compete when both R_{pu} and R_{pr} are close to fully on-resonance conditions and there could be a phase relationship between the ground and excited state vibrational coherences. In contrast, the unchanged broad line shape of high-frequency modes above ~1000 cm^{-1} reveal that the $\chi^{(5)}$ process is more prominent than the HL terms (e.g., Eq.(1), leading to dispersive line shapes when b $\rightarrow$ 0). We expect that line shape changes may be observed at other resonant R_{pu} wavelengths with a larger variation of the R_{pu} power.

When R_{pu} is pre-resonant on the blue side of GSA band, R_{pr} is more resonant in Stokes FSRS while less resonant in anti-Stokes FSRS. The weaker resonance of anti-Stokes R_{pr} favors $\chi^{(5)}$ processes that lead to the broadened and red-shifted high-frequency peaks with R_{pu} from 512 nm to 479 nm (Figure 3.5a). In contrast, the low-frequency

mode at 611 cm^{-1} shows dispersive character due to the comparable resonance of R_{pr} and thus the HL contribution. It also explains a slight dispersion of the 614 cm^{-1} mode on the Stokes side. The high-frequency modes above 1000 cm^{-1} in Stokes FSRS exhibit certain mode dependence. The 1182, 1311, 1364, and 1578 cm^{-1} modes appear as broadened positive peaks with frequency red shift at 1311 and 1578 cm^{-1} (highlighted by magenta arrows in Figure 3.5b), implying that $\chi^{(5)}$ pathways are likely dominant. The 1513 cm^{-1} mode red shifts and diminishes as R_{pu} becomes bluer. It is plausible that the vibronic transition along this vibrational degree of freedom only constitutes the red edge of the GSA band and as a result, the resonance enhancement of the 1513 cm^{-1} mode is much weaker than other modes at blue R_{pu} wavelengths (see above). As support, the 1513 cm^{-1} mode is the strongest peak at off-resonant R_{pu} wavelengths (e.g., 648 nm) due to the proximity of R_{pu} and R_{pr} to this vibronic transition beneath the broad GSA band (Figure 3.4). Regarding the 1656 cm^{-1} mode at GS vibrational frequency, its peak width at these blue R_{pu} wavelengths remains narrow and unchanged so the RRS(I) pathway could be a main contributor. The new peak around 1600 cm^{-1} that may evolve from the 1656 cm^{-1} peak is consistent with an ES vibrational coherence generated through a $\chi^{(5)}$ process. Therefore, we speculate that this vibrational motion undergoes a notable frequency change upon photoexcitation typically as mode softening, corroborated by the experimentally observed mode frequency at 1647 cm^{-1} using resonance Raman at 532 nm excitation and 1600 cm^{-1} in resonance Raman with 488 nm excitation, while the $\chi^{(5)}$ contribution is comparable to the $\chi^{(3)}$ contribution. In addition, two other red-shifted modes at 1311 and 1578 cm^{-1} do not show clear GS peaks at these blue R_{pu} wavelengths (479, 491, 500, and 512 nm in Figure 3.5b)

probably because $\chi^{(5)}$ pathways contribute more to the FSRS signal than the RRS(I) terms.

On the mechanistic level and molecular time scales, we can attribute these observed peak frequency, intensity, and line shape variations in Figure 3.5 to the vibrational-mode-dependent nature on a multidimensional potential energy surface.[6,11,30,31,38] However, one intrinsic and potentially key difference between the pre-resonance HL terms in Figure 3.6a and 3.6c could explain why dispersive line shapes are generally more prevalent in anti-Stokes FSRS than Stokes FSRS. Since the nascent ES vibrational coherence relaxes (i.e., pure dephasing and vibrational population relaxation) during the FSRS signal generation typically on the ps time scale, the HL term favors a less energetic (redder) R_{pu} than a more energetic (bluer) R_{pu} during its second interaction with the relevant vibrational state. In other words, the ES vibrational relaxation leads to much less population on the higher lying vibrational state, which is required to interact with the bluer R_{pu} in the HL pathways on the Stokes side. As a result, less dispersive line shapes are observed in the Stokes FSRS, which is beneficial for spectral data analysis especially at pre-resonance conditions to simultaneously avoid large sloping baselines. Alternatively, the resonance conditions can be exploited at strategic R_{pu} and R_{pr} combinations mostly on the red side of an electronic band to achieve absorptive line shapes with enhanced SNR to access the GS and/or ES species.

In summary, we have systematically investigated the relationship between the Raman pump and probe resonance conditions with an electronic transition band and the

stimulated Raman line shape using a highly fluorescent dye in solution. The fine tuning of Raman pump wavelengths with small increments from the red to blue side of the ground-state absorption band of R6G in methanol has enabled the exploration of comprehensive resonance conditions across a broader spectral range. The resonance condition of Raman probe is revealed to play an important role in determining the circular line shape changes (i.e., absorptive to absorptive peak) involving the oppositely phased dispersion. The broadened and red-shifted peaks at resonant Raman pump wavelengths suggest that the higher-order $\chi^{(5)}$ pathways make significant contributions and generate some excited-state population and vibrational coherences in addition to ground-state vibrational coherences generated via the $\chi^{(3)}$ pathways. With the same Raman pump, the low- and high-frequency modes exhibit distinct line shape patterns which can be essentially attributed to the competition between different pathways due to different resonance conditions achieved by the mode-corresponding Raman probe. This comprehensive line shape study lays the foundation for exploiting the FSRS methodology on both the Stokes and anti-Stokes sides, and with the incorporation of a preceding actinic pump that can be separately tuned, to study photosensitive systems with desirable SNR and obtain crucial information about reaction dynamics on molecular time scales and the structure-energy-function relationships.

3.3 Excited-state FSRS line shapes: resonance with ESA[b]

The typical FSRS technique employs three pulses: an actinic pump initiates photochemistry by creating a population and sometimes coherence in an electronic excited state, followed by a narrowband Raman pump and broadband probe pair which generates the stimulated Raman scattering photon.[1,19] The broadband probe simultaneously samples vibrational modes in a wide spectral range (ca. 200−2000 cm^{-1}), and the multiple pulses that drive the stimulated Raman process result in much stronger signals compared to those of the spontaneous counterpart. In the stimulated Stokes region, when the lower frequency probe is used with the pump to create transient vibrational coherences in the electronic ground state (S_0), the dominant off-resonance contribution to a sharp gain signal is depicted in Figure 3.7 (left). In contrast, when a higher frequency probe is used, the inverse Raman loss scattering can occur (Figure 3.7, right), which is termed as the anti-Stokes process used in the spontaneous Raman terminology mainly because the emitting Raman scattering photon has a higher frequency than the Raman pump photon, although the exact use of terminology has been discussed in the literature.[14,15,17,19,20,24,29] Multi-wave mixing diagrams with different pulse sequences and interaction schemes contribute to the observed Raman signal from a realistic ensemble average system, and the situation is further complicated by the fact that all three laser pulses can be tuned to overlap with electronic absorption bands in the ground and/or excited state. Unlike vibrational spectroscopy using IR transitions, the resonance Raman effect can be exploited in wavelength-tunable FSRS

---

[b]This section is based on the publication: Oscar, B. G.; Chen, C.; Liu, W.; Zhu, L.; Fang, C. Dynamic Raman Line Shapes on an Evolving Excited-State Landscape: Insights from Tunable Femtosecond Stimulated Raman Spectroscopy. *J. Phys. Chem. A* **2017**, *121*, 5428-5441.

to greatly improve the signal-to-noise ratio (SNR)[30,35,39,40] but additional signal generation pathways become readily available, which could complicate the observed Raman line shape.[6,10,17,21,26,29]
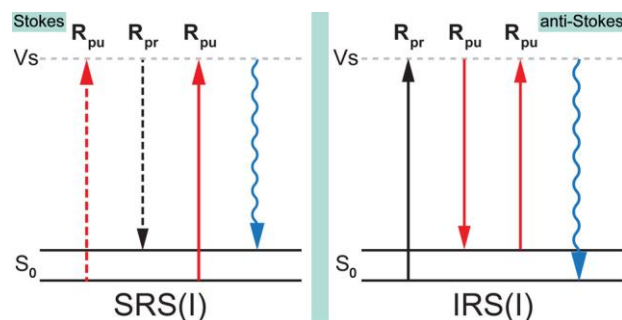
Figure 3.7. Off-resonance four-wave mixing process involving R_{pu} and R_{pr} generating the stimulated Raman scattering photons collinear with the probe. The SRS(I) process on the left leads to sharp gain peaks in the electronic ground state (S_0) with a Stokes Raman shift ($\omega_{pr} < \omega_{pu}$). The IRS(I) process on the right can generate sharp loss peaks with an anti-Stokes shift ($\omega_{pr} > \omega_{pu}$). The dashed and solid lines denote the interactions of incident light fields with the bra and ket side of the density matrix of the molecular system under study. "Vs" stands for a virtual state (gray dashed line). Reproduced with permission from Ref. [9]. Copyright 2017 American Chemical Society.

The resonance Raman effect has been characterized for both Stokes and anti-Stokes stimulated Raman peaks in the electronic ground state, S_0. Frontiera et al. showed the emergence of evolving dispersive anti-Stokes Raman loss peaks as the pump pulse was tuned toward the rhodamine 6G (R6G) absorption band from pre-resonance (on the red side) to resonance.[17] These results agreed with the theoretical predictions of Sun et al.,

who attributed the loss signal to the inverse Raman process (IRS(I), Figure 3.7, right panel) and additional contributions from the hot luminescence pathways available near resonance which lead to dispersive line shapes.[20,22] Similarly, Umapathy et al. observed the -1620 cm^{-1} mode (i.e., the Raman probe is on the blue side of the Raman pump) of crystal violet in ethanol changing from gain to loss through a dispersive intermediate, using ultrafast Raman loss spectroscopy (URLS) with a range of R_{pu} and bluer R_{pr} wavelengths, which is experimentally equivalent to the anti-Stokes FSRS approach.[15,18]

Despite efforts to characterize the R_{pu} dependence of the ground-state spectra, a thorough experimental study of the effect of R_{pu} and R_{pr} wavelengths on the excited-state Raman line shape has not been undertaken. Recently, the excited-state time-resolved URLS spectra of bis(phenylethynyl)benzene (BPEB) were collected with a R_{pu} at the excited-state absorption (ESA) peak maximum of 621 nm.[26] It is notable that only the Raman loss signal beyond ca. -1100 cm^{-1} was recorded, which means that the vibrational modes as well as the R_{pr} photons closer to resonance with the ESA maximum are not available for comparative analysis. On the contrary, we recently reported the FSRS signal sign change with nondispersive line shapes for a photoacid undergoing excited-state proton transfer (ESPT) reaction in aqueous solution. The R_{pu} wavelength, however, was fixed at 580 nm and fortunately achieved pre-resonance enhancement conditions for the photoreactant with an ESA band and the photoproduct with a stimulated emission (SE) band within the same spectral window. However, it remains unclear how the Raman line shapes change when the R_{pu} and R_{pr} pulses are scanned across a transient electronic band that also evolves after photoexcitation, which

is generally applicable for the real-time analysis of dynamic molecular systems and the relevant excited-state potential energy surface (PES) in condensed phase.

Here, we examine the intricate relationship between the R_{pu} and R_{pr} wavelengths and the excited-state resonance condition by systematically collecting the excited-state Stokes and anti-Stokes FSRS spectra of the photoacid pyranine (or HPTS) in neat methanol across a broad spectral window. HPTS is a model photoacid that is unable to undergo ESPT in methanol,[29,41-43] so we track only the electronic and vibrational features of the photoexcited protonated chromophore (PA*) without complication features originating from the photobase form (PB*). This system is of particular interest because there are several isolated Raman modes below 800 cm^{-1} as well as clusters of peaks at higher frequencies serving as marker bands, so we can assess different regions of the R_{pr} profile as well as obtain structural dynamics insights into the multidimensional photophysical and photochemical reaction coordinate. The ESA band of HPTS spans the visible range, which is ideally suited for the ca. 480−720 nm wavelength tunability of our home-built picosecond R_{pu} pulse.[29,30,35,40] We show that as the R_{pu} is tuned closer to resonance with the ESA band, the FSRS signal becomes dispersive on the anti-Stokes side but mostly for the low-frequency modes below ~1000 cm^{-1}. This mode dependence of the Raman line shape can be understood by different resonance conditions achieved by the R_{pu} and R_{pr} in reference to the ESA band maximum. More importantly, the Raman mode dynamics exhibit time dependence related to the ultrafast electronic dynamics and nonstationary change of resonance conditions. We therefore propose useful guidelines in selecting optimal conditions for

excited-state FSRS on the basis of the routinely acquired electronic spectra in both the equilibrium and non-equilibrium states.

3.3.1 Resonance condition

Provided that the FSRS line shapes depend on the position of the picosecond R_{pu} pulse with respect to the excited-state (S_1) resonance, it is important to evaluate the resonance conditions in the electronic excited states and their respective time dependence, which are recorded by the fs-TA spectra (Figure 3.8). In the case of HPTS in methanol, when the ESA band maximum after photoexcitation blue-shifts in time due to solvation events,[44-46] R_{pu} experiences a dynamic resonance condition that could change the apparent Raman line shapes in a mode-dependent manner.[15,26,28]
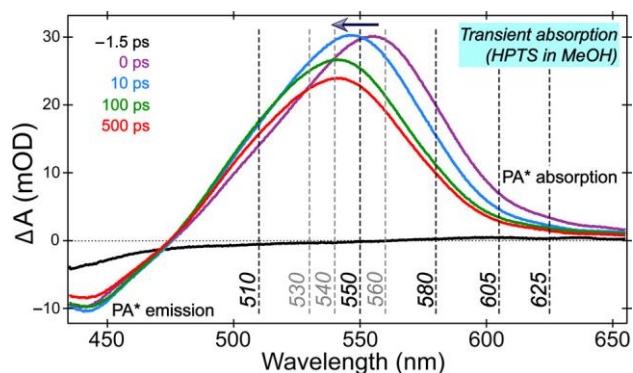
Figure 3.8. TA spectra of HPTS in methanol at representative time delays upon 400 nm photoexcitation. A broad ESA band attributed to PA* of the solute chromophore is centered at 555 nm at time zero (magenta trace) and blue-shifts on ultrafast time scales. The Raman pump wavelengths used are indicated by dashed vertical lines. Reproduced with permission from Ref. [9]. Copyright 2017 American Chemical Society.

For HPTS in methanol, the prominent ESA band centered at 555 nm exhibits a distinct blueshift to 542 nm with a ~9 ps time constant and its intensity decays over several hundred picoseconds (Figure 3.8).[41,44,46] An SE feature below ~470 nm is also present and slightly red-shifts in time due to molecular relaxation in the first excited state. In our previous FSRS experiments on HPTS in methanol, we have used both an 800 nm R_{pu} and a 580 nm R_{pu}. We observed orders of magnitude increase in SNR in the stimulated Stokes Raman gain with the bluer pump pulse for a much less concentrated sample (i.e., 1.5 mM, compared to 15 mM with the 800 nm R_{pu}). On the basis of Figure 3.8, it is apparent that the tunable R_{pu} at 580 nm with the accompanying Stokes R_{pr}, which extends to ~640 nm, are both pre-resonant with the ESA feature and the detuning of the R_{pu} from the ESA peak at 550 nm is ~940 cm^{-1}. At different conditions, it is possible for either one or both R_{pu} and R_{pr} to be strongly resonant with the ESA band, especially in the region where scattering from low-frequency modes is generated and detected (i.e., both R_{pu} and R_{pr} are very close in the spectral domain). Using the R_{pu} wavelengths marked in Figure 3.8, excited-state Stokes and anti-Stokes FSRS spectra are systematically collected for HPTS in neat methanol. The R_{pu} wavelengths cover pre-resonance through resonance on the red edge of the ESA band. We also extend our investigation by also probing the blue edge of the ESA band and extending into the red edge of the SE band of the PA* form of HPTS that is further to the blue side of the ESA band (Figures 3.8).

3.3.2 Stokes and anti-Stokes FSRS line shapes at fixed time delays

Near resonance, the raw exited-state Stokes and anti-Stokes spectra with baselines (Figure 3.9) are strongly influenced by the background electronic signal. Transient Raman peaks are visible on top of the smooth and largely featureless spectral baseline at each R_{pu} condition, and resonance enhancement regions correspond to the R_{pr} overlap with the ESA band. For example, the Stokes mode at 423 cm^{-1} is particularly strong using a 580 nm R_{pu} due to the pre-resonance enhancement on the red side of ESA. The same logic applies to the high-frequency region on the anti-Stokes side with a 605 nm R_{pu} because an ~1520 cm^{-1} mode, for instance, arises from a 554 nm R_{pr}, which almost matches the ESA maximum at 500 fs time delay after 400 nm photoexcitation (Figure 3.8).[46] In general, smooth spline baselines (red, Figure 3.9) can be drawn on the red and blue edges of the ESA band, which arise from the Raman-pump-induced excited-state population change (reminiscent of but not identical to the fs-TA experimental data).[30,47] However, resonance contributions from an SE band are possible on the blue side of the ESA, especially when the anti-Stokes measurement is performed. In the scenario that some broad electronic features are present in Figure 3.9, their widths are much broader than the Raman modes. Moreover, the occurrence of such broad features is correlated with strong resonance conditions (e.g., R_{pu} = 580, 550 nm in Figure 3.9), which cannot rule out contributions from hot luminescence terms (e.g., HL(I) and HL(II), see below).

Upon baseline subtraction, the excited-state Raman peaks are clearly resolved (Figure 3.10). When the R_{pu} is positioned at the red edge of ESA band (e.g., 625 and 605 nm),

both the Stokes and anti-Stokes FSRS signals are Raman gain. The anti-Stokes peaks have greater intensities largely due to the resonance conditions we exploit, and the closer match between the R_{pr} wavelength and the ESA band is responsible for the observed peak enhancement. As the R_{pu} is tuned to bluer wavelengths, the Stokes signal remains as largely gain features, but the high-frequency peak doublet loses resolution at the R_{pu} wavelengths close to resonance. At 510 nm, all the features are Raman gain (except one mode at ~678 cm^{-1} that shows Raman loss possibly resulting from the strong vibronic coupling with the $S_1 \rightarrow S_n$ transition), indicating that the Stokes FSRS is overall less sensitive to the R_{pu} position in reference to the ESA band, though the high-frequency modes clearly undergo some enhancement at this condition which can be correlated with a resonance match between the ESA band maximum and R_{pr}.
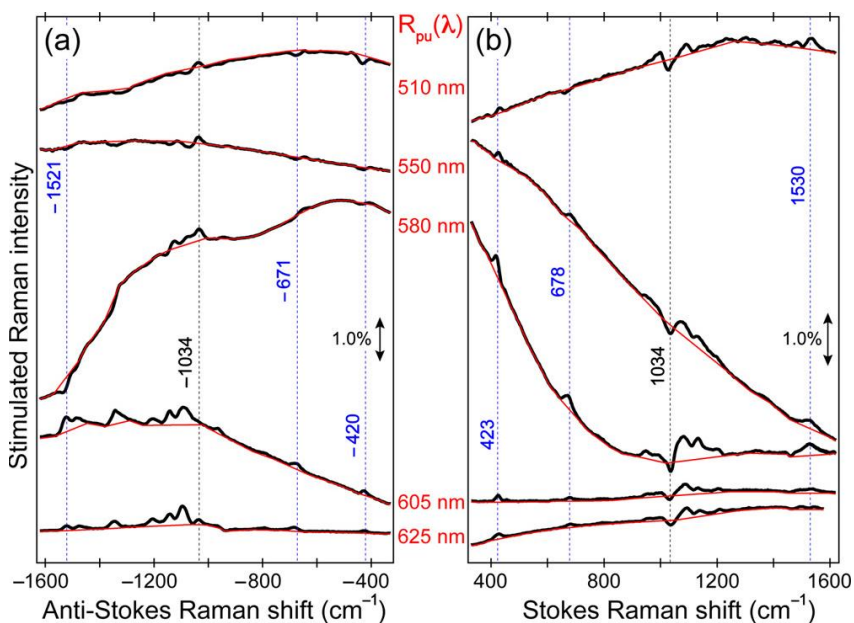
Figure 3.9. Raman line shape dependence on the R_{pu} wavelengths. (a) Anti-Stokes and (b) Stokes ground-state-subtracted excited-state Raman spectra of 1.0 mM HPTS in methanol at 500 fs after 400 nm photoexcitation. The Raman gain or loss magnitude is

indicated by the double-headed arrow. Vertical dashed lines indicate selected excited-state peak frequencies of HPTS (blue) and the methanol solvent band at 1034 cm^{-1} (black). The smooth, broad spectral baselines in red are superimposed on the FSRS data traces in black. Reproduced with permission from Ref. [9]. Copyright 2017 American Chemical Society.
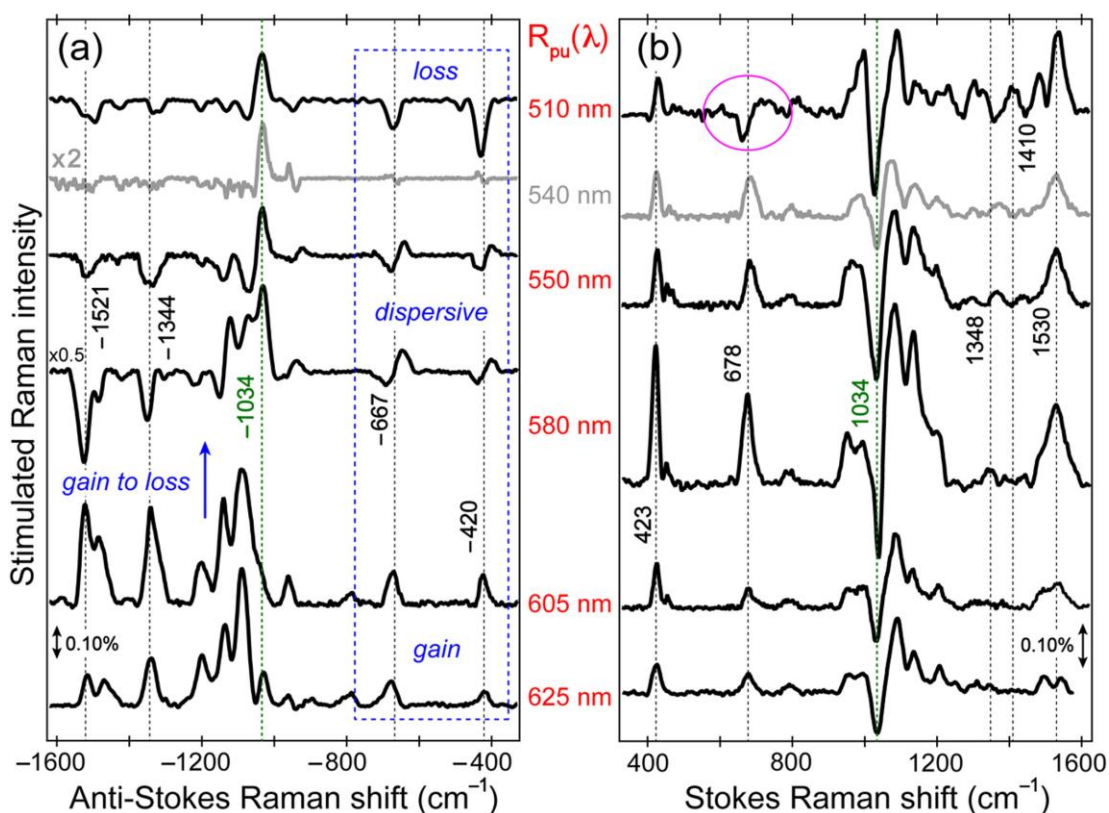
Figure 3.10. Excited-state FSRS spectra with different R_{pu} wavelengths on the (a) anti-Stokes and (b) Stokes side at 500 fs following 400 nm photoexcitation. Black and gray traces are the results of baseline subtraction from the raw spectra in Figure 3.9. Dashed lines indicate the excited-state peak frequencies of HPTS (black) and the methanol band at 1034 cm^{-1} (green). The stimulated Raman intensity magnitude of 0.10% is

given by the double-headed arrow. The anti-Stokes spectra at R_{pu} = 580 and 540 nm are scaled for clarity. Key Raman bands are denoted by vertical dotted lines with the average mode frequencies. Reproduced with permission from Ref. [9]. Copyright 2017 American Chemical Society.

In comparison, the anti-Stokes spectra undergo a dramatic change when the Raman pulses are tuned toward the strongly resonant condition. The line shapes for the low-frequency modes become dispersive (Figure 3.10, blue dashed box) with R_{pu} = 580 nm, and the signal phase changes once R_{pu} is tuned to the blue side of the ESA band, e.g., 540 nm. Meanwhile, starting with the 580 nm R_{pu}, the high-frequency modes become Raman loss (Figure 3.10). Raman loss signals were reported in excited-state URLS experiments at a similar resonance condition,[26] and there is additional evidence that overlap of the Raman pulses with an SE band (to the blue side of the ESA band for HPTS in methanol, Figure 3.8) may also result in a Raman loss signal in the anti-Stokes FSRS spectra.[29,48] The 510 nm anti-Stokes spectrum is weak because of overlapping resonance conditions (e.g., ESA and SE) and fewer R_{pr} photons due to the spectral profile of the broadband SCWL that is generated by an 800 nm fundamental pulse.[49,50]

The excited-state Stokes spectra of HPTS in methanol have been reported before, and the vibrational mode positions are highly reproducible.[30,46,51] In the excited-state anti-Stokes spectra, the ~1335 cm^{-1} mode is greatly enhanced compared to the weak mode at ~1355 cm^{-1} in the Stokes spectra at all Raman pump wavelengths, especially at

conditions where the anti-Stokes Raman probe corresponding to this mode (e.g., R_{pu} = 605, 580 nm so R_{pr} = 559, 538 nm) is highly resonant with the ESA band at early time (Figure 3.8). The modes in this region have considerable intensity on the Stokes side only when R_{pu} = 510 nm in Figure 3.10b so the high-frequency modes are close to the ESA peak maximum (e.g., for a 1412 cm^{-1} mode, R_{pr} = 550 nm). The 1335 cm^{-1} mode has been assigned to an in-plane ring deformation with a COH rocking component. This coordinate may be strongly coupled to the transition to higher lying excited states for a planar, conjugated four-ring system like HPTS.[43,51,52] As a result, when the optimal resonance conditions are not met (e.g., R_{pu} > 540 nm and R_{pr} > 582 nm, Figure 3.10b except the top trace) for a mode with strong vibronic coupling to an electronic transition (e.g., ESA from $S_1 \rightarrow S_2$), the Raman mode intensity is small. Furthermore, the 678 cm^{-1} in-plane ring symmetric deformation mode on the Stokes side exhibits line shape changes (likely due to its vibronic structure) as the Raman pump is tuned across the ESA band. Once the Raman probe photons responsible for the transition are on the higher energy side of ESA the mode begins to take on dispersive characteristics.

In Figure 3.10a, the FSRS peak intensity of the ~1520 cm^{-1} mode on the anti-Stokes side significantly drops when the Raman pump is tuned from 580 to 550 nm (i.e., the ESA peak). This observation confirms that the mode intensity is significantly affected by the Raman excitation profile of the corresponding vibration,[32,53,54] and in this case, masked under the broad ESA band (Figure 3.8). The R_{pr} wavelength at those conditions is ~533 and 508 nm, respectively, which is very close to the ESA peak position and away from it. This result demonstrates the dominance of R_{pr} resonance condition in

determining the Raman peak intensity, in contrast to conventional wisdom that the Raman pump alone in resonance with an electronic band can exploit the resonance enhancement effect, irrespective of the probe wavelength. In comparison, the intensity variation for low-frequency modes below 800 cm^{-1} is much less notable because the resonance conditions remain largely unchanged with the Raman probe wavelength (e.g., varying from ∼566 to 538 nm for a 420 cm^{-1} mode).

Raman peak frequencies are determined from the baseline-subtracted spectra shown in Figure 3.10 and tabulated in Table 3.1 for R_{pu} = 580 nm in conjunction with R_{pr} = 590−640 nm (Stokes side) and R_{pr} = 530−570 nm (anti-Stokes side). In general, the anti-Stokes modes appear at lower frequencies compared to the Stokes counterpart with the same Raman pump wavelength after photoexcitation. For example, the ring C=C stretching mode at ∼1530 cm^{-1} on the Stokes side appears at ∼1520 cm^{-1} (negative sign omitted) on the anti-Stokes side. With Raman pump and probe wavelengths approaching the ESA peak resonance (i.e., anti-Stokes FSRS with R_{pu} = 580, 550 nm) the 420 cm^{-1} in-plane ring deformation mode is dispersive. We note that the FSRS peak intensity difference in S_0 (Figure 3.7) does not apply in S_1 mainly due to the excited-state resonance conditions dominating the generation of Stokes and anti-Stokes FSRS signals (see below for the Feynman diagrams). Because the methanol peak consistently appears at 1034 cm^{-1} as an internal solvent standard, the aforementioned solute peak frequency variations are attributed to higher vibrational levels of HPTS.

Table 3.1. Excited-state FSRS peak frequencies of HPTS in methanol with a 580 nm Raman pump at 500 fs after 400 nm photoexcitation.

Stokes frequency (cm^{-1})	Anti-Stokes frequency (cm^{-1})
422	−414
673	−666
949	−943
1034[a]	−1033[a]
1132	−1128
1488	−1481
1528	−1524

[a]Solvent peak that is dominant in this work.

3.3.3 Dynamic FSRS line shape change in time

The R_{pu} and R_{pr} positions relative to the excited-state resonance conditions exert a large impact on the recorded Raman spectrum. Figures 3.9 and 3.10 show excited-state FSRS spectra at only one time point, but the ESA band of HPTS in methanol undergoes a pronounced, ~13 nm blue shift on ultrafast time scales attributed to ultrafast solvation events (Figure 3.8). Thus, the R_{pu} and R_{pr} wavelengths close to resonance may complicate the Raman mode dynamics especially for an evolving ESA band.

Figure 3.11 presents the time-resolved anti-Stokes FSRS spectra with a 580 nm Raman pump up to 600 ps after 400 nm photoexcitation. The excited-state Stokes FSRS spectra have been reported at this condition[46] so an informative comparison can be made. The broader electronic dynamics are manifested in the ultrafast shift of the ground-state-

subtracted FSRS data traces (Figure 3.11a, blue arrow),[30,55,56] and because they are plotted against the anti-Stokes Raman shift in Figure 3.11b, the corresponding R_{pr} wavelengths are decreasing (e.g., a blue shift of ~12 nm from 548 to 536 nm) with the increase of the Raman mode frequency (e.g., a blueshift of ~400 cm^{-1} from −1000 to −1400 cm^{-1}). We note that these ground-state-subtracted experimental Raman traces largely mirror the profile of the solute ESA band. This feature could thus serve as a experimental validation for the proper chopper phase in the R_{pu} and/or actinic pump beam paths to collect the accurate difference FSRS signal induced by photoexcitation.[29]
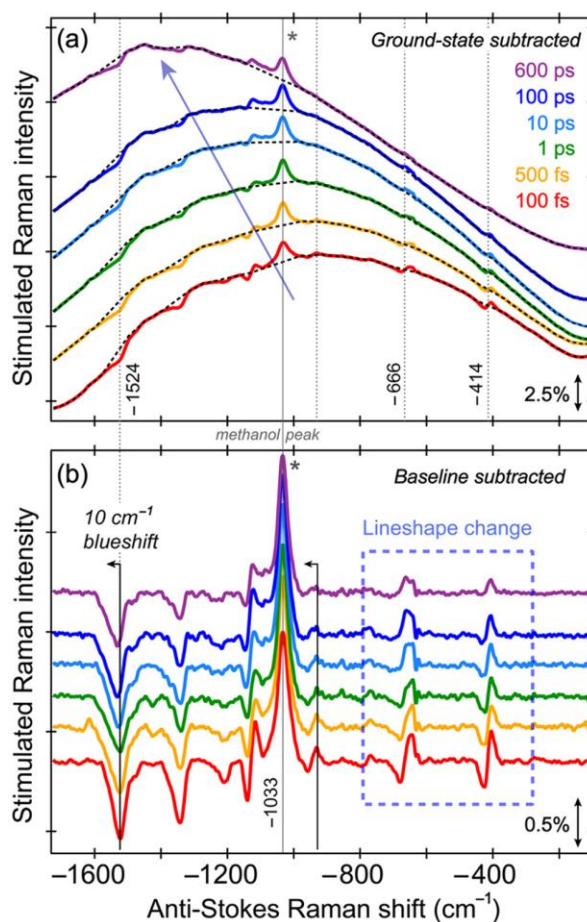
Figure 3.11. Time-resolved anti-Stokes FSRS spectrum of HPTS in methanol with a 580 nm R_{pu} following 400 nm photoexcitation. (a) The raw spectra track the blueshift of the ESA band in time (blue arrow). Broad spectral baselines are shown in dashed

curves. (b) The baseline-subtracted spectra show dispersive low-frequency modes at early times that evolve into purely gain signals at later times. High-frequency modes are Raman loss and their frequencies blue-shift in time. The methanol solvent peak at 1033 cm^{-1} is marked by the vertical gray line and an asterisk. Reproduced with permission from Ref. [9]. Copyright 2017 American Chemical Society.

Furthermore, we subtract the baselines in Figure 3.11a and plot the transient Raman spectra in time (Figure 3.11b). Interestingly, the dispersive peaks in the low-frequency modes transition into gain signals after hundreds of picoseconds (highlighted by the dashed box) while R_{pu} remains fixed at 580 nm. This result confirms that an increased gap between the fixed R_{pr} and the blue-shifting ESA band maximum (Figure 3.8) is responsible for the diminution of dispersive features. In other words, the specific resonance condition of the R_{pr} could play an important role in the origin of dispersive features in anti-Stokes FSRS whereas the R_{pu} is largely off or pre-resonance. In our previous work, the time-resolved anti-Stokes spectra of HPTS in water were presented below ~900 cm^{-1} but the low-frequency modes therein (e.g., ~426 cm^{-1} on the Stokes side and 410 cm^{-1} on the anti-Stokes side) exhibit nondispersive line shapes[29] because the solute ESA band of HPTS in aqueous solution is centered at ~530 nm. This wavelength represents a 20 nm blueshift from the ESA band maximum of HPTS in methanol at 550 nm (Figure 3.8), which is sufficient to cause the observed Raman line shape variation in S_1. Particularly with the R_{pu} at 580 nm, the corresponding anti-Stokes R_{pr} photons in generating the ~414 and 666 cm^{-1} modes of HPTS in methanol (Figure

3.11b and Table 3.1) are at ~566 and 558 nm, respectively. It is clear that these wavelengths of the Raman probe are $\sim$30 nm to the red side of the ESA peak in water but this gap decreases to $\sim$10 nm in methanol, and as a result, dispersive Raman peaks are only observed in methanol due to an effective on-resonance condition of R_{pr}. Note that the R_{pu} remains at a fixed pre-resonance condition in both cases. We suspect that various four-wave mixing pathways in the electronic excited state with different R_{pu} and R_{pr} pulse orderings, resonance conditions, and the stimulated Raman nature of the time-resolved FSRS signal photons are responsible for the specific sensitivity of the observed transient Raman line shape and dynamics to the Raman probe frequency.[6,29,48]

3.3.4 Origin of excited-state FSRS line shapes

Like the previously conducted ground-state resonance experiments, the sign of the Stokes and anti-Stokes FSRS peaks in the electronic excited state are strongly dependent on the specific resonance condition achieved by both R_{pu} and R_{pr} pulses after the excited-state population is generated by the preceding actinic pump pulse. In the case where R_{pu} (625 nm) is tuned furthest from the ESA band maximum, both the Stokes and anti-Stokes peaks are Raman gain which benefit the ensuing spectral data analysis. This is expected for the FSRS signal generation on the Stokes side, as the dominant off-resonance mixing diagram SRS(I) results in a Raman gain (Figure 3.7 with Vs replaced by a real state) as many previous FSRS studies have supported and verified this observation. The anti-Stokes FSRS peaks, however, can also display a gain signal that was observed in pre-resonance ground-state experiments with molecules

such as R6G.[13,17] In our experiment, the R_{pr} photon wavelength corresponding to the low-frequency modes overlaps the red side of the ESA band for a near-off-resonance R_{pu} (600 nm), which leads to positive Raman peaks within the broad spectral window (Figure 3.10a). Between the R_{pu} of $\sim$580 and 540 nm, the R_{pr} goes across the ESA band maximum, hence the experimentally observed dispersive Raman line shapes.

In the previous section (section 3.2), we introduced the investigation on the ground-state FSRS line shape using R6G.[13] As R_{pu} was tuned from the red edge of the absorption band toward the blue edge, the low-frequency modes below $\sim$1000 cm^{-1} change from negative to dispersive, purely positive, and then oppositely phased dispersion as the R_{pu} approaches the absorption peak maximum. However, the relationship between the line shape in the Stokes and anti-Stokes FSRS with the excited-state electronic resonances remains actively studied and debated.

Since the double-sided Feynman diagrams for the ground-state FSRS have been discussed in the literature, we depict the excited-state Stokes (Fig. 3.12) and anti-Stokes (Fig. 3.13) FSRS pathways with an ESA band to lay out central contributions to the sign and line shape of the observed FSRS signal.[14,22] Vibronic states are intimately involved in sequential interactions between a molecular system and incident laser pulses, and four-wave mixing processes in the electronic excited state can adopt various forms of response functions to generate the Raman gain, Raman loss, or dispersive Raman line shapes, when the off-resonance and on-resonance conditions are separately considered for the excited-state FSRS signal generation.[7]
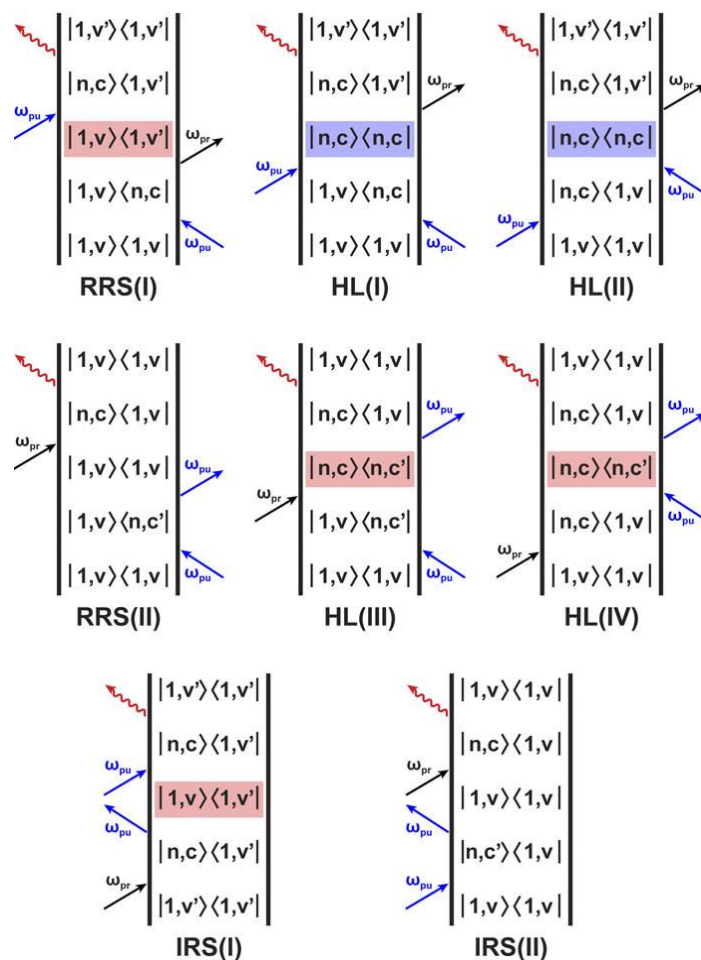
Figure 3.12. Double-sided Feynman diagrams depicting the density matrix evolution during excited-state four-wave mixing processes in Stokes FSRS on resonance with an ESA band. Lower and higher electronic levels are represented by $|1\rangle$ and $|n\rangle$, respectively, while vibrational levels are represented by $|v\rangle$, $|c\rangle$ and $|v'\rangle$, $|c'\rangle$ and $v' = v + 1$, $c' = c + 1$. R_{pu} and R_{pr} are shown in blue and black, respectively. Time evolves from bottom to top. The emitting FSRS signal is shown as a red wavy arrow pointing outward on the ket side. Red and blue shades represent the nascent vibrational coherence and population, respectively. Reproduced with permission from Ref. [7]. Copyright 2019 AIP Publishing.
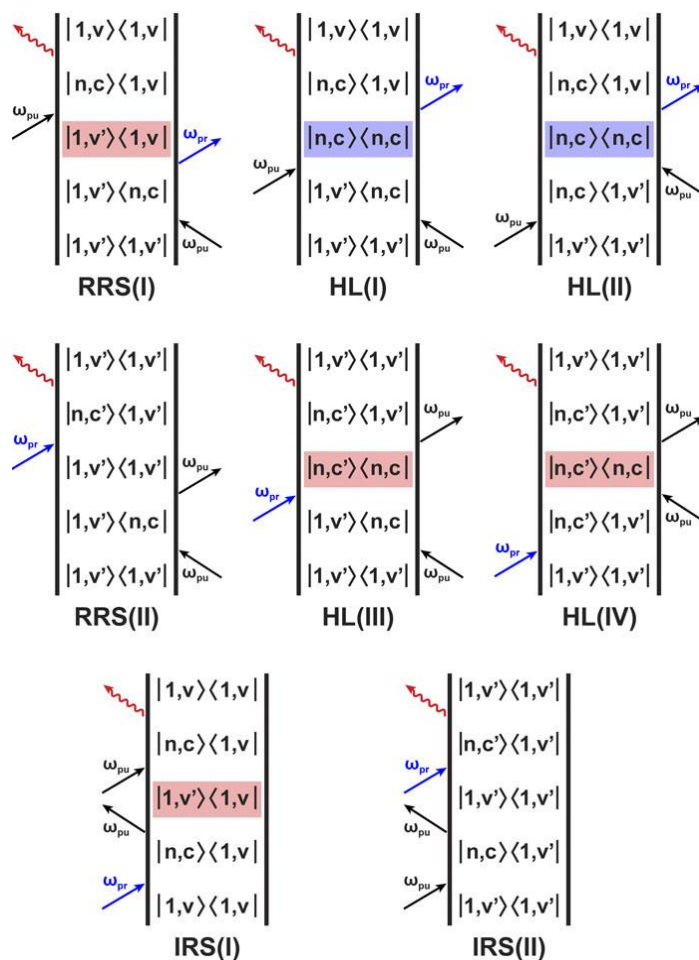
Figure 3.13. Double-sided Feynman diagrams depicting the density matrix evolution during excited-state four-wave mixing processes in the anti-Stokes FSRS on resonance with an ESA band. The electronic and vibrational quantum notations, indications of red and blue shades, and grouping of relevant terms are identical to Figure 3.12. R_{pr} and R_{pu} shown in blue and black, respectively. Reproduced with permission from Ref. [7]. Copyright 2019 AIP Publishing.

In this ESA-dominant scheme for HPTS in methanol, the RRS(I) and IRS(I) pathways involve the generation of vibrational coherences in S_1. In contrast, HL(III) and HL(IV)

involve the generation of vibrational coherences in a higher-lying electronic excited state. HL(I) and HL(II) involve the creation of an excited state population. RRS(II) and IRS(II) only involve the population in S_1 (i.e., no vibrational coherence hence only contributing to very broad signals such as the baseline). R_{pr} leads to de-excitation in RRS(I), HL(I), and HL(II) while excitation in all other terms. The sum of these eight terms contribute to the overall FSRS signal and observed line shape. To understand the FSRS signal line shape change particularly on the anti-Stokes side, we remark the following regions with characteristic R_{pu} and R_{pr} wavelengths.

First, when the Raman pulses are off-resonance with an ESA band, a virtual state is involved to generate the relatively long-lived vibrational coherence in the lower-lying electronic state (e.g., S_1) that is responsible for narrow Raman peaks. Hence, RRS(I) is the main contributor to the observed narrow Stokes and anti-Stokes gain signals (i.e., R_{pr} acts as a de-excitation pulse) under the off-resonance condition, which leads to the excited state gain signal. Because the HL(I–IV) terms are not associated with a real higher-lying electronic state, they would not contribute to narrow Raman line shapes.[14]

Second, when the Raman pulses are pre-resonance or on resonance with the ESA band, the HL(I– IV) terms may also contribute to the overall FSRS signal. In particular, HL(III) and HL(IV) generate a vibrational coherence in a real higher-lying electronic excited state while RRS(I) generates a vibrational coherence in S_1. We speculate that the mixing of these two vibrational coherences results in dispersive line shapes and perform the relevant simulations on two damping modes with close frequencies but

various phases.[9] We note that dispersive line shapes are prominent for low-frequency modes because the R_{pu} and R_{pr} photons are close in frequency so the HL(III) and HL(IV) terms can be significant and generate vibrational coherences in S_n more easily. In contrast for the high-frequency modes, larger difference in the R_{pu} and R_{pr} wavelengths makes it more difficult to achieve optimal resonance conditions for both pulses at the same time, hence the more rapid transition from positive to negative Raman peaks without a clear dispersive intermediate.

Third, as Raman pulses move closer to and across the ESA band, the IRS(I) term may be the dominant contributor to the observed negative line shape due to the longer wavelength of R_{pu} than R_{pr} in anti-Stokes FSRS (Fig. 3.13). This rationale explains the observed excited-state anti-Stokes Raman peaks at lower frequencies than Stokes counterparts (Table 3.1). High- and low-frequency modes do not behave exactly the same because the corresponding Raman probe wavelengths are different and together with the Raman pump pulse, achieving various resonance conditions.

Note that these diagrams and interpretations are based on logical comparisons between experimental observations and previous theories. We hope that our comprehensive experimental data could motivate more theory groups to perform rigorous calculations and simulations to better understand the effect of Raman picosecond pump and femtosecond probe pulses (close in arrival time at the sample, but in various time orderings) on the different Raman line shapes in the equilibrium as well as transient FSRS data.

3.4 Excited-state FSRS line shapes: resonance with SE

In excited-state FSRS, the investigation of line shapes when on resonance with SE has been more underexplored with respect to that with ESA despite that many FSRS works have taken advantage of the resonance with SE.[6,10-12,29] The earliest related study was reported by McCamant et al. where they attributed the dispersive line shapes in excited-state Stokes FSRS to "Raman initiated by nonlinear emission " (RINE) when R_{pu} is on resonance with the SE band of bacteriorhodopsin.[10] This is equivalent to the HL (III) and (IV) as mentioned in the previous sections. The interference between the R_{pr} field and the out-of-sync signal field during heterodyne detection leads to dispersive line shapes, which are dependent on the vibrational mode frequency, Franck-Condon (FC) factor, and coherence lifetime. Later, Niu et al. adopted quantum wave-packet theory to simulate the FSRS line shapes in this scenario and concluded, however, that the dispersive line shapes are due to the inverse Raman scattering, i.e., IRS (I), out of the eight Feynman diagrams (Figure 3.12 and 3.13) rather than RINE or HL processes.[22] Thus, the exact origin of the dispersive line shapes in excited-state FSRS when Raman pulses are on resonance with SE remains debatable and deserves further exploration.

Experimentally, our laboratory provides appreciable insights of the FSRS line shapes in case of resonance with SE and also shows that SE could be a great choice for resonance enhancement.[11,12,29,31,57-59] In 2016, we reported the Stokes and anti-Stokes FSRS spectra of the photoacid HPTS in water in which ESPT is present.[29] The R_{pu} wavelength is tuned to 580 nm, which is red-sided to the ESA band of the photoreactant (protonated HPTS) and also to the SE band of the photoproduct (deprotonated HPTS).

In the latter resonance condition, the FSRS peaks below 1000 cm^{-1} exhibit positive and negative line shapes on the Stokes and anti-Stokes sides, respectively. Some other works from our laboratory have also taken advantage of this resonance condition, e.g., Stokes FSRS with a red-sided R_{pu} to the SE band, to improve the signal-to-noise ratio with non-dispersive line shapes.[5,12,31,57,59]

Furthermore, we have also explored the effect of a blue-sided R_{pu} to the SE band on the line shape and intensity enhancement, which has not been investigated before to the best of our knowledge. It turned out that it represents an excellent resonance condition particularly for Stokes FSRS that yields non-dispersive line shapes with strong dependence on the R_{pr} wavelength and significant intensity enhancement.[11,58] We investigated the ESPT of a GFP chromophore-derived superphotoacid (*p*-HO-3,5-diF-BDI:BF$_2$) in methanol where the R_{pu} wavelength is between the SE bands of the protonated (photoreactant) and deprotonated (photoproduct) forms (Figure 3.14). For the protonated form (PA*), the 510-nm R_{pu} is to the red side of SE band. As a result, the Stokes FSRS spectra exhibit weak intensity for a couple of PA* modes (e.g., 1580 cm^{-1}) with positive line shape (Figure 3.14b) while anti-Stokes FSRS spectra show more intense peaks with negative and dispersive line shapes (Figure 3.14a). These line shapes are consistent with the abovementioned FSRS results for HPTS except the presence of some dispersive peaks. It also suggests that the resonance of R_{pr} plays an important role in the intensity enhancement. On the other hand, the deprotonated form (PB*) is almost absent in the anti-Stokes FSRS spectrum (Figure 3.14a) while several intense PB* modes appear in the Stokes FSRS spectra (Figure 3.14b) due to the

simultaneous resonance of both R_{pu} and R_{pr} pulses with the SE band. Interestingly, the PB* modes show opposite line shapes in low-frequency (<1000 cm^{-1}) and high-frequency (>1000 cm^{-1}) regions with positive and negative peaks, respectively.
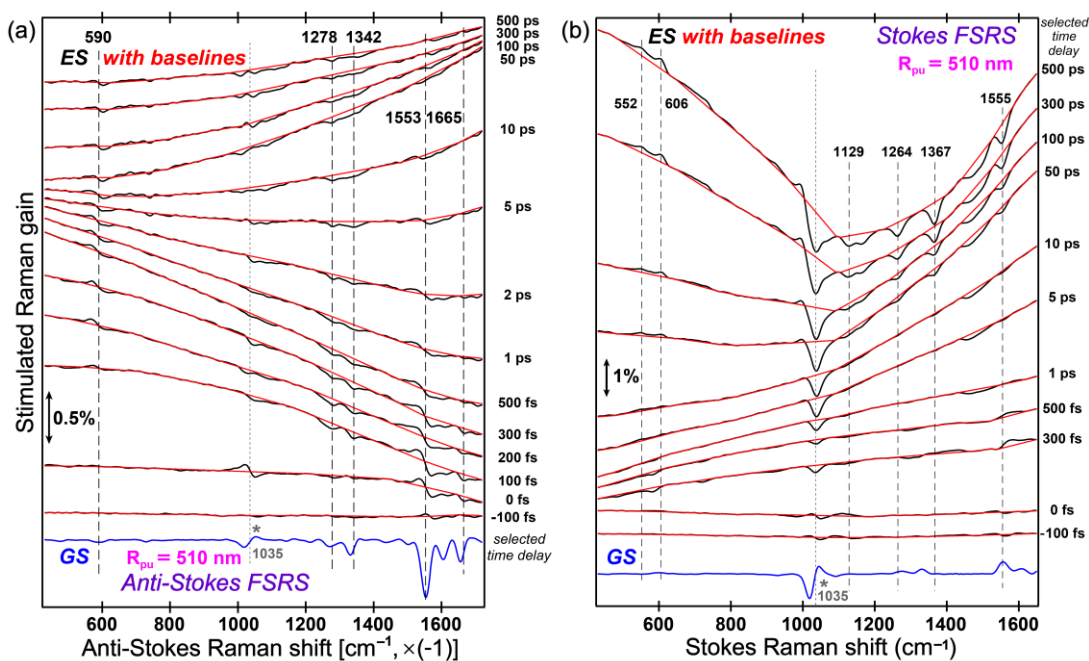
Figure 3.14. Representative raw excited-state anti-Stokes and Stokes FSRS spectra of GFP chromophore-derived superphotoacid p-HO-3,5-diF-BDI:BF$_2$ in methanol upon 400 nm actinic excitation with 510 nm R_{pu}. The spline baselines (red) are shown between −100 fs and 500 ps. The R_{pu} wavelength is at 510 nm. The ground-state (GS, blue) spectrum is shown at the bottom for comparison. Adapted with permission from Ref. [11]. Copyright 2017 American Chemical Society.

As the R_{pu} was tuned to 520 nm, the low-frequency peaks below 1000 cm^{-1} changes to negative sign while the high-frequency peaks above 1000 cm^{-1} remain negative. This

observation implies that the position of R_{pr} in reference to the SE band is crucial to the line shape in case of a blue-sided R_{pu}. Based on these observations, it seems that the negative sign originates from the resonance condition that R_{pu} is at the blue side of the SE band (~540 nm) while the R_{pr} photon wavelengths corresponding to the vibrational modes are at the red side. The positive sign appears when R_{pu} and R_{pr} wavelengths are both at the blue side of the SE band. Similar phenomena have also been observed in the Stokes FSRS of a similar photoacid system. A detailed theoretical modeling on the basis of all the involving Feynman diagrams (see Figure 3.12 and 3.13 above) could reveal more insights into the nonlinear FSRS signal generation mechanism.
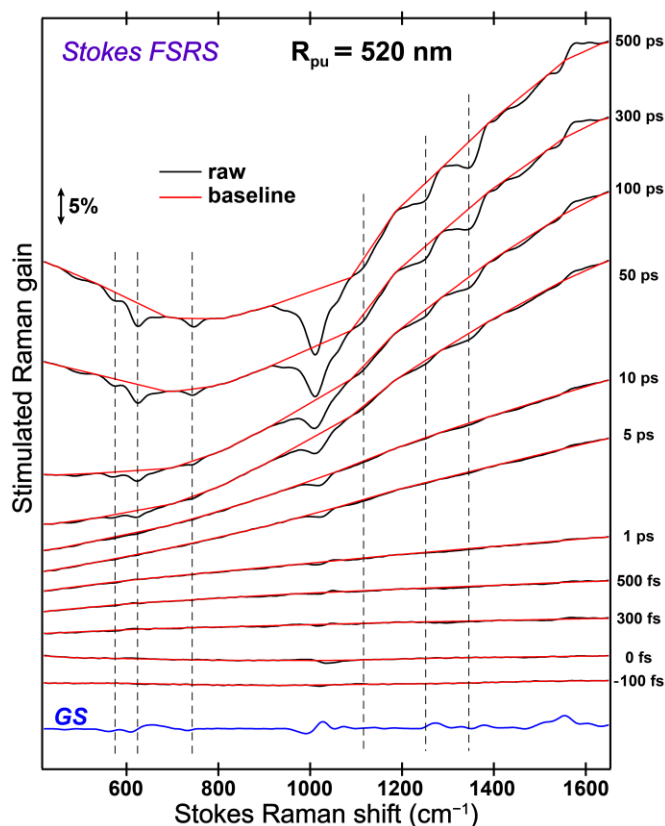
Figure 3.15. Representative raw excited-state Stokes FSRS spectra of GFP chromophore-derived superphotoacid p-HO-3,5-diF-BDI:BF_2 in methanol upon 400

nm actinic excitation with 520 nm R_{pu}. The spline baselines (red) are shown between –100 fs and 500 ps. The ground-state (GS) spectrum is shown at the bottom for comparison.

In spite of these experimental advances in promoting the resonance with SE, theoretical explanations or even systematic experiments to explore the line shape are still lacking. These efforts are highly in demand due to the demonstrated excellence in resonance enhancement without the generation of dispersive line shapes. Considering that the SE transition is common for varieties of molecular systems particularly for fluorescent materials, a comprehensive understanding of line shapes and intensity enhancement under this readily achievable resonance condition will greatly advance the FSRS methodology in versatility and broad applications, providing more reliable dynamics information for the systems under investigation.

3.5 References

[1]   Kukura, P.; McCamant, D. W.; Mathies, R. A. Femtosecond Stimulated Raman Spectroscopy. *Annu. Rev. Phys. Chem.* **2007**, *58*, 461-488.

[2]   Shen, Y. R. *The principles of nonlinear optics*; J. Wiley: New York, 1984.

[3]   Buhrke, D.; Hildebrandt, P. Probing Structure and Reaction Dynamics of Proteins Using Time-Resolved Resonance Raman Spectroscopy. *Chem. Rev.* **2020**, *120*, 3577-3630.

[4]   Dhar, L.; Rogers, J. A.; Nelson, K. A. Time-resolved vibrational spectroscopy in the impulsive limit. *Chem. Rev.* **1994**, *94*, 157-193.

[5]   Fang, C.; Tang, L.; Oscar, B. G.; Chen, C. Capturing Structural Snapshots during Photochemical Reactions with Ultrafast Raman Spectroscopy: From Materials Transformation to Biosensor Responses. *J. Phys. Chem. Lett.* **2018**, *9*, 3253-3263.

[6]   Weigel, A.; Dobryakov, A.; Klaumünzer, B.; Sajadi, M.; Saalfrank, P.; Ernsting, N. P. Femtosecond Stimulated Raman Spectroscopy of Flavin after Optical Excitation. *J. Phys. Chem. B* **2011**, *115*, 3656.

[7]   Fang, C.; Tang, L.; Chen, C. Unveiling coupled electronic and vibrational motions of chromophores in condensed phases. *J. Chem. Phys.* **2019**, *151*, 200901.

[8]   Quick, M.; Dobryakov, A. L.; Kovalenko, S. A.; Ernsting, N. P. Resonance Femtosecond-Stimulated Raman Spectroscopy without Actinic Excitation Showing Low-Frequency Vibrational Activity in the S_2 State of All-Trans β-Carotene. *J. Phys. Chem. Lett.* **2015**, *6*, 1216-1220.

[9]   Oscar, B. G.; Chen, C.; Liu, W.; Zhu, L.; Fang, C. Dynamic Raman Line Shapes on an Evolving Excited-State Landscape: Insights from Tunable Femtosecond Stimulated Raman Spectroscopy. *J. Phys. Chem. A* **2017**, *121*, 5428-5441.

[10]   McCamant, D. W.; Kukura, P.; Mathies, R. A. Femtosecond Stimulated Raman Study of Excited-State Evolution in Bacteriorhodopsin. *J. Phys. Chem. B* **2005**, *109*, 10449.

[11]   Chen, C.; Liu, W.; Baranov, M. S.; Baleeva, N. S.; Yampolsky, I. V.; Zhu, L.; Wang, Y.; Shamir, A.; Solntsev, K. M.; Fang, C. Unveiling Structural Motions of a Highly Fluorescent Superphotoacid by Locking and Fluorinating the GFP Chromophore in Solution. *J. Phys. Chem. Lett.* **2017**, *8*, 5921-5928.

[12]   Tang, L.; Zhu, L.; Taylor, M. A.; Wang, Y.; Remington, S. J.; Fang, C. Excited State Structural Evolution of a GFP Single-Site Mutant Tracked by Tunable Femtosecond-Stimulated Raman Spectroscopy. *Molecules* **2018**, *23*, 2226.

[13] Chen, C.; Zhu, L.-d.; Fang, C. Femtosecond stimulated Raman line shapes: Dependence on resonance conditions of pump and probe pulses. *Chin. J. Chem. Phys.* **2018**, *31*, 492-502.

[14] Sun, Z.; Qiu, X. Q.; Lu, J.; Zhang, D. H.; Lee, S.-Y. Three-state model for femtosecond broadband stimulated Raman scattering. *J. Raman Spectrosc.* **2008**, *39*, 1568-1577.

[15] Umapathy, S.; Mallick, B.; Lakshmanna, A. Mode-Dependent Dispersion in Raman Line Shapes: Observation and Implications from Ultrafast Raman Loss Spectroscopy. *J. Chem. Phys.* **2010**, *133*, 024505.

[16] McHale, J. L. *Molecular Spectroscopy*; CRC Press, 2017.

[17] Frontiera, R. R.; Shim, S.; Mathies, R. A. Origin of Negative and Dispersive Features in Anti-Stokes and Resonance Femtosecond Stimulated Raman Spectroscopy. *J. Chem. Phys.* **2008**, *129*, 064507.

[18] Qiu, X.; Li, X.; Niu, K.; Lee, S. Y. Inverse Raman Bands in Ultrafast Raman Loss Spectroscopy. *J. Chem. Phys.* **2011**, *135*, 164502.

[19] Lee, S.-Y.; Zhang, D.; McCamant, D. W.; Kukura, P.; Mathies, R. A. Theory of femtosecond stimulated Raman spectroscopy. *J. Chem. Phys.* **2004**, *121*, 3632-3642.

[20] Sun, Z.; Lu, J.; Zhang, D. H.; Lee, S. Y. Quantum Theory of (Femtosecond) Time-Resolved Stimulated Raman Scattering. *J. Chem. Phys.* **2008**, *128*, 144114.

[21] Niu, K.; Cong, S.; Lee, S. Y. Femtosecond Stimulated Raman Scattering for Polyatomics with Harmonic Potentials: Application to Rhodamine 6G. *J. Chem. Phys.* **2009**, *131*, 054311.

[22] Niu, K.; Zhao, B.; Sun, Z.; Lee, S. Y. Analysis of Femtosecond Stimulated Raman Spectroscopy of Excited-State Evolution in Bacteriorhodopsin. *J. Chem. Phys.* **2010**, *132*, 084510.

[23] Zhao, B.; Niu, K.; Li, X.; Lee, S.-Y. Simple aspects of femtosecond stimulated Raman spectroscopy. *Sci. China Chem.* **2011**, *54*, 1989-2008.

[24] Harbola, U.; Umapathy, S.; Mukamel, S. Loss and gain signals in broadband stimulated-Raman spectra: Theoretical analysis. *Phys. Rev. A* **2013**, *88*, 011801.

[25] Yoon, S.; McCamant, D. W.; Kukura, P.; Mathies, R. A.; Zhang, D.; Lee, S.-Y. Dependence of line shapes in femtosecond broadband stimulated Raman spectroscopy on pump-probe time delay. *J. Chem. Phys.* **2005**, *122*, 024505.

[26] Roy, K.; Kayal, S.; Ariese, F.; Beeby, A.; Umapathy, S. Mode Specific Excited State Dynamics Study of Bis(phenylethynyl)benzene from Ultrafast Raman Loss Spectroscopy. *J. Chem. Phys.* **2017**, *146*, 064303.

[27] Mallick, B.; Lakhsmanna, A.; Umapathy, S. Ultrafast Raman loss spectroscopy (URLS): instrumentation and principle. *J. Raman Spectrosc.* **2011**, *42*, 1883-1890.

[28] Zhu, L.; Liu, W.; Wang, Y.; Fang, C. Sum-Frequency-Generation-Based Laser Sidebands for Tunable Femtosecond Raman Spectroscopy in the Ultraviolet. *Appl. Sci.* **2015**, *5*, 48-61.

[29] Liu, W.; Tang, L.; Oscar, B. G.; Wang, Y.; Chen, C.; Fang, C. Tracking Ultrafast Vibrational Cooling During Excited State Proton Transfer Reaction with Anti-Stokes and Stokes Femtosecond Stimulated Raman Spectroscopy. *J. Phys. Chem. Lett.* **2017**, *8*, 997-1003.

[30] Liu, W.; Wang, Y.; Tang, L.; Oscar, B. G.; Zhu, L.; Fang, C. Panoramic Portrait of Primary Molecular Events Preceding Excited State Proton Transfer in Water. *Chem. Sci.* **2016**, *7*, 5484-5494.

[31] Tang, L.; Wang, Y.; Zhu, L.; Lee, C.; Fang, C. Correlated Molecular Structural Motions for Photoprotection after Deep-UV Irradiation. *J. Phys. Chem. Lett.* **2018**, *9*, 2311-2319.

[32] Shim, S.; Stuart, C. M.; Mathies, R. A. Resonance Raman Cross-Sections and Vibronic Analysis of Rhodamine 6G from Broadband Stimulated Raman Spectroscopy. *ChemPhysChem* **2008**, *9*, 697-699.

[33] Cen, Q.; He, Y.; Xu, M.; Wang, J.; Wang, Z. Wavelength dependent resonance Raman band intensity of broadband stimulated Raman spectroscopy of malachite green in ethanol. *J. Chem. Phys.* **2015**, *142*, 114201.

[34] Dorfman, K. E.; Fingerhut, B. P.; Mukamel, S. Time-resolved broadband Raman spectroscopies: A unified six-wave-mixing representation. *J. Chem. Phys.* **2013**, *139*, 124113.

[35] Zhu, L.; Liu, W.; Fang, C. A Versatile Femtosecond Stimulated Raman Spectroscopy Setup with Tunable Pulses in the Visible to Near Infrared. *Appl. Phys. Lett.* **2014**, *105*, 041106.

[36] Fang, C.; Frontiera, R. R.; Tran, R.; Mathies, R. A. Mapping GFP Structure Evolution During Proton Transfer with Femtosecond Raman Spectroscopy. *Nature* **2009**, *462*, 200-204.

[37] Frontiera, R. R.; Fang, C.; Dasgupta, J.; Mathies, R. A. Probing Structural Evolution along Multidimensional Reaction Coordinates with Femtosecond Stimulated Raman Spectroscopy. *Phys. Chem. Chem. Phys.* **2012**, *14*, 405-414.

[38] Watanabe, H.; Hayazawa, N.; Inouye, Y.; Kawata, S. DFT Vibrational Calculations of Rhodamine 6G Adsorbed on Silver: Analysis of Tip-Enhanced Raman Spectroscopy. *J. Phys. Chem. B* **2005**, *109*, 5012-5020.

[39] Pontecorvo, E.; Kapetanaki, S. M.; Badioli, M.; Brida, D.; Marangoni, M.; Cerullo, G.; Scopigno, T. Femtosecond stimulated Raman spectrometer in the 320–520 nm range. *Opt. Express* **2011**, *19*, 1107-1112.

[40] Han, F.; Liu, W.; Zhu, L.; Wang, Y.; Fang, C. Initial Hydrogen-Bonding Dynamics of Photoexcited Coumarin in Solution with Femtosecond Stimulated Raman Spectroscopy. *J. Mater. Chem. C* **2016**, *4*, 2954-2963.

[41] Agmon, N.; Huppert, D.; Masad, A.; Pines, E. Excited-State Proton-Transfer to Methanol Water Mixtures. *J. Phys. Chem.* **1991**, *95*, 10407-10413.

[42] Leiderman, P.; Genosar, L.; Huppert, D. Excited-State Proton Transfer: Indication of Three Steps in the Dissociation and Recombination Process. *J. Phys. Chem. A* **2005**, *109*, 5965-5977.

[43] Han, F.; Liu, W.; Fang, C. Excited-State Proton Transfer of Photoexcited Pyranine in Water Observed by Femtosecond Stimulated Raman Spectroscopy. *Chem. Phys.* **2013**, *422*, 204-219.

[44] Spry, D. B.; Goun, A.; Fayer, M. D. Deprotonation Dynamics and Stokes Shift of Pyranine (HPTS). *J. Phys. Chem. A* **2007**, *111*, 230-237.

[45] Simkovitch, R.; Shomer, S.; Gepshtein, R.; Huppert, D. How Fast Can a Proton-Transfer Reaction Be beyond the Solvent-Control Limit? *J. Phys. Chem. B* **2015**, *119*, 2253-2262.

[46] Oscar, B. G.; Liu, W.; Rozanov, N. D.; Fang, C. Ultrafast Intermolecular Proton Transfer to a Proton Scavenger in an Organic Solvent. *Phys. Chem. Chem. Phys.* **2016**, *18*, 26151-26160.

[47] Hoffman, D. P.; Mathies, R. A. Femtosecond Stimulated Raman Exposes the Role of Vibrational Coherence in Condensed-Phase Photoreactivity. *Acc. Chem. Res.* **2016**, *49*, 616-625.

[48] Nakamura, R.; Hamada, N.; Abe, K.; Yoshizawa, M. Ultrafast Hydrogen-Bonding Dynamics in the Electronic Excited State of Photoactive Yellow Protein Revealed by Femtosecond Stimulated Raman Spectroscopy. *J. Phys. Chem. B* **2012**, *116*, 14768-14775.

[49] Zheltikov, A. Editorial: Supercontinuum Generation. *Appl. Phys. B: Lasers Opt.* **2003**, *77*, 143.

[50] Wang, W.; Liu, W.; Chang, I. Y.; Wills, L. A.; Zakharov, L. N.; Boettcher, S. W.; Cheong, P. H. Y.; Fang, C.; Keszler, D. A. Electrolytic Synthesis of Aqueous Aluminum Nanoclusters and in situ Characterization by Femtosecond Raman Spectroscopy & Computations. *Proc. Natl. Acad. Sci. U. S. A.* **2013**, *110*, 18397-18401.

[51] Wang, Y.; Liu, W.; Tang, L.; Oscar, B. G.; Han, F.; Fang, C. Early Time Excited-State Structural Evolution of Pyranine in Methanol Revealed by Femtosecond Stimulated Raman Spectroscopy. *J. Phys. Chem. A* **2013**, *117*, 6024-6042.

[52] Liu, W.; Han, F.; Smith, C.; Fang, C. Ultrafast Conformational Dynamics of Pyranine during Excited State Proton Transfer in Aqueous Solution Revealed by Femtosecond Stimulated Raman Spectroscopy. *J. Phys. Chem. B* **2012**, *116*, 10535-10550.

[53] Myers, A. B.; Mathies, R. A.; Spiro, T. G. *Biological Applications of Raman Spectroscopy*, 1987; Vol. 2.

[54] Batignani, G.; Pontecorvo, E.; Giovannetti, G.; Ferrante, C.; Fumero, G.; Scopigno, T. Electronic Resonances in Broadband Stimulated Raman Spectroscopy. *Sci. Rep.* **2016**, *6*, 18445.

[55] Cina, J. A.; Kovac, P. A. How Fissors Works: Observing Vibrationally Adiabatic Conformational Change through Femtosecond Stimulated Raman Spectroscopy. *J. Phys. Chem. A* **2013**, *117*, 6084-6095.

[56] Lee, J.; Challa, J. R.; McCamant, D. W. Pump Power Dependence in Resonance Femtosecond Stimulated Raman Spectroscopy. *J. Raman Spectrosc.* **2013**, *44*, 1263-1272.

[57] Tachibana, S. R.; Tang, L.; Zhu, L.; Liu, W.; Wang, Y.; Fang, C. Watching an Engineered Calcium Biosensor Glow: Altered Reaction Pathways before Emission. *J. Phys. Chem. B* **2018**, *122*, 11986-11995.

[58] Chen, C.; Zhu, L.; Baranov, M. S.; Tang, L.; Baleeva, N. S.; Smirnov, A. Y.; Yampolsky, I. V.; Solntsev, K. M.; Fang, C. Photoinduced Proton Transfer of GFP-Inspired Fluorescent Superphotoacids: Principles and Design. *J. Phys. Chem. B* **2019**, *123*, 3804-3821.

[59] Taylor, M. A.; Zhu, L.; Rozanov, N. D.; Stout, K. T.; Chen, C.; Fang, C. Delayed vibrational modulation of the solvated GFP chromophore into a conical intersection. *Phys. Chem. Chem. Phys.* **2019**, *21*, 9728-9739.

Chapter 4 ESPT Dynamics in Alcohols of a Highly Fluorescent Superphotoacid by Locking and Fluorinating the GFP Chromophore[c]

4.1 Introduction

Green fluorescent protein (GFP) has revolutionized molecular and cellular biology for decades. The heart of this biomolecular machine is a three-residue chromophore that responds to UV light as a photoacid. When outside of the protein matrix, the GFP chromophore loses excited-state proton transfer (ESPT) capability and becomes dark, attributed to ultrafast ring twisting motions.[1] What remains unclear is the interplay between its structure and function in various environments. Such an understanding will power ways to engineer the chromophore in solution to acquire functionality originally only inside of the protein or develop new capabilities.

The photoacidity phenomenon has been known for more than 80 years.[2] Such light-controlled molecules have enabled advances in driving photoreactions,[3-7] inducing pH changes,[8,9] performing photolithography,[10] catalyzing reactions, and modifying materials.[11] Superphotoacids are molecules with a negative excited-state pK_a (pK_a*)

---

and the ability to undergo ESPT in nonaqueous solvents. Huppert et al. studied quinone−cyanine photoacids,[12] and QCy9 is the strongest photoacid with the same ESPT rate in water, methanol, and ethanol, going beyond the solvent control limit.[13] The ESPT rate of a strong photoacid $NM6HQ^+$ is controlled by solvent motions that minimize the intermolecular dipole interaction.[14] Notably, the photoacidity in homologues can be enhanced by the strategic placement of electron-withdrawing groups (EWGs) at positions of increased electron density in aromatic systems.[1,15-17]

Here, we report the chemical synthesis and excited-state structural motions of a novel superphotoacid as a functional analogue to the GFP chromophore. Over the years, many chromophores have been synthesized to investigate chemical properties and fluorogenic behaviors in the repertoire of GFP and RNA.[18-20] In particular, (Z)-4-(4-hydroxybenzylidene)-1,2-dimethyl-1H-imidazol-5(4H)-one (p-HBDI, Figure 4.1) represents the core of wild-type (wt)GFP, but its emission behavior in solution differs drastically from that in protein. Due to an efficient photoisomerization-induced deactivation, no ESPT is observed for p-HBDI in solution, and the fluorescence quantum yield (QY) drops by 4 orders of magnitude with respect to wt-GFP[1,21]
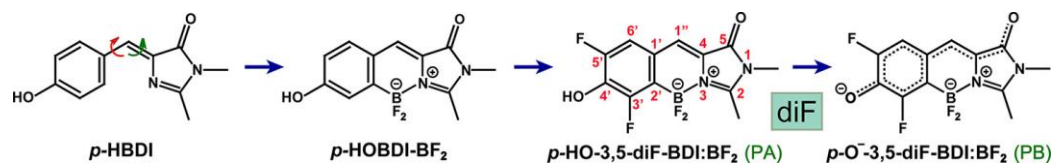
Figure 4.1. Structures of the GFP-Derived HBDI Chromophore Analogues and Engineered Superphotoacids. Reproduced with permission from Cheng Chen et al., *J. Phys. Chem. Lett.* **2017**, 8, 5921-5928. Copyright 2017 American Chemical Society.

Recently, Solntsev et al. reported the synthesis and study of a GFP-chromophore analogue (Z)-4-(2-(difluoroboryl)-4-hydroxybenzylidene)-1,2-dimethyl-1H-imidazol-5(4H)-one (p-HOBDI-BF$_2$), and the phenolic and imidazolinone rings are irreversibly locked by a BF$_2$ group. This fully planar structure suppresses photoisomerization, enables intermolecular ESPT, and greatly improves the fluorescence QY (e.g., 0.73 in acetonitrile with a lifetime of 3.2 ns).[22] The measured pK_a* ≈ 0.6 implies its moderate photoacidity, which cannot support ESPT in methanol or other alcohols. In this work, our newly synthesized superphotoacid, p-HO-3,5-diF-BDI:BF$_2$ (abbreviated as diF) incorporates two fluorine atoms as EWGs to the rigid skeleton of p-HOBDI-BF$_2$ and simultaneously achieves high QY and fast ESPT outside of a restraining protein matrix.

We exploited FSRS to study diF in solution. FSRS is a powerful tool to resolve atomic motions of chemical and biological systems with simultaneously high temporal (< 30 fs) and spectral (< 10 cm^{-1}) resolutions.[5,6,23-26] Because the stimulated emission (SE) bands of diF dominate fs transient absorption upon 400-nm excitation of the protonated form,[26,27] we strategically selected a Raman pump between two SE band maxima due to the protonated (PA*) and deprotonated (PB*) chromophore, respectively (the asterisk means the electronic excited state). We employed a bluer probe on the anti-Stokes side to acquire PA* Raman modes. Because the PB* SE band shifts to the red side, we used a redder probe on the Stokes side to highlight the PB* Raman modes. This unique complementary approach of fs-TA-aided FSRS enabled us to track the excited-state conformational events for the newly synthesized diF molecule and gain crucial structural insights into the bioinspired engineering of superphotoacidity.

4.2 Experimental

4.2.1 Synthesis

Non-borylated fluorinated GFP chromophores were recently used in aptamer labeling.[28,29] The model compounds **3** (HOBDIBF$_2$, monoF-HOBDI-BF$_2$, and diF HOBDI-BF$_2$ or abbreviated as diF; Figure 4.2) were synthesized using typical procedures from the non-borylated imidazolones by heating with boron tribromide in the presence of molecular sieves.[22,30,31] All the organic solvents used were HPLC grade.
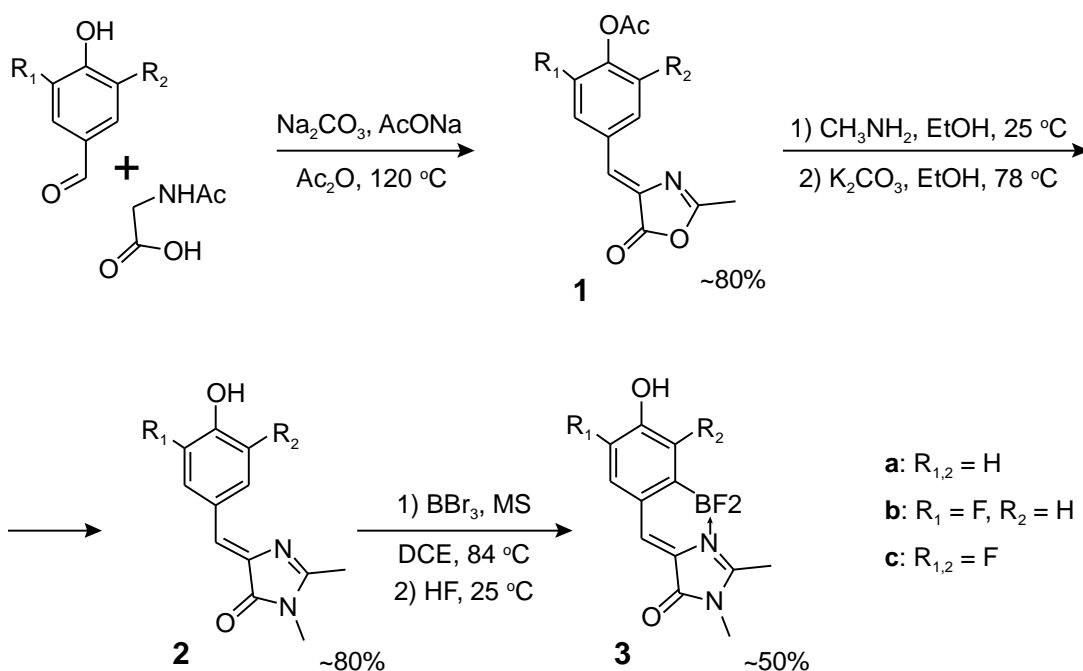
Figure 4.2. Synthesis of compounds 1-3 with various functional group substitutions. Reproduced with permission from Cheng Chen et al., *J. Phys. Chem. Lett.* **2017**, 8, 5921-5928. Copyright 2017 American Chemical Society.

Commercially available reagents were used without additional purification. For column chromatography, E. Merck Kieselgel (silica gel) 60 was used. NMR spectra were recorded on a 700 MHz Bruker Avance III spectrometer at room temperature (293 K). Chemical shifts were reported relative to residual peaks of $CDCl_3$ (7.27 ppm for ^1H and 77.0 ppm for ^{13}C) or DMSO-d_6 (2.51 ppm for 1H and 39.5 ppm for ^{13}C). Melting points were measured on an SMP 30 apparatus. High-resolution mass spectra (HRMS) spectra were recorded on an Agilent 6224 TOF LC/MS System (Agilent Technologies, Santa Clara, CA, USA) equipped with a dual-nebulizer electrospray ionization (ESI) source. Data acquisition and analysis were performed by the MassHunter Workstation software (Agilent Technologies, Santa Clara, CA, USA).

(Z)-2-methyl-(4-acetoxybenzylidene)oxazol-5(4H)-ones (1). Corresponding 4 hydroxybenzaldehyde (0.1 mol), *N*-acetyl glycine (14 g, 0.12 mol), sodium carbonate (10.6 g, 0.1 mol) and sodium acetate (16.6 g, 0.2 mol) were mixed in acetic anhydride (60 mL) at room temperature and gently heated to complete dissolution of inorganic salts. The mixture was heated at 150°C for 2 h and dried on a rotary evaporator. The mixture was then purified by flash chromatography (hexane/EtOAc 1:1). The crude product was used in the next stage without further purification.

(Z)-4-(4-acetoxybenzylidene)-2-methyloxazol-5(4H)-one (1a): greenish-yellow solid (23.5 g, ~80%).[32]

(*Z*)-4-(3-fluoro-4-acetoxybenzylidene)-2-methyloxazol-5(4*H*)-one (1b): greenish yellow solid (22.4 g, ~85%); 1H NMR (CDCl$_3$) δ 7.51 (m, 2H), 7.43 (d, J=11.0 Hz, 1H), 6.90 (t, J=7.3 Hz, 1H), 6.55 (m, 1H), 2.42 (s, 3H), 2.24 (s, 3H).

(*Z*)-4-(3,5-difluoro-4-acetoxybenzylidene)-2-methyloxazol-5(4*H*)-one (1c): greenish yellow solid (18.3 g, ~65%); ^{1}H NMR (DMSO-d$_6$) δ 8.09 (d, J=8.9 Hz, 2H), 7.23 (s, 1H), 2.43 (s, 3H), 2.42 (s, 3H).[18]

(*Z*)-4-(4-hydroxybenzylidene)-1,2-dimethyl-1H-imidazol-5(4*H*)-ones (2). The product of previous stage (**1**) (0.05 mol) was suspended in ethanol (100 mL) and mixed with aqueous methylamine (40%, 11.6 g, 0.15 mol). The mixture was stirred at room temperature for 2 h, potassium carbonate (13.8 g, 0.1 mol) was added and the mixture was refluxed for 8 h. The mixture was dried on a rotary evaporator and dissolved in water (100 mL). The solution was acidified with aqueous hydrochloric acid (10%) to pH=6. The precipitate was filtered, washed by cold (–20°C) ethanol and diethyl ether and dried in vacuo.

(*Z*)-4-(4-hydroxybenzylidene)-1,2-dimethyl-1H-imidazol-5(4*H*)-one (2a): yellow solid (9.5 g, 88%); ^{1}H NMR (DMSO-d$_6$) δ 10.08 (s, 1H), 8.08 (d, J=8.6 Hz, 2H), 6.88 (s, 1H), 6.83 (d, J=8.6 Hz, 2H), 3.08 (s, 3H), 2.33 (s, 3H).[33]

(*Z*)-4-(3-fluoro-4-hydroxybenzylidene)-1,2-dimethyl-1*H*-imidazol-5(4*H*)-one (2b):

yellow solid (9.1 g, 78%); m. p. 232–234°C; ^{1}H NMR (DMSO-d$_6$) δ 10.52 (s, 1H), 8.19 (m, 1H), 7.76 (m, 1H), 6.99 (t, J=8.8 Hz, 1H), 6.89 (s, 1H), 3.09 (s, 3H), 2.34 (s, 3H); ^{13}C NMR (DMSOd6) δ 15.2 (CH$_3$), 26.1 (CH$_3$), 117.7 (d, J=2.3 Hz), 118.8 (d, J=19.4 Hz), 123.9 (d, J=2.4 Hz), 125.9 (d, J=7.36 Hz), 129.5, 137.3, 150.6 (d, J=240 Hz), 152.5 (d, J=8.8 Hz), 163.2, 169.6; HRMS (ESI) calculated for C$_{12}$H$_{12}$FN$_2$O$_2$ ([M+H]+) 235.0883, found 235.0894.[18]

(Z)-4-(3,5-difluoro-4-hydroxybenzylidene)-1,2-dimethyl-1H-imidazol-5(4H)-one (2c): yellow solid (10.5 g, 83%); m. p. 283–287°C; ^{1}H NMR (DMSO-d$_6$) δ 10.88 (s, 1H), 7.97 (m, 2H), 6.89 (s, 1H), 3.09 (s, 3H), 2.36 (s, 3H); ^{13}C NMR (DMSO-d$_6$) δ 15.3 (CH$_3$), 26.2 (CH$_3$), 115.1 (dd, J$_1$=17 Hz, J$_2$=5.4 Hz), 122.7, 124.7 (t, J=9.2 Hz), 135.6 (t, J=16.5 Hz), 138.4, 151.8 (dd, J$_1$=242 Hz, J$_2$=7.4 Hz), 164.3, 169.5; HRMS (ESI) calculated for C$_{12}$H$_{11}$F$_2$N$_2$O$_2$ ([M+H]$^+$) 253.0789, found 253.0794.[18]

(Z)-4-(2-(difluoroboryl)-4-hydroxybenzylidene)-1,2-dimethyl-1H-imidazol 5(4H)-ones (3). The product of previous stage (**2**) (5.0 mmol) was dissolved in dry CH$_2$Cl$_2$ (50 mL), molecular sieves 4 Å (4 g) and 3 Å (4 g) were added, followed by a solution of boron tribromide in CH$_2$Cl$_2$ (1 M, 20 mL, 20.0 mmol) and the reaction mixture was refluxed for 6 h in inert atmosphere. The mixture was cooled and filtered; molecular sieves were washed twice with ethanol (20 mL) and CH$_2$Cl$_2$ (100 mL). The solution was mixed with aqueous HF (20%, 5 mL) and stirred for 30 minutes. The mixture was dissolved in EtOAc (100 mL), washed with water (2×50 mL) and brine (2×50 mL) and

dried over Na_2SO_4. The solvent was evaporated and the product was purified by column chromatography (CHCl$_3$/EtOH 10:1).

(*Z*)-4-(2-(difluoroboryl)-4-hydroxybenzylidene)-1,2-dimethyl-1*H*-imidazol 5(4*H*)-one (3a): yellow solid (615 mg, 47%); m. p. ~250°C with decomposition; ^{1}H NMR (DMSO-d$_6$) 10.2 (s, 1H, OH), 7.56 (s, 1H), 7.48 (d, J=8.3 Hz, 1H), 7.00 (d, J=2.2 Hz, 1H), 6.74 (dd, J1=8.3 Hz, J2=2.5 Hz, 1H), 3.22 (s, 3H), 2.71 (s, 3H).[22]

(*Z*)-4-(2-(difluoroboryl)-5-fluoro-4-hydroxybenzylidene)-1,2-dimethyl-1*H*-imidazol-5(4*H*)-one (3b): yellow solid (620 mg, 44%); m. p. ~275°C with decomposition; ^{1}H NMR (DMSO-d$_6$) δ 10.64 (s, 1H), 7.55 (s, 1H), 7.47 (d, J=12.1 Hz, 1H), 7.15 (d, J=9.4 Hz, 1H), 3.22 (s, 3H), 2.72 (s, 3H); ^{13}C NMR (DMSO-d$_6$) δ 12.9 (CH$_3$), 26.5 (CH$_3$), 118.6 (d, J=17.1 Hz), 120.4, 124.9, 125.2, 127.8, 148.8 (m), 150.3 (d, J=241.9 Hz), 162.7, 165.9; HRMS (ESI) calculated for $C_{12}H_{11}BF_3N_2O_2$ ([M+H]$^+$) 283.0866, found 283.0854.

(*Z*)-4-(2-(difluoroboryl)-3,5-difluoro-4-hydroxybenzylidene)-1,2-dimethyl-1*H*-imidazol-5(4*H*)-one (3c): yellow solid (780 mg, 52%); m. p. ~300°C with decomposition; ^{1}H NMR (DMSO-d$_6$) δ 10.91 (s, 1H), 7.55 (s, 1H), 7.39 (d, J=10.5 Hz, 1H), 3.22 (s, 3H), 2.73 (s, 3H); ^{13}C NMR (DMSO-d$_6$) δ 13.0 (CH$_3$), 26.5 (CH$_3$), 115.2 (d, J=17.7 Hz), 123.9 (m), 125.9, 126.8, 137.4 (dd, J_1=19.4 Hz, J_2=15.1 Hz), 151.3 (dd, J_1=241 Hz, J_2=6.7 Hz), 154.6 (dd, J_1=240 Hz, J_2=5.4 Hz), 162.6, 166.7; HRMS (ESI) calculated for $C_{12}H_{10}BF_4N_2O_2$ ([M+H]$^+$) 301.0771, found 301.0773.

4.2.2 Spectroscopic measurement and DFT calculations

The detailed description of our fs-TA and FSRS setups can be found in Chapter 2 and elsewhere.[25] In brief, for both fs-TA and FSRS, the 400 nm, ~0.5 mW excitation pump is generated by the second harmonic generation of the ~4 mJ, 800 nm fundamental pulse (FDP) with a 35 fs pulse duration and 1 kHz repetition rate based on a mode-locked Ti:sapphire oscillator (Mantis-5) and a regenerative amplifier (Coherent, Inc.). The probe pulses for both fs-TA and FSRS are produced by the supercontinuum white light (SCWL) that is generated by focusing a portion of FDP onto 3-mm-thick sapphire plate. The Raman pump pulse for FSRS is generated through a two-stage ps non-collinear optical parametric amplifier (NOPA) with the ps seed produced by a preceding fs-NOPA and spectral filter and 400-nm ps pump produced by the second harmonic bandwidth compressor (SHBC). The details of these optical compartments can be found in Chapter 2 and pertinent literatures. In this work, the Raman pump wavelength was tuned to 510 nm with ~3 mW beam power, which is between the SE bands of the protonated and deprotonated diF. The spectra were collected on both Stokes and anti-Stokes sides and cyclohexane was used to calibrate the FSRS spectra.

The ground- and excited-state vibrational frequencies were calculated with density functional theory (DFT) and time-dependent (TD) DFT RB3LYP level with 6-31G+(d, p) basis sets in Gaussian 09, respectively.[34] TD-DFT frequency calculations are preceded by excited-state geometric optimization calculations. The methanol solvent effect is described by the integral equation formalism variant polarizable continuum model (IEFPCM) method. The normal mode frequency scaling factor is 0.96.

4.3 Results and discussions

4.3.1 Steady-state absorption and emission

DiF in methanol shows an absorption peak at ~395 nm and a shoulder at 495 nm (Figure 4.3). The emission exhibits two peaks at 476 (weaker) and 539 nm. In contrast, diF in water has two absorption bands at ~402 and 480 nm, with a dominant 530 nm emission peak. These spectral changes confirm that diF exists in a mixture of protonated (PA) and deprotonated (PB) forms in solution, and the ground-state (S_0) equilibrium can be shifted by the H-bonding capability of the solvent. Notable Stokes shift provides strong evidence for ESPT. In methanol, PA dominates (395 nm absorption) while PB population is small. In S_1, the PA* species undergoes ESPT and converts to PB* (539 nm emission). In water, the major absorption band at 480 nm arises from PB. The 400-nm actinic pump matches the PA absorption peak and initiates the photochemical events of interest. Notably, a weaker photoacid such as HPTS in methanol is trapped in PA* and emits in the blue region.[35,36] In contrast, diF in methanol still forms PB* to some extent but the emission peak is redshifted from diF in water (Figures 4.3). This result shows that solvation of both PB* and PB species plays an important role in determining the S_1–S_0 energy gap and in this case, water likely solvates and stabilizes the PB state more than the PB* state (i.e., to a larger extent than that in methanol).

The fluorescence QY of diF is enhanced by several orders in magnitude when compared to the unlocked chromophore, e.g., *p*-HBDI, representing an effective chemical modification to control functionality. Notably, non-adiabatic ESPT typically correlates with weak coupling between the solute and surrounding solvent.[37,38] For *p*-

HBDI, the reactant and product are both in deep potential wells, so the chromophore does not exhibit ESPT in solution. In contrast, the fully planar *p*-HOBDI-BF*2* (Figure 4.1) is highly fluorescent and undergoes adiabatic ESPT with a pK_a* of ~0.6.[22] This moderate photoacidity similar to the photoacid pyranine[3,39-41] allows it to transfer proton to water, but not to other protic solvents like methanol or ethanol. The EWGs at ortho sites to the phenolic hydroxyl achieve the superphotoacidity (undergoing ESPT in various protic solvents) and maintain high fluorescence QY.
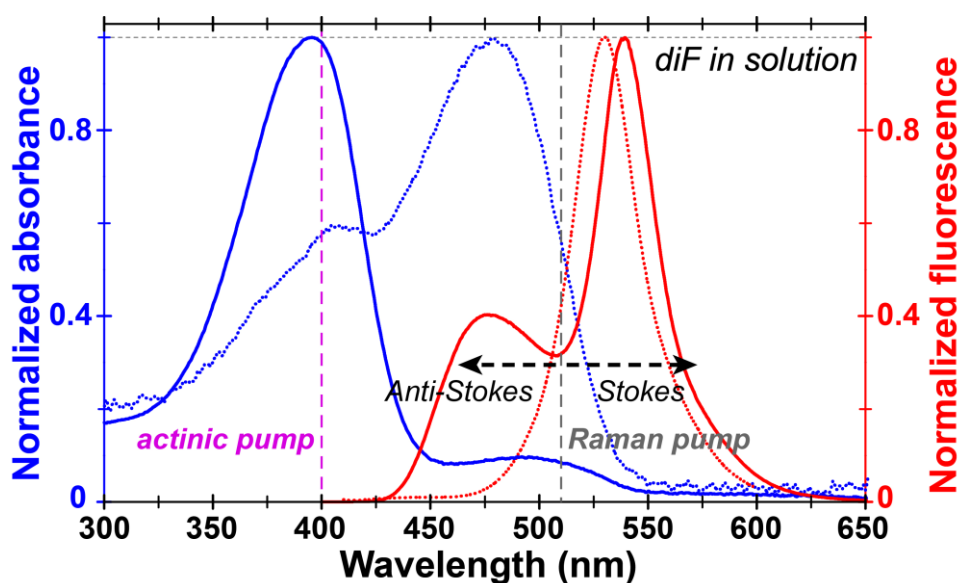
Figure 4.3. Normalized absorption (blue) and emission (red) spectra of diF in methanol (solid) and water with pH ≈ 4 (dotted). The actinic pump and Raman pump positions in FSRS experiments are noted by vertical magenta and gray dashed lines, respectively. The dashed arrows depict the Raman probe wavelength regions in the anti-Stokes and Stokes FSRS. Reproduced with permission from Cheng Chen et al., *J. Phys. Chem. Lett.* **2017**, 8, 5921-5928. Copyright 2017 American Chemical Society.

4.3.2 fs-TA dynamics and global/target analysis

As shown in Figure 4.4, the 400 nm excitation prepares the PA* population (see Figure 4.3 for the absorption spectrum). The fs-TA spectra of diF in methanol (Figure 4.4b) exhibit strong SE bands from ~450 to 600 nm and an excited-state absorption (ESA) band above 650 nm. At early times, the PA* SE band at ~460 nm dominates, and then it rapidly red shifts to 476 nm after ~450 fs, reaching the PA* fluorescence maximum (Figure 4.4a). The SE band continues to red-shift to ~500 nm due to solvation,[42-45] in correlation with the excited-state stabilization. Meanwhile, another SE band at ~540 nm emerges, attributed to PB* after ESPT After ~100 ps, the PA* SE band diminishes while the PB* SE band at ~544 nm rises and becomes dominant.
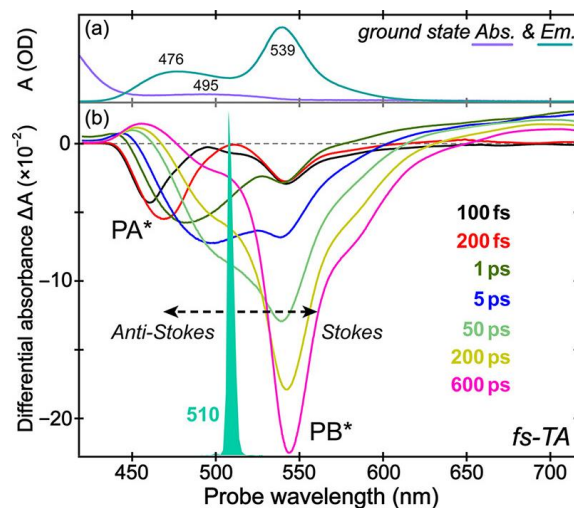
Figure 4.4. Steady-state (a) and fs-TA (b) spectra of diF in methanol. Representative data with time delays are displayed. The 510 nm Raman pump is flanked by dashed lines depicting the anti-Stokes and Stokes sides. Reproduced with permission from Cheng Chen et al., *J. Phys. Chem. Lett.* **2017**, 8, 5921-5928. Copyright 2017 American Chemical Society.

The fs-TA spectra of the solute exhibit the spectral shift and conversion of SE bands, indicative of a sequential evolution as ESPT proceeds. We performed global analysis[46] and uncovered four evolution-associated difference spectra (EADSs, Figure 4.4a) with lifetimes providing insights into the electronic dynamics and population change. The earliest EADS shows a 467 nm emission peak with ~570 fs decay (black trace, Figure 4.4a). The second EADS appears with a red-shifted SE peak at 485 nm due to an intermediate after relaxation from the Franck−Condon (FC) region in S_1, likely a charge-separated (CS) state adjacent to the locally excited (LE) PA* state (Figure 4.4b).[35,44,47] Meanwhile, a small PB* population appears (dotted arrow, Figure 4.4b). The PA* SE band red-shifts as the polar methanol molecules achieve an equilibrium in S_1 by rearranging to the newly formed dipole of photoexcited diF on the ~8 ps time scale, matching the average methanol solvation time.[3,43,48,49] Later, a dual band with comparable intensities (blue trace, Figure 4.4a) shows the solute deprotonation that starts to occur prior to completion of the solvent rearrangement (solid arrow, Figure 4.4b), indicating that a portion of PA* has converted to PB*. The ESPT reaction from diF to methanol does not go beyond the solvent control limit.[14,41] In the fourth EADS (green), the PA* SE band has diminished while the PB* SE band dominates.

Notably, PB* species emerges during FC relaxation (Figure 4.4a). A small emission band at 540 nm at early time could involve an ultrafast, unresolved ESPT phase (Figure 4.3b), but its prompt growth (black to red EADS) suggests that main deprotonation occurs following the initial charge separation, consistent with small-scale coherent proton motions.[26,50] This picture is strengthened by target analysis[51] which adopts a

branched scheme in converting PA* to PB* via ESPT reaction. In particular, the similarity between the retrieved four temporal components from the experimental fs-TA spectra via global analysis (Figure 4.4a) and target analysis (see below) arises from a reasonable kinetic model to elucidate the underlying physicochemical picture.
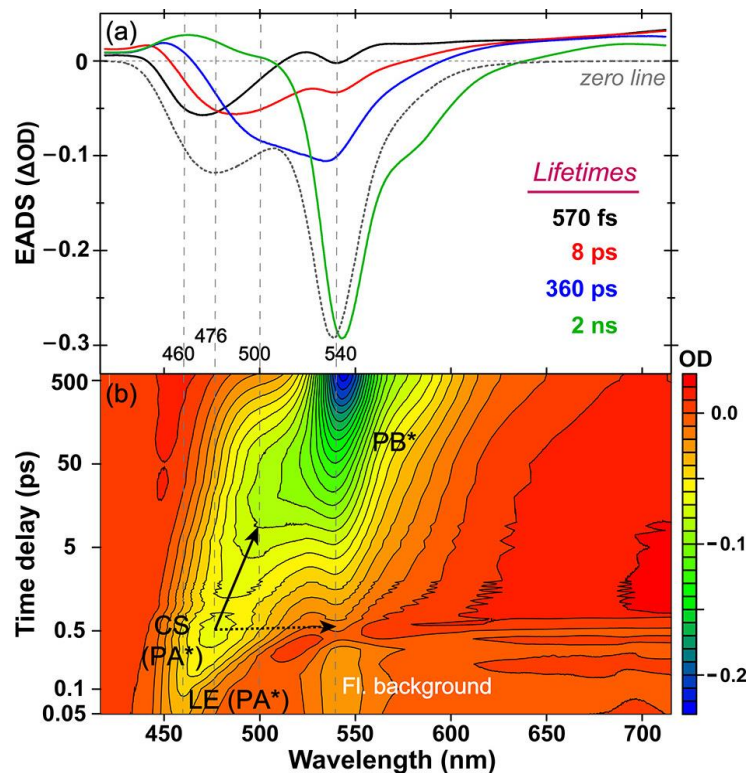
Figure 4.5. Global analysis and contour plot of the TA spectra for diF in methanol. (a) Global analysis reveals four evolutional spectra with lifetimes of 570 fs (black), 8 ps (red), 360 ps (blue), and 2 ns (green). (b) Contour plot of TA on a semilogarithmic scale with transient electronic states labeled. The solid and dotted arrows highlight the bifurcation of the CS state for the multistep ESPT reaction. The steady-state fluorescence spectrum (gray dotted curve) is inverted and scaled for comparison. Reproduced with permission from Cheng Chen et al., *J. Phys. Chem. Lett.* **2017**, 8, 5921-5928. Copyright 2017 American Chemical Society.

Our control experiments of diF in other solvents lend further support to the ESPT mechanism. The lifetimes of the second EADS become 10.4 ps in CD$_3$OD (see Figure 4.6 for an alternative fs-TA data analysis),[52] 17.8 ps in ethanol,[43,45,48] and 1.1 ps in H$_2$O.[3,40,44] These values match solvation times and confirm that solvent rearrangement plays a key role in stabilizing new charge distribution and facilitating ESPT. The lifetime of the third EADS (~360 ps) lengthens to ~850 ps in CD$_3$OD, with a kinetic isotope effect (KIE) of ~2.4, corroborating proton motions via diffusion that lead to significant deprotonation following solvation events. The PB* excited-state lifetime of ~2 ns (green EADS) corresponds to fluorescence while the SE band intensity decays.
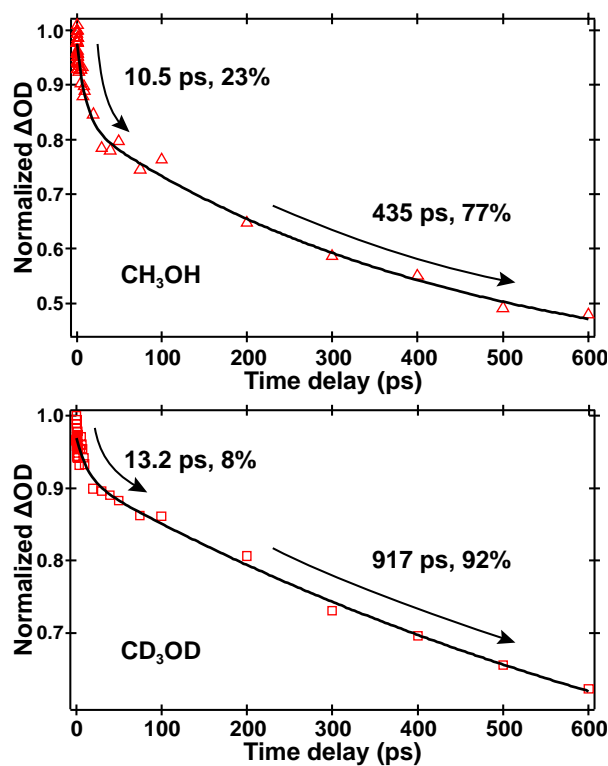
Figure 4.6. TA dynamics of the protonated diF in (a) CH$_3$OH and (b) CD$_3$OD at 700 nm after 400-nm photoexcitation. The first and second decay has a KIE of ~1.3 and ~2.1, respectively. Reproduced with permission from Cheng Chen et al., *J. Phys. Chem. Lett.* **2017**, 8, 5921-5928. Copyright 2017 American Chemical Society.

To gain more explicit insights into the ESPT dynamics, we performed target analysis to examine the assumed model and disentangle the compartments associated with each reaction species. Figure 4.7 presents the target analysis results termed by species-associated difference spectrum (SADS) based on a branched kinetic model. The transfer matrix K for the target analysis model[53] is given by:

$$K = \begin{pmatrix} 0 & 0 & 0 & 0 \\ 1 & 0 & 0 & 0 \\ 0 & 2 & 0 & 0 \\ 0 & 2 & 3 & 4 \end{pmatrix}$$

where compartments 1 to 4 represent the LE (PA*), CS, solvated CS, and PB* states, respectively. We constrained the initial population as 100% LE state as the transition to adjacent electronic states (such as CS) occurs on the sub-ps timescale which renders spontaneous emission from LE state negligible for modeling the ESPT reaction pathway. The non-zero off-diagonal elements represent the compartmental transitions. The non-zero diagonal elements represent the relaxation to electronic ground state. The matrix elements K_{32}, K_{42} indicate the branching with irreversible steps: solvation + ESPT pathway is $2 \rightarrow 3 \rightarrow 4$ whereas direct ESPT pathway is $2 \rightarrow 4$. The branching ratio shown in Figure 4.7 is 1:1 (i.e., 50% each) which well models the time-resolved fs-TA spectra particularly with respect to the area under each SADS curve related to population. Further information regarding the pertinent oscillator strength is needed to obtain the optimal branching ratio but the current unnormalized SADS in Figure 4.7 are reasonably describing the ESPT reaction kinetic scheme considering the similarity in band shape and intensity as well as the expected shift in peak position (due to solvation) between the CS and solvated CS states. Notably, the solvated CS spectrum exhibits the most contrast to the third temporal component (blue EADS in Figure 4.5a)

while the other three components are very similar to the global analysis results. This difference reveals that blue EADS is essentially a mixture of the solvated CS state (blue SADS) and PB* state (green SADS) due to simultaneous occurrence of CS solvation events and deprotonation events as part of the overall ESPT reaction.
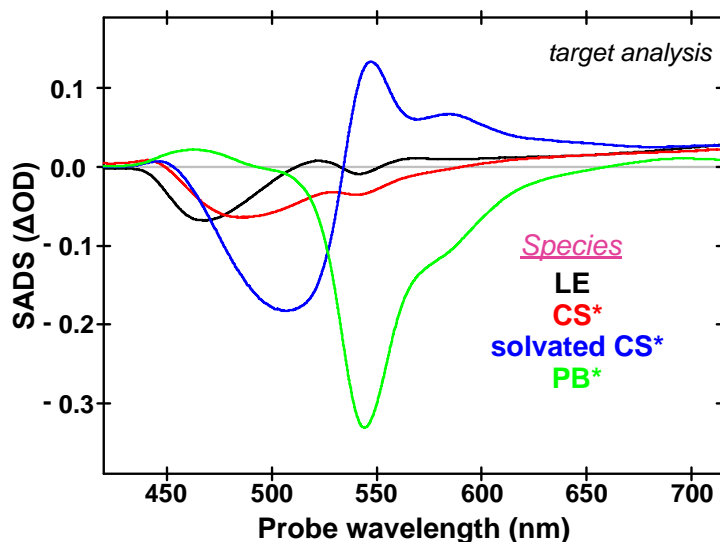
Figure 4.7. Species-associated difference spectra (SADS) of diF in methanol from target analysis of the TA spectra. Four electronic states (principal components linked by the assumed kinetic scheme) are obtained with their time constants by which the states evolve into one another sequentially: LE (locally excited state, PA*, ~560 fs, in black), CS (charge-separated state, PA*-like, ~8 ps due to solvation of the nascent contact-ion pair, in red), solvated CS (converting PA* to PB* via the diffusion events and further proton separation in solution, ~350 ps, in blue), and PB* (~2 ns due to fluorescent emission to PB, in green). No clear ground-state bleaching is observed. Reproduced with permission from Cheng Chen et al., *J. Phys. Chem. Lett.* **2017**, 8, 5921-5928. Copyright 2017 American Chemical Society.

4.3.3 Excited-state FSRS dynamics

In FSRS experiments, signals are greatly enhanced when Raman pulses are resonant with an electronic transition to generate vibrational coherences. On the basis of fs-TA, we tuned the Raman pump to 510 nm, the midpoint between PA* and PB* SE bands (Figure 4.4b). Resonance enhancement is simultaneously achieved for both PA* and PB* species while avoiding the right-on-resonance conditions that could lead to dispersive Raman line shapes.[54-56] Because a redder probe with the 510 nm Raman pump is closer to the PB* SE band, enhanced PB* signals appear in the Stokes FSRS (Figure 4.8a) with a delayed onset. Due to weak PA* emission and probe photons far from the PA* SE band, the signal-to-noise ratio of PA* modes remains low. To address this issue, we collected the anti-Stokes FSRS in S_1.[55,56] As bluer probe photons are energetically closer to the PA* SE band, the PA* signals get enhanced at early times (Figure 4.8c). This work thus represents a unique experimental scenario that a photochemical reaction can be tracked by the anti-Stokes FSRS for reactant species and by the Stokes FSRS for product species.

The ground-state Stokes spectrum shows four major peaks at 1277, 1331, 1556, and 1607 cm^{-1} as Raman gain (See Table 4.1 for mode assignment). This is due to an off-resonance Raman pump (510 nm) to the S_0 absorption peak (395 nm). In contrast, the excited-state FSRS with resonance enhancement shows clear signal rise with a negative sign in the high-frequency region and a positive sign in the low-frequency region, and the associated PB* modes at 552, 606, 1129, 1264, 1367, and 1555 cm^{-1} are highlighted (Figure 4.8a). The nondispersive line shapes and large intensities manifest the signal

enhancement with a pre-resonance Raman pump on the blue side of the PB* SE band and an on-resonance Raman probe.

Table 4.1. Ground-state Raman mode assignment for diF in methanol.

FSRS[a] freq. (cm^{-1})	Calc.[b] freq. (cm^{-1})	Raman mode assignment (major)
600	624	Imidazolinone ring breathing and sidechain motions, middle ring in-plane deformation
1277	1296	Phenol ring C–O stretch and ring breathing, ring-H rocking, imidazolinone ring in-plane deformation
1331	1332	Phenol C–OH rocking and ring asymmetric C=C stretch, middle ring-H rocking
1556	1555	Phenol C–OH rocking, $C_4=C_{1''}$ and phenol ring C=C stretch, ring-H rocking
1607	1620	$C_4=C_{1''}$ and phenol ring C=C stretch, ring-H scissoring

[a]The Raman mode frequencies are obtained from the GS-FSRS peaks on the Stokes side with the 510 nm Raman pump.

[b]The GS vibrational frequencies from the normal modes of a geometrically optimized protonated diF molecule are calculated with density functional theory (DFT) RB3LYP level with 6-31G+(d, p) basis sets in Gaussian software.[34]
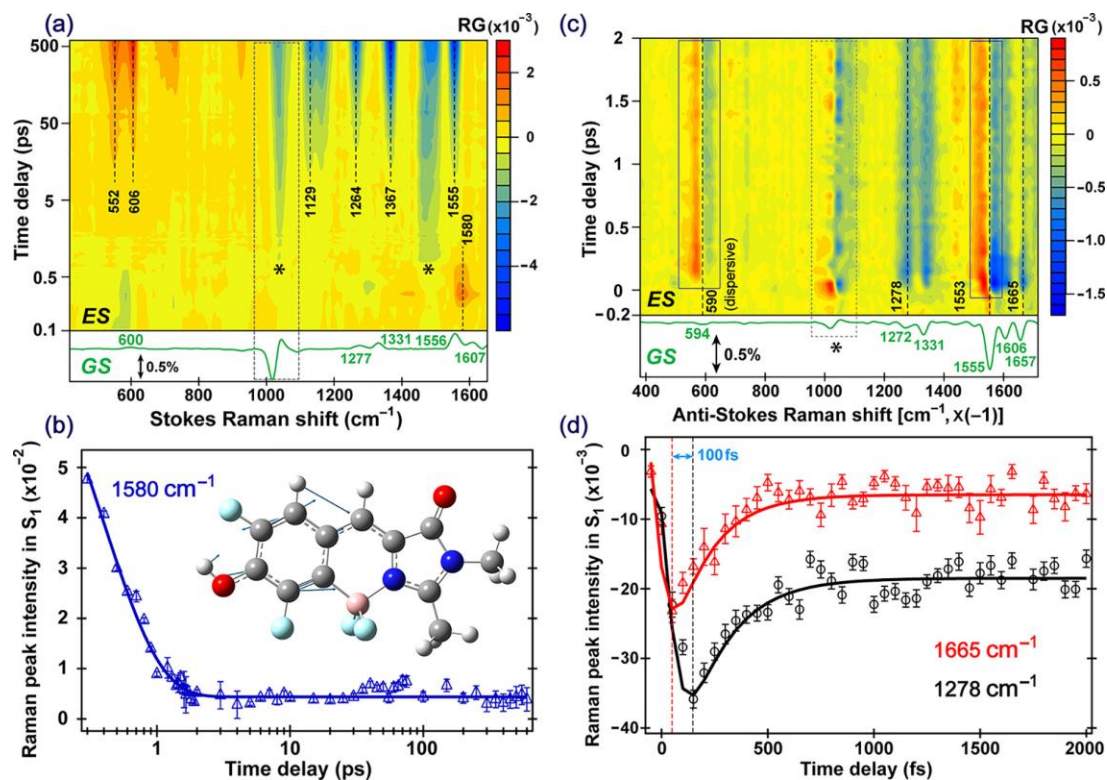
Figure 4.8. Intensity dynamics from time-resolved Stokes and anti-Stokes FSRS spectra for diF in methanol. (a) Semilogarithmic contour plot of Stokes FSRS of diF in methanol after 400 nm photoexcitation. The solvent signal is indicated by asterisks and scaled by 0.2 within the dotted box. The ground-state (GS) spectrum in green is plotted below. (b) Semilogarithmic plot of the PA* 1580 cm^{-1} mode intensity decay, with the pertinent normal mode illustrated. (c) Contour plot of the anti-Stokes FSRS data. Two dispersive bands are highlighted by the solid rectangles. The solvent signal is indicated by the asterisk and a dotted box. The GS spectrum in green is plotted below. (d) Two negative (Raman loss) modes exhibit a common 210 fs intensity decay within 1 ps (least-squares fits in solid curves). The time difference in reaching the maximal signal magnitude is shown, which could be related to dispersion of the broad-band probe pulse in this region. Reproduced with permission from Cheng Chen et al., *J. Phys. Chem. Lett.* **2017**, 8, 5921-5928. Copyright 2017 American Chemical Society.

Table 4.2. Excited-state FSRS dynamics and mode assignment for diF in methanol.

	Obs. freq.[a] (cm^{-1})	Calc. freq. (cm^{-1})	τ_1(ps)/A_1	τ_2(ps)/A_2	Vibrational assignment (major)[a]
Stokes	1555	1540	13.4/0.10	351/0.90	phenol ring C=C and C=O stretch, C$_4$=C$_{1''}$ stretch, ring-H scissoring
	1367	1370	13.5/0.11	334/0.89	phenol ring asymmetric C=C stretch, ring-H rocking
	1264	1263	14.0/0.05	290/0.95	ring-H scissoring, phenol ring asymmetric C=C stretch, imidazolinone ring in-plane deformation
	1129	1127	13.5/0.12	399/0.88	ring-H scissoring, imidazolinone ring in-plane deformation
	606	620	14.0/0.13	390/0.87	imidazolinone ring breathing and sidechain motions, middle ring in-plane deformation
	552	547	14.0/0.15	436/0.85	C$_{1'}$–C$_{2'}$ stretch, imidazolinone ring and middle ring in-plane deformation
	1580[c]	1584	0.40/1.00	–	phenol ring C=C stretch and C–OH rocking, phenol ring-H rocking
anti-Stokes	1665	1637	0.22/1.00	–	imidazolinone ring C=O stretch
	1553	1584	–	–	phenol ring C=C stretch and C–OH rocking, phenol ring-H rocking
	1278	1283	0.21/1.00	–	ring-H scissoring, phenol C–OH rocking, C–O and C=C stretch, imidazolinone ring in-plane deformation

[a]The Raman pump wavelength for excited-state FSRS is 510 nm.

[b]The excited-state vibrational frequencies are calculated using the TD-DFT method with RB3LYP 6-31G+(d, p) basis sets in Gaussian. The frequency scaling factor is 0.96.

Biexponential fit of the excited-state Raman intensities in Figure 4.8a reveal two time constants of ~13.5 and 350 ps, consistent among all of the rising PB* modes (Table 4.2). The fast component of 13.5 ps is slower than the 8 ps lifetime from fs-TA data in Figure 4.5 because TA probes electronic states from transient populations whereas FSRS reports on the polarizability changes, population conversion, and structural dynamics.[5,26] Therefore, the 13.5 ps component may include solvation of the contact ion pair and vibrational relaxation within PB* after ESPT. The slow component of 350 ps arises from the diffusion-controlled ESPT step after initial proton separation and solvent reorientation.[26,39,40] The 1129 cm^{-1} mode intensity of PB* exhibits a KIE ≈ 2.1 when CH$_3$OH is replaced by CD$_3$OD as the solvent. The time constant and KIE from FSRS measurements match the TA results (~360 ps and 2.4, respectively), confirming primary events in S$_1$ as structural motion-facilitated ESPT. The ~90% amplitude weight of the 350 ps component indicates that diffusion is the main driving force of proton transfer in solution. This process likely involves rotational diffusion of the proton donor and acceptor as well.[14,26,38,49]

The opposite signal signs within one spectral window stem from a unique "mixed" resonance condition of diF in methanol: the Raman pump is located at the red/blue side of the PA*/PB* emission band, respectively (Figure 4.4b). Notably, only one prominent PA* mode appears at ~1580 cm^{-1} around time zero and rapidly decays with a ~ 400 fs time constant (Figure 4.8b), which implies electronic redistribution and initial proton dissociation in S$_1$. Quantum calculations assign this mode to the phenol ring C=C stretch, COH rocking, and phenol ring−H rocking (Table 4.2), which explain

its high sensitivity to vibrational relaxation out of the FC region. However, the proton has not departed from diF significantly because PB* features are largely absent at this stage (black EADS, Figure 4.5a). A contact ion pair $R*O^-\cdots H^+\cdots OHCH_3$ could form on the sub-ps time scale, faster than pyranine in water[4,26,39,55] due to the superphotoacidity of diF in methanol. This intermediate can be represented by a CS state with similar electronic properties to those of PA*, corroborating the importance of charge rearrangement between diF and surrounding solvent molecules on the sub-ps time scale.[43] In addition, the largely negative peak at 1035 cm^{-1} (Figure 4.8a) is from methanol molecules.[35,55] The dispersive line shape at the methanol C−O stretch peak region in S_1 is indicative of the nascent protonated methanol species because of ESPT from diF.

For anti-Stokes FSRS, the 1278, 1342, 1614, and 1665 cm^{-1} modes have nondispersive line shape while the 590 and 1553 cm^{-1} modes are dispersive (Figure 4.8c). The mode-specific line shapes were found in ultrafast Raman loss spectroscopy when the Raman pump was tuned toward the S_0 absorption band,[57] equivalent to the anti-Stokes FSRS.[58] In this work, we observed unique mode-dependent line shapes in S_1 with evolving SE bands from the reactant to product. The 1278, 1553, 1614, and 1665 cm^{-1} modes emerge around time zero and decay rapidly, consistent with ultrafast charge separation of PA* during FC relaxation and the initial proton dissociation, as evinced by the dotted arrow in Figure 4.5b. The intensity dynamics of the 1278 and 1665 cm^{-1} modes (Figure 4.8d) show a dominant decay time constant of ~210 fs, which is shorter than the 1580 cm^{-1} mode with ~400 fs decay in Stokes FSRS. This comparison confirms that the

1580 cm^{-1} mode (i.e., largely concentrated on the phenol ring, Figure 4.8b inset) is more sensitive to the energy relaxation pathway into a CS state (i.e., beyond FC relaxation) and tracks formation of the contact ion pair involving the chromophore phenolic hydroxyl group. The corresponding $\sim 1553 \text{ cm}^{-1}$ mode on the anti-Stokes side is also the strongest, but due to its dispersive line shape, we did not fit its intensity dynamics. We also note that vibrational anharmonicity may result in small frequency shifts from the Stokes to anti-Stokes FSRS peaks in S_1 when vibrationally hot states are involved.[55,56] Significant mode intensity rise is not observed in anti-Stokes FSRS due to unfavorable resonance conditions of the Raman probe with the much redder PB* SE band. However, the PA* SE red shifts with time while the PB* SE rises (Figure 4.5). Consequently, the Raman intensity at later time could have both PA* and PB* contributions, which causes difficulty in resolving pure PA* dynamics (e.g., see modes between ~ 500 and 740 cm^{-1} with rather complex evolution in Figures 4.8c).

4.3.4 Potential energy surface

The match between time constants from TA and FSRS reveals an ultrafast ESPT reaction from diF to methanol with unprecedented details. Upon 400 nm photoexcitation into PA*, the LE state (~ 467 nm SE peak) converts to an intermediate CS state (~ 485 nm SE peak) with a time constant of ~ 560 fs (Figure 4.5). We consider during this initial stage that a contact ion pair forms between the partially relaxed PA* and a nearby solvent molecule; because diF is a superphotoacid, methanol can act as a proton acceptor. On this sub-ps time scale, the 1580 cm^{-1} PA* marker band has the

largest intensity in Stokes FSRS despite the Raman probe being off-resonant with the PA* SE band (Figure 4.4b), owing to the significant polarizability change associated with phenol ring C=C stretch and COH rocking motions. The mode intensity rapidly decays (Figure 3b) because the pertinent small-scale directional proton motions help to form the reacting complex between the superphotoacid and solvent, essentially bridging two early stages of the ESPT reaction (Figure 4.9).
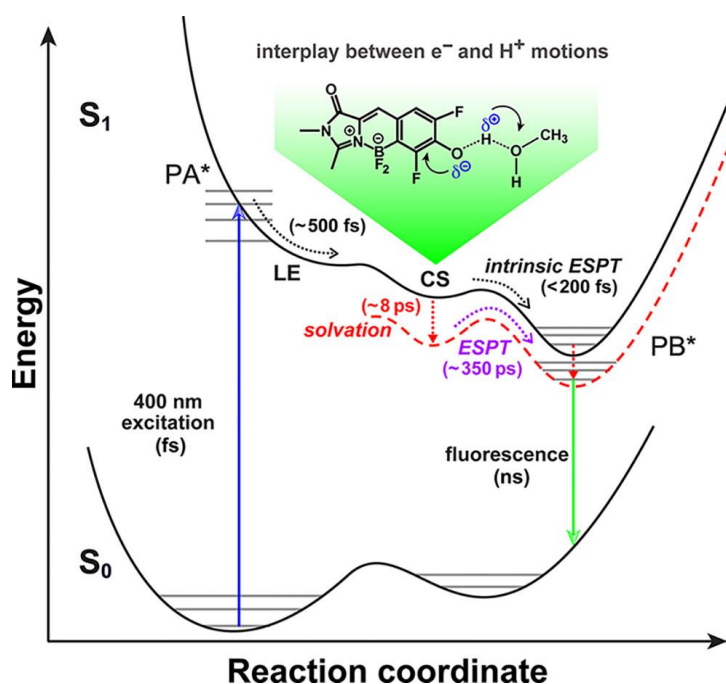
Figure 4.9. Kinetic scheme and diagram of the photoexcited diF in methanol. The dashed PES highlights the solvated electronic states in S_1, with red dotted arrows depicting solvation. Key steps before and during ESPT are noted with time constants in parentheses. Gray lines represent the vibrational levels. A transient contact ion pair involving diF and a methanol molecule in one geometry is illustrated above the corresponding CS (PA*) state. Reproduced with permission from Cheng Chen et al., *J. Phys. Chem. Lett.* **2017**, 8, 5921-5928. Copyright 2017 American Chemical Society.
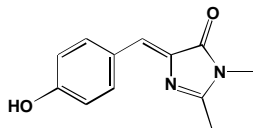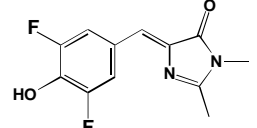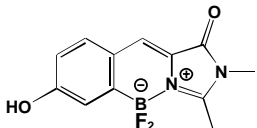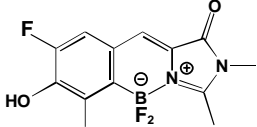
4.3.5 Photoacidity analysis

An interesting comparison to a strong quinone cyanine dye QCy7 in water with pK_a* ≈ -6 shows the ESPT rate coefficients of $k_{PT} \approx 1.5 \times 10^{12}$, 1.8×10^{12}, and 2.2×10^{12} s^{-1} with zero, two, and four sulfonate group substitutions and time constants of 667, 556, and 455 fs, respectively.[12] The diF in methanol undergoes initial ESPT on a similar time scale, which generates the contact ion pair and initial PB* population from the "intrinsic" ESPT over a small barrier via a pre-existing H-bonding chain (Figure 4.9). This mechanism agrees with fs-TA because the red EADS (Figure 4.5a) already shows a small PB* SE band at 540 nm, where the horizontal arrow from the CS (PA*) state terminates in Figure 4.5b. Moreover, the TA dynamics across the PB* SE band show an intensity rise time constant of ~600 fs, matching the CS state formation time of ~500 fs and the direct ESPT step within 200 fs between the optimally oriented donor and acceptor in a largely adiabatic manner.[4,37,40,41] Meanwhile, the chromophore population with less optimized or nonexistent H-bonding chains needs to undergo further solvation before ESPT, illustrated by the bifurcation of reaction pathways from the CS state in Figure 4.9, which indicates the intrinsic heterogeneity of diF in solution.

Comparisons among diF analogues (Table 4.3) show multiple factors in determining photoacidity. On one hand, EWGs lower the pK_a on the pull-push conjugated π-electron system. Due to the strong electron-withdrawing capability of fluorine,[59] compounds 2 and 4 have a lower pK_a by ~2.5 units than compounds 1 and 3. On the other hand, conformational locking restricts the structural flexibility and forces larger conjugation so that electrons on the phenolic COH group become more delocalized and migrate

over a planar system.[16] This results in a more reactive, dissociable proton and lower

pK_a. Therefore, compounds 3 and 4 are more acidic than compounds 1 and 2, respectively, with a pK_a drop by ~1.5 units. These two factors affect pK_a, and the addition of fluorine atoms increases acidity more than the locking does. Due to electron redistribution in S_1, more factors contribute and the above criteria may be insufficient to estimate pK_a^*. However, the Förster model gives a useful quantitative relationship:

$pK_a^* = pK_a + \Delta pK_a^* = pK_a - (h\nu_1 - h\nu_2)/(2.3k_BT)$, where $h\nu_{1(2)}$ is the 0−0 electronic transition energy of the conjugate acid (base). We use the averages of absorption and fluorescence maxima to represent ν_1 and ν_2 because absorption/fluorescence usually overestimates/underestimates the 0-0 transition (FC principle).[1,22]

Table 4.3. Acidity and photoacidity of diF analogues with optical properties.

	Compound	Structure	PA abs./em. (nm)	PB abs./em. (nm)	pK_a	ΔpK_a^*	pK_a^*
1	*p*-HBDI		370/448	425/494	7.8	−5.9	1.9
2	DF*p*-HBDI		363/445	418/500	5.4	−6.5	−1.1
3	p-HOBDI-BF$_2$		404/485	485/520	6.4	−5.8	0.6
4	p-HO-3,5-BDI-BF$_2$ (this work)		402/n.d.[a]	480/530	3.9	−8.4	−4.5

[a]Not detected due to highly efficient ESPT in water.

The ΔpK_a* can be qualitatively estimated from molecular structures. Treating the conjugated planar structure as a quantum box, locking increases the box size and lowers the transition energy for PA and PB. Our calculations show that both forms of the unlocked compounds 1 and 2 are nearly planar at equilibrium. The slight size increase and other competing factors such as solvation and H-bonding lead to a similar acidity drop upon excitation of all four compounds in Table 4.3. In contrast, QCy9 shows a ΔpK_a* of -12.8 due to a large bathochromic shift of PB relative to PA. Ground-state calculations indicate that PB gains planarity and significantly extends conjugation, resulting in a much redder electronic transition and the strongest superphotoacid to date. These molecular scaffolds with controllable substitutions and skeletal flexibility thus provide excellent models for ESPT with applications to mimic fluorescent protein properties, engineer molecular functions in various environments, and design systems with bright and tunable fluorescence.

4.4 Conclusions

In this work, we reported a synthetic superphotoacid derived from the GFP model chromophore with conformational locking and strategic addition of EWGs at ortho sites to the phenolic hydroxyl group to elevate the photoacidity to "super" strength while maintaining high fluorescence QY. On the basis of its electronic excited-state landscape, we implemented tunable resonance FSRS to glean ultrafast structural dynamics from the reactant to product and, for the first time, before and during an intermolecular ESPT reaction of a superphotoacid in solution. Our approach demonstrates the power of bioinspired synthesis and spectroscopic characterization of a target functionality involving photoinduced proton transfer for widespread applications. Excellent match between fs-TA and FSRS elucidates a solvent-controlled ESPT reaction frame by frame on molecular time scales. Marker vibrational bands of diF in methanol after 400 nm photoexcitation exhibit time constants of ~210−400 fs from PA* decay and ~13.5 and 350 ps from PB* rise. These processes reveal the initial proton dissociation, formation of an intermediate CS state, solvation of the contact ion pair, and diffusion-controlled proton motion to reach the fully solvated PB* fluorescent state. A phenol ring COH rocking and C=C stretching mode at ~1580 cm^{-1} is implied to play an active role along the reaction coordinate toward the proposed contact ion pair/CS state formation. This work exploits a unique resonance condition for FSRS (Stokes and anti-Stokes) and reveals the intricate working mechanism of a rationally engineered photosensitive molecule. Such comprehensive knowledge correlating electron and nuclear motions will guide the precise functional control via organic synthesis and genetic code expansion methods in chemical and biological systems.

4.5 References

[1] Tolbert, L. M.; Solntsev, K. M. Excited-State Proton Transfer: From Constrained Systems to ″Super″ Photoacids to Superfast Proton Transfer. *Acc. Chem. Res.* **2002**, *35*, 19-27.

[2] Weber, K. The Close Relationship of Fluorescence Obliteration to the Inhibition of Photochemical Reactions. *Z. Phys. Chem., Abt. B* **1931**, *15*, 18-44.

[3] Agmon, N.; Huppert, D.; Masad, A.; Pines, E. Excited-State Proton-Transfer to Methanol Water Mixtures. *J. Phys. Chem.* **1991**, *95*, 10407-10413.

[4] Rini, M.; Magnes, B. Z.; Pines, E.; Nibbering, E. T. J. Real-Time Observation of Bimodal Proton Transfer in Acid-Base Pairs in Water. *Science* **2003**, *301*, 349-352.

[5] Fang, C.; Frontiera, R. R.; Tran, R.; Mathies, R. A. Mapping GFP Structure Evolution During Proton Transfer with Femtosecond Raman Spectroscopy. *Nature* **2009**, *462*, 200-204.

[6] Oscar, B. G.; Liu, W.; Zhao, Y.; Tang, L.; Wang, Y.; Campbell, R. E.; Fang, C. Excited-State Structural Dynamics of a Dual-Emission Calmodulin-Green Fluorescent Protein Sensor for Calcium Ion Imaging. *Proc. Natl. Acad. Sci. U. S. A.* **2014**, *111*, 10191-10196.

[7] Chou, P. T.; Solntsev, K. M. Photoinduced Proton Transfer in Chemistry and Biology. *J. Phys. Chem. B* **2015**, *119*, 2089.

[8] Nunes, R. M. D.; Pineiro, M.; Arnaut, L. G. Photoacid for Extremely Long-Lived and Reversible pH-Jumps. *J. Am. Chem. Soc.* **2009**, *131*, 9456-9462.

[9] Abeyrathna, N.; Liao, Y. A Reversible Photoacid Functioning in PBS Buffer under Visible Light. *J. Am. Chem. Soc.* **2015**, *137*, 11282-11284.

[10] Wu, H.; Gonsalves, K. E. Preparation of a Photoacid Generating Monomer and Its Application in Lithography. *Adv. Funct. Mater.* **2001**, *11*, 271-276.

[11] Shi, Z.; Peng, P.; Strohecker, D.; Liao, Y. Long-Lived Photoacid Based upon a Photochromic Reaction. *J. Am. Chem. Soc.* **2011**, *133*, 14699-14703.

[12] Presiado, I.; Karton-Lifshin, N.; Erez, Y.; Gepshtein, R.; Shabat, D.; Huppert, D. Ultrafast Proton Transfer of Three Novel Quinone Cyanine Photoacids. *J. Phys. Chem. A* **2012**, *116*, 7353.

[13] Simkovitch, R.; Karton-Lifshin, N.; Shomer, S.; Shabat, D.; Huppert, D. Ultrafast Excited-State Proton Transfer to the Solvent Occurs on a Hundred-Femtosecond Time-Scale. *J. Phys. Chem. A* **2013**, *117*, 3405-3413.

[14] Pérez-Lustres, J. L.; Rodriguez-Prieto, F.; Mosquera, M.; Senyushkina, T. A.; Ernsting, N. P.; Kovalenko, S. A. Ultrafast Proton Transfer to Solvent: Molecularity and Intermediates from Solvation- and Diffusion-Controlled Regimes. *J. Am. Chem. Soc.* **2007**, *129*, 5408-5418.

[15] Tolbert, L. M.; Haubrich, J. E. Enhanced Photoacidities of Cyanonaphthols. *J. Am. Chem. Soc.* **1990**, *112*, 8163-8165.

[16] Agmon, N.; Rettig, W.; Groth, C. Electronic Determinants of Photoacidity in Cyanonaphthols. *J. Am. Chem. Soc.* **2002**, *124*, 1089-1096.

[17] Oltrogge, L. M.; Boxer, S. G. Short Hydrogen Bonds and Proton Delocalization in Green Fluorescent Protein (GFP). *ACS Cent. Sci.* **2015**, *1*, 148-156.

[18] Paige, J. S.; Wu, K. Y.; Jaffrey, S. R. RNA Mimics of Green Fluorescent Protein. *Science* **2011**, *333*, 642-646.

[19] Walker, C. L.; Lukyanov, K. A.; Yampolsky, I. V.; Mishin, A. S.; Bommarius, A. S.; Duraj-Thatte, A. M.; Azizi, B.; Tolbert, L. M.; Solntsev, K. M. Fluorescence Imaging using Synthetic GFP Chromophores. *Curr. Opin. Chem. Biol.* **2015**, *27*, 64-74.

[20] Bose, S.; Chakrabarty, S.; Ghosh, D. Electrostatic Origin of the Red Solvatochromic Shift of DFHBDI in RNA Spinach. *J. Phys. Chem. B* **2017**, *121*, 4790-4798.

[21] Vengris, M.; van Stokkum, I. H. M.; He, X.; Bell, A. F.; Tonge, P. J.; van Grondelle, R.; Larsen, D. S. Ultrafast Excited and Ground-State Dynamics of the Green Fluorescent Protein Chromophore in Solution. *J. Phys. Chem. A* **2004**, *108*, 4587-4598.

[22] Baranov, M. S.; Lukyanov, K. A.; Borissova, A. O.; Shamir, J.; Kosenkov, D.; Slipchenko, L. V.; Tolbert, L. M.; Yampolsky, I. V.; Solntsev, K. M. Conformationally Locked Chromophores as Models of Excited-State Proton Transfer in Fluorescent Proteins. *J. Am. Chem. Soc.* **2012**, *134*, 6025-6032.

[23] McCamant, D. W.; Kukura, P.; Yoon, S.; Mathies, R. A. Femtosecond Broadband Stimulated Raman Spectroscopy: Apparatus and Methods. *Rev. Sci. Instrum.* **2004**, *75*, 4971.

[24] Kovalenko, S. A.; Dobryakov, A. L.; Ernsting, N. P. An Efficient Setup for Femtosecond Stimulated Raman Spectroscopy. *Rev. Sci. Instrum.* **2011**, *82*, 063102.

[25] Zhu, L.; Liu, W.; Fang, C. A Versatile Femtosecond Stimulated Raman Spectroscopy Setup with Tunable Pulses in the Visible to Near Infrared. *Appl. Phys. Lett.* **2014**, *105*, 041106.

[26] Liu, W.; Wang, Y.; Tang, L.; Oscar, B. G.; Zhu, L.; Fang, C. Panoramic Portrait of Primary Molecular Events Preceding Excited State Proton Transfer in Water. *Chem. Sci.* **2016**, *7*, 5484-5494.

[27] Tang, L.; Liu, W.; Wang, Y.; Zhao, Y.; Oscar, B. G.; Campbell, R. E.; Fang, C. Unraveling Ultrafast Photoinduced Proton Transfer Dynamics in a Fluorescent Protein Biosensor for Ca^{2+} Imaging. *Chem. Eur. J.* **2015**, *21*, 6481-6490.

[28] Riedl, J.; Ménová, P.; Pohl, R.; Orság, P.; Fojta, M.; Hocek, M. GFP-like Fluorophores as DNA Labels for Studying DNA–Protein Interactions. *J. Org. Chem.* **2012**, *77*, 8287-8293.

[29] Han, K. Y.; Leslie, B. J.; Fei, J.; Zhang, J.; Ha, T. Understanding the Photophysics of the Spinach–DFHBI RNA Aptamer–Fluorogen Complex To Improve Live-Cell RNA Imaging. *J. Am. Chem. Soc.* **2013**, *135*, 19033-19038.

[30] Ishida, N.; Moriya, T.; Goya, T.; Murakami, M. Synthesis of Pyridine−Borane Complexes via Electrophilic Aromatic Borylation. *J. Org. Chem.* **2010**, *75*, 8709-8712.

[31] Baranov, M. S.; Solntsev, K. M.; Baleeva, N. S.; Mishin, A. S.; Lukyanov, S. A.; Lukyanov, K. A.; Yampolsky, I. V. Red-Shifted Fluorescent Aminated Derivatives of a Conformationally Locked GFP Chromophore. *Chem. Eur. J.* **2014**, *20*, 13234-13241.

[32] Wong, H. N. C.; Xu, Z. L.; Chang, H. M.; Lee, C. M. A Modified Synthesis of (±)-β-Aryllactic acids. *Synthesis* **1992**, *1992*, 793-797.

[33] Kojima, S.; Ohkawa, H.; Hirano, T.; Maki, S.; Niwa, H.; Ohashi, M.; Inouye, S.; Tsuji, F. I. Fluorescent properties of model chromophores of tyrosine-66 substituted mutants of *Aequorea* green fluorescent protein (GFP). *Tetrahedron Lett.* **1998**, *39*, 5239-5242.

[34] Frisch, M.; Trucks, G.; Schlegel, H. B.; Scuseria, G. E.; Robb, M. A.; Cheeseman, J. R.; Scalmani, G.; Barone, V.; Mennucci, B.; Petersson, G. *Gaussian 09*, Revision d. 01, Gaussian. Inc.*, Wallingford CT* **2009**, *201*.

[35] Wang, Y.; Liu, W.; Tang, L.; Oscar, B. G.; Han, F.; Fang, C. Early Time Excited-State Structural Evolution of Pyranine in Methanol Revealed by Femtosecond Stimulated Raman Spectroscopy. *J. Phys. Chem. A* **2013**, *117*, 6024-6042.

[36] Oscar, B. G.; Liu, W.; Rozanov, N. D.; Fang, C. Ultrafast Intermolecular Proton Transfer to a Proton Scavenger in an Organic Solvent. *Phys. Chem. Chem. Phys.* **2016**, *18*, 26151-26160.

[37] Staib, A.; Borgis, D.; Hynes, J. T. Proton Transfer in Hydrogen-Bonded Acid-Base Complexes in Polar Solvents. *J. Chem. Phys.* **1995**, *102*, 2487.

[38] Siwick, B. J.; Cox, M. J.; Bakker, H. J. Long-Range Proton Transfer in Aqueous Acid-Base Reactions. *J. Phys. Chem. B* **2008**, *112*, 378-389.

[39] Leiderman, P.; Genosar, L.; Huppert, D. Excited-State Proton Transfer: Indication of Three Steps in the Dissociation and Recombination Process. *J. Phys. Chem. A* **2005**, *109*, 5965-5977.

[40] Liu, W.; Han, F.; Smith, C.; Fang, C. Ultrafast Conformational Dynamics of Pyranine during Excited State Proton Transfer in Aqueous Solution Revealed by Femtosecond Stimulated Raman Spectroscopy. *J. Phys. Chem. B* **2012**, *116*, 10535-10550.

[41] Simkovitch, R.; Shomer, S.; Gepshtein, R.; Huppert, D. How Fast Can a Proton-Transfer Reaction Be beyond the Solvent-Control Limit? *J. Phys. Chem. B* **2015**, *119*, 2253-2262.

[42] Maroncelli, M.; Fleming, G. R. Comparison of Time-Resolved Fluorescence Stokes Shift Measurements to a Molecular Theory of Solvation Dynamics. *J. Chem. Phys.* **1988**, *89*, 875.

[43] Horng, M. L.; Gardecki, J. A.; Papazyan, A.; Maroncelli, M. Subpicosecond Measurements of Polar Solvation Dynamics: Coumarin 153 Revisited. *J. Phys. Chem.* **1995**, *99*, 17311-17337.

[44] Spry, D. B.; Goun, A.; Fayer, M. D. Deprotonation Dynamics and Stokes Shift of Pyranine (HPTS). *J. Phys. Chem. A* **2007**, *111*, 230-237.

[45] Ghosh, R.; Mondal, J. A.; Palit, D. K. Ultrafast Dynamics of the Excited States of Curcumin in Solution. *J. Phys. Chem. B* **2010**, *114*, 12129-12143.

[46] Snellenburg, J. J.; Laptenok, S. P.; Seger, R.; Mullen, K. M.; van Stokkum, I. H. M. Glotaran: A Java-Based Graphical User Interface for the R-Package TIMP. *J. Stat. Soft.* **2012**, *49*, 1-22.

[47] Mohammed, O. F.; Dreyer, J.; Magnes, B.-Z.; Pines, E.; Nibbering, E. T. J. Solvent-Dependent Photoacidity State of Pyranine Monitored by Transient Mid-Infrared Spectroscopy. *ChemPhysChem* **2005**, *6*, 625-636.

[48] Chase, W. J.; Hunt, J. W. Solvation Time of the Electron in Polar Liquids. Water and Alcohols. *J. Phys. Chem.* **1975**, *79*, 2835-2845.

[49] Simon, J. D. Time-Resolved Studies of Solvation in Polar Media. *Acc. Chem. Res.* **1988**, *21*, 128-134.

[50] Westlake, B. C.; Brennaman, M. K.; Concepcion, J. J.; Paul, J. J.; Bettis, S. E.; Hampton, S. D.; Miller, S. A.; Lebedeva, N. V.; Forbes, M. D. E.; Moran, A. M.; Meyer, T. J.; Papanikolas, J. M. Concerted Electron-Proton Transfer in the Optical Excitation of Hydrogen-Bonded Dyes. *Proc. Natl. Acad. Sci. U. S. A.* **2011**, *108*, 8554-8558.

[51]   Snellenburg, J. J.; Laptenok, S. P.; DeSa, R. J.; Naumov, P.; Solntsev, K. M. Excited-State Dynamics of Oxyluciferin in Firefly Luciferase. *J. Am. Chem. Soc.* **2016**, *138*, 16252-16258.

[52]   Shirota, H.; Pal, H.; Tominaga, K.; Yoshihara, K. Deuterium Isotope Effect on the Solvation Dynamics of Methanol: CH_3OH, CH_3OD, CD_3OH, and CD_3OD. *J. Phys. Chem.* **1996**, *100*, 14575-14577.

[53]   van Stokkum, I. H. M.; Larsen, D. S.; van Grondelle, R. Global and target analysis of time-resolved spectra. *Biochim. Biophys. Acta* **2004**, *1657*, 82-104.

[54]   Sun, Z.; Lu, J.; Zhang, D. H.; Lee, S. Y. Quantum Theory of (Femtosecond) Time-Resolved Stimulated Raman Scattering. *J. Chem. Phys.* **2008**, *128*, 144114.

[55]   Liu, W.; Tang, L.; Oscar, B. G.; Wang, Y.; Chen, C.; Fang, C. Tracking Ultrafast Vibrational Cooling During Excited State Proton Transfer Reaction with Anti-Stokes and Stokes Femtosecond Stimulated Raman Spectroscopy. *J. Phys. Chem. Lett.* **2017**, *8*, 997-1003.

[56]   Oscar, B. G.; Chen, C.; Liu, W.; Zhu, L.; Fang, C. Dynamic Raman Line Shapes on an Evolving Excited-State Landscape: Insights from Tunable Femtosecond Stimulated Raman Spectroscopy. *J. Phys. Chem. A* **2017**, *121*, 5428-5441.

[57]   Umapathy, S.; Mallick, B.; Lakshmanna, A. Mode-Dependent Dispersion in Raman Line Shapes: Observation and Implications from Ultrafast Raman Loss Spectroscopy. *J. Chem. Phys.* **2010**, *133*, 024505.

[58]   Qiu, X.; Li, X.; Niu, K.; Lee, S. Y. Inverse Raman Bands in Ultrafast Raman Loss Spectroscopy. *J. Chem. Phys.* **2011**, *135*, 164502.

[59]   Laptenok, S. P.; Conyard, J.; Page, P. C. B.; Chan, Y.; You, M.; Jaffrey, S. R.; Meech, S. R. Photoacid Behaviour in a Fluorinated Green Fluorescent Protein Chromophore: Ultrafast Formation of Anion and Zwitterion States. *Chem. Sci.* **2016**, *7*, 5747-5752.

Chapter 5 Rational Design and ESPT Dynamics of GFP Chromophore-Derived Fluorescent Superphotoacids[d]

5.1 Introduction

Photoacids represent excellent model systems to study excited-state proton transfer (ESPT), one of the most fundamental and essential steps in numerous chemical and biological processes. The name "photo" and "acid" combines two important concepts in chemistry, photoinduced and acid-base reactions, or on a more fundamental level, light-matter interactions and proton motions. This class of molecules usually possesses aromatic frameworks and exhibits a decrease in the pK_a value, namely, an increase of acidity, upon photoexcitation from the electronic ground state to the excited state. The photoacidity strength can be characterized and classified by the excited-state pK_a (pK_a*) and solute (acid)−solvent interactions.[1] Among this chemical group, the term "superphotoacid" defines the photoacids with a negative pK_a* and their capability of transferring a proton to nonaqueous solvents, which typically involves the protic and basic organic molecules in a hydrogen (H)-bonding network.[2] Due to the peculiar functionality of superphotoacids to undergo proton transfer in a wide range of solvents well beyond water, significant efforts have been devoted to understanding and manipulating photoacidity over the past few decades.[1,3-13]

Previous studies of cyano-substituted naphthols have provided valuable insights into the rational design of superphotoacids.[14] The main consideration is that photoacidity can be enhanced by applying the electron-withdrawing groups (EWGs) at electron-rich sites to lower the energy of the conjugate base.[5] For 2-naphthol, two atomic sites of C-5 and C-8 (Figure 5.1) show distinctly more electron density in the first singlet excited state (S_1) of the anionic form, in contrast to the ground state (S_0). As a result, cyano substitution at either of these two sites can lead to a greater increase of photoacidity than substitutions at other sites of the molecule. The pK_a^* values of 5- and 8-cyano-2-naphthols (5CN and 8CN) were determined to be ca. −0.8 according to the Förster equation,[2,8] a value that is more acidic than the 6- and 7-cyano-2-naphthols (6CN and 7CN). Moreover, an additive effect is present when both sites are substituted. The dicyano-substituted derivative 5,8-dicyano-2-naphthol (DCN2, Figure 5.1) exhibits significantly stronger photoacidity ($pK_a^*=-4.5$) than the monocyano derivatives, so DCN2 can undergo ESPT to various alcohols and basic solvents besides water.[1,14-17]
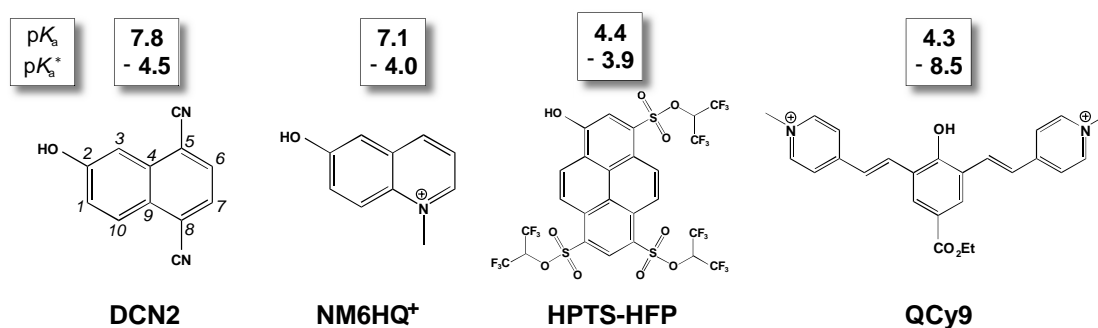
Figure 5.1. Structures of four representative superphotoacids based on different molecular scaffolds with their ground- and excited-state acidities (pK_a and pK_a^*). Adapted with permission from Cheng Chen et al., *J. Phys. Chem. B* **2019**, 123, 3804-3821. Copyright 2019 American Chemical Society.

Alternative methods or routes exist to achieve a higher acidity and/or photoacidity for these functional molecules. Without additional EWG substitutions, a replacement of the naphthalene backbone with an electron-deficient methylquinolinium produces an interesting superphotoacid N-methyl-6-hydroxyquinolinium (NM6HQ$^+$, Figure 5.1) with a photoacidity strength (pK_a* $\approx$ −4.0)[7] similar to that of DCN2. We note that subsequent studies adopted direct kinetic measurements, extensive Brownian dynamics simulations, and spherically symmetric diffusion problem (SSDP) calculations with the adapted force field, which led to the determination of pK_a* $\approx$ −7.0 for NM6HQ$^+$ with non-associating counterions in water, and its ESPT activation energy is smaller than that of DCN2 in water.[18,19] Another pertinent example is the modification of 8-hydroxypyrene-1,3,6-trisulfonate (pyranine or HPTS), a well-investigated photoacid.[3,4,6,20,21] By converting three side-chain sulfonic acid groups to the more electron-withdrawing sulfonamides and sulfonic esters, the photoacidity can be increased by ca. 2−5 pK_a units from the parent HPTS (pK_a* $\approx$ 0.4).[22] The strongest photoacid synthesized in this substitution series is tris(1,1,1,3,3,3-hexafluoropropan-2-yl)-8-hydroxypyrene-1,3,6-trisulfonate (HPTS-HFP, Figure 5.1) with a pK_a* of −3.9.[10] In addition, the cyanine-based photoacids have recently drawn great attention due to their extraordinary photoacidities as well as their nonfluorescent characters.[23] Quinone cyanine 9 (QCy9) has been reported to be the strongest photoacid to date with the ESPT rate of $\sim 1 \times 10^{13}$ s^{-1} and an incredibly low pK_a* of −8.5, which essentially correlate with a barrierless ESPT reaction from QCy9 to water, methanol, and ethanol with the same rate.[24]

Among these synthesized and engineered superphotoacids, intramolecular charge transfer (ICT) has been identified as an important feature for the energy lowering of excited states.[5,25,26] This stabilization effect is more pronounced for the deprotonated form (PB) than for the protonated form (PA) of the photoacid, hence leading to a more exergonic/exothermic PT reaction and a consequently lower pK_a^*. The aforementioned strengthened photoacids all adopt the "donor-acceptor" structures with an enhanced ICT character, which is achieved by placing strong EWGs at the acceptor moieties that are typically located at the distal ring(s) from the original hydroxylated ring. The electrophilic substitutions at more electronegative sites of the PB form would be expected to achieve stronger photoacidity due to a better dispersed and delocalized electron density with respect to substituted cases at those less electronegative sites. This is supported by the fact that, in the excited state, 5CN and 8CN are more acidic than 6CN and 7CN among the monocyano naphthols (see Figure 5.1 for the atomic numbering).[5,16] For the multiring systems like naphthol and hydroxypyrene, the proximal ring bound to the hydroxyl group is conventionally considered as the donor moiety. It is noteworthy that the systematic study of substituent and site effect on photoacidity upon substitution at the donor ring remains to date experimentally underexplored.[27] For instance, the 1- and 3-cyano-2-naphthols (1CN and 3CN) have not yet been synthesized to further examine the ICT principle despite semiempirical calculations that predicted 3CN to be a strong photoacid.[25] HPTS and its derivatives have EWGs at both proximal and distal rings which, however, complicate the elucidation of the effect of clearly isolated proximal-ring substitutions.[10,22]

In this work, we designed two series of photoacids and comprehensively characterized the most photoacidic compound of each series using a number of advanced spectroscopic techniques, which enrich the understanding of fundamental determinants of photoacidity as well as the excited-state structural behaviors of superphotoacids. The design of these photoacids has been inspired by the photochemical properties of green fluorescent protein (GFP) which has revolutionized molecular and cellular biology for decades.[28-31] It is known that the wild-type GFP emits green light upon ultraviolet irradiation because the core chromophore undergoes ESPT on ultrafast time scales and converts to a deprotonated intermediate I*.[32-34] This transient process is highly energy-conserving, indicated by the high fluorescence quantum yield (FQY, $\Phi=0.79$) of wild-type GFP upon excitation of the neutral form of the embedded chromophore. However, the synthetic GFP chromophore 4′-hydroxybenzylidene-1,2-dimethyl-imidazolinone (*p*-HBDI, Figure 5.2) loses not only high FQY but also the ESPT capability in solution phase.[35] This observation reveals the important role of a restrictive protein matrix in functionalizing the chromophore.[31] In contrast to a rigid protein environment, ring twisting motions around the bridge bond of *p*-HBDI are allowed and become favorable in solution, therefore opening up nonradiative decay pathways and leading to a very low FQY of $\sim10^{-4}$, essentially deeming it nonfluorescent at room temperature.[8,35]

Interestingly, with a relatively small molecular footprint, *p*-HBDI is not capable of ESPT in aqueous solution. This is mainly due to the following reasons. (1) Altered electronic structure under flexible conformations intrinsically weakens photoacidity. This is evinced by a large red-shift in the absorption and emission peak of both the

neutral and anionic *p*-HBDI from solution to the protein pocket. This indicates better stabilization of the excited state in a more rigid nuclear framework by the protein matrix. The ground-state pK_a was determined to be ~8.2 in aqueous solution[36] while it is ~6 or lower in GFP with various mutations.[37] The latter agrees well with theoretical pK_a calculations of a coordinate-frozen *p*-HBDI (~6.4 estimated from the Förster equation), which suggests that the entropic contributions due to internal rotational modes (not the surrounding residues of the protein host *per se*) mainly explain the pK_a increase from protein to solution in a ground-state deprotonation reaction.[38] As a result, *p*-HBDI has a higher pK_a* in solution according to the Förster cycle. (2) The short excited-state lifetime of neutral *p*-HBDI limits the ESPT efficiency. In essence, there exists an intrinsic competition between different excited-state energy dissipation pathways, e.g., ESPT, internal conversion, and fluorescence. The pK_a* of *p*-HBDI is estimated to be 2.1,[13,36,39] corresponding to a very slow ESPT rate. Therefore, the <1 ps excited-state lifetime of neutral *p*-HBDI in solution causes a negligible ESPT quantum yield.[35]
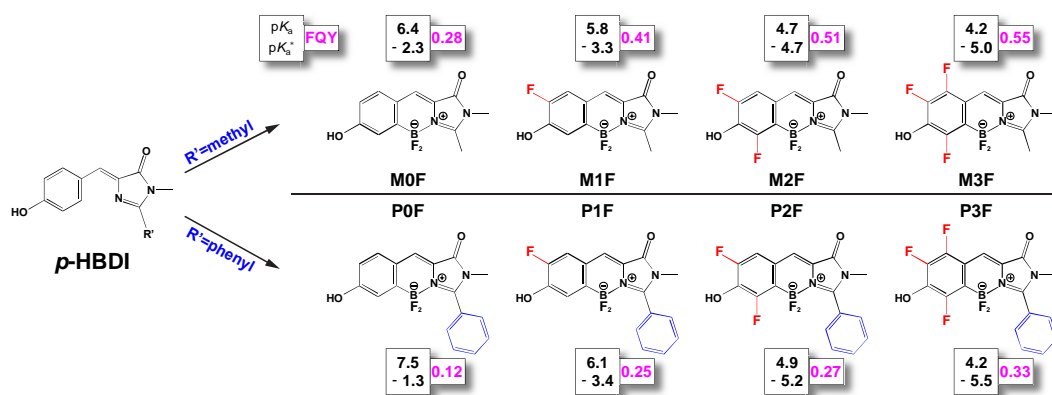
Figure 5.2. Structures of *p*-HBDI derivatives with an increasing photoacidity and the anionic form FQY upon neutral form excitation in water. Reproduced with permission from Cheng Chen et al., *J. Phys. Chem. B* **2019**, 123, 3804-3821. Copyright 2019 American Chemical Society.

It is notable that other studies on the modified GFP-core chromophore in a protein or solution environment have shed more light on the influence of structural flexibility and EWGs on photoacidity. For instance, GFP with a fluorinated chromophore has a lower pK_a and pK_a^* than the nonfluorinated GFP, and the photoacidity increase as well as spectral changes exhibit the site dependence of fluorination.[40,41] Such engineered GFP derivatives have found important applications in live-cell imaging of RNAs[42] and protein-binding fluorogenic dyes for live-cell imaging.[43] When outside of the protein matrix, the difluorinated *p*-HBDI is more photoacidic than p-HBDI but less than the conformationally locked difluorinated *p*-HBDI.[13,39]

With such deepened understandings of structure-photoacidity relationships, we carried out a multistep enhancement of photoacidity on the basis of the *p*-HBDI framework. First, the phenolic and imidazolinone rings are locked by a recently developed coordination-assisted borylation approach to improve FQY and increase photoacidity to some extent.[8] Second, EWGs (−F in this work) are incorporated into the adjacent sites of the phenolic hydroxyl group to significantly boost photoacidity. Furthermore, the methyl at C2 of the distal imidazolinone ring is replaced by a phenyl ring (as an EWG and charge acceptor) to presumably increase photoacidity to a further extent due to the enhanced ICT from the phenolic/phenolate to the imidazolinone ring (Figure 5.2).

We observed the photoacidity increase with more sites fluorinated. The di- and trifluorinated derivatives (M2F,[13] M3F, P2F, and P3F) exhibit superphotoacidity which can undergo ESPT in organic solvents such as alcohols. The pK_a^* decrease from 2F to

3F is smaller than that of 0F → 1F and 1F → 2F likely due to less electron density situated at the meta site. Fluorinated phenyl series are generally more photoacidic than their counterparts in the methyl series, confirming that an enhanced excited-state ICT improves photoacidity. Meanwhile, these photoacids are highly fluorescent in solution, and the measured anionic FQY increases from 0F to 3F upon neutral form excitation (Figure 5.2), which agrees with the increasing photoacidity and the resultant ESPT efficiency. These FQYs represent the anionic form emission (from ESPT) after photoexcitation of the neutral form. The phenyl series exhibits a lower FQY than the methyl series[44] mainly because of the twisting-induced nonradiative decay channels enabled by a flexible phenyl ring at the side chain. This point is on the basis of prior knowledge that isomerization/twisting promotes radiationless decay such as internal conversion.[35,39,45,46] Moreover, corroborating evidence comes from the density functional theory (DFT) and time-dependent (TD) DFT calculations that show different dihedral angles between the side-chain phenyl ring and the main phenol-imidazolinone backbone, indicative of phenyl ring torsion in the electronic excited state after photoexcitation.

To delineate the ESPT reaction dynamics, the superphotoacidity phenomenon demands a time-resolved spectroscopic technique with high resolution to track the initial ultrafast ESPT step as well as its structural dynamics that are of fundamental importance to mechanistically understand ESPT. Here, we employed a combined approach of femtosecond transient absorption (fs-TA) and tunable femtosecond stimulated Raman spectroscopy (FSRS) to dissect the ESPT dynamics of M3F and P3F in methanol. This

integrated technical approach has been adopted by several research groups to investigate complex systems along multidimensional reaction coordinates with previously unattainable structural information.[47-51] In particular, the dynamic resonance Raman enhancement of FSRS enables one to selectively probe transient or reaction species of interest by increasing the signal-to-noise ratio (SNR).[46] In this work, we strategically positioned the Raman pump (R_{pu}) wavelength in between the PA* and PB* (asterisk represents excited state) electronic bands and tracked the structural evolution of both photoreactant (PA*) and photoproduct (PB*) species within one spectral window and with high SNR. Aided by fs-TA data and global analysis results, we revealed at least three inhomogeneous ESPT pathways likely in a parallel manner including direct ESPT facilitated by preexisting H-bonding chains, the solvation-controlled ESPT, and rotational diffusion-controlled ESPT on multiple time scales after the initial charge separation (CS) or small-scale proton separation in forming a contact ion pair (CIP)[5,6,21,52] on the <300 fs time scale. Note that an intermediate CIP state for superphotoacid molecular systems in polar solvent does not indicate a complete electron transfer. These CIPs may take some time to be stabilized by the surrounding solvent, and methanol provides such a suitable local environment for a more in-depth mechanistic study because ESPT is decelerated (e.g., versus water) to enable more scrutiny into multiple ESPT stages and competing pathways with sufficient temporal resolution. Moreover, we provide new concise guidelines in promoting photoacidity in a synergistic manner, i.e., incorporating EWGs into the electron donor moiety to lower pK_a and into the acceptor moiety to increase ΔpK_a.

5.2 Experimental

5.2.1 Synthesis

Commercially available reagents were used without additional purification. For column chromatography, E. Merck Kieselgel (silica gel) 60 was used. NMR spectra were recorded on a 700 MHz Bruker Avance III spectrometer at room temperature (RT=293 K). Chemical shifts were reported relative to residual peaks of DMSO-d_6 (2.51 ppm for ^{1}H and 39.5 ppm for ^{13}C). Melting points were measured on an advanced digital apparatus (Stuart SMP30). High-resolution mass spectra (HRMS) were recorded with an LTQ Orbitrap XL (ThermoFisher Scientific, USA) equipped with a dual-nebulizer electrospray ionization (ESI) source. The detailed synthesis steps are summarized in Figure 5.3 and presented in the ensuing sections (also see Chapter 4 for M2F synthesis).
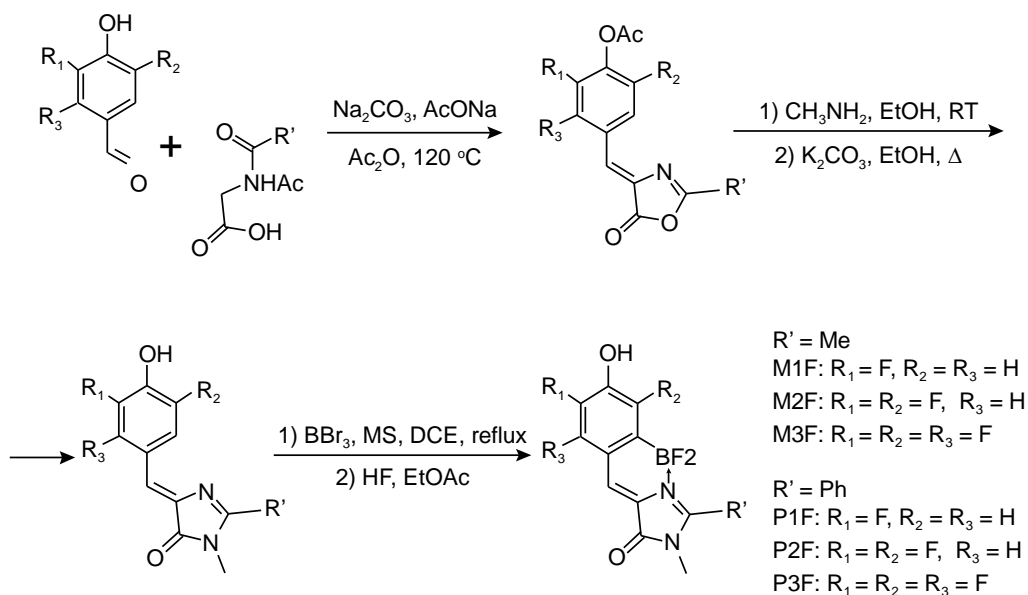
Figure 5.3. Synthesis of compounds MnF and PnF (n=1−3). Reproduced with permission from Cheng Chen et al., *J. Phys. Chem. B* **2019**, 123, 3804-3821. Copyright 2019 American Chemical Society.

Typical synthetic procedure for imidazolones. 1 mmol of corresponding fluorinated 4-hydroxybenzaldehyde, 1.1 mmol of hippuric acid or acetylglycine and 1.2 mmol (100 mg) of anhydrous NaOAc were dissolved in 1 ml of warm Ac_2O, then 1.3 mmol (140 mg) of anhydrous Na_2CO_3 was added. The mixture was stirred at 165ºC in inert atmosphere until no aldehyde was observed by thin-layer chromatography (TLC, typically 2–4 h). Reaction mixture was cooled, all volatiles were removed in vacuo. Residue was purified with flash chromatography (eluent-hexane-ethyl acetate 1:1). The crude product was used in the next stage without further purification.

The product of previous stage (1 mmol) was suspended in ethanol (10 mL) and mixed with aqueous methylamine (40%, 1.5 mmol). The mixture was stirred at room temperature for 2 h, potassium carbonate (10 mmol) was added and the mixture was refluxed for 8 h. The mixture was then dried on a rotary evaporator and dissolved in water (20 mL). With aqueous hydrochloric acid (10%), the solution was acidified to pH=6. The precipitate was filtered, washed by cold (–20°C) ethanol and diethyl ether and dried *in vacuo*.

Typical synthetic procedure for difluoroboryl imidazolones. The corresponding imidazolone (1.0 mmol) was dissolved in dry $C_2H_4Cl_2$ (50 mL), molecular sieves 4Å (3 g) and 3Å (3 g) added, which was followed by a solution of boron tribromide in $C_2H_4Cl_2$ (1M, 5.0 mmol). The reaction mixture was refluxed for 5 h in inert atmosphere, and then cooled and filtered; molecular sieves were washed twice with ethanol (10 mL) and $C_2H_4Cl_2$ (50 mL). The solution was mixed with aqueous HF (20%, 5 mL) and

stirred for 30 minutes. The mixture was dissolved in EtOAc (100 mL), washed with water (3×30 mL) and brine (3×30 mL) and dried over Na_2SO_4. The solvent was evaporated and the product was purified by column chromatography ($CHCl_3$/EtOH 10:1).

(Z)-4-(2-(difluoroboryl)-5-fluoro-4-hydroxybenzylidene)-1,2-dimethyl-1*H*-imidazol-5(4*H*)- one (**M1F**): yellow solid, ^{1}H NMR (700 MHz, DMSO-d_6) δ: 10.64 (s, 1H), 7.55 (s, 1H), 7.47 (d, *J*=12.1 Hz, 1H), 7.15 (d, *J*=9.4 Hz, 1H), 3.22 (s, 3H), 2.72 (s, 3H); ^{19}F NMR (564 MHz, DMSO-d_6) d: –138.97 (br. s), –138.23 (s).

(Z)-4-(2-(difluoroboryl)-3,5-difluoro-4-hydroxybenzylidene)-1,2-dimethyl-1*H*-imidazol- 5(4*H*)-one (M2F): yellow solid, ^{1}H NMR (DMSO-d_6) δ: 10.91 (s, 1H), 7.55 (s, 1H), 7.39 (d, *J*=10.5 Hz, 1H), 3.22 (s, 3H), 2.73 (s, 3H); ^{19}F NMR (564 MHz, DMSO-d_6) d: –138.06 (br. s), – 134.30 (d, *J*=14.31 Hz), –125.76 (dd, *J*=12.78, 5.62 Hz)

(Z)-4-(2-(difluoroboryl)-3,5,6-trifluoro-4-hydroxybenzylidene)-1,2-dimethyl-1*H*-imidazol- 5(4*H*)-one (**M3F**): dark yellow solid (98 mg, 31%), m.p. ~310 °C with decomposition; ^{1}H NMR (700 MHz, DMSO-d_6) d: 2.75 (s, 3 H), 3.23 (s, 3 H), 7.44 (s, 1 H), 11.56 (br. s., 1 H), ^{13}C NMR (151 MHz, DMSO-d_6) d: 13.2, 26.7, 111.5, 117.2, 126.4, 139.3 (dd, *J*=23.31, 12.19 Hz), 139.8 (ddd, *J*=242.66, 14.31, 7.42 Hz), 146.2 (dd, *J*=253.78, 10.07 Hz), 150.4 (dd, *J*=238.42, 2.65 Hz), 162.5, 167.9; ^{19}F NMR (564 MHz, DMSO-d_6) d: –157.55 (dd, *J*=17.36, 7.16 Hz), –144.66 (t, *J*=16.86 Hz), –137.73

(br. s.), −129.90 (s); HRMS (ESI) calculated for $C_{12}H_7BF_5N_2O_2$ ([*M*–H]⁻) 317.0526, found 317.0530.

(*Z*)-4-(2-(difluoroboryl)-5-fluoro-4-hydroxybenzylidene)-1-methyl-2-phenyl-1*H*-imidazol- 5(4*H*)-one (P1F): dark yellow solid (173 mg, 51%), m.p. ~310 °C with decomposition; ¹H NMR (700 MHz, DMSO-*d*₆) d: 3.09 (s, 3 H), 7.06 (d, *J*=9.21 Hz, 1 H), 7.53 (d, *J*=11.84 Hz, 1 H), 7.65 (t, *J*=7.65 Hz, 2 H), 7.73 (t, *J*=7.56 Hz, 1 H), 7.75 (s, 1 H), 7.87 (d, *J*=7.40 Hz, 2 H), 10.76 (br. s., 1 H); ¹³C NMR (151 MHz, DMSO-*d*₆) d: 28.0, 118.7 (d, *J*=16.95 Hz), 120.3, 124.0, 124.6 (br. s), 125.8, 128.0, 129.5, 129.9, 132.1, 149.4 (d, *J*=11.66 Hz), 150.2 (d, *J*=241.60 Hz), 162.9, 163.2; ¹⁹F NMR (564 MHz, DMSO-*d*₆) d: −138.29 (t, *J*=10.73 Hz), −134.81 (br. s); HRMS (ESI) calculated for $C_{17}H_{11}BF_3N_2O_2$ ([*M*–H]⁻) 343.0871, found 343.0871.

(*Z*)-4-(2-(difluoroboryl)-3,5-difluoro-4-hydroxybenzylidene)-1-methyl-2-phenyl-1*H*-imidazol-5(4*H*)-one (P2F): dark yellow solid (89 mg, 25%), m.p. 280–287 °C with decomposition; ¹H NMR (700 MHz, DMSO-*d*₆) d: 3.07 (s, 3 H), 7.47 (d, *J*=10.78 Hz, 1 H), 7.66 (t, *J*=7.74 Hz, 2H), 7.71–7.75 (m, 1 H), 7.75 (d, *J*=1.11 Hz, 1 H), 7.87 (d, *J*=7.19 Hz, 2 H), 10.92 (s, 1 H); ¹³C NMR (151 MHz, DMSO-*d*₆) d: 28.3, 115.4 (d, *J*=18.54 Hz), 123.6 (br. s), 124.0, 126.6, 128.2, 128.9, 129.6, 132.4, 137.9 (t, *J*=17.22 Hz), 151.3 (dd, *J*=240.54, 5.83 Hz), 154.6 (dd, *J*=241.07, 5.83 Hz), 163.1, 164.2; ¹⁹F NMR (564 MHz, DMSO-*d*₆) d: −134.31 (d, *J*=13.28 Hz), −133.11 (br. s.), −125.99 (t, *J*=12.27 Hz); HRMS (ESI) calculated for $C_{17}H_{10}BF_4N_2O_2$ ([*M*–H]⁻) 361.0777, found 361.0785.

(*Z*)-4-(2-(difluoroboryl)-3,5,6-trifluoro-4-hydroxybenzylidene)-1-methyl-2-phenyl-1*H*imidazol-5(4*H*)-one (P3F): dark yellow solid (98 mg, 31%), m.p. 277–282 °C with decomposition; ^{1}H NMR (700 MHz, DMSO-d_6) d: 3.08 (s, 3 H), 7.61 (s, 1 H), 7.66 (t, *J*=7.67 Hz, 2 H), 7.74 (t, *J*=7.53 Hz, 1 H), 7.87 (d, *J*=7.46 Hz, 2 H), 11.60 (br. s, 1 H); ^{13}C NMR (151 MHz, DMSO-d_6) d: 28.2 (s) 119.0 (br. s.) 123.6, 127.1, 128.1, 129.4, 132.4, 139.5 (dd, *J*=19.07, 10.60 Hz), 146.0 (dd, *J*=320.01, 16.42 Hz), 146.3 (dd, *J*=271.80, 8.48 Hz), 150.2 (d, *J*=235.77 Hz), 162.8 , 165.2; ^{19}F NMR (564 MHz, DMSO-d_6) d: –157.56 (dd, *J*=19.92, 9.71 Hz), –144.20 (t, *J*=16.86 Hz), –132.84 (br. s.), –130.08 (s); HRMS (ESI) calculated for $C_{17}H_9BF_5N_2O_2$ ([*M*–H]$^-$) 379.0683, found 379.0684.

5.2.2 Spectroscopic measurement and DFT calculations

The detailed description of our fs-TA and FSRS setups can be found elsewhere.[53] In short, both optical setups are based on a mode-locked Ti:sapphire oscillator and a laser regenerative amplifier (Coherent, Inc.), providing a ∼4 mJ, 800 nm fundamental pulse (FDP) with a 35 fs pulse duration and 1 kHz repetition rate of the output pulse train. In fs-TA, the 400 nm pump pulse is generated by the second harmonic of the 800 nm FDP, followed by temporal compression using a prism pair (06SB10, transmission range of 185 nm to 2.7 μm, Newport, Inc.). The probe pulse is a supercontinuum white light (SCWL) that is generated by focusing a portion of FDP onto a 3-mm-thick Z-cut sapphire plate, and then temporally compressed by a chirped mirror pair (DCM-9, 450−950 nm, Laser Quantum, Inc.). The cross-correlation time between pump and

probe pulses is measured to be ~60 fs via an optical Kerr effect of methanol solvent in a 1-mm-thick sample cuvette. The tunable FSRS consists of three incident pulses: a femtosecond actinic pump to initiate photochemistry that is generated and compressed in the same way as the pump in fs-TA; a ps Raman pump generated by a home-built two-stage noncollinear optical parametric amplifier (NOPA); a femtosecond Raman probe that is SCWL, generated and compressed in the same way as the probe in the fs-TA setup. We used a ~0.3 μJ/pulse, 400 nm actinic pump, and a ~1 μJ/pulse, 500 nm Raman pump, for the excited-state FSRS experiments. The 500-nm Raman pump was selected to achieve simultaneous resonance enhancement for the PA* and PB* species.

The ground- and excited-state vibrational frequencies for M3F and P3F were calculated by the DFT and TD-DFT methods, respectively, at the RB3LYP level with the 6-311G+(d, p) basis set using the Gaussian 09 software. The integral equation formalism variant polarizable continuum model (IEFPCM) was used to model methanol as the bulk solvent. The electron density maps of the frontier molecular orbitals (HOMO and LUMO) during vertical excitation can be visualized. The ΔpK_a values were calculated through the Förster equation by minimizing the electronic S_0 and S_1 energies of the neutral and anionic forms of the fluorophore. The corresponding DFT and TD-DFT molecular geometrical optimization calculations were also performed at the RB3LYP level with the 6-311G(d,p) basis set and IEFPCM water as solvent.

5.3 Results and discussions

5.3.1 Steady-state absorption and emission

The pK_a* estimation by the Förster equation shows that M3F and P3F are only slightly more acidic than M2F and P2F in the excited state, respectively. The spectral difference in photoacidity is hardly recognizable in water where all 2F and 3F photoacids undergo almost complete ESPT into PB*. In methanol, it is discernible that 3F is more acidic than 2F in both series (Figure 5.4a), and we hereby focus our data presentation on the fluorinated chromophores, particularly M3F and P3F. The PA*, PB* emission bands of MnF and PnF are centered around 480, 535 nm and 505, 565 nm, respectively, showing a notable red-shift from the methyl to the phenyl series.

In particular, M1F and P1F appear inefficient in delivering proton to methanol upon PA excitation. M2F (case reported, see Chapter 4) and P2F show rather stronger photoacidity, and a considerable portion of PA* converts to PB*. For comparison, M3F and P3F undergo deprotonation in methanol to a much greater extent, confirming a photoacidity that is stronger than that of their 2F counterparts. Notably for the trifluorinated derivatives, the PB* emission band of P3F is redder (by ∼33 nm, see Table S1) and broader (by ∼32% after converting the nm to cm^{-1} unit, i.e., ∼1315 and 1000 cm^{-1} full width at half-maximum (fwhm) in P3F and M3F, respectively, see Figure 5.4b) than that of M3F due to a more pronounced ICT in the former that grants extra stability to its electronic excited state and likely a more inhomogeneous PB* population. One further piece of evidence to support the enhanced excited-state ICT in P3F (i.e., not just a larger distribution of ground-state conformers of P3F than M3F)

arises from the peak width analysis of the electronic absorption spectra in Figure 5.4b, wherein the PA absorption band of P3F (fwhm ≈ 4065 cm^{-1}) has essentially the same width as that of M3F (fwhm ≈ 3930 cm^{-1}).
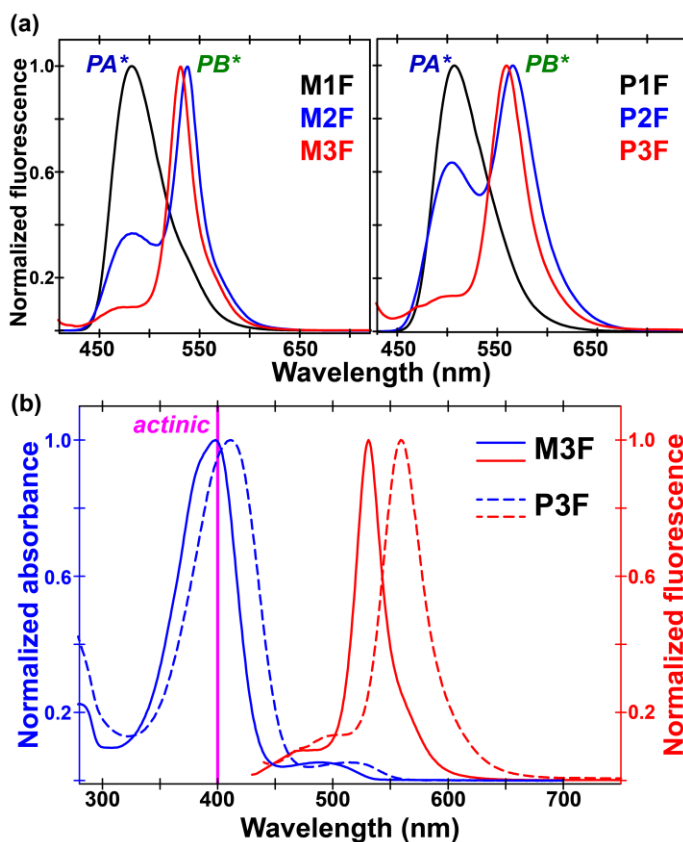
Figure 5.4. Steady-state electronic spectra of MnF and PnF (n=1, 2, 3). (a) Normalized emission spectra of 1F (black), 2F (blue), and 3F (red) of the methyl and phenyl series in methanol upon photoexcitation of the protonated form. (b) Normalized absorption (blue) and emission (red) spectra of M3F (solid line) and P3F (dashed line) in methanol. The emission spectra are obtained by exciting the protonated form at ~400 nm. The excitation wavelength at 400 nm for fs-TA and FSRS is denoted by the magenta vertical line. Reproduced with permission from Cheng Chen et al., *J. Phys. Chem. B* **2019**, 123, 3804-3821. Copyright 2019 American Chemical Society.

5.3.2 ESPT dynamics from fs-TA

The fs-TA spectroscopy monitors excited-state electronic dynamics following 400 nm excitation that prepares the PA* population at time zero. It is worth noting that because M3F has much weaker ESA bands than its SE bands while P3F has strong ESA bands comparable to its SE bands, we had to set different colors at ΔOD=0 for M3F (Figure 5.5a, set with light red) and P3F (Figure 5.5b, set with yellow) to achieve the best contrast for the positive and negative features without color saturation. The TA spectra of M3F in methanol are dominated by stimulated emission (SE) bands from 450 to 600 nm, consisting of two regions corresponding to PA* and PB* (Figure 5.5a) as supported by the emission peaks in Figure 5.4b. The PA* SE band peaks at 450−500 nm while PB* appears within ca. 500−600 nm. The shoulder band located between 560 and 580 nm is due to a vibronic progression which also exists in some fluorescent proteins[54,55] and synthetic chromophores[56] with the *p*-HBDI core. Both the PA* and PB* SE bands red-shift with time, indicating some relaxation processes within PA* and PB* states as the photoexcited chromophore undergoes various energy dissipation pathways. The initial step of the ESPT reaction occurs within the first 1 ps when the PA* SE band starts to convert into the PB* SE band. P3F exhibits similar TA features except for the stronger excited-state absorption (ESA) bands and redder SE bands (Figure 5.5b). In comparison to M3F, the PB* SE band of P3F is markedly broadened likely due to the formation of an ICT or twisted ICT (TICT) state with a flexible side-chain phenyl group linked to the conjugated chromophore ring backbone,[45,57] consistent with the aforementioned broader steady-state fluorescence emission peak for P3F than M3F (Figure 5.4b). This observation is also in accord with all the experimental ensemble-

average measurements so contributions from multiple species or adjacent states could overlap in the spectral domain.
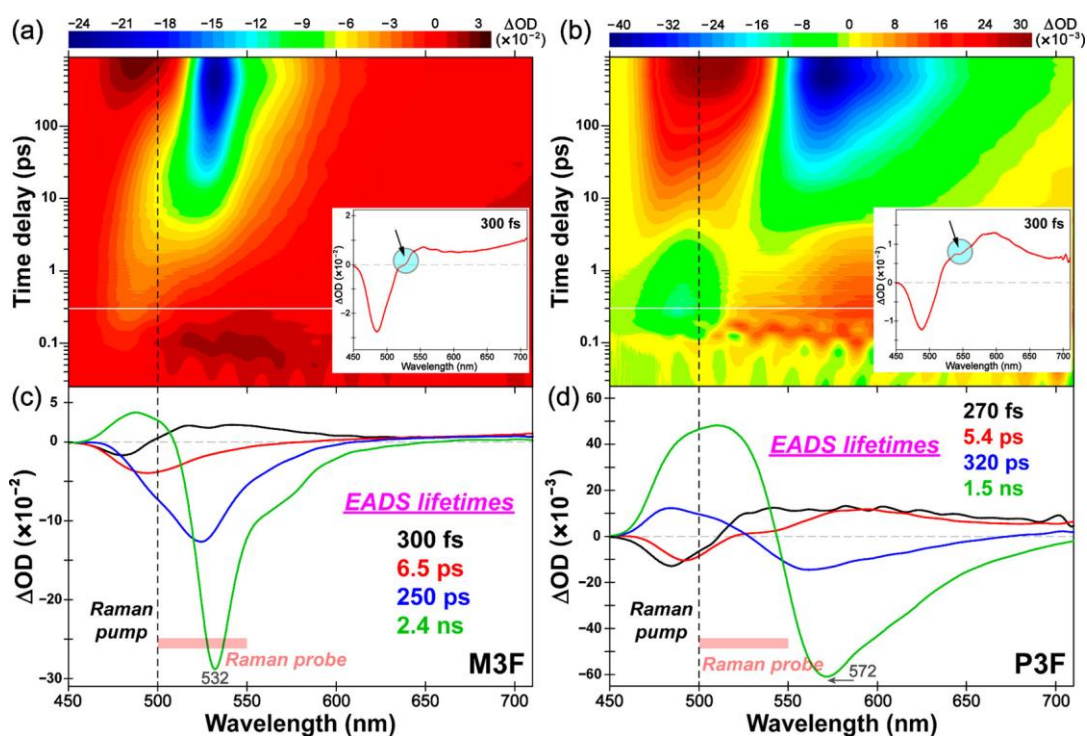
Figure 5.5. Semilogarithmic contour map and global analysis of the fs-TA spectra for (a) M3F and (b) P3F in methanol with 400 nm photoexcitation. The spectrum at 300 fs time delay is shown in the inset where the arrow denotes the PB* SE band seen from the curvature. Global analysis yields four stepwise components termed as evolution-associated difference spectrum (EADS) in the order by color (black, red, blue, green) with their characteristic lifetime constants listed. For subsequent FSRS experiments, the Raman pump at 500 nm and the broadband Raman probe are denoted by the black dashed line and the semitransparent light-red rectangle in parts c and d for M3F and P3F, respectively. Reproduced with permission from Cheng Chen et al., *J. Phys. Chem. B* **2019**, 123, 3804-3821. Copyright 2019 American Chemical Society.

To deconvolute the overlapping band dynamics in fs-TA, global analysis[58] was performed using Glotaran[59] following a sequential kinetic scheme wherein the system is assumed to evolve in a stepwise fashion. This scheme is closely tied to reaction dynamics from the photoreactant to product due to deprotonation events at the chromophore phenolic hydroxyl end, although it is conceivable that multiple H-bonded complexes with a range of intermolecular distances between proton donor and acceptor could exist (i.e., starting from the electronic ground state).[1,46,60] On the other hand, although the decay-associated difference spectra (DADS) could also provide important information about the involved states or species, DADS do not consider transitions between different states of the same species,[58,61] which cannot completely model our current molecular system wherein ESPT involves reactions from the acid form to its conjugate base. Such limitations of the DADS analysis can be visualized for the photoexcited M3F and P3F in methanol (Figure 5.6), and the two obtained long-lifetime components exhibit largely mirrored profiles due to inaccuracy of the purely parallel model. There may exist some sophisticated pathways or complex kinetic schemes, such as branching coupled with sequential ones, which might be the case in the current system. In essence, when the system does not evolve in a purely sequential or parallel manner, neither EADS nor DADS can represent true species spectra. Moreover, a complicated target analysis with parallel ESPT modeling could not converge likely due to the intrinsic spectral overlap issues and lack of details about certain population ratios and the pertinent electronic transition oscillator strengths along the ESPT reaction coordinate.[13,58] Notwithstanding, DADS analysis still corroborates the EADS analysis in exposing the main transient electronic dynamics,

particularly about the gradual red-shift of the SE band from the PA* species via some

intermediates to the PB* species, which is the main fluorescent species.
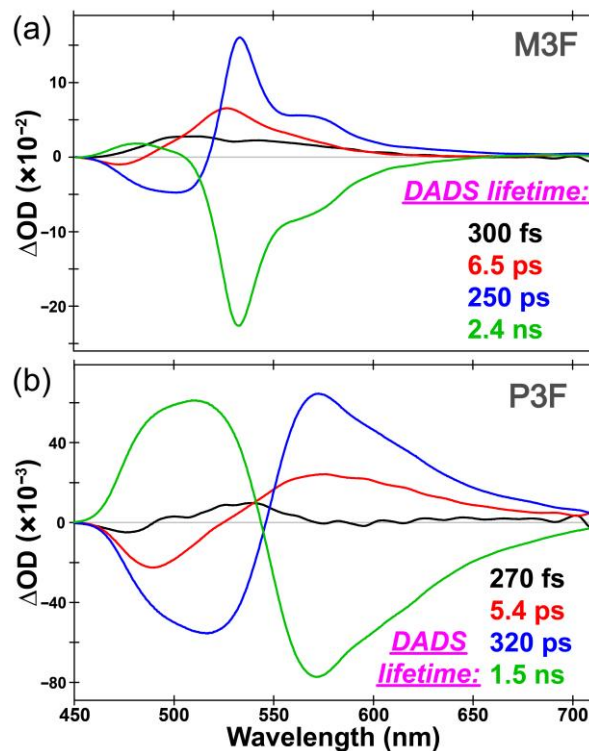
Figure 5.6. Decay-associated difference spectra (DADS) of the fs-TA spectra for (a)

M3F and (b) P3F in methanol after 400 nm photoexcitation. The parallel kinetic model

yields four underlying components with their individual lifetimes listed, color coded

with their corresponding spectra (black, red, blue, and green). Reproduced with

permission from Cheng Chen et al., *J. Phys. Chem. B* **2019**, 123, 3804-3821. Copyright

2019 American Chemical Society.

Four EADS components are uncovered to provide rich insights into the ESPT dynamics

(Figure 5.5). The first EADS (black trace) featured by a PA* SE band at ~481 nm for

M3F and 484 nm for P3F is attributed to the locally excited state (LE) generated by the 400 nm photoexcitation pulse. Its sub-picosecond lifetime represents the formation time of a transient CIP, which is usually referred to as the intrinsic ESPT rate.[5,62] P3F (~270 fs) has a slightly faster time constant than M3F (~300 fs) in terms of this initial stage. The second EADS (red trace) exhibits a red-shifted SE band (M3F, ~494 nm; P3F, ~491 nm) due to the formation of CIP with some charge-separated (CS) character. Notably, this intermediate or CIP mainly resembles PA* in both cases of M3F and P3F considering the proximity of their SE band positions, while the PB* electronic feature is largely absent in the longer-wavelength region. In contrast, the known strongest photoacid QCy9 has a PB*-like intermediate[63] which might suggest a different solute−solvent electronic structure or ESPT mechanism. We note that the CIP was originally invoked to model the proton transfer process and defined as a solvent-stabilized ion pair after rapid short-range charge separation, followed by diffusion-controlled further ion separation.[5,6,21,64] In recent years, the superphotoacid studies have required modification of this model when solvent reorientation becomes the rate-limiting step.[1,13,24] Therefore, superphotoacidity drives proton separation, but the unoptimized local H-bonding configuration could trap the population in an intermediate state. In many cases, this intermediate state is spectrally recognizable and shows a discernible spectral shift in comparison to the Franck−Condon species, while it likely involves slight O−H bond lengthening along the H-bonding chain.[13,65] In this work, the intermediate species shows a redder SE band wavelength when compared to the vertically excited PA* species (Figure 5.5) but still retains PA* character given the proximity of their SE band wavelengths. A detailed comparison between the

intermediate SE band maximum position and the PA* and PB* emission peak wavelengths of M3F and P3F in water (*vide infra*) further corroborates the CIP formation en route to complete proton transfer on longer time scales, and the spectral distinction between the CIP state and a relaxed PA* state. Such a scheme is applicable for strongly interacting systems like superphotoacids in polar and protic solvents, because the distinguishing definition of photoinduced reactant (PA*) and product (PB*) cannot be based on the whole charge but rather the electron density distribution within an H-bonding complex wherein the donor, proton, and acceptor wave functions have noticeable overlap.

The dual SE band in the third EADS (blue trace) of M3F indicates the occurrence of deprotonation and is assigned to a solvation process. This assignment can be rationalized by the further red-shifted SE band from CIP as well as the second EADS lifetime of ~6.5 ps, in close agreement with the characteristic solvation time of methanol.[3] The shorter-wavelength SE band of the doublet of P3F is not apparent because it may be hidden under the large PB* ESA profile between ca. 450 and 540 nm. Such an interpretation is further corroborated by global analysis of M3F and P3F in pH=3 aqueous solution (see below as a control experiment, more details in Figure 5.10 after the discussion of the superphotoacid in alcohol experiments) where the lifetime is 1.9 and 1.5 ps, respectively, in agreement with the average solvation time of water.[3,5] However, due to the presence of the residual population of the solvated CIP (with PA* character) at this stage, the deprotonation process has not reached completion. The photoexcited chromophore may undergo a longer ESPT process

presumably through diffusion events (likely rotational diffusion due to the pertinent long lifetime,[64] see below for details) on the time scale of hundreds of picoseconds (250 ps for M3F and 320 ps for P3F) before arriving at the emissive PB* state as denoted by the fourth EADS (green trace). Our previous study of M2F in methanol provided evidence for the diffusion-assisted PT of this step using isotopically labeled solvents, so this work was designed to focus on the difference between M3F and P3F in the same organic and protic solvent. Moreover, the observed SE band red-shift during this process implies the lowering of the excited-state potential energy surface (PES) caused by rotation of solute molecules that could be accompanied by other relaxation processes such as the solvent dielectric (or Debye) relaxation.[66] The fourth EADS involves the effective fluorescence lifetime of a relaxed PB* state, but not just fluorescence. The shorter lifetime of P3F (1.5 ns) than M3F (2.4 ns) is caused by the additional nonradiative decay pathways enabled by the flexible side-chain phenyl ring at the imidazolinone end, corroborated by the smaller FQY of P3F (0.37) than M3F (0.42) measured in methanol after 400 nm excitation.

We note that global analysis of fs-TA spectra in this work assumes a sequential route wherein one state unidirectionally evolves into another. Essentially, other models such as branching from an intermediate state are not considered. If these competing or intrinsic pathways do exist, global analysis cannot be considered as an accurate or complete description of the ESPT dynamics. Instead, target analysis with a specific model should be beneficial. In fact, our previous M2F work unveiled a bifurcated ESPT mechanism through target analysis, evinced by the prompt growth of PB* after the

formation of a CS (or CIP) state. For M3F and P3F, similar spectral features are observed and the initial PB* population appears right after CIP formation on the time scale of ~300 fs (marked by cyan circles and black arrows in the inset, Figure 5.5a and 5.5b), in parallel to the solvation-limited ESPT pathway on the few picosecond time scale. Therefore, it is reasonable that faster ESPT channels are present due to the pre-existing or largely optimized H-bonding wires between the photoacid and adjacent solvent molecules, while the highly efficient ESPT occurs via moving the proton over a small distance within a tightly bound complex on the ~150 fs time scale.[4,20,21,24] In comparison to M2F with the second EADS showing an ~8 ps lifetime, the shorter lifetimes of 6.5 ps in M3F (Figure 5.5c) and 5.4 ps in P3F (Figure 5.5d) could represent the averaged time constants of branching pathways, which suggest that the weight of the fast ESPT channel on the sub-picosecond time scale becomes larger in the order of M2F, to M3F, to P3F. Therefore, the swift CS state and CIP formation (still with significant PA* character as shown by the second EADS in Figure 5.5c and 5.5d) on the ~300 fs time scale can be considered as a common preparatory step for all the subsequent ESPT pathways (vide inf ra, also see the Abstract graphic for a summary scheme). Nevertheless, global analysis provides a good overview of dominant processes on ultrafast time scales and reveals the important role of solvent activity in the ESPT process of photoacids and superphotoacids.

5.3.3 ESPT dynamics from FSRS: intensity dynamics

Following 400 nm excitation to promote the PA* populations, FSRS spectra at different time delays were collected at the Stokes side with the Raman pump (R_{pu}) wavelength of 500 nm. Figure 5.7a and 5.7b presents the non-equilibrium excited-state FSRS spectra of M3F and P3F in methanol, respectively, where both PA* and PB* modes were observed. In the M3F spectra (Figure 5.7a), a 1575 cm^{-1} mode is assigned to PA* due to its prompt appearance after photoexcitation, followed by intensity decay. Several PB* marker modes at 1566, 1370, 1260, and 953 cm^{-1} with a largely absorptive line shape show rise dynamics (i.e., peak intensity magnitude increases) on the time scale of hundreds of picoseconds after an initial dwell time of ~2 ps. In the P3F spectra (Figure 5.7b), a number of pronounced PA* modes (e.g., 1355, 1404, 1553, 1606, 1630 cm^{-1}) were observed while the 1355 cm^{-1} mode exhibits the best SNR. Two prominent PB* modes appearing at 1414 and 1184 cm^{-1} with a clear positive sign exhibit rise dynamics (i.e., getting more positive) on the few to hundreds of picoseconds time scales.

Regarding the contour color selection in Figure 5.7a and 5.7b, we remark that since M3F exhibits both positive and negative features while P3F has mostly positive features throughout the PA* → PB* transition following photoexcitation, it is difficult to simply set zero intensity at the same color (e.g., green or blue) without losing the necessary contrast. Our current spectral data presentation aims to enhance the visual perception of transient Raman mode intensity change as an ultrafast ESPT reaction proceeds from the photoinduced reactant to product in real time.
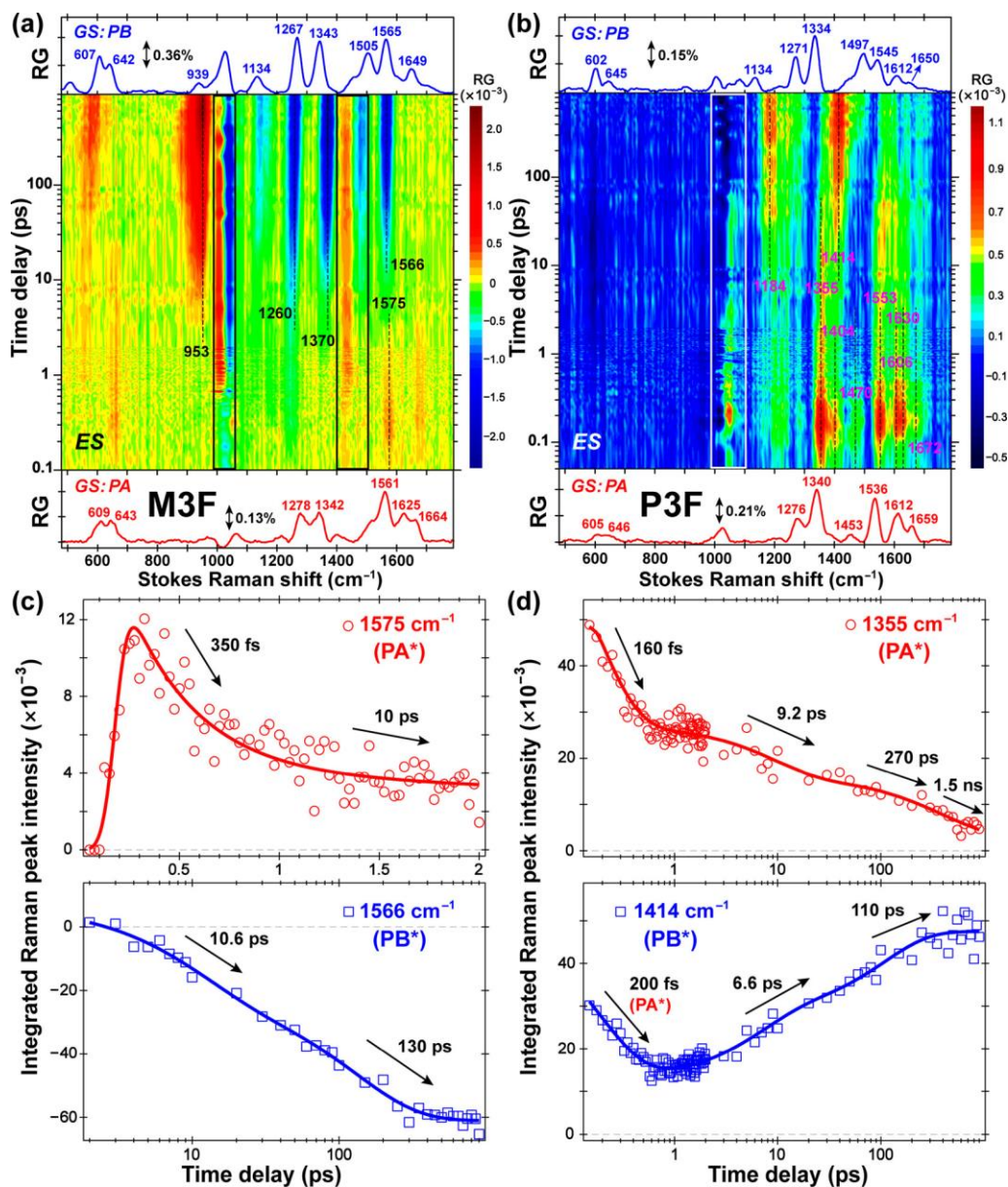
Figure 5.7. Semilogarithmic 2D contour map of the time-resolved Stokes FSRS spectra of (a) M3F and (b) P3F in methanol following 400 nm photoexcitation. The Raman pump wavelength is 500 nm. The marker band intensity dynamics of PA* and PB* are plotted with least-squares fitting in parts c and d, respectively. The time constants are listed by their respective black arrows. The ground-state FSRS spectra of PA and PB are plotted below (red) and above (blue) the 2D contour plots in parts a and b for comparison (see Figure 5.11 for details). The Raman pump wavelengths for the ground-

state FSRS of PB species are tuned to 560 and 590 nm for M3F and P3F, respectively. The solvent-influenced regions are highlighted by the black and white rectangle boxes in parts a and b, respectively. Reproduced with permission from Cheng Chen et al., *J. Phys. Chem. B* **2019**, 123, 3804-3821. Copyright 2019 American Chemical Society.

The least-squares multiexponential fit was performed for the excited-state Raman peak intensity. Two or more components were obtained for both PA* and PB*, providing a coherent description of the underlying ESPT process (Figures 5.7c and 5.7d). The 1575 cm^{-1} PA* mode of M3F shows fast decay within the first 1 ps and yields two time constants of ~350 fs and 10 ps with amplitude weights of ~72% and 28%, respectively. The 350 fs component is consistent with the global analysis result of TA spectra (Figure 5.5c, first EADS with a lifetime of ~300 fs) and therefore assigned to the initial charge separation or small-scale protolytic dissociation due to the photoinduced increased acidity. Though there is no quantitative definition of how much a distance change can be viewed as "small scale" because it intimately depends on the photoacid electronic structure as well as the electronic coupling between the reactant and product states, we consider that the small-scale proton separation should be less than a few tenths of an angstrom (Å).[65] For instance, modest H-bond strength is achieved at an O···O distance of ~2.7 Å,[67] while a typical O−H bond length is ~1 Å. The small-scale proton motion along an H-bond could then be estimated with an upper bound of 0.35 Å (i.e., 2.7 Å/2−1 Å) with equal sharing of the proton at the middle point, and the actual proton motion should be much less than this value given the PA*-like intermediate (e.g., CIP).

The 10 ps component largely matches the methanol solvation time that limits the further ESPT reaction rate, rather than the nonradiative deactivation such as internal conversion, because the similar time constant is observed in the rise of PB* modes. Moreover, the locked chromophore ring structure should significantly inhibit the nonradiative decay channels in solution. Several PB* modes show similar biphasic dynamics (Figure 5.7c, note the negative sign so it represents an increase of mode intensity magnitude). The excited-state vibrational mode assignment and dynamics fitting results are provided in Table 5.1. The fast component with a time constant of ca. 10−20 ps across different vibrational modes suggests that solvent molecular reorientation is the rate-limiting step for large-scale deprotonation. The slow component of ca. 90−260 ps reflects a further ESPT step likely assisted by diffusion and also accompanied by other relaxation processes such as solvent Debye relaxation. The variation in this time constant of different PB* modes suggests the mode-dependent sensitivity to solute−solvent interactions during ESPT, in accord with an anisotropic chromophore molecule pushing away a terminal proton at one end. Such mode dependence is also observed in the fast component but to a lesser extent.

In contrast, the PA* modes of P3F exhibit better SNR with a 500 nm R_{pu}, and in particular, the 1355 cm^{-1} is the best-resolved mode which shows multistage dynamics (Figure 5.7d, Table 5.2). The first two components of ∼160 fs (57%) and 9.2 ps (18%) are similar to the 1575 cm^{-1} mode of M3F (Figure 5.7c) and are attributed to the initial charge separation (or CIP formation) and solvation, respectively. The third and fourth time constants (270 ps, 13%, and 1.5 ns, 12%) are in excellent agreement with the

global analysis of TA spectra, further consolidating the essential role of the diffusion-assisted ESPT (270 ps) channel to methanol (Figure 5.5) before fluorescence. Other PA* modes do not show as high an SNR as the 1355 cm^{-1} mode; therefore, only one component can be resolved on the sub-picosecond time scale. Spectral overlap with the emerging PB* modes on the few picoseconds time scale also occurs for some PA* modes due to their close frequencies (Table 5.2). As a result, the strongest PB* mode at 1414 cm^{-1} overlaps with the PA* mode at 1404 cm^{-1} at early times (Figure 5.7b and 5.7d). The initial ~200 fs decay time constant from least-squares fitting is ascribed to the overlapping PA* 1404 cm^{-1} mode, while the PB* 1414 cm^{-1} mode dominates after ~1 ps with biexponential rise dynamics. The two pertinent rise time constants of ~6.6 and 110 ps track the solvation- and diffusion-controlled PT steps, respectively. Another PB* mode at 1184 cm^{-1} yields two notably longer time constants of ~10.5 and 172 ps, reminiscent of the nonuniform time constants in the PB* modes of M3F. These results manifest the subtle difference among different vibrational degrees of freedom along the multidimensional reaction coordinate[46,68] even for a single hydroxyl (−OH) bond breaking reaction. Though this work focuses on dynamics contrast between M3F and P3F in methanol, our previous study on M2F in deuterated methanol (CD_3OD) confirmed the assignment of these time constants to several ESPT reaction steps.[13]

Table 5.1. Excited-state Raman mode dynamics and assignments for M3F in methanol.

	FSRS freq. (cm^{-1})	Calc. freq.^{a} (cm^{-1})	Dynamics		Mode assignment (major motions)^{c}
			τ_1(ps)/ $A_1{}^{b}$	τ_2(ps)/ $A_2{}^{b}$	
PA*	1575	1618	0.35/0.72	10.0/0.28	Phenolic $C_{5'}=C_{6'}$, $C_{2'}=C_{3'}$ stretching, COH rocking
PB*	1566	1577	10.6/0.37	131/0.63	Phenolic $C_{5'}=C_{6'}$, $C_{2'}=C_{3'}$ stretching; bridge C=C stretching
	1370	1354	11.2/0.37	90/0.63	Imidazolinone C_4-N_3 stretching, ring deformation; weak phenolate ring deformation; bridge H rocking
	1260	1254	18.3/0.37	261/0.63	Phenolate ring deformation; bridge H rocking; imidazolinone ring deformation, methyl (N_1) twisting
	953	950	13.0/0.25	163/0.75	Middle ring C–C (C–phenolate) stretching, ring deformation; imidazolinone ring deformation, methyl (N_1) twisting

^{a}The normal mode scaling factor is 0.975.

^{b}The double-exponential time constants τ_i and amplitude weights A_i (i =1, 2) from the least-squares fit of the observed excited-state vibrational mode intensity dynamics.

^{c}The motions on separate rings (phenolic, middle or bridge, imidazolinone) are described in the order of prominence from normal mode calculations.

Table 5.2. Excited-state Raman mode dynamics and assignments for P3F in methanol.

	FSRS freq. (cm^{-1})	Calc. freq.^{a} (cm^{-1})	Dynamics (τ_1(ps)/A_1^b)	Mode assignment (major motions)^c
PA*	1664	1649	0.36/1.00	Imidazolinone C=O stretching.
	1630	1625	–	Phenolic C$_{5'}$=C$_{6'}$, C$_{2'}$=C$_{3'}$ stretching, COH rocking.
	1606	1567	0.32/1.00	Phenyl ring symmetric C=C stretching and ring-H scissoring
	1553	1539	0.15/1.00	Phenyl asymmetric ring-H rocking and C–C stretching
	1470	1485	0.40/1.00	Phenyl symmetric ring-H rocking; phenolic COH rocking, C$_2$=C$_3$ stretching; imidazolinone methyl bending; bridge H rocking
	1404	1411	0.20/1.00	Phenolic ring breathing, C–O stretching; bridge H rocking; imidazolinone N$_3$–C$_4$ stretching; phenyl ring-H rocking.
	1355	1361	0.16/0.57; 9.2/0.18; 270/0.13; 1500/0.12	Imidazolinone C$_4$–N$_3$ stretching, ring deformation, methyl bending; bridge H rocking; phenolic COH rocking; phenyl ring-H rocking
PB*	1184	1180	10.5/0.67; 173/0.33	Phenyl symmetric ring-H scissoring
	1414	1410	6.6/0.45; 110/0.55	Phenyl ring-H rocking; imidazolinone C$_2$-phenyl stretching, methyl bending

^{a}The normal mode scaling factor is 0.975.

^{b}The single- or multi-exponential time constants τ_i and amplitude weights A_i from the least-squares fit of the observed excited-state vibrational mode intensity dynamics.

^{c}The motions on separate rings (phenolic, middle or bridge, imidazolinone) are described in the order of prominence from normal mode calculations.

5.3.4 ESPT dynamics from FSRS: frequency dynamics

When compared with the FSRS peak intensity that is an extensive property subject to resonance condition, pulse power, and sample concentration, the observed vibrational mode frequency in FSRS is an intensive property that does not change with the aforementioned experimental conditions and therefore provides important insights into the intrinsic ESPT process.[46,47] In particular, the vibrational frequency blue-shift usually implies vibrational relaxation through intra- or intermolecular degrees of freedom or structural changes in some occasions. We found that two PB* modes of M3F at 1260 and 1370 cm^{-1} (these mode frequencies were taken at 900 ps when the PB* species are largely relaxed in S_1) significantly blue-shift in frequency, concomitant with the mode intensity rise (Figure 5.7a and Table 5.1). The biexponential fit yields two time constants comparable to the intensity dynamics (Figure 5.8a and 5.8c). We exclude the possibility of structural change-induced blue-shift considering the rigid skeleton of M3F. The observed blue-shift likely arises from the relaxation of excess vibrational energy of the deprotonated chromophore following ESPT, corroborated by the temporal dwell of ~2 ps when sufficient SNR for the PB* species allows the dynamic fit of the mode integrated intensity and center frequency. In essence, the chromophore must dissipate energy by interacting with the external solvent and internal vibrational, rotational, and translational degrees of freedom. The close match between frequency and intensity dynamics elucidates two well-resolved solvation- and diffusion-controlled ESPT regimes for the superphotoacids like M3F in alcohols where the excited-state PES is stabilized through vibrational relaxation, in accord with the PB* SE band red-shift in the time-resolved TA spectra (Figure 5.5a).
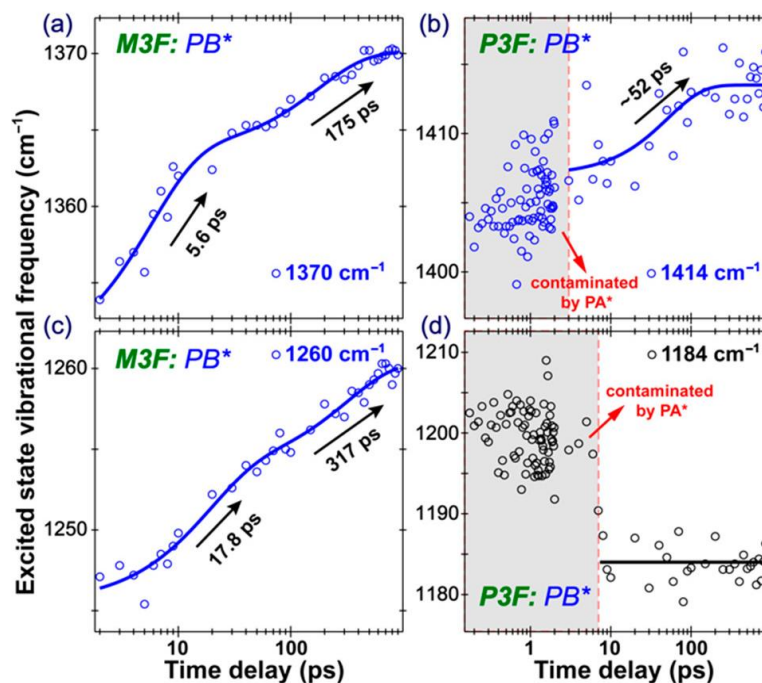
Figure 5.8. Excited-state vibrational frequency dynamics for the PB* modes of M3F and P3F in methanol. The biexponential fit time constants are shown for the ~1370 and 1260 cm^{-1} modes in parts a and c for M3F. The gray areas in parts b and d for P3F denote the temporal range when the overlapping PA* mode dominates and contaminates the PB* mode frequency dynamics. Reproduced with permission from Cheng Chen et al., *J. Phys. Chem. B* **2019**, 123, 3804-3821. Copyright 2019 American Chemical Society.

In P3F, the ~1184 cm^{-1} PB* mode does not exhibit a blueshift at time delays after ~7 ps while the early time frequency determination is contaminated by the overlapped more intense PA* mode centered around 1200 cm^{-1} (Figure 5.8d). The strongest PB* mode at 1414 cm^{-1} shows a slight blue-shift, and the observed frequency at time delays

before ~3 ps is "pulled" by the nearby ~1404 cm^{-1} PA* mode, leading to a shorter time constant (~52 ps, Figure 5.8b) than its intrinsic value. On the other hand, a readily available side-chain phenyl ring twisting motion could introduce a red-shift and complicate the observed frequency dynamics of these two modes. Notably, both PB* marker bands involve ring-H bending motions on the phenyl ring according to the TD-DFT calculations (Table 5.2). To examine the effect of conformational change on the mode frequency (focusing on the trend) at a reasonable computational cost, we performed DFT calculations with a range of dihedral angles fixed between the backbone imidazolinone and side-chain phenyl rings of P3F in the PB form solvated by methanol. The calculated Raman mode frequency red-shifts (by ~30 cm^{-1}) from 0° toward 80° or −80° for the 1184 cm^{-1} mode, but it remains largely unchanged (within ~7 cm^{-1}) for the 1484 cm^{-1} mode except for the 0° starting geometry. The resultant frequency shift trend from quantum calculations qualitatively demonstrates that (1) the observed 1484 cm^{-1} mode frequency blue-shift arises from vibrational relaxation during ESPT on the few picoseconds to hundreds of picoseconds time scales, and (2) the observed stagnant 1184 cm^{-1} mode frequency could be reflective of a cancellation effect by two competing processes: a blue-shift due to vibrational cooling and a red-shift due to sidechain phenyl ring twisting.[12,46,54] This dynamic conformational twisting in the excited state is in accord with the formation of a TICT state in P3F that could help increase the nonradiative energy relaxation back to the electronic ground state (hence smaller FQY than M3F).

5.3.5 Resonance enhancement and line shape analysis

The power of wavelength-tunable FSRS lies in the experimental capability of selectively probing the molecular/reaction species of interest via resonance enhancement due to the four-wave mixing mechanism in the nonlinear spectral signal generation.[46,69,70] In brief, the stimulated Raman signal intensity can be significantly enhanced by tuning the R_{pu} to be on or close to resonance with electronic transitions, e.g., the ground-state absorption bands for the equilibrium species,[71] or the ESA and SE bands for the excited-state species.[70,72] In this work, the Rpu was tuned in between the SE bands of PA* and PB* (Figure 5.5) so we could achieve decent resonance enhancement for both the PA* and PB* species within one 2D spectral window. This is equivalent to performing an in operando experiment because the spectroscopic characterization occurs during the photochemical reaction (i.e., ESPT for the photoacid) that governs its macroscopic function (fluorescence in this case). The excited-state FSRS spectra of M3F and P3F were collected on the Stokes side with the same R_{pu} at 500 nm. The Raman modes with decay and rise dynamics on ultrafast time scales are clearly observed, corresponding to the photoreactant (PA*) and photoproduct (PB*) species, respectively (Figure 5.7).

Notably, some complexity is observed about the FSRS line shape, which is listed as follows. (1) The PA* modes of both M3F and P3F show a positive sign (Raman gain) due to the resonance condition using a red-sided R_{pu} with respect to the PA* SE band.[72] (2) The high-frequency PB* modes (>1000 cm^{-1}) of M3F exhibit a negative sign (Raman loss) while those of P3F are positive. This is because the Raman probe (R_{pr}) is

located at different sides of the resonant electronic band with a blue-sided R_{pu} in these two cases. Regarding M3F, the negative sign originates from a unique resonance condition that R_{pu} is located at the blue side of the PB* SE band while the R_{pr} wavelengths that correspond to high-frequency modes are at the red side of that SE band.[13] For example, the R_{pr} photon that leads to the observed 1566 cm^{-1} mode with a 500 nm R_{pu} can be found at 542.5 nm, which is redder than the PB* SE band maximum of 532 nm (reddest at 900 ps). In contrast for P3F, both the R_{pu} and R_{pr} wavelengths for modes below 2000 cm^{-1} are bluer than the PB* SE band maximum of 572 nm (reddest at 900 ps). Consequently, the same-sided R_{pu} and R_{pr} to an SE band with pre-resonance conditions could lead to positive FSRS signals. It is also plausible that the resonance with a PB* ESA band contributes to the positive sign in P3F as the R_{pu} is located around the ESA band maximum. This resonance condition[70] has been previously reported to generate positive signals on the Stokes FSRS side for a photoacid in solution.

To provide further insights into which the aforementioned resonance factor is mainly responsible for the observed FSRS signal sign, we performed a control experiment for P3F in methanol with the R_{pu} tuned to 540 nm. The observed low-frequency modes (<1000 cm^{-1}) become negative (see original publication). Because 540 nm remains pre-resonant with (i.e., on the red side of) ESA, the positive signal (Raman gain) should be expected for low-frequency modes if the resonance enhancement with ESA dominates; however, we observed the negative signal (Raman loss). Therefore, the resonance with an SE band constitutes the major contribution to the FSRS signal in P3F. One may find that, for the Raman modes <1000 cm^{-1}, the negative sign corresponds to R_{pu} at 540 nm

and R_{pr} at <571 nm, which are bluer than the apparent SE band maximum at 572 nm. This observation seems to contradict the abovementioned PB* Raman gain signal for P3F with the 500 nm R_{pu} (Figure 5.7b). However, this discrepancy can be rationalized by the actual PB* SE band maximum that is bluer than the apparent value due to a strong overlap between the prominent ESA and SE bands (Figure 5.5d). In essence, the visible difference between the PA*, PB* spectral patterns and peak evolution in Figure 5.7a and 5.7b for M3F and P3F substantiates the intimate dependence of the FSRS signal on resonance conditions including both the Raman pump and probe pulses.[13,71,72]

5.3.6 Heterogenous ESPT pathways

A typical ESPT reaction can be described by the Eigen-Weller model, which involves a two-step mechanism consisting of an initial small-scale proton transfer into CIP and a following diffusion-controlled further proton separation into free anions.[4-6,21,46,52] This model works well particularly for weak or moderate photoacids but needs to be revised for superphotoacids in which solvent reorientation becomes the rate-limiting step. In general, an ESPT reaction can be understood along two coordinates: the proton transfer coordinate and the solvent coordinate.[15,73] The former is determined by the intrinsic photoacidity which dictates the proton transfer rate. The latter reflects the reaction barrier exerted by surrounding solvent molecular reorientation in order to adapt to the altered dipole moment of the photoacid from the ground to the excited state. When the solvent motion is slower than the proton motion, the former is the rate-limiting step and vice versa. For superphotoacids, the intrinsic/local proton transfer rate

is so fast that solvation becomes the apparent rate-limiting step. Therefore, the solvation-limited ESPT can be another characteristic property of superphotoacids. One exception is the cyanine-derived superphotoacids, e.g., QCy9 that was reported to go beyond the solvent control limit (see Chapter 9.1 below).

M3F and P3F are solvation-limited superphotoacids based on our series of steady-state (Figure 5.4) and time-resolved excited-state (Figures 5.5, 5.7, 5.8) spectroscopies. The FSRS intensity dynamics of different PB* modes yield consistent time constants within 10−20 ps for the solvation-influenced PT step, close to but slightly longer than the longitudinal relaxation time (τ_L) of methanol (~9 ps).[66] This general match hints that the solvent reorientation gates proton transfer from the initially formed CS state or a $RO^-*\cdots H^+\cdots S$ complex (i.e., CIP, and S represents solvent) likely within the first solvation shell. Notably, we adopt the useful "CIP" terminology to denote an intermediate state which does not consist of two absolute ions (i.e., complete PB* and a fully separated proton) but rather the electron-density-redistributed or charge-separated photoacid-solvent complex with a certain extent of proton and other nuclear motions. In other words, the intermediate is in a different state from a relaxed PA* state although both show a red-shifted SE band. This interpretation is nicely supported by the comparison of steady-state fluorescence and fs-TA spectra when the ultrafast CIP formation is more pronounced in a solvent with better proton transfer capabilities. The common deviations of experimental solvation times from τ_L lie in the inaccurate treatment of solvent as a simple dielectric continuum in the presence of solute molecules. In fact, most experimentally observed solvation times (τ_S) are between the

longitudinal and Debye dielectric relaxation time (τ_D), i.e., $\tau_L < \tau_S < \tau_D$.[73] Debye relaxation usually involves the dipolar reorientation of bulk solvent molecules and was originally defined as the response of noninteracting dipoles to alternating external electric field. In contrast, the smaller τ_L reflects more on local solvent reorganization for strongly interacting solute−solvent systems like M3F and P3F in methanol or water.

Theoretically, solvent reorientation times should follow a distribution as a function of intermolecular distance to the solute for which the dipolar interaction between them varies. It has been found that the first solvation shell contribution dominates the total solvent response and is much faster than the outer shells.[66] Therefore, the difference in the experimentally deduced time scale between different vibrational modes might be indicative of the involvement of more outer solvation shells in a mode-dependent manner (the chromophore is not isotropic and the single dissociable proton is only at one end), and solvation events would exert different effects on the probing vibrational modes depending upon the actual mode composition. Besides H-bonding interactions between the solute and solvent molecules, additional site-specific intermolecular interactions could involve steric hindrance. Nevertheless, solvent reorientation within the first solvation shell plays an essential role in the efficient ESPT of superphotoacids M3F and P3F to solvent via the H-bonding network. Notably, the relatively shorter time in TA (6.5 ps for M3F and 5.4 ps for P3F, Figure 5.5) as well as the observed prompt rise of the PB* species parallel to the solvation-controlled PT pathway following the CIP formation entail the existence of a competing faster PT pathway, which most likely involves the pre-existing and largely optimized H-bonding chain.[4]

The slower component in the ESPT process is typically attributed to the diffusion-assisted further proton transfer into well-separated ions. The TA global analysis retrieves time constants of this process at 250 and 320 ps for M3F and P3F in methanol, respectively. Meanwhile, the excited-state FSRS data demonstrate varying time constants in the range 90−320 ps for M3F and 110−270 ps for P3F. These characteristic long time constants go beyond the commonly acceptable translational diffusion time that is usually on the tens of picoseconds time scale.[12] Therefore, rotational diffusion of the solute has to be invoked to account for the experimental observations because other possible processes such as the solvent Debye relaxation and intermolecular vibrational energy transfer are either shorter than 100 ps or supposed to deactivate the PB* population.[6,21,64] The classical formulism for diffusion-controlled ESPT based on the Debye-Smoluchowski equation (DSE) only considers the translational degree of freedom since it assumes rather fast rotational diffusion.[12,62] However, in most cases, rotational diffusion is slower than translational diffusion, and this difference is more drastic for large molecules in strongly H-bonded solvents.[1,18,60]

The rotational relaxation times are typically on the longer time scales of 0.1−10 ns, depending on the temperature and solvent viscosity.[74] For a rough estimate, if one considers the solute molecule as an isotropic sphere, the rotational time by Debye theory is $\tau_{rot} = \frac{1}{6D_{rot}} = \frac{\eta V}{k_B T}$ where η is the viscosity of the solvent and V is the volume of the sphere. Approximating the radius as half of the molecular long axis for the M3F and P3F chromophore (Figure 5.9), i.e., ~5.5 and 6.5 Å, the τ_{rot} is predicted to be ~100 and 170 ps in methanol at 20 °C, respectively, largely matching the experimental values.

In realistic reactions, the isotropic approximation breaks down due to the non-spherical shape and limited reactive sites (e.g., a single proton dissociation site) of the solute. In other words, most diffusion-controlled reactions are anisotropic so we should not expect a uniform rate for all the reaction coordinates.[18] The long time constants of PB* rise dynamics from FSRS data exhibit a range across a few hundreds of picoseconds, suggesting that various vibrational modes track the diffusion-controlled PT along different rotational degrees of freedom. On the other hand, translational diffusion and solvent relaxation are still expected to accompany the rotational diffusion but not in a rate-limiting capacity due to their faster rates. In particular, following electronic excitation of the chromophore and the ultrafast formation of a CS state/CIP, the solvent must undergo changes from a non-equilibrium state toward thermal equilibrium, while continuing to reorient itself to accommodate the rotating solute to form suitable H-bonding chains for the ESPT process on longer time scales.
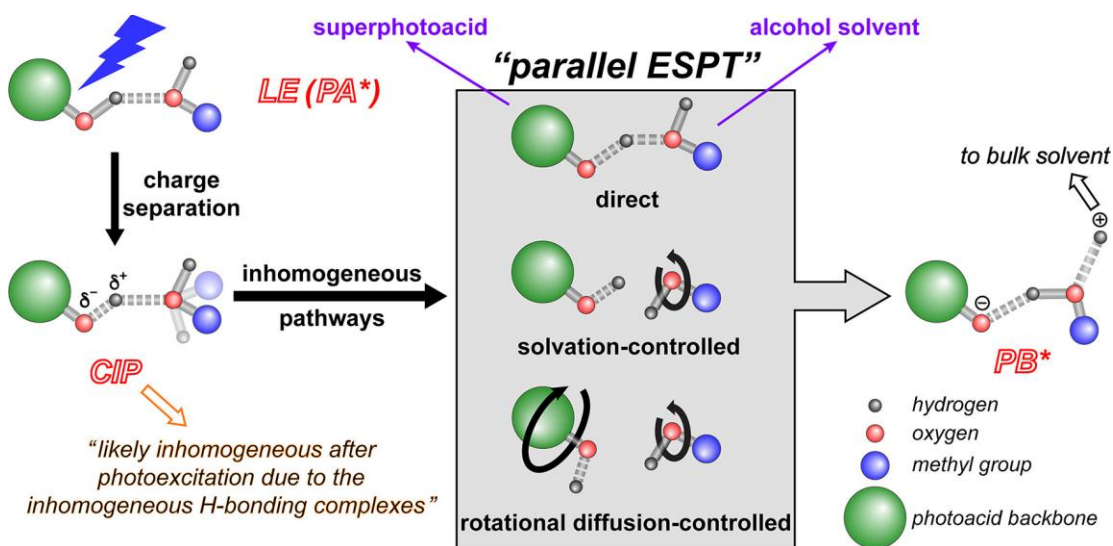
Figure 5.9. Schematic depicting the ESPT dynamics of superphotoacids M3F and P3F in alcohols (e.g., methanol). Red and gray balls represent oxygen and hydrogen atoms

for both the photoacid and solvent molecules, respectively. Green and blue balls represent the remaining structure of the photoacid and solvent, respectively. Chemical bonds are denoted by light gray sticks. The solid stick indicates a covalent bond while the dashed stick indicates an H-bond or weakened covalent bond. Photoexcitation of the superphotoacid in solution is denoted by the lightning symbol. The middle box illustrates the essence of parallel ESPT pathways via coupled electron and nuclear motions of the inhomogeneous solute-solvent complexes on ultrafast time scales from PA* en route to PB*. Reproduced with permission from Cheng Chen et al., *J. Phys. Chem. B* **2019**, 123, 3804-3821. Copyright 2019 American Chemical Society.

In aggregate, we observed an inhomogeneous ESPT mechanism consisting of at least three major proton transfer routes for our newly engineered superphotoacids M3F and P3F in methanol, which is expected to represent the photoinduced PT reaction pathways in other alcohols (Figure 5.9). The first route occurs on an ultrafast time scale, facilitated by the pre-existing or largely optimized local H-bonding structure around the tightly bound ground-state solute-solvent complexes. This is evidenced by the prompt rise of the PB* population after CIP formation (Figure 5.5, insets at 300 fs time delay) and the shortened average solvation time in TA (Figure 5.5c and 5.5d). The second route is gated by solvent reorientation mainly involving the first solvation shell. The rapidly changing dipole moment of PA* (upon photoexcitation of PA) requires nearby solvent molecules to reorient themselves to overcome the reaction barrier imposed by the perturbed dipole-dipole interaction. The third route is the slow PT step

controlled by rotational diffusion of the photoacid.[6,64,75] This is probably because methanol is a relatively bulky solvent and its H-bonding network is rather intricate. A portion of the solute photoacid molecules thus need to rotate themselves to form a suitable H-bonding network for PT over larger distances, also enabled by the photoexcitation energy. The anisotropic reactivity of the photoacid with low symmetry as well as the initial inhomogeneous orientation between solute and solvent molecules (i.e., H-bonded complexes as the reactant pairs before photons hit) would lead to a distribution of rotational relaxation time in the electronic excited state, in accord with the observed FSRS mode dynamics and time constants (Figure 5.7, Tables 5.1 and 5.2).

Notably, these three ESPT pathways occur in a parallel manner instead of being strictly stepwise (Figure 5.9). The least-squares fitting in Figure 5.7c and 5.7d assumes the same time zero for all the exponential processes, supporting the individual pathways as concomitants. For example, if only the solvent reorientation enables or gates proton transfer, then it would not require further rotational diffusion of the solute to separate the proton because PB* production would be complete via the solvation step. The mismatch between the intermediate picosecond time constant (i.e., 6.5 ps in Figure 5.5c and 10 ps in Figure 5.7c for M3F; 5.4 ps in Figure 5.5d and 9.2 ps in Figure 5.7d for P3F) also corroborates the ESPT reaction mechanism deviating from a purely sequential model. Our correlated ultrafast electronic and vibrational spectroscopic results manifest an inhomogeneous environment upon a sudden change of electron distribution of the excited superphotoacid in a model alcohol solution (e.g., methanol). Furthermore, both the absence of sub-picosecond time constants in PB* vibrational

mode rise dynamics (Figure 5.7) and the presence of a 300/270 fs time constant in the PA* electronic dynamics for M3F/P3F (Figure 5.5) suggest that the main ESPT pathways occur after the initial formation of a CIP or a CS state (associated with a time constant below ∼300 fs). Such ultrafast Franck−Condon dynamics reaching an intermediate state close to the PA* LE state is consistent with the substitution-enhanced ICT upon actinic electronic excitation and a great tendency for protolytic dissociation driven by the chromophore superphotoacidity.[1,13]

5.3.7 ESPT dynamics in alcohols versus in water

In comparison to methanol or other alcohols, water is a smaller molecule, is a better proton acceptor, and has a much faster solvent response. The τ_L and τ_D of water are 0.54 and 8.27 ps at 298 K, respectively.[66] The average solvation time of water could be dominated by proton hopping with a ∼1.5 ps time constant,[3,5,76] while in other molecular systems the sub-picosecond (as fast as ∼50 fs) aqueous solvation dynamics could be significant.[4,20,65,77] According to the Grotthuss mechanism,[78] the H-bond cleavage and formation in the first two solvation shells determine the proton transfer rate, so we would anticipate it to be a rate-limiting step for superphotoacids. A direct comparison between the transient electronic dynamics of M3F and P3F in methanol versus in water should provide deeper insights into the underlying ESPT mechanism.

Figure 5.10 presents the global analysis of fs-TA spectra on the basis of a sequential model for M3F and P3F in aqueous solution. The initial two components reveal ESPT

processes similar to those in methanol. The first EADS (black) denotes the PA* locally excited (LE) state that undergoes initial proton motion to reach an intermediate state (CS state or CIP), which can be represented by the second EADS (red) featured by a redshifted SE band due to charge separation (more pronounced than the methanol case, Figure 5.5). Clearly, M3F and P3F exhibit shorter time constants in water (120 and 100 fs, respectively) than in methanol (300 and 270 fs, respectively, Figure 5.5c and 5.5d). The intermediate state then decays and forms PB* (third EADS, blue) with a time constant of 1.9 ps (M3F) and 1.5 ps (P3F), characteristic of the proton hopping in water. The slightly longer time constant of M3F than P3F may reflect their different local H-bonding strengths that determine the rate of bond cleavage and formation during the course of photoinduced proton hopping. We also note that the SE band maxima of the red EADS for M3F and P3F are at ~510 and 528 nm, respectively, which manifest additional redshifts with respect to their PA* fluorescence peaks (~455 and 470 nm for M3F and P3F, respectively) but still to the blue side of the corresponding PB* SE bands (~523 and 543 nm, blue EADS in Figure 5.10). These experimental results further corroborate the existence of an ultrafast ESPT reaction stage that leads to the formation of an intermediate CIP state, which should not be assigned to a relaxed PA* state.

Starting from this point, aqueous dynamics of M3F and P3F start to differ from the alcohol solution case. Instead of further PT by diffusion and the continued rise of PB*, the PB* SE band decays in two steps denoted by the third (blue) and fourth (green) EADS. This observation indicates that PT is largely completed in the course of hopping among water molecules likely within the first few solvation shells. The diffusion-

controlled PT is not discernible, which suggests that the PB* formation does not require a long-range proton displacement from the intermediate state or rotational diffusion to generate more PB* (Figure 5.9). In sharp contrast, when methanol is the solvent, the complex H-bonding environment and relatively inert proton-accepting ability of methanol molecules require further proton separation via diffusion events to effectively produce PB*.
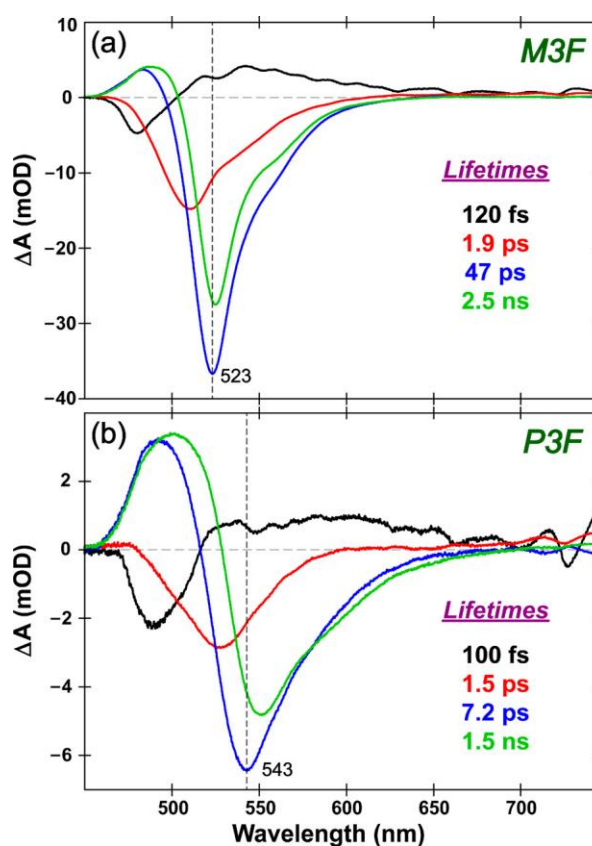
Figure 5.10. Global analysis of the fs-TA spectra for M3F and P3F in pH=3 aqueous solution after 400 nm photoexcitation.The acidic pH ensures a dominant PA population in S_0. The difference in TA signal intensity (in milli-OD unit) is because the solubility of P3F is much smaller than M3F in acidic aqueous solution. A sequential model yields four EADS in the order of black, red, blue, and green traces (with the time constants

listed). The PB* SE band center wavelength is denoted by the vertical dashed line. Reproduced with permission from Cheng Chen et al., *J. Phys. Chem. B* **2019**, 123, 3804-3821. Copyright 2019 American Chemical Society.

It is noteworthy that the long excited-state lifetime plays an important role in the efficient ESPT of M3F and P3F in both water and methanol. The third and fourth EADS manifest the nonradiative and radiative decay pathways of the PB* state, respectively. The ~47 ps of M3F is due to thermal cooling through diffusion, typical of rigid molecules. A similar time constant has been reported for another relatively rigid photoacid, HPTS, in water.[72] In contrast, P3F possesses a flexible side-chain phenyl ring and can dissipate its energy in a more efficient way, e.g., twisting motions. The observed ~7 ps is thereby attributed to the ring-twisting-induced deactivation of PB*, likely via a conical intersection between S_1 and S_0,[45,79] which also explains why the excited-state lifetime is shortened to some extent (1.5 ns in Figure 5.10b) when compared to the M3F case (2.5 ns in Figure 5.10a, fourth EADS). In other words, there might be two reasons for the shorter 1.5 ns observed for P3F. One is that the 1.5 ns lifetime could be an average time of the radiative and nonradiative decay pathways other than the aforementioned ring twisting (~7 ps component); the other is that the addition of a side-chain phenyl ring intrinsically shortens the fluorescence lifetime of P3F because the molecular/electronic structure is changed with respect to M3F. Despite these notable nonradiative decay channels with more twisting motions than M3F, P3F remains highly fluorescent due to conformational locking of the main backbone.

5.3.8 Intramolecular charge transfer and photoacidity

As mentioned above, superphotoacidity can be achieved by lowering the potential energy of the conjugate base via an ICT process. Conventionally, solvatochromism can confirm the ICT mechanism mainly due to dipole-dipole interactions between the solute and polar solvents, which differ for the electronic ground state compared to excited states.[8] In comparison, the ground-state (Figure 5.11) and excited-state FSRS data (Figure 5.7) in methanol solvent offer more direct evidence for the charge migration because the vibrational frequency particularly for localized modes is highly sensitive to the electron density change across the chromophore ring system.

For M3F, the ground-state PA marker band at 1664 cm^{-1} is shown to be phenolic C=C stretching and bridge C=C stretching motion according to DFT calculations (Figure 5.11 and Table 5.3), which is thus a good indicator of electron density at the phenolic moiety. This mode red-shifts to 1575 cm^{-1} in the excited state (Table 5.1), implying the electron density reduction at the donor site (Figure 5.7a, lower to middle panel). A similar red-shift occurs for the PB mode at 1649 cm^{-1} assigned to the phenolate C=C stretching and bridge C=C stretching motion (Figure 5.11, Table 5.1), which redshifts to 1566 cm^{-1} in the excited state. In addition, the PB mode at 1343 cm^{-1} mainly involving motions on the imidazolinone ring, e.g., imidazolinone C−N stretching, exhibits a blue-shift from the ground to the excited state (1370 cm^{-1}, supported by the calculations: 1333 → 1354 cm^{-1}) and indicates an increase of electron density at the imidazolinone moiety (Figure 5.7a, upper to middle panel). These two observations substantiate the charge migration or ICT primarily from the phenolic (in PA) or

phenolate (in PB) ring to the imidazolinone ring following electronic excitation, which essentially correlates to the superphotoacidity of M3F.
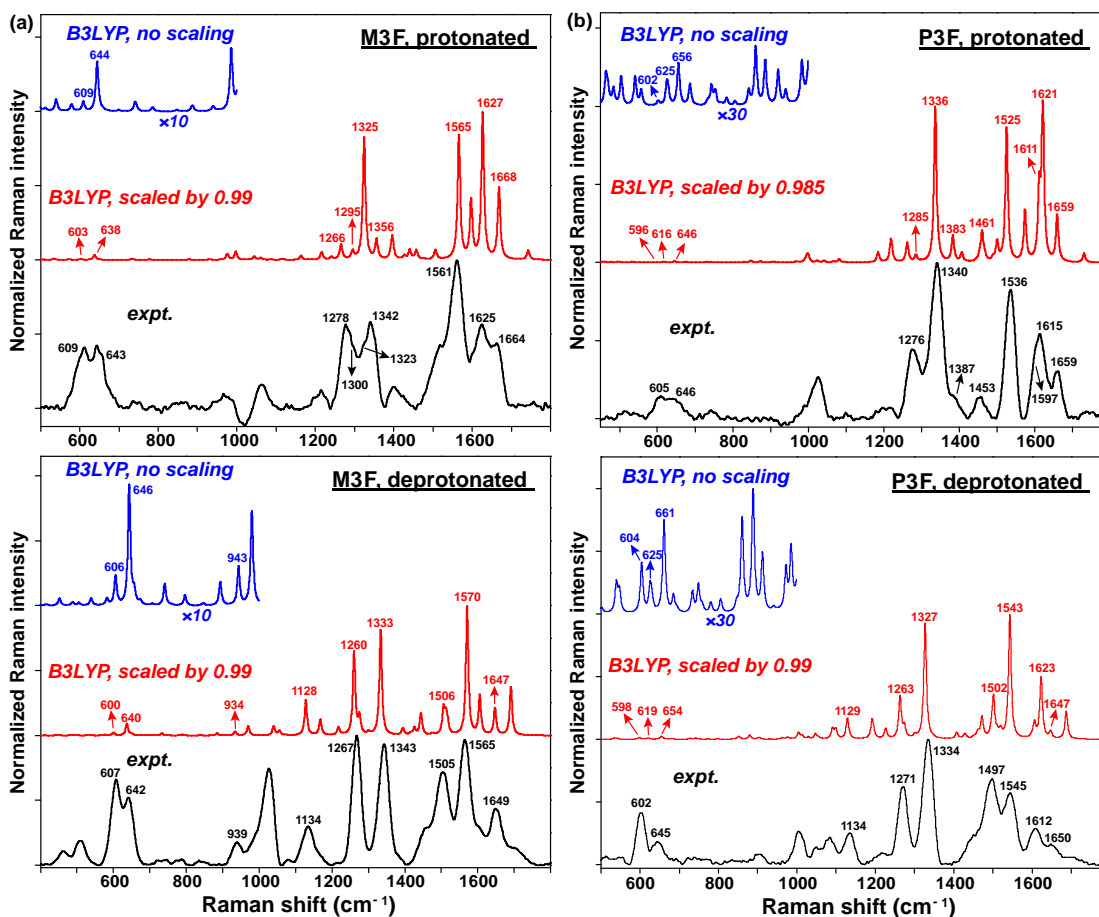
Figure 5.11. Experimental (black) and calculated (red and blue) ground-state Raman spectra for (a) M3F and (b) P3F in methanol.The R_{pu} wavelength for FSRS is 500/500 and 560/590 nm for PA (upper panels) and PB (lower panels) of M3F/P3F, respectively. The scaled spectrum is colored in red while the unscaled low-frequency region (<1000 cm^{-1}) is colored in blue. Adapted with permission from Cheng Chen et al., *J. Phys. Chem. B* **2019**, 123, 3804-3821. Copyright 2019 American Chemical Society.

Table 5.3. Ground-state Raman mode assignment for M3F in methanol.

	FSRS freq. (cm^{-1})	Calc. freq.[a] (cm^{-1})	Mode assignment (major motions)
PA	1664	1668	bridge C=C stretching, H rocking; phenolic C$_{5'}$=C$_{6'}$, C$_{2'}$=C$_{3'}$, C–O stretching; weak imidazolinone C=O stretching
	1625	1627	phenolic COH rocking; bridge C=C stretching, C−H rocking; weak imidazolinone breathing
	1561	1565	imidazolinone C$_2$=N$_3$ stretching, methyl (N$_1$ and C$_2$) bending; weak bridge H rocking; phenolic COH rocking
	1342	1356	imidazolinone C$_4$–N$_3$ stretching; bridge H rocking; phenolic COH rocking, in plane ring deformation
	1323	1325	phenolic C=C stretching, COH rocking; bridge H rocking
	1300	1295	phenolic ring in-plane deformation, COH rocking; bridge H rocking; imidazolinone ring deformation
	1278	1266	phenolic ring deformation, C–O stretching; bridge H rocking, C–B stretching; imidazolinone ring deformation
	643	644[b]	in-plane three-ring asymmetric deformation
	609	609[b]	in-plane phenolic ring breathing; middle ring deformation; imidazolinone deformation
PB	1649	1647	Phenolate C$_{5'}$=C$_{6'}$, C$_{2'}$=C$_{3'}$ stretching, weak C=O stretching; bridge C=C stretching, H rocking
	1565	1570	Imidazolinone C$_2$=N$_3$ stretching, methyl (C$_2$) twisting; phenolate C=O stretching; bridge H rocking
	1505	1506	Imidazolinone C$_2$–N$_1$ stretching, methyl (N$_1$ and C$_2$) twisting
	1343	1333	Imidazolinone C$_4$–N$_3$ stretching, ring deformation; bridge H rocking; weak phenolate ring deformation
	1267	1260	Phenolate ring deformation, C–F stretching; bridge H rocking; imidazolinone ring in-plane deformation
	1134	1128	bridge H rocking; phenolate C–F stretching, ring in-plane deformation, C–B stretching
	939	934	Middle ring breathing, B–F stretching; imidazolinone methyl (N$_1$) twisting
	642	643[b]	In-plane three-ring asymmetric deformation
	607	606[b]	In-plane phenolic ring breathing; middle ring deformation; imidazolinone ring deformation

[a]The normal mode scaling factor is 0.99.

[b]Low-frequency modes (<1000 cm^{-1}) are not scaled.

Table 5.4. Ground-state Raman mode assignment for P3F in methanol.

	FSRS freq. (cm^{-1})	Calc. freq.[a] (cm^{-1})	Mode assignment (major motions)
PA	1659	1659	phenolic $C_{5'}$=$C_{6'}$, $C_{2'}$=$C_{3'}$ stretching, C–O stretching; bridge C=C stretching
	1615	1621	phenolic C=C stretching, COH rocking; bridge H rocking and C=C stretching; phenyl ring H scissoring
	1597	1611	phenyl ring symmetric C=C stretching
	1536	1525	imidazolinone C_2=N_3 stretching and methyl twisting; phenyl symmetric C=C stretching and ring-H rocking
	1453	1461	phenyl symmetric ring-H rocking; phenolic COH rocking, C_2=C_3 stretching; imidazolinone in-plane breathing
	1387	1383	phenolic ring breathing, C–O stretching; bridge H rocking; imidazolinone C_4–N_3 stretching, in-plane ring deformation
	1340	1336	imidazolinone C_4–N_3 stretching; bridge H rocking; phenolic COH rocking and ring breathing.
	1276	1285	phenolic ring deformation, C−F stretching; bridge H rocking; imidazolinone ring deformation; phenyl one-sided H rocking.
	646	625[b]	in-plane middle and imidazolinone ring deformation; phenolic ring breathing; weak phenyl ring out-of-plane deformation
	605	602[b]	In-plane three-ring asymmetric deformation; phenyl ring out-of-plane deformation
PB	1650	1647	Phenolate $C_{5'}$=$C_{6'}$, $C_{2'}$=$C_{3'}$ stretching, C=O stretching; bridge C=C stretching
	1612	1623	Phenyl symmetric ring-H scissoring and C=C stretching
	1545	1543	Phenyl symmetric ring-H rocking; imidazolinone C_2=N_3 stretching, methyl bending; phenolate $C_{2'}$=$C_{3'}$, C=O stretching
	1497	1502	Imidazolinone C_2=N_3 stretching, methyl bending; phenyl H rocking; bridge H rocking; weak phenolate C=O, C_2=C_3 stretching
	1334	1327	Imidazolinone C_4−N_3 stretching; bridge H rocking; weak phenolate ring deformation
	1271	1263	Phenolate ring deformation, weak C–F stretching; bridge H rocking; imidazolinone ring deformation; phenyl H rocking;
	1134	1129	Bridge H rocking; phenolate C–F stretching, ring in-plane deformation; C–B stretching
	645	625[b]	In-plane middle and imidazolinone ring deformation; phenolate ring breathing; weak phenyl ring out-of-plane deformation
	602	604[b]	In-plane three-ring asymmetric deformation; phenyl ring out-of-plane deformation

[a]The normal mode scaling factor is 0.985 for PA and 0.99 for PB.

[b]Low-frequency modes (<1000 cm^{-1}) are not scaled.

In general, the excitation of a photoacid promotes intramolecular charge transfer from the phenolic ring to the remaining conjugated ring system with π-π* transition character (Figure 5.12),[80,81] also accompanied by a significant electron density change around the methylene bridge. The charge redistribution weakens the phenolic OH bond and makes the photoacid more acidic in the excited state than in the ground state. Likewise, for the PA form of P3F, the 1659 cm^{-1} phenolic C=C stretching and bridge C=C stretching mode (Figure 5.11, Table 5.4) red-shifts to 1630 cm^{-1} (Table 5.2) while the 1340 cm^{-1} imidazolinone C−N stretching and bridge C−H rocking mode blue-shifts to 1355 cm^{-1} (Figure 5.7b, bottom to middle panel) upon 400 nm photoexcitation. The two corresponding characteristic PB modes are at 1650 and 1334 cm^{-1} (Figure 5.11, Table 5.4, and Figure 5.7b, upper panel). Unfortunately, the two counterpart modes in the excited state (PB*) were either not observed or obscured by the weak SNR under the current experimental resonance Raman condition, so a direct mode frequency shift between PB and PB* cannot be explicitly stated herein.
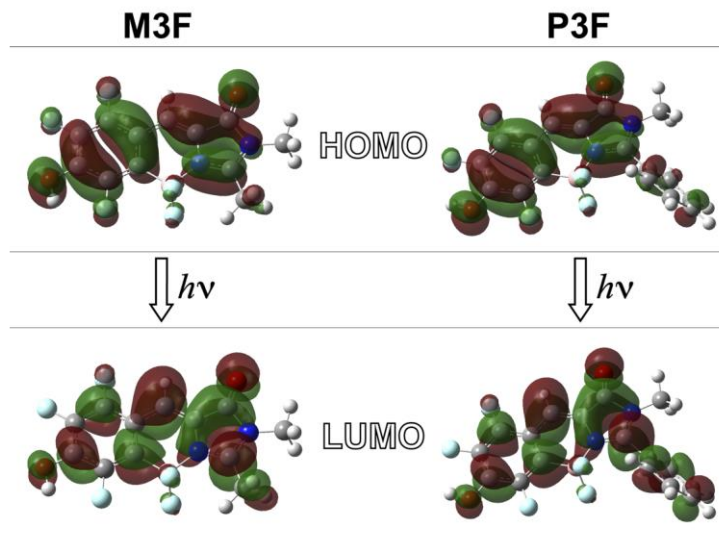
Figure 5.12. Calculated electron density distributions of the frontier molecular orbitals of neutral M3F and P3F in methanol during vertical excitation. The HOMO and LUMO orbitals were obtained using the TD-DFT/RB3LYP/6-311G+(d, p) method at the ground-state optimized geometry with the implicit IEFPCM solvent model. The HOMO→LUMO transition constitutes the primary $S_0 \rightarrow S_1$ excitation according to the calculated oscillator strength. Reproduced with permission from Cheng Chen et al., *J. Phys. Chem. B* **2019**, 123, 3804-3821. Copyright 2019 American Chemical Society.

5.3.9 Origin and design of superphotoacidity

On the basis of the pK_a* values calculated by the Förster equation, the photoacidity increases from 0F to 3F for both the methyl and phenyl series. However, 2F → 3F exhibits a smaller increase of acidity in both S_0 and S_1 when compared to 0F → 1F or 1F → 2F (Table 5.5). This increase is even smaller for pK_a* due to the decreased ΔpK_a value from 2F to 3F, corroborated by our time-resolved spectroscopic data (e.g.,

$k_{\text{ESPT,fast}} = \dfrac{1}{570\,fs}$ and $\dfrac{1}{300\,fs}$ for M2F and M3F in methanol, respectively; while M0F and M1F can barely undergo ESPT in methanol). To understand photoacidity in more detail, two factors need to be considered: the ground-state acidity (pK_a), and the acidity increase ($\Delta pK_a = pK_a - pK_a^*$) from S_0 to S_1 (Figure 5.13).

Table 5.5. Ground (S_0) and excited (S_1) state acidity of MnF and PnF in water.

	methyl series				phenyl series			
	$pK_a{}^a$	$pK_a^*{}^b$	$\Delta pK_a{}^b$	$\Delta pK_a'{}^c$	$pK_a{}^a$	$pK_a^*{}^b$	$\Delta pK_a{}^b$	$\Delta pK_a'{}^c$
0F	6.4	−2.3	8.7	5.7	7.5	−1.3	8.8	6.5
1F	5.8	−3.3	9.1	6.1	6.1	−3.4	9.5	6.9
2F	4.7	−4.7	9.4	6.4	4.9	−5.2	10.1	7.1
3F	4.2	−5.0	9.2	6.1	4.2	−5.5	9.7	6.8

[a]The ground-state pK_a values were measured by titrating 10−20 μM chromophore solution in water using a Varian Cary 100 UV−Vis spectrophotometer (Agilent Technologies, Inc.).

[b]These values were calculated using the Förster equation with the PA and PB absorption peak energy from the steady-state electronic spectroscopy:

$$pK_a^* = pK_a - \frac{hc}{2.303 k_B T}\left(\frac{1}{\lambda_{PA}} - \frac{1}{\lambda_{PB}}\right),$$

mainly due to the undetected emission peak from the fleeting PA* in water.

[c]The $\Delta pK_a'$ values were calculated using the Förster equation with the minimized energy of PA (S_0), PA* (S_1), PB (S_0), and PB* (S_1) from DFT and TD-DFT geometrical optimizations. The more complete Förster equation can now include all the pertinent S_0-S_1 energy gaps for the protonated and deprotonated chromophore species:

$$pK_a^* = pK_a - \frac{1}{2.303 k_B T}[(E_{PA*} - E_{PA}) - (E_{PB*} - E_{PB})]$$
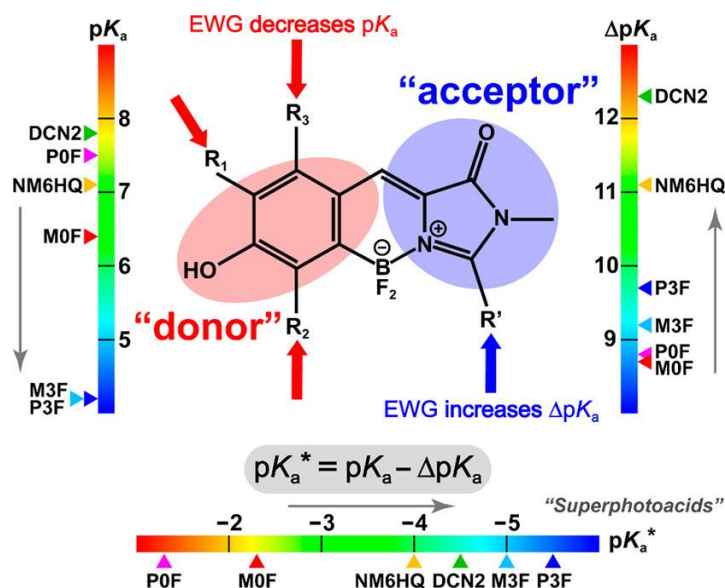
Figure 5.13. Design strategy for superphotoacidity on the basis of pK_a, ΔpK_a, and pK_a^* comparison between various photoacids.Gray arrows depict the synergistic tuning to achieve smaller pK_a^*. Reproduced with permission from Cheng Chen et al., *J. Phys. Chem. B* **2019**, 123, 3804-3821. Copyright 2019 American Chemical Society.

First, it is well-known that pK_a can be lowered by applying EWGs to the electron-rich sites.[1,5,13,27] However, we need to emphasize that these sites should be proximal to the dissociable −OH group. EWGs at a distant end would not induce significant electron density reduction on an O−H bond at the equilibrium ground state due to weak long-range interactions. In this work, the replacement of methyl by phenyl at C2 (Figure 5.2) can be viewed as an addition of EWG at a distal ring. Therefore, PnF does not show a pK_a decrease from the MnF counterpart. Instead, PnF has weaker acidity (i.e., larger pK_a, Table 5.5) than the MnF counterpart, which is the most significant for 0F, and the effect gradually diminishes from 0F to 3F. This is because the flexible phenyl group

has internal rotational degrees of freedom, which introduce an extra entropic contribution to the overall free energy (ΔG) of the ground-state dissociation reaction. With more fluorination at the chromophore phenolic ring sites, the enthalpy change overwhelms the entropy, and in consequence, an equality of pK_a (i.e., 4.2) between MnF and PnF is reached at 3F (Table 5.5). Moreover, in the same series, fluorination at the proximal phenolic ring significantly drops the pKa and exhibits an additive effect (see red arrows in Figure 5.13).

Second, ΔpK_a is determined by the difference between the S_0-S_1 energy gaps of the acid and its conjugate base (see Table 5.5 footnotes), which are energetically close to the electronic absorption or emission transitions. To increase the magnitude of ΔpK_a, an effective strategy would be to enhance the excited-state ICT by incorporating EWG(s) at the acceptor end in a donor−acceptor system (Figure 5.13). The anionic form typically exhibits more ICT character with respect to the neutral form due to the stronger electron-donating ability of $-O^{(-)}$ compared to that of $-OH$ and may be associated with a larger dipole moment. The anionic form would be stabilized more than the neutral form in S_1, leading to a larger ΔpK_a. Previous superphotoacids such as DCN2 and NM6HQ$^+$ have very large ΔpK_a of ∼12.3 and 11.1 (Figure 5.1 and 5.13), respectively, because the EWGs are located at the distal ring acting as the acceptor moiety so ICT is promoted. As a result, their pK_a* values are small (i.e., high photoacidity) despite the large pK_a in S_0.

In aggregate, one could achieve superphotoacidity through either or both of the following strategies: (1) Incorporate EWGs to the donor moiety (usually the proximal ring bound to the dissociable hydroxyl group) to increase the ground-state acidity (i.e., decrease the pK_a). Even with a largely unchanged intrinsic energy gap difference between neutral and anionic forms of the photoacid backbone (i.e., ΔpK_a), the pK_a^* still drops. (2) Incorporate EWGs to the acceptor moiety (usually the distal ring) to increase ΔpK_a enabled by ICT. Even with a relatively high pK_a, one could still obtain a low pK_a^* due to a significantly large ΔpK_a. Though these two modification routes are not isolated from each other, one commonly dominates over the other in either case, making the two-pronged strategy effective (e.g., M3F and P3F in Figure 5.13, see the gray arrows). However, if large electron-withdrawing groups were to be substituted into the donor ring, they could serve as new major acceptor sites, and then a reassessment of the entire chromophore electronic structure becomes necessary (e.g., the peculiar molecular framework of QCy9, see Figure 5.1).

In our current synthetic MnF and PnF series, fluorination at the phenolic ring lowers the pK_a to a great extent. However, the ΔpK_a does not show an appreciable increase with the lowering of pK_a. The introduction of a side-chain phenyl ring in PnF enhances ICT (see Figure S8 for example) and hence increases ΔpK_a. PnF does exhibit an increase in ΔpK_a compared to the MnF counterpart but to a small extent, probably due to the weak electron-withdrawing ability of phenyl. As a result, PnF series species are slightly stronger photoacids than MnF series species. We predict that stronger EWGs at the C2 position would generate even stronger superphotoacids. We also note that 2F

→ 3F exhibits smaller changes than 0F → 1F and 1F → 2F in terms of pK_a and pK_a^*.

Accordingly, ΔpK_a increases from 0F to 2F but decreases from 2F to 3F (Table 5.5).

To shed further light on this intriguing molecular property, we performed DFT and TD-DFT calculations using the minimized S_0 and S_1 energies of the neutral and anionic forms of MnF and PnF. The calculated ΔpK_a results well reproduce the experimental trend (Table 5.5) although with a reduced magnitude. These results imply that the third −F (*meta* to the −OH) imposes a smaller effect on the neutral and anionic form energies than the first two −F (*ortho* to the −OH). We consider that the *meta* site might have less electron density than the two *ortho* sites, therefore lowering the overall chromophore electronic energy to a smaller extent upon electrophilic substitution, i.e., fluorination. As further theoretical support, we carried out the natural bond orbital (NBO) calculations for isolated M0F and P0F in Gaussian 09, which demonstrate significant electron density difference between meta and ortho sites before substitution: the *meta* site has less electron density than the two ortho sites (Figure 5.14 for M0F, and Figure 5.15 for P0F). A similar trend has previously been observed for cyanonaphthol derivatives (Figure 5.1) where C5, C6, C7, and C8 have unevenly distributed electron density in S_0 and S_1, which leads to different pK_a and pK_a^* values for the corresponding cyano-naphthols.[5,25]
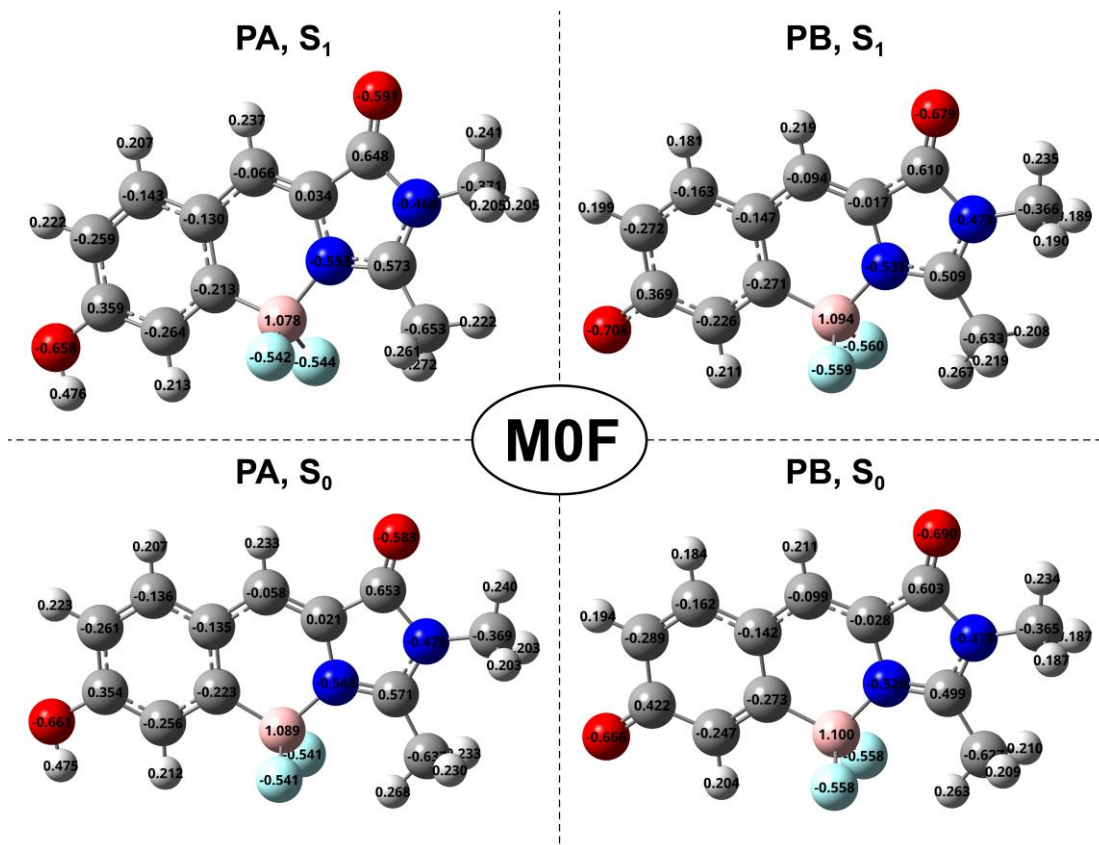
Figure 5.14. NBO calculations of the protonated (PA form) and deprotonated (PB form) M0F in the electronic ground (S_0) and excited (S_1) state in vacuum.On the phenolic ring side, the C atom at meta site to the terminal hydroxyl group exhibits significantly less electron density than the two ortho sites (e.g., in the upper left panel for PA in S_1, $|–0.143| < |–0.259|, |–0.264|$) in all four electronic states being calculated. Note that the NBO calculations are considered to be less basis set dependent compared to the Mülliken charge calculations, hence the former is chosen as the method to examine the electron density difference between various phenolic ring sites in reference to the dissociable hydroxyl end group. Reproduced with permission from Cheng Chen et al., *J. Phys. Chem. B* **2019**, 123, 3804-3821. Copyright 2019 American Chemical Society.
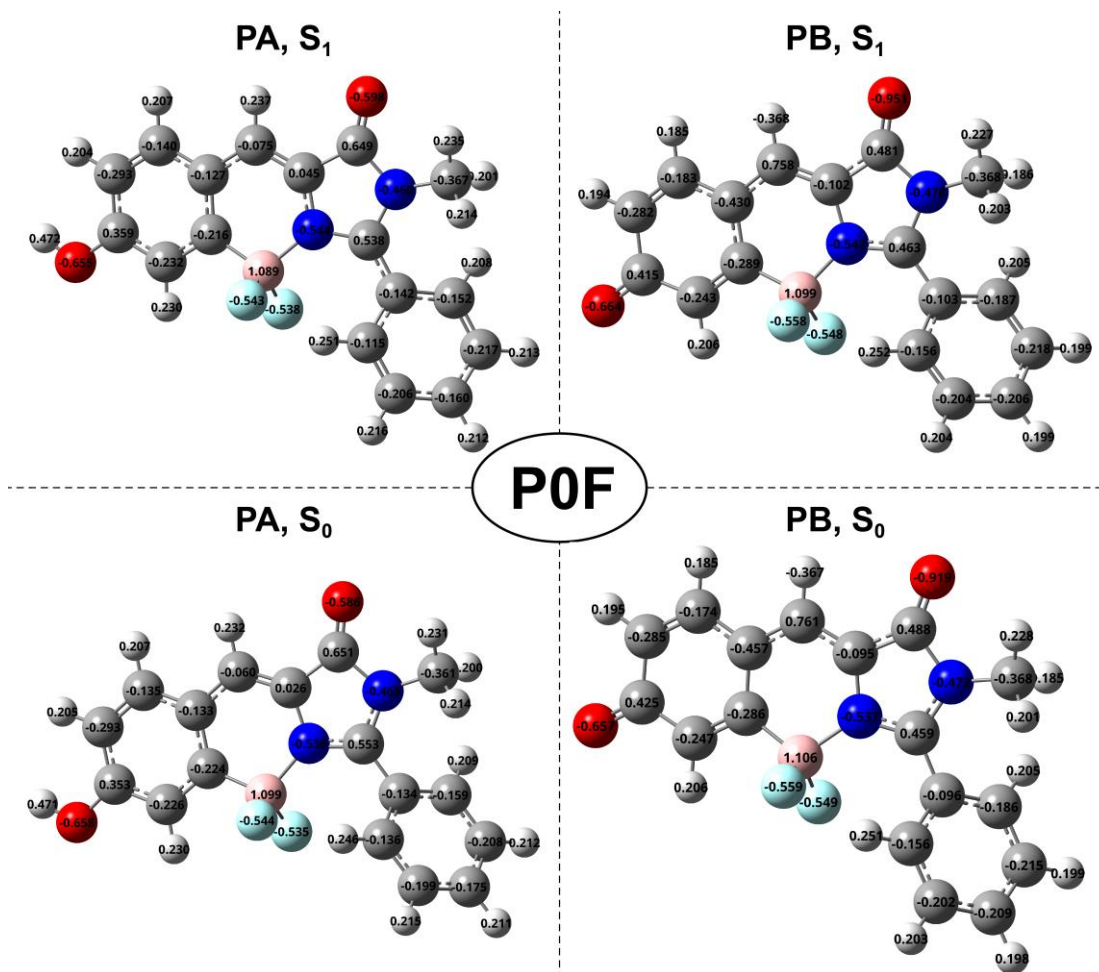
Figure 5.15. NBO calculations of the protonated (PA form) and deprotonated (PB form) P0F in the electronic ground (S_0) and excited (S_1) state in vacuum. The C atom at meta site to the terminal hydroxyl group exhibits significantly less electron density than the two ortho sites (e.g., in the upper left panel for PA in S_1, $|-0.140| < |-0.293|$, $|-0.232|$) in all four states being calculated. Reproduced with permission from Cheng Chen et al., *J. Phys. Chem. B* **2019**, 123, 3804-3821. Copyright 2019 American Chemical Society.

5.4 Conclusions

Inspired by the naturally occurring GFP that emits bright fluorescence, we chemically modified the GFP-core chromophore into highly fluorescent photoacids by fluorinating the phenolic ring bound to the dissociable hydroxyl group and conformationally locking the chromophore backbone. Two series of photoacids differing in the substituents ($-CH_3$ and $-Ph$) at the imidazolinone C2 position and the number of fluorine groups on the phenolic ring (MnF and PnF, n=0−3) were synthesized via the coordination-assisted borylation reaction to demonstrate the effect of EWGs at both acceptor and donor moieties on the overall chromophore photoacidity. Photoacidity increases with the number of $-F$ substituents (0F → 3F) mainly due to the decreasing pK_a. PnF shows a slightly stronger photoacidity than the MnF counterpart due to the enhanced ICT process upon electronic excitation and hence an increased ΔpK_a.

We utilized a field-proven fs-TA and tunable FSRS integrated experimental platform to spectroscopically characterize M3F and P3F, the most photoacidic compounds in the two series. They qualify as superphotoacids because of their very negative pK_a^* values below −5 and an efficient ESPT reaction in organic solvents like methanol. We revealed inhomogeneous ESPT pathways of M3F and P3F in methanol following the formation of an initial CS state or CIP on the ∼300 fs time scale. The multiple parallel ESPT pathways include an ultrafast ESPT pathway facilitated by the preexisting or largely optimized H-bonding chain, a solvation-controlled ESPT pathway, and a rotational diffusion-controlled ESPT pathway. In excited-state FSRS, the PA* marker bands track the early time ESPT events and reveal that the initial charge separation or

CIP formation occurs on an ultrafast time scale of ~150−350 fs. This key "preparatory" step is powered by the superphotoacidity of the engineered chromophores in methanol upon photoexcitation, representing an important underpinning for these photoactivatable molecular "machines".

The PB* marker bands exhibit biphasic dynamics with a consistent ~9−11 ps fast component and the other mode-dependent slow component ranging from ~90 to 320 ps. The first time constant matches the average solvation time of methanol, confirming that solvent reorientation is the rate-limiting step for ESPT of the superphotoacids studied here. The longer time constant is ascribed to the rotational diffusion that controls the ESPT reaction rate in alcohols beyond the first solvation shell. Furthermore, the vibrational mode specificity reflects the anisotropic reactivity of an asymmetric superphotoacid with a solvent of complex H-bonding structure like methanol, which holds general relevance for engineered GFP chromophore derivatives in protic solvents.

This work demonstrates the power of tunable FSRS via dynamic resonance enhancement, aided by global analysis of fs-TA and quantum calculations of normal-mode frequencies and electronic structures, to dissect a multidimensional, multi-staged, and inhomogeneous ESPT reaction mechanism of a superphotoacid from the sub-picosecond CS/CIP formation to the sub-nanosecond ESPT pathways in solution. The significance of an intermediate CIP state within a superphotoacid-solvent H-bonding complex en route to the photoproduct is substantiated. Notably, such a deep level of fundamental mechanistic understanding of the photoinduced proton transfer reaction in

solution could inspire future experimental studies and theoretical calculations to map out electron-coupled nuclear dynamics and potentially control chemical reactions, which is of paramount interest to all molecular sciences and engineering. Our findings also lay a solid foundation for the rational design of even stronger superphotoacids and other functionalities such as fluorescent and fluorogenic properties for the next generation of biosensing and bioimaging applications.

5.5 References

[1] Simkovitch, R.; Shomer, S.; Gepshtein, R.; Huppert, D. How Fast Can a Proton-Transfer Reaction Be beyond the Solvent-Control Limit? *J. Phys. Chem. B* **2015**, *119*, 2253-2262.

[2] Tolbert, L. M.; Solntsev, K. M. Excited-State Proton Transfer: From Constrained Systems to "Super" Photoacids to Superfast Proton Transfer. *Acc. Chem. Res.* **2002**, *35*, 19-27.

[3] Agmon, N.; Huppert, D.; Masad, A.; Pines, E. Excited-State Proton-Transfer to Methanol Water Mixtures. *J. Phys. Chem.* **1991**, *95*, 10407-10413.

[4] Rini, M.; Magnes, B. Z.; Pines, E.; Nibbering, E. T. J. Real-Time Observation of Bimodal Proton Transfer in Acid-Base Pairs in Water. *Science* **2003**, *301*, 349-352.

[5] Agmon, N. Elementary Steps in Excited-State Proton Transfer. *J. Phys. Chem. A* **2005**, *109*, 13-35.

[6] Leiderman, P.; Genosar, L.; Huppert, D. Excited-State Proton Transfer: Indication of Three Steps in the Dissociation and Recombination Process. *J. Phys. Chem. A* **2005**, *109*, 5965-5977.

[7] Pérez-Lustres, J. L.; Rodriguez-Prieto, F.; Mosquera, M.; Senyushkina, T. A.; Ernsting, N. P.; Kovalenko, S. A. Ultrafast Proton Transfer to Solvent: Molecularity and Intermediates from Solvation- and Diffusion-Controlled Regimes. *J. Am. Chem. Soc.* **2007**, *129*, 5408-5418.

[8] Baranov, M. S.; Lukyanov, K. A.; Borissova, A. O.; Shamir, J.; Kosenkov, D.; Slipchenko, L. V.; Tolbert, L. M.; Yampolsky, I. V.; Solntsev, K. M. Conformationally Locked Chromophores as Models of Excited-State Proton Transfer in Fluorescent Proteins. *J. Am. Chem. Soc.* **2012**, *134*, 6025-6032.

[9] Tolbert, L. M.; Baldridge, A.; Kowalik, J.; Solntsev, K. M. Collapse and Recovery of Green Fluorescent Protein Chromophore Emission through Topological Effects. *Acc. Chem. Res.* **2012**, *45*, 171-181.

[10] Spies, C.; Shomer, S.; Finkler, B.; Pines, D.; Pines, E.; Jung, G.; Huppert, D. Solvent Dependence of Excited-State Proton Transfer from Pyranine-Derived Photoacids. *Phys. Chem. Chem. Phys.* **2014**, *16*, 9104-9114.

[11] Chou, P. T.; Solntsev, K. M. Photoinduced Proton Transfer in Chemistry and Biology. *J. Phys. Chem. B* **2015**, *119*, 2089.

[12] Oscar, B. G.; Liu, W.; Rozanov, N. D.; Fang, C. Ultrafast Intermolecular Proton Transfer to a Proton Scavenger in an Organic Solvent. *Phys. Chem. Chem. Phys.* **2016**, *18*, 26151-26160.

[13] Chen, C.; Liu, W.; Baranov, M. S.; Baleeva, N. S.; Yampolsky, I. V.; Zhu, L.; Wang, Y.; Shamir, A.; Solntsev, K. M.; Fang, C. Unveiling Structural Motions of a Highly Fluorescent Superphotoacid by Locking and Fluorinating the GFP Chromophore in Solution. *J. Phys. Chem. Lett.* **2017**, *8*, 5921-5928.

[14] Tolbert, L. M.; Haubrich, J. E. Photoexcited Proton Transfer from Enhanced Photoacids. *J. Am. Chem. Soc.* **1994**, *116*, 10593-10600.

[15] Carmeli, I.; Huppert, D.; Tolbert, L. M.; Haubrich, J. E. Ultrafast Excited-State Proton Transfer from Dicyano-Naphthol. *Chem. Phys. Lett.* **1996**, *260*, 109-114.

[16] Huppert, D.; Tolbert, L. M.; Linares-Samaniego, S. Ultrafast Excited-State Proton Transfer from Cyano-Substituted 2-Naphthols. *J. Phys. Chem. A* **1997**, *101*, 4602-4605.

[17] Solntsev, K. M.; Tolbert, L. M.; Cohen, B.; Huppert, D.; Hayashi, Y.; Feldman, Y. Excited-State Proton Transfer in Chiral Environments. 1. Chiral Solvents. *J. Am. Chem. Soc.* **2002**, *124*, 9046-9047.

[18] Popov, A. V.; Gould, E. A.; Salvitti, M. A.; Hernandez, R.; Solntsev, K. M. Diffusional Effects on the Reversible Excited-State Proton Transfer. From Experiments to Brownian Dynamics Simulations. *Phys. Chem. Chem. Phys.* **2011**, *13*, 14914-14927.

[19] Gould, E. A.; Popov, A. V.; Tolbert, L. M.; Presiado, I.; Erez, Y.; Huppert, D.; Solntsev, K. M. Excited-State Proton Transfer in *N*-methyl-6-hydroxyquinolinium Salts: Solvent and Temperature Effects. *Phys. Chem. Chem. Phys.* **2012**, *14*, 8964-8973.

[20] Liu, W.; Han, F.; Smith, C.; Fang, C. Ultrafast Conformational Dynamics of Pyranine during Excited State Proton Transfer in Aqueous Solution Revealed by Femtosecond Stimulated Raman Spectroscopy. *J. Phys. Chem. B* **2012**, *116*, 10535-10550.

[21] Liu, W.; Wang, Y.; Tang, L.; Oscar, B. G.; Zhu, L.; Fang, C. Panoramic Portrait of Primary Molecular Events Preceding Excited State Proton Transfer in Water. *Chem. Sci.* **2016**, *7*, 5484-5494.

[22] Finkler, B.; Spies, C.; Vester, M.; Walte, F.; Omlor, K.; Riemann, I.; Zimmer, M.; Stracke, F.; Gerhards, M.; Jung, G. Highly Photostable "Super"-Photoacids for Ultrasensitive Fluorescence Spectroscopy. *Photochem. Photobiol. Sci.* **2014**, *13*, 548-562.

[23] Presiado, I.; Karton-Lifshin, N.; Erez, Y.; Gepshtein, R.; Shabat, D.; Huppert, D. Ultrafast Proton Transfer of Three Novel Quinone Cyanine Photoacids. *J. Phys. Chem. A* **2012**, *116*, 7353.

[24] Simkovitch, R.; Karton-Lifshin, N.; Shomer, S.; Shabat, D.; Huppert, D. Ultrafast Excited-State Proton Transfer to the Solvent Occurs on a Hundred-Femtosecond Time-Scale. *J. Phys. Chem. A* **2013**, *117*, 3405-3413.

[25]   Agmon, N.; Rettig, W.; Groth, C. Electronic Determinants of Photoacidity in Cyanonaphthols. *J. Am. Chem. Soc.* **2002**, *124*, 1089-1096.

[26]   Karton-Lifshin, N.; Albertazzi, L.; Bendikov, M.; Baran, P. S.; Shabat, D. Donor–Two-Acceptor" Dye Design: A Distinct Gateway to NIR Fluorescence. *J. Am. Chem. Soc.* **2012**, *134*, 20412-20420.

[27]   Szczepanik, B.; Styrcz, S. Protolytic Dissociation of Cyanophenols in Ground and Excited States in Alcohol and Water Solutions. *Spectrochim. Acta, Part A* **2011**, *79*, 451-455.

[28]   Shimomura, O.; Johnson, F. H.; Saiga, Y. Extraction, Purification and Properties of Aequorin, a Bioluminescent Protein from the Luminous Hydromedusan, Aequorea. *J. Cell. Comp. Physiol.* **1962**, *59*, 223-239.

[29]   Chalfie, M.; Tu, Y.; Euskirchen, G.; Ward, W. W.; Prasher, D. C. Green Fluorescent Protein as a Marker for Gene Expression. *Science* **1994**, *263*, 802-805.

[30]   Tsien, R. Y. The Green Fluorescent Protein. *Annu. Rev. Biochem.* **1998**, *67*, 509-544.

[31]   Zimmer, M. Green Fluorescent Protein (GFP): Applications, Structure, and Related Photophysical Behavior. *Chem. Rev.* **2002**, *102*, 759-782.

[32]   Chattoraj, M.; King, B. A.; Bublitz, G. U.; Boxer, S. G. Ultra-Fast Excited State Dynamics in Green Fluorescent Protein: Multiple States and Proton Transfer. *Proc. Natl. Acad. Sci. U. S. A.* **1996**, *93*, 8362-8367.

[33]   Fang, C.; Frontiera, R. R.; Tran, R.; Mathies, R. A. Mapping GFP Structure Evolution During Proton Transfer with Femtosecond Raman Spectroscopy. *Nature* **2009**, *462*, 200-204.

[34]   Meech, S. R. Excited State Reactions in Fluorescent Proteins. *Chem. Soc. Rev.* **2009**, *38*, 2922-2934.

[35]   Mandal, D.; Tahara, T.; Meech, S. R. Excited-State Dynamics in the Green Fluorescent Protein Chromophore. *J. Phys. Chem. B* **2004**, *108*, 1102-1108.

[36]   Bell, A. F.; He, X.; Wachter, R. M.; Tonge, P. J. Probing the Ground State Structure of the Green Fluorescent Protein Chromophore Using Raman Spectroscopy. *Biochemistry* **2000**, *39*, 4423-4431.

[37]   Kneen, M.; Farinas, J.; Li, Y.; Verkman, A. S. Green Fluorescent Protein as a Noninvasive Intracellular pH Indicator. *Biophys. J.* **1998**, *74*, 1591-1599.

[38]   Scharnagl, C.; Raupp-Kossmann, R. A. Solution pKa Values of the Green Fluorescent Protein Chromophore from Hybrid Quantum-Classical Calculations. *J. Phys. Chem. B* **2004**, *108*, 477-489.

[39] Laptenok, S. P.; Conyard, J.; Page, P. C. B.; Chan, Y.; You, M.; Jaffrey, S. R.; Meech, S. R. Photoacid Behaviour in a Fluorinated Green Fluorescent Protein Chromophore: Ultrafast Formation of Anion and Zwitterion States. *Chem. Sci.* **2016**, *7*, 5747-5752.

[40] Pal, P. P.; Bae, J. H.; Azim, M. K.; Hess, P.; Friedrich, R.; Huber, R.; Moroder, L.; Budisa, N. Structural and Spectral Response of *Aequorea victoria* Green Fluorescent Proteins to Chromophore Fluorination. *Biochemistry* **2005**, *44*, 3663-3672.

[41] Villa, J. K.; Tran, H. A.; Vipani, M.; Gianturco, S.; Bhasin, K.; Russell, B. L.; Harbron, E. J.; Young, D. D. Fluorescence Modulation of Green Fluorescent Protein Using Fluorinated Unnatural Amino Acids. *Molecules* **2017**, *22*, 1194.

[42] Paige, J. S.; Wu, K. Y.; Jaffrey, S. R. RNA Mimics of Green Fluorescent Protein. *Science* **2011**, *333*, 642-646.

[43] Povarova, N. V.; Bozhanova, N. G.; Sarkisyan, K. S.; Gritcenko, R.; Baranov, M. S.; Yampolsky, I. V.; Lukyanov, K. A.; Mishin, A. S. Docking-Guided Identification of Protein Hosts for GFP Chromophore-Like Ligands. *J. Mater. Chem. C* **2016**, *4*, 3036-3040.

[44] Chen, C.; Baranov, M. S.; Zhu, L.; Baleeva, N. S.; Smirnov, A. Y.; Zaitseva, S.; Yampolsky, I. V.; Solntsev, K. M.; Fang, C. Designing Redder and Brighter Fluorophores by Synergistic Tuning of Ground and Excited States. *Chem. Commun.* **2019**, *55*, 2537-2540.

[45] Kumpulainen, T.; Lang, B.; Rosspeintner, A.; Vauthey, E. Ultrafast Elementary Photochemical Processes of Organic Molecules in Liquid Solution. *Chem. Rev.* **2017**, *117*, 10826-10939.

[46] Fang, C.; Tang, L.; Oscar, B. G.; Chen, C. Capturing Structural Snapshots during Photochemical Reactions with Ultrafast Raman Spectroscopy: From Materials Transformation to Biosensor Responses. *J. Phys. Chem. Lett.* **2018**, *9*, 3253-3263.

[47] Hoffman, D. P.; Ellis, S. R.; Mathies, R. A. Characterization of a Conical Intersection in a Charge-Transfer Dimer with Two-Dimensional Time-Resolved Stimulated Raman Spectroscopy. *J. Phys. Chem. A* **2014**, *118*, 4955-4965.

[48] Quick, M.; Dobryakov, A. L.; Ioffe, I. N.; Granovsky, A. A.; Kovalenko, S. A.; Ernsting, N. P. Perpendicular State of an Electronically Excited Stilbene: Observation by Femtosecond-Stimulated Raman Spectroscopy. *J. Phys. Chem. Lett.* **2016**, *7*, 4047-4052.

[49] Hall, C. R.; Conyard, J.; Heisler, I. A.; Jones, G.; Frost, J.; Browne, W. R.; Feringa, B. L.; Meech, S. R. Ultrafast Dynamics in Light-Driven Molecular Rotary Motors Probed by Femtosecond Stimulated Raman Spectroscopy. *J. Am. Chem. Soc.* **2017**, *139*, 7408-7414.

[50] Chen, C.; Liu, W.; Baranov, M. S.; Baleeva, N. S.; Yampolsky, I. V.; Zhu, L.; Wang, Y.; Shamir, A.; Solntsev, K. M.; Fang, C. Unveiling Structural Motions of a Highly Fluorescent Superphotoacid by Locking and Fluorinating the GFP Chromophore in Solution. *J. Phys. Chem. Lett.* **2017**, *8*, 5921-5928.

[51] Hontani, Y.; Kloz, M.; Polívka, T.; Shukla, M. K.; Sobotka, R.; Kennis, J. T. M. Molecular Origin of Photoprotection in Cyanobacteria Probed by Watermarked Femtosecond Stimulated Raman Spectroscopy. *J. Phys. Chem. Lett.* **2018**, *9*, 1788-1792.

[52] Eigen, M. Proton Transfer, Acid-Base Catalysis, and Enzymatic Hydrolysis. *Angew. Chem., Int. Ed. Engl.* **1964**, *3*, 1-19.

[53] Zhu, L.; Liu, W.; Fang, C. A Versatile Femtosecond Stimulated Raman Spectroscopy Setup with Tunable Pulses in the Visible to Near Infrared. *Appl. Phys. Lett.* **2014**, *105*, 041106.

[54] Tachibana, S. R.; Tang, L.; Zhu, L.; Liu, W.; Wang, Y.; Fang, C. Watching an Engineered Calcium Biosensor Glow: Altered Reaction Pathways before Emission. *J. Phys. Chem. B* **2018**, *122*, 11986-11995.

[55] Tang, L.; Zhu, L.; Taylor, M. A.; Wang, Y.; Remington, S. J.; Fang, C. Excited State Structural Evolution of a GFP Single-Site Mutant Tracked by Tunable Femtosecond-Stimulated Raman Spectroscopy. *Molecules* **2018**, *23*, 2226.

[56] Baleeva, N. S.; Myannik, K. A.; Yampolsky, I. V.; Baranov, M. S. Bioinspired Fluorescent Dyes Based on a Conformationally Locked Chromophore of the Fluorescent Protein Kaede. *Eur. J. Org. Chem.* **2015**, *2015*, 5716-5721.

[57] Sasaki, S.; Drummen, G. P. C.; Konishi, G. i. Recent Advances in Twisted Intramolecular Charge Transfer (TICT) Fluorescence and Related Phenomena in Materials Chemistry. *J. Mater. Chem. C* **2016**, *4*, 2731-2743.

[58] van Stokkum, I. H. M.; Larsen, D. S.; van Grondelle, R. Global and Target Analysis of Time-Resolved Spectra. *Biochim. Biophys. Acta, Bioenerg.* **2004**, *1657*, 82-104.

[59] Snellenburg, J. J.; Laptenok, S. P.; Seger, R.; Mullen, K.; van Stokkum, I. H. M. Glotaran: A Java-based Graphical User Interface for the R-package TIMP. *J. Stat. Softw.* **2012**, *49*, 1-22.

[60] Kuzmin, M. G.; Soboleva, I. V.; Ivanov, V. L.; Gould, E. A.; Huppert, D.; Solntsev, K. M. Competition and Interplay of Various Intermolecular Interactions in Ultrafast Excited-State Proton and Electron Transfer Reactions. *J. Phys. Chem. B* **2015**, *119*, 2444-2453.

[61] Berera, R.; van Grondelle, R.; Kennis, J. M. Ultrafast Transient Absorption Spectroscopy: Principles and Application to Photosynthetic Systems. *Photosynth. Res.* **2009**, *101*, 105-118.

[62] Pines, E.; Huppert, D.; Agmon, N. Geminate Recombination in Excited-State Proton-Transfer Reactions: Numerical Solution of the Debye–Smoluchowski Equation with Backreaction and Comparison with Experimental Results. *J. Chem. Phys.* **1988**, *88*, 5620.

[63] Simkovitch, R.; Akulov, K.; Shomer, S.; Roth, M. E.; Shabat, D.; Schwartz, T.; Huppert, D. Comprehensive Study of Ultrafast Excited-State Proton Transfer in Water and D2O Providing the Missing RO$^-\cdots$H$^+$ Ion-Pair Fingerprint. *J. Phys. Chem. A* **2014**, *118*, 4425-4443.

[64] Mohammed, O. F.; Dreyer, J.; Magnes, B. Z.; Pines, E.; Nibbering, E. T. J. Solvent-Dependent Photoacidity State of Pyranine Monitored by Transient Mid-Infrared Spectroscopy. *ChemPhysChem* **2005**, *6*, 625-636.

[65] Pines, E.; Pines, D.; Ma, Y. Z.; Fleming, G. R. Femtosecond Pump-Probe Measurements of Solvation by Hydrogen-Bonding Interactions. *ChemPhysChem* **2004**, *5*, 1315-1327.

[66] Maroncelli, M.; Macinnis, J.; Fleming, G. R. Polar Solvent Dynamics and Electron-Transfer Reactions. *Science* **1989**, *243*, 1674-1681.

[67] Tang, L.; Wang, Y.; Zhu, L.; Kallio, K.; Remington, S. J.; Fang, C. Photoinduced Proton Transfer Inside an Engineered Green Fluorescent Protein: A Stepwise-Concerted-Hybrid Reaction. *Phys. Chem. Chem. Phys.* **2018**, *20*, 12517-12526.

[68] Hoffman, D. P.; Mathies, R. A. Femtosecond Stimulated Raman Exposes the Role of Vibrational Coherence in Condensed-Phase Photoreactivity. *Acc. Chem. Res.* **2016**, *49*, 616.

[69] Kukura, P.; McCamant, D. W.; Mathies, R. A. Femtosecond Stimulated Raman Spectroscopy. *Annu. Rev. Phys. Chem.* **2007**, *58*, 461-488.

[70] Oscar, B. G.; Chen, C.; Liu, W.; Zhu, L.; Fang, C. Dynamic Raman Line Shapes on an Evolving Excited-State Landscape: Insights from Tunable Femtosecond Stimulated Raman Spectroscopy. *J. Phys. Chem. A* **2017**, *121*, 5428-5441.

[71] Chen, C.; Zhu, L.; Fang, C. Femtosecond Stimulated Raman Line Shapes: Dependence on Resonance Conditions of Pump and Probe Pulses. *Chin. J. Chem. Phys.* **2018**, *31*, 492.

[72] Liu, W.; Tang, L.; Oscar, B. G.; Wang, Y.; Chen, C.; Fang, C. Tracking Ultrafast Vibrational Cooling during Excited-State Proton Transfer Reaction with Anti-Stokes and Stokes Femtosecond Stimulated Raman Spectroscopy. *J. Phys. Chem. Lett.* **2017**, *8*, 997-1003.

[73] Cohen, B.; Huppert, D. Unusual Temperature Dependence of Excited State Proton Transfer Rates in Alcohols. *J. Phys. Chem. A* **2000**, *104*, 2663-2667.

[74] Baumler, S. M.; Mutchler, J. M.; Blanchard, G. J. Comparing Rotational and Translational Diffusion to Evaluate Heterogeneity in Binary Solvent Systems. *J. Phys. Chem. B* **2019**, *123*, 216-224.

[75] Tolbert, L. M.; Solntsev, K. M.; Hynes, J. T.; Klinman, J. P.; Limbach, H. H.; Schowen, R. L. *Hydrogen-Transfer Reactions*, 2007.

[76] Han, F.; Liu, W.; Fang, C. Excited-State Proton Transfer of Photoexcited Pyranine in Water Observed by Femtosecond Stimulated Raman Spectroscopy. *Chem. Phys.* **2013**, *422*, 204-219.

[77] Jimenez, R.; Fleming, G. R.; Kumar, P. V.; Maroncelli, M. Femtosecond Solvation Dynamics of Water. *Nature* **1994**, *369*, 471-473.

[78] Agmon, N. The Grotthuss Mechanism. *Chem. Phys. Lett.* **1995**, *244*, 456-462.

[79] Levine, B. G.; Martínez, T. J. Isomerization Through Conical Intersections. *Annu. Rev. Phys. Chem.* **2007**, *58*, 613-634.

[80] Granucci, G.; Hynes, J. T.; Millie, P.; Tran-Thi, T. H. A Theoretical Investigation of Excited-State Acidity of Phenol and Cyanophenols. *J. Am. Chem. Soc.* **2000**, *122*, 12243-12253.

[81] Westlake, B. C.; Brennaman, M. K.; Concepcion, J. J.; Paul, J. J.; Bettis, S. E.; Hampton, S. D.; Miller, S. A.; Lebedeva, N. V.; Forbes, M. D. E.; Moran, A. M.; Meyer, T. J.; Papanikolas, J. M. Concerted Electron-Proton Transfer in the Optical Excitation of Hydrogen-Bonded Dyes. *Proc. Natl. Acad. Sci. U. S. A.* **2011**, *108*, 8554-8558.

Chapter 6 ESPT Dynamics of GFP Chromophore-Derived Photoacids in Water: Fluorescent *versus* Non-fluorescent Superphotoacids[e]

6.1 Introduction

The green fluorescent protein (GFP) discovered in the jellyfish *Aequorea victoria* has been widely used as a fluorescence marker in bioimaging applications.[1-3] The pertinent mechanistic research has facilitated the development of a broad library of fluorescent proteins (FPs) with versatile functions for various imaging and sensing applications.[4,5] Despite their diverse properties, many FPs share the same chromophore motif, p-hydroxybenzylidene-imidazolinone (*p*-HBDI, Figure 6.1), which highlights the importance of sidechain modifications and protein environment-chromophore interactions in governing the FP functions. Notably, in contrast to an intact protein chromophore undergoing efficient excited-state proton transfer (ESPT) with a high fluorescence quantum yield (FQY),[4,6,7] the synthetic chromophore *p*-HBDI exhibits distinctly different excited-state dynamics in solution, leading to no fluorescence. It has been established that the FQY loss in solution is caused by facile torsional motions around the methine bridge of the chromophore; however, the exact mechanism is still

unclear. Two mechanisms centered on the C=C isomerization coordinate have been proposed: one-bond-flip (C=C torsion) and hula-twist (concerted C=C and C−C torsion).[8-11] This nonradiative decay is rather fast (up to a few picoseconds), and the excited-state dynamics are essentially dominated by the S_1/S_0 internal conversion instead of an ESPT reaction followed by fluorescence as prevalent in the protein matrix.

In essence, the competition between ESPT and other decay pathways determines the photophysics/photochemistry of the protonated p-HBDI in solution and GFP. The pK_a* (photoacidity or excited-state acidity) of p-HBDI in aqueous solution is predicted to be ~2.1 by the Förster equation, hence classified as a weak photoacid.[12] It corresponds to a 2–3 orders of magnitude slower ESPT process with respect to torsional motions.[10,13] Baranov et al. reported that the conformationally locked GFP chromophores resemble GFP in terms of ESPT, electronic transitions, and FQY.[14] The borylation-locked chromophore, p-HOBDI-BF$_2$, exhibits ESPT to water with a rate constant of 0.45 ns^{-1}. Such a slow ESPT process is enabled by conformational locking that extends the excited-state lifetime. The internal locking greatly suppresses both free C−C rotation and C=C isomerization (Figure 6.1) and hence leads to a high FQY in solution. This case differs from another modified p-HBDI analog, p-LHBDI, where only the C−C bond is exolocked such that C−C rotational motion is restricted. As a result, p-LHBDI does not experience a significant FQY boost and remains nonfluorescent (FQY ~ 10^{-4}).[15] These studies support the double-bond isomerization as a major decay pathway. We note that the pK_a value of p-HOBDI-BF$_2$ (~6.4) with structural restraints is lower than those of p-HBDI (~8.5) and p-LHBDI[16] (~8.2) in aqueous solution. This could be

ascribed to the torsional degrees of freedom of non-BF$_2$-locked compounds that lead to an enhanced entropic contribution ($\Delta S^0 < 0$, hence larger $|T\Delta S^0|$) to the free energy change (ΔG^0) in the ground-state PT reaction (deprotonation in this case).[17,18]

Recently, we reported the fluorinated and internally locked *p*-HBDI analogs that are highly fluorescent superphotoacids.[18,19] They undergo ESPT not only in water but also in nonaqueous solvents such as alcohols. In methanol, the elucidated inhomogeneous dynamics consist of three parallel ESPT pathways: direct, solvation-controlled, and rotational diffusion-controlled across a broad time regime from sub-picosecond (sub-ps) to hundreds of picoseconds. The nanosecond (ns) excited-state lifetimes of these locked molecules play an important role in the observation of slower ESPT processes, since otherwise a slower ESPT may be truncated or overwhelmed by faster nonradiative decay pathways. However, little light has been shed on ESPT dynamics of these superphotoacids in aqueous solution, and several intriguing questions arise that need to be addressed. First, how does dihalogenation near the proton dissociation site affect the ESPT rate? Second, how would the conformational locking or reduced nonradiative decay modulate the ESPT pathways?

To address these questions, we modified p-HBDI into nonfluorescent and fluorescent superphotoacids to enable and disable the ultrafast isomerization-induced decay, respectively. The superphotoacidity is achieved by difluorinating and dibrominating the phenolic ring at the sites adjacent to the phenolic hydroxyl group. Fluorescence is turned on by conformationally locking *p*-HBDI through borylation (Figure 6.1). The

four molecules under study are labeled 2F, 2Br, L2F, and L2Br, where "L" denotes the locked version. Halogenation weakens the O−H bond and decreases the pK_a by several units from 8.5 in *p*-HBDI to 4–6 in these photoacids (Table 6.1). The dibrominated compounds exhibit lower pK_a than the difluorinated counterparts, and their pK_a* values have the same ordering on the basis of the Förster equation.[14,19] The locked photoacids show slightly lower pK_a than the unlocked counterparts due to the entropic contributions (ΔS^0), and the small difference is likely because the dihalogenation-induced enthalpy difference (ΔH^0) dominates the free energy change (ΔG^0) over the entropy term ($-T\Delta S^0$), which is also observed in our previous work. Furthermore, the locked compounds (L2F and L2Br) are highly fluorescent (FQY ~ 0.8), while the unlocked compounds (2F and 2Br) are essentially nonfluorescent (FQY ~ 10^{-4}).
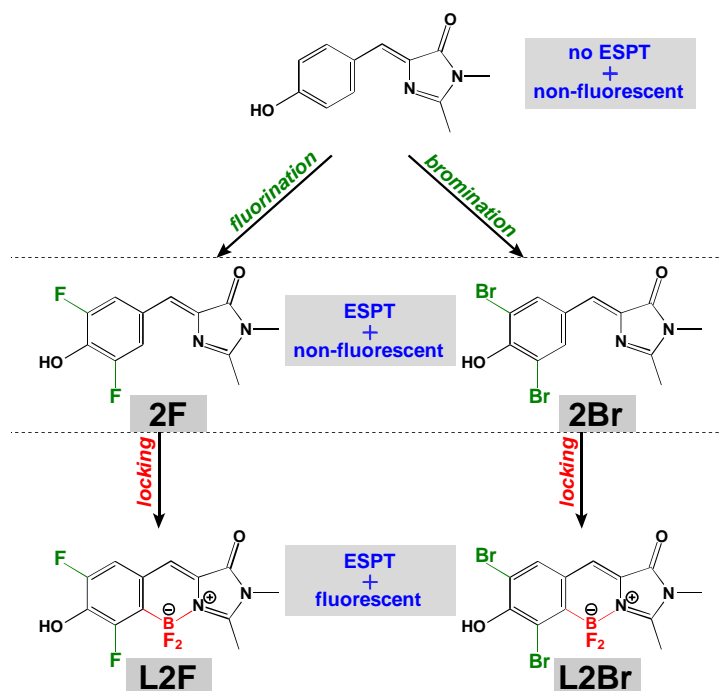
Figure 6.1. Chemical structures of difluorinated and dibrominated *p*-HBDI without and with conformational locking: 2F, 2Br, L2F, and L2Br. Adapted with permission from Cheng Chen et al., *J. Chem. Phys.* **2020**, 152, 021101. Copyright 2020 AIP Publishing.

6.2 Experimental

1a, 2a: $R_1=R_2=F$ **1b, 2b:** $R_1=R_2=Br$
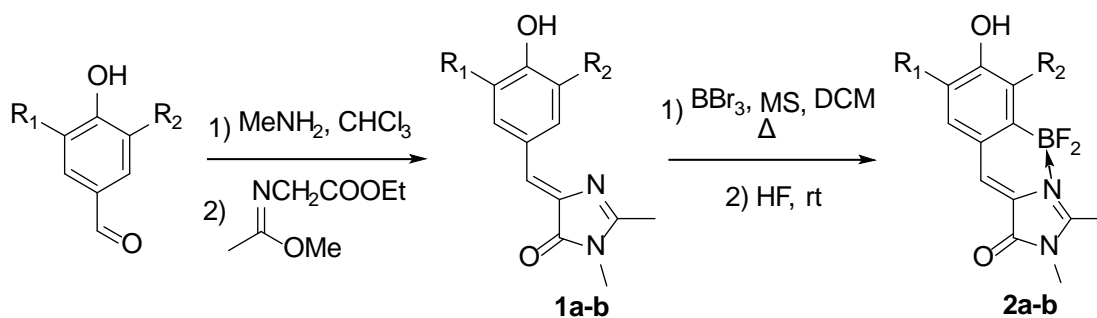
Figure 6.2. Synthesis of compounds 2F, 2Br, L2F, and L2Br. Reproduced with permission from Cheng Chen et al., *J. Chem. Phys.* **2020**, 152, 021101. Copyright 2020 AIP Publishing.

Synthesis procedures of the unlocked dihalogenated compounds. A 40% aqueous methylamine solution (60 mmol) and anhydrous sodium sulfate (20 g) were added to the solution of corresponding aldehyde (20 mmol) in chloroform (100 mL). The mixture was stirred for 48 hours at room temperature, filtered and dried over additional Na_2SO_4. The solvent was evaporated and ethyl ((1-methoxy)amino)acetate[20] (3.5 g, 22 mmol) and methanol (3 mL) were added. The mixture was stirred for 24 hours at room temperature, solvents were removed in vacuum, and the product **1** was purified by column chromatography (CHCl$_3$-EtOH 20:1).

(*Z*)-4-(3,5-difluoro-4-hydroxybenzylidene)-1,2-dimethyl-1*H*-imidazol-5(4*H*)-one (1a) Yellow solid (3.33 g, 66%); ^{1}H NMR (700 MHz, 303 K, DMSO-d_6) δ ppm 10.88 (s, 1H), 7.96 (d, *J*=9.7 Hz, 2H), 6.89 (s, 1H), 3.09 (s, 3H), 2.36 (s, 3H).[19]

(*Z*)-4-(3,5-dibromo-4-hydroxybenzylidene)-1,2-dimethyl-1*H*-imidazol-5(4*H*)-one

(1b) Yellow solid (2.02 g, 27%); ^{1}H NMR (700 MHz, 303 K, DMSO-d_6) δ ppm 10.52

(br. s., 1H), 8.46 (s, 2H), 6.89 (s, 1H), 3.09 (s, 3H), 2.36 (s, 3H).[21]

Synthesis procedures of the locked dihalogenated compounds. (*Z*)-4-(3,5-dibromo-

4- hydroxybenzylidene)-1,2-dimethyl-1*H*-imidazol-5(4*H*)-one (**1b**) (5.0 mmol) was

dissolved in 50 mL dry $(CH_2Cl)_2$. Molecular sieves 4Å (4 g) and 3Å (4g) were added,

followed by a solution of boron tribromide in CH_2Cl_2 (1M, 20 mL, 20.0 mmol). The

reaction mixture was refluxed for 6 hours under inert atmosphere, followed by cooling

and filtering; molecular sieves were washed two times with ethanol (20 mL) and

CH_2Cl_2 (100 mL). The obtained solution was mixed with aqueous HF (20%, 5 mL) and

stirred for 30 minutes. The mixture was then dissolved in EtOAc (100 mL), washed

with potassium carbonate solution (5%, 2×50mL), water (2×50 mL), brine (2×50 mL),

and dried over Na_2SO_4. The solvent was evaporated and the product **2b** was purified

by column chromatography ($CHCl_3$-EtOH 10:1). A similar procedure for (*Z*)-4-(2-

difluoroboryl-3,5-difluoro-4-hydroxybenzylidene)-1,2-dimethyl-1*H*-imidazol-5(4*H*)-

one **(2a)** has been reported in our previous publications.[19,22]

(*Z*)-4-(3,5-difluoro-2-(difluoroboryl)-4-hydroxybenzylidene)-1,2-dimethyl-1*H*-

imidazol-5(4*H*)-one (2a) Yellow solid, ^{1}H NMR (DMSO-d_6) δ ppm 10.91 (s, 1H), 7.55

(s, 1H), 7.39 (d, *J*=10.5 Hz, 1H), 3.22 (s, 3H), 2.73 (s, 3H); ^{13}C NMR (DMSO-d_6) δ

ppm 166.7, 162.6, 154.6, 151.3, 137.4, 126.8, 125.9, 123.9, 115.2, 26.5, 13.0;2 and [19]F

NMR (564 MHz, DMSO-d_6) δ: −138.06 (br. s), −134.30 (d, J=14.31 Hz), −125.76 (dd, J=12.78, 5.62 Hz).[22]

(Z)-4-(3,5-dibromo-2-(difluoroboryl)-4-hydroxybenzylidene)-1,2-dimethyl-1*H*-imidazol-5(4*H*)-one (2b) Dark yellow solid (568 mg, 27%); m.p. ~310 °C with decomposition; ^{1}H NMR (700 MHz, 303 K, DMSO-d_6) δ ppm 10.33 (br. s., 1H), 7.92 (s, 1H), 7.57 (s, 1H), 3.22 (s, 3H), 2.74 (s, 3H); ^{13}C NMR (176 MHz, 303 K, DMSO-d_6) δ ppm 166.8, 162.6, 153.4, 135.7, 128.1, 126.0, 125.5, 117.4, 110.2, 26.6, 13.0; HRMS (high-resolution mass spectra, via ESI) m/z: 420.8997 found (calculated for $C_{12}H_8BBr_2F_2N_2O_2{}^-$, [M–H]$^-$ 420.8999).

6.3 Results and discussions

6.3.1 Steady-state absorption and emission

Upon varying pH, two forms are present in L2F and L2Br, attributed to the neutral and anionic forms (Figure 6.3c and 6.3d), while 2F and 2Br show a cationic form due to N-protonation at the imidazolinone ring at very low pH in addition to the neutral/anionic forms at the phenolic moiety (Figure 6.3a and 6.3b). In the absorption spectra, the cation peak is red-shifted with respect to the neutral form. This result is rationalizable by the photobase nature of the imidazolinone moiety at the π-conjugated N site for which its protonated state lies lower in energy than its unprotonated state.[23] The emission spectra show that the excitation of neutral and/or cationic states results in ESPT for all four chromophores. In particular, the emission spectrum after excitation of the cationic form has a dual-band profile, with the higher-energy band clearly attributable to the cationic emission that is redder than the neutral emission (Figure 6.3a and 6.3b). The lower-energy band is likely due to the zwitterion rather than the anion because it is to the red side of the anionic emission band (Table 6.1). More importantly, the photoinduced intramolecular charge transfer (ICT) from the phenolic to imidazolinone moiety of the *p*-HBDI backbone[18,22] would lead to an increase in photobasicity at the imidazolinone N site, rendering the protonation even more robust with a further stabilized zwitterionic emission state.
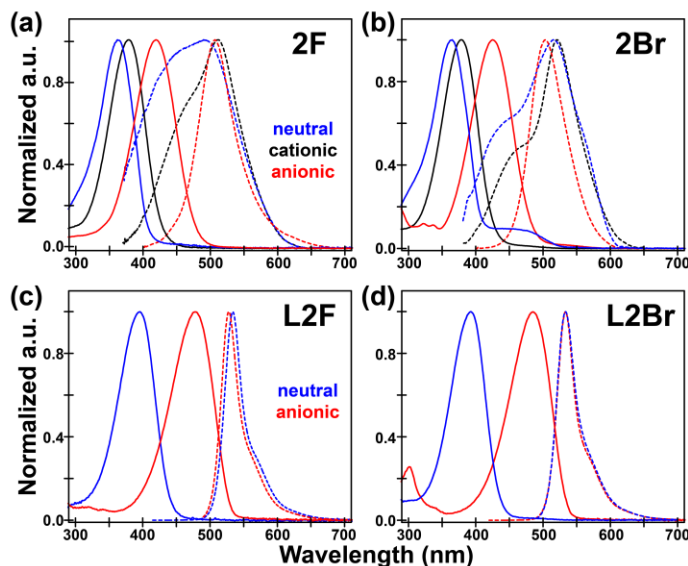
Figure 6.3. Normalized absorption (solid) and emission spectra (dotted) of (a) 2F, (b) 2Br, (c) L2F, and (d) L2Br in aqueous solution. The absorption spectra of cationic, neutral, and anionic forms are colored in black, blue, and red, respectively, the excitation of which leads to the corresponding color-coded emission spectra. Adapted with permission from Cheng Chen et al., *J. Chem. Phys.* **2020**, 152, 021101. Copyright 2020 AIP Publishing.

Table 6.1. Photophysical properties of dihalogenated *p*-HBDI derivatives in water.

	Abs./em. (nm/nm)[a]				pK_a	ΔpK_a[b]	pK_a*[b]	FQY[c]
	neutral	anion	cation	zwitterion				
2F	364/445	419/506	377/458	$-$[d]/514	5.7	7.6	-1.9	2×10^{-4}
2Br	365/445	425/500	379/453	$-$[d]/520	4.9	8.1	-3.2	3×10^{-4}
L2F	395/$-$[e]	478/527	$-$/$-$[f]	$-$/$-$[f]	5.5	9.2	-3.7	0.81
L2Br	392/$-$[e]	485/532	$-$/$-$[f]	$-$/$-$[f]	4.6	10.3	-5.7	0.80

[a]Emission maxima are extracted by second-derivative spectral analysis.

[b]Absorption maxima are used to estimate ΔpK_a and pK_a*. The temperature is 298 K.

[c]FQY of the anionic form upon anionic form excitation. Coumarin 153 and fluorescein sodium salt were used as standards for the FQY measurements of 2F/2Br and L2F/L2Br, respectively. We also removed the water scattering band fit by a gaussian (especially needed for 2F/2Br with low emission counts).

[d]No zwitterionic form is present in the electronic ground state or resolvable from the absorption spectrum.

[e]Not observed due to the highly efficient ESPT in water.

[f]No cationic and zwitterionic forms at N site in L2F and L2Br due to BF_2 locking.

6.3.2 ESPT dynamics from fs-TA

To elucidate the ESPT dynamics of these fluorescent and nonfluorescent chromophores in aqueous solution, time-resolved femtosecond transient absorption (fs-TA) spectroscopy[24] was employed by the excitation of the cationic form of 2F and 2Br and the neutral form of L2F and L2Br. Details about our ultrafast spectroscopic setups and fs-TA experiments using the femtosecond 400 nm pump and supercontinuum white light probe can be found in some previous reports.[19,25-27] The neutral form excitation was not chosen for 2F and 2Br due to their low solubility at the corresponding pH conditions while the resultant weak absorption band between 350 and 400 nm does not support an effective excitation by a 400 nm pulse (i.e., from second harmonic generation of the 800 nm laser fundamental output).[7,28] In comparison, the cationic form with better solubility in water absorbs redder than the neutral form, therefore

making the 400 nm excitation viable. Besides, Meech et al. reported time-resolved fluorescence dynamics for the difluorinated *p*-HBDI (termed 2F in this work) and showed that the cationic and neutral excitations yield very similar ESPT dynamics, reflective of their similar photoacidity.[29]

Notably, fs-TA spectra of 2F, 2Br, L2F, and L2Br in Figure 6.4a, 6.4b, 6.5a, and 6.5b all feature a stimulated emission (SE) band conversion from blue (~450–480 nm) to red (~520–530 nm), characteristic of ESPT. This can be verified by comparing the SE band positions to steady-state emission spectra (Figure 6.3). It appears that starting from the reactant species (i.e., the photoexcited acid form or A*), the locked compounds (L2F and L2Br) have slower ESPT rates than the unlocked compounds (2F and 2Br). The SE band of the photoproduct (i.e., the conjugate base or B*) reaches its maximum intensity within the first picosecond for the unlocked superphotoacids (Figure 6.4), while the locked ones reach the maximum at a few tens of picoseconds (Figure 6.5). The subsequent B* decay dynamics in 2F and 2Br are dominated by the torsional coordinates that lead to picosecond excited-state lifetimes (Figure 6.4a and 6.4b). Meanwhile, this SE band decay is accompanied by the rise of a positive absorption band at ~480 nm that decays afterward on the tens of picoseconds timescale. The origin of this transient band cannot be the trans isomer as the $C=C$ bond isomerization usually leads to a long-lived trans photoproduct that needs to overcome a high barrier of reverse isomerization in the ground state (S_0).[11,30] Due to the passage through a peaked S_1/S_0 conical intersection with branching into two conformational states,[27,31] the hot ground state (HGS)[26] of the zwitterionic cis form is supported by the

red-shifted peak at ~480 nm with respect to the equilibrated ground-state absorption peak of the chromophore anion (~420 nm, Figure 6.3a and 6.3b, and Table 6.1) and zwitterion [not available from the experimental spectra but predicted to be 436 nm for 2F and 442.5 nm for 2Br by our time-dependent density functional theory (DFT) calculations at the B3LYP level with 6-311G+(d, p) basis sets].[32] In contrast, L2F and L2Br exhibit much lengthened B* decay dynamics on the nanosecond time scale due to the suppression of facile torsional motions (Figure 6.5a and 6.5b).

Global analysis of the fs-TA spectra dissects the ESPT dynamics via the evolution-associated difference spectra (EADS) shown in Figure 6.4c, 6.4d, 6.5c, and 6.5d, wherein three and five components under a sequential scheme were found to produce the best fit for the unlocked and locked superphotoacids, respectively. For 2F and 2Br, the first EADS exhibits dual SE peaks at ~460 and 520 nm, characteristic of A* (protonated at −OH) and B* species, respectively (black trace, Figure 6.4c and 6.4d). This indicates the ultrafast formation of B* within the cross-correlation time (~140 fs) following A* excitation. The A* SE band diminishes within 200 fs and converts to a B* SE band. Since a dominant species could be tracked at a key probe wavelength,[33] the "local" TA dynamics at ~520 nm reveal the B* population rise component of 90 fs for 2F (Figure 6.4e) and 150 fs for 2Br (Figure 6.4f), comparable to the decay at 460 nm (A*) but faster than the early-time decay at ~480 nm. As the B* rise is a better indicator for ESPT, the larger time constant retrieved from global analysis (i.e., 140 fs for 2F and 200 fs for 2Br) suggests that it goes beyond a directional two-state model and other nonradiative decay pathways depopulate A* in parallel with ESPT.
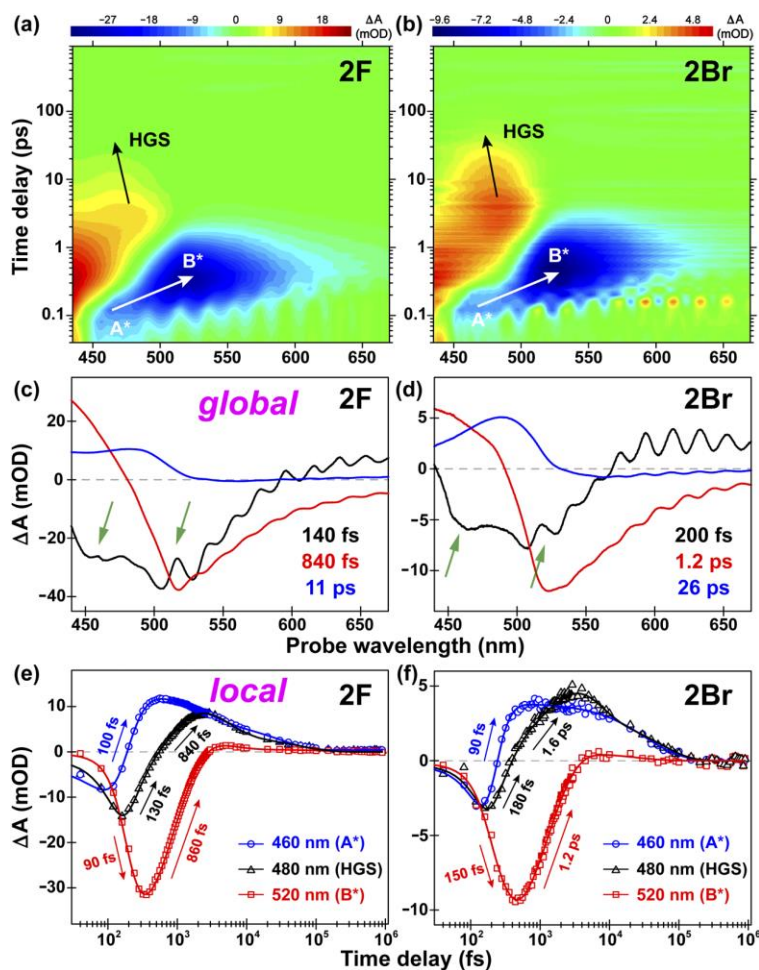
Figure 6.4. Time-resolved fs-TA dynamics of the unlocked HBDI derivatives. Semilogarithmic contour plots of fs-TA spectra of the cationic (a) 2F and (b) 2Br in pH=0.5 aqueous solution after 400 nm excitation. The ESPT reaction (A* → B*) is indicated by the white arrow marking the SE band evolution. The hot ground state (HGS) evolution is indicated by the tilted black arrow. Global analysis results of panels (a) and (b) are displayed in (c) and (d) for 2F and 2Br, respectively. Probe-dependent dynamics at three characteristic wavelengths are shown for (e) 2F and (f) 2Br with the least-squares fits in color-coded solid curves and the early-time constants listed. Reproduced with permission from Cheng Chen et al., *J. Chem. Phys.* **2020**, 152, 021101. Copyright 2020 AIP Publishing.
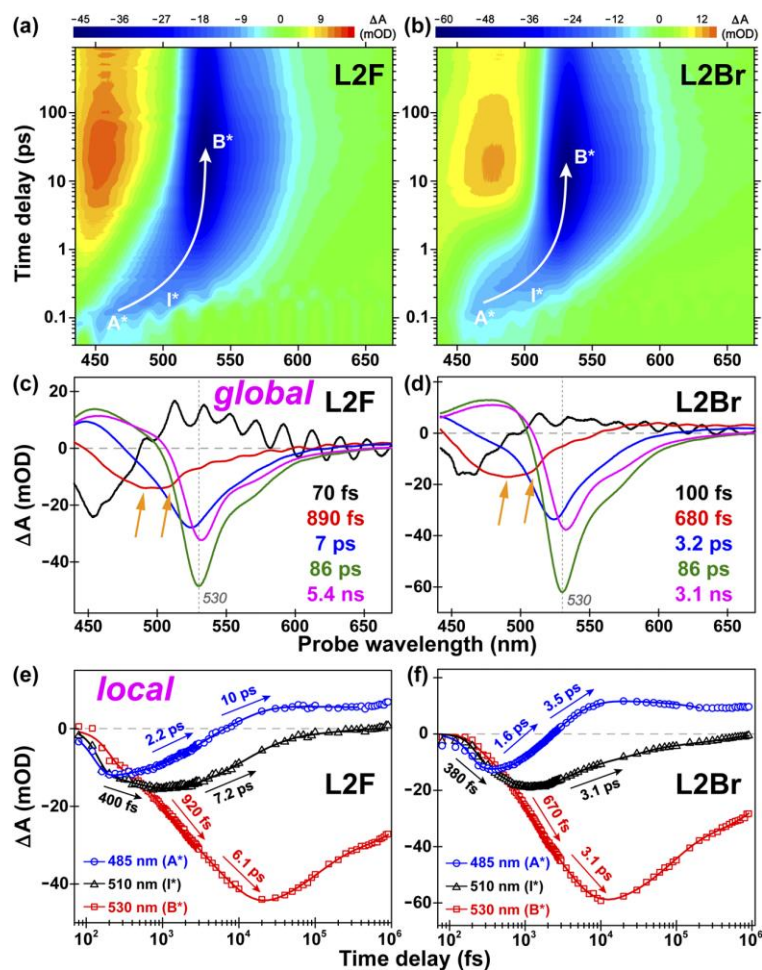
Figure 6.5. Time-resolved fs-TA dynamics of the locked HBDI derivatives. Semilogarithmic contour plots of fs-TA spectra of the neutral (a) L2F and (b) L2Br in pH=3 aqueous solution after 400 nm excitation. ESPT reaction (A* → I* → B*) is indicated by the curved arrow. Global analysis results of fs-TA data are shown in (c) L2F and (d) L2Br. Probe-wavelength-dependent "local" kinetic analyses at three characteristic locations are shown for (e) L2F and (f) L2Br with the least-squares fits in color-coded solid curves and time constants (up to 10 ps) listed. Reproduced with permission from Cheng Chen et al., *J. Chem. Phys.* **2020**, 152, 021101. Copyright 2020 AIP Publishing.

Further corroborating pieces of evidence are as follows: (1) The presence of A* and B* fluorescence upon excitation of A indicates that some A* population is trapped and decays through radiative emission despite the highly efficient ESPT (Figure 6.3a and 6.3b). (2) The decay-associated difference spectra (DADS, Figure 6.6) show that the ensemble-averaged A* lifetime is ~140 fs for 2F and 200 fs for 2Br, longer than their fastest ESPT time constant obtained by the B* rise (Figure 6.4e and 6.4f), in accord with various decay pathways from multiple A* subpopulations with different solute-solvent environments (e.g., H-bonding configurations).[18,19] Notably, the difference between A* lifetime and ESPT time constant may be reduced by our experimental cross-correlation time. The fluorescence up-conversion method used by Meech et al. yielded a larger difference between A* decay (~200 fs) and B* rise (~50 fs) dynamics of the same compound (2F here) with a sub-50 fs time resolution. Therefore, the ESPT reaction of 2F and 2Br in aqueous solution is ultrafast with a sub-100 fs time constant and can be considered kinetically barrierless.[13,19,29,34]

Following ESPT, the zwitterionic photoproduct or B* decays via isomerization likely through a conical intersection to the HGS,[27,35] characterized by the red → blue EADS conversion with a lifetime of ~1 ps (840 fs for 2F and 1.2 ps for 2Br). The zwitterionic HGS could then relax to the ground vibrational state (in accord with an apparent blueshift of the HGS absorption band) and undergo ground-state back proton transfer to regenerate the cationic form in water. These two processes may correspond to the ~480 nm HGS band biexponential decay time constants of 4.3−4.9 ps and 55–59 ps, respectively (see the long-time decay of black traces in Figure 6.4e and 6.4f).
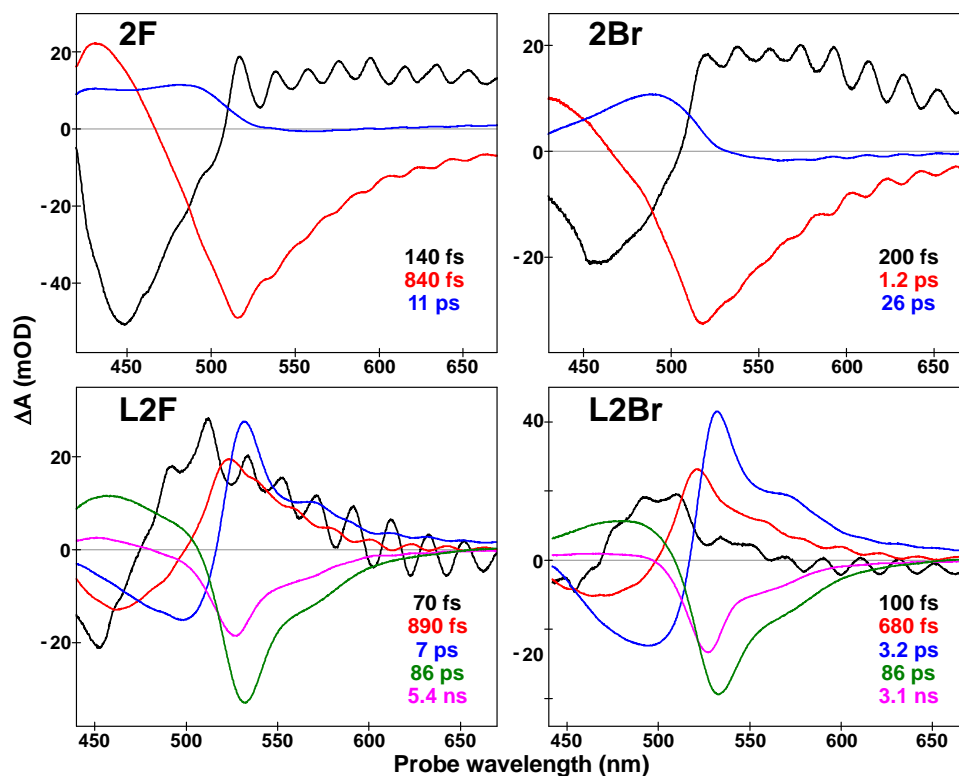
Figure 6.6. Decay-associated difference spectra (DADS) of time-resolved fs-TA spectra for the cationic 2F & 2Br and neutral L2F & L2Br in aqueous solutions after 400 nm excitation. The corresponding lifetimes are shown by the same colors. Reproduced with permission from Cheng Chen et al., *J. Chem. Phys.* **2020**, 152, 021101. Copyright 2020 AIP Publishing.

In contrast, L2F and L2Br show more complex dynamics involving solvent activities. The first EADS (black trace, Figure 6.5c and 6.5d) with a lifetime of 70–100 fs features an SE band at ~460 nm, assigned to the A* Franck-Condon (FC) region. The second EADS (red) exhibits a multiband profile with two dominant peaks at 485–490 and 505–510 nm. The former band is likely associated with the FC-relaxed A* inferred from Kamlet-Taft analysis in our previous work,[22] and hence, the vibrational cooling time

within A* is in the ~100 fs range. The latter, however, is debatable as its peak wavelength lies between the relaxed A* (~485 nm) and B* (~530 nm). The departure from the A* emission peak indicates that it undergoes certain degrees of O−H bond elongation or breaking from A* species, which remains solvated by the largely unoptimized H-bonding matrix due to the ultrashort reaction time of ~100 fs (lifetime of the initial EADS)[13,19,34] and can be denoted as I*.

Previous photoacid studies invoked a contact ion-pair (CIP) as an intermediate to account for the multistep dynamics, although the terminology has continued to be discussed in the literature.[18,36,37] Superphotoacids provide valuable insights into the intermediate state because they are typically rate-limited by solvent reorientation as a result of the photoinduced dipole moment change from S_0 to S_1.[13,38] In the case of L2F and L2Br, the red to blue EADS conversion is characteristic of local solvent reorientation or proton hopping in water since the time constant of 680–890 fs largely matches the literature value of 0.5–1.5 ps.[39-41] However, the notion that the aforementioned I* state characterized by the SE band at 505–510 nm is directly followed by further solvent reorientation, as the sequential model suggests, requires caution because global analysis with a sequential scheme may not represent true kinetics.[18] In this case, the probe-wavelength-dependent dynamics can provide complementary insights into ESPT pathways, especially when the retrieved time constants for ultrafast electronic dynamics match to a large extent.

In Figure 6.5e and 6.5f, the multiexponential fits at 485, 510, and 530 nm represent ultrafast dynamics of the FC-relaxed A*, I*, and the equilibrated B* states, respectively. After an initial ~100 fs rise, the A* SE band (at 485 nm) decay shows a solvent reorientation stage (2.2 ps for L2F and 1.6 ps for L2Br) and a longer time constant of 3.5–10 ps owing to the increase in an adjacent excited-state absorption band of B* (Figure 6.5). Interestingly, the I* SE band (at 510 nm) features an initial ~400 fs rise and a slower decay (7.2 ps for L2F and 3.1 ps for L2Br) that matches one component of the B* SE band rise dynamics (6.1 ps for L2F and 3.1 ps for L2Br, Figure 6.5e and 6.5f, while missing the local solvent reorientation component on a shorter timescale (670–920 fs).[13,39-41] This result is corroborated by the DADS analysis (Figure 6.6) showing a more defined SE band ascribed to I*, which has characteristic lifetimes of 7 and 3.2 ps for L2F and L2Br, respectively, and can be further validated by the target analysis (see below).

These results suggest that two distinct ESPT pathways are present for L2F and L2Br in water. One is the local solvent reorientation-controlled ESPT pathway, which can be considered as the "standard" dynamics for superphotoacids.[13,19] Note that the CIP is not invoked here due to the absence of a structurally distinct state from the relaxed A* (emission at 485–490 nm). The other pathway is mediated by an intermediate (I*) state that energetically lies between A* and B* states and is formed within the first ~400 fs (Figure 6.5a-d), which then undergoes a process longer than local solvent reorientation time to convert to B*. Due to the redder wavelength of the I* SE band with respect to the relaxed A* SE band, I* species has acquired B* or anionic character to some extent,

and its formation is favored by a relatively optimized local H-bonding configuration such that only small-scale solvent motions are required. The I* decay time constant (3–7 ps) is consistent with the Debye relaxation of water (~8 ps),[39] which usually involves long-range solvent reorganization or H-bond switching between water molecules beyond the first solvation shell. This process further stabilizes the solute, manifested as a Stokes shift of the SE band that was observed in L2F and L2Br (see curved arrows in Figure 6.5a and 6.5b). Due to the lengthened excited-state lifetimes in these locked compounds, the ESPT processes can be effectively completed and no discernible A* fluorescence is observed (Figure 6.3c and 6.3d, Table 6.1). The last two EADS characterize the B* decay dynamics with time constants of 86 ps and 3.1–5.4 ns, which are associated with major nonradiative and radiative pathways, respectively (green and magenta traces in Figure 6.3c and 6.3d).

In accord with this kinetic scheme, target analysis was performed (Figure 6.7), where the branching pathways occur from the Franck-Condon region. Reasonable species spectra are yielded when the I*-mediated ESPT pathway is greater than ~70% and 75% weight for L2F and L2Br, respectively. As we mentioned in Chapter 2, an important standard in examining the kinetic model in target analysis is that the output spectra should match the assumed spectral features of each species proposed in this model. Note that the SE positions of each SADS reasonably agree with the species assignment, validating the proposed reaction schemes. For instance, the I* SE band position lies between A* and B*, which agrees with the characteristics of I* likely with some degree of charge separation or bond elongation. We also found that when the branching ratio

of $1 \rightarrow 2$ transition is greater than ~30% for L2F and ~25% for L2Br (alternatively, the ratio of $1 \rightarrow 3$ transition is smaller than ~70% for L2F and ~75% for L2Br), the sign at ~530 nm of the red SADS would become negative (i.e., leading to dual SE features), making its specific assignment to an FC-relaxed A* state unreasonable. We therefore imply that the I*-mediated ESPT pathway constitutes at least ~70% for L2F and ~75% for L2Br, respectively, and present the reasonable branching ratios in the figure.
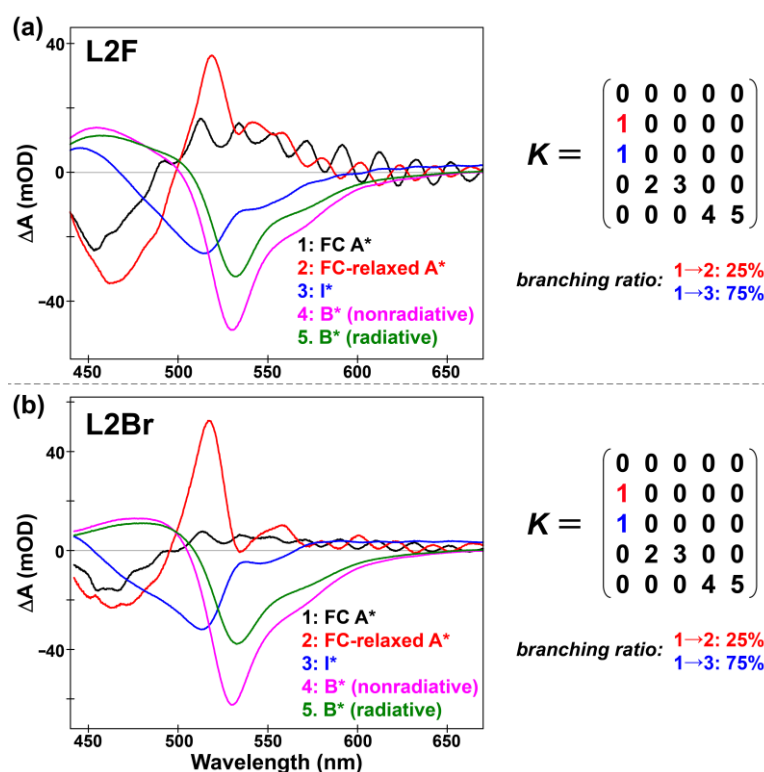
Figure 6.7. Species-associated difference spectra (SADS) of fs-TA spectra for (a) L2F and (b) L2Br in aqueous solutions. The kinetic scheme is described by the transfer matrix K where the off-diagonal elements indicate transitions from column to row. The branching ratios of $1 \rightarrow 2$ (Franck-Condon relaxation) and $1 \rightarrow 3$ transitions (I* formation) are set to be 25% and 75%, respectively. Reproduced with permission from Cheng Chen et al., *J. Chem. Phys.* **2020**, 152, 021101. Copyright 2020 AIP Publishing.

6.3.3 ESPT dynamics: fluorescent versus non-fluorescent superphotoacids

In aggregate, the unlocked superphotoacids (2F and 2Br) exhibit direct and ultrafast ESPT, whereas their locked counterparts (L2F and L2Br) are rate-limited by solvent motions and exhibit an overall slower ESPT reaction. Meanwhile, thermodynamics predicts L2F and L2Br to be more exergonic than 2F and 2Br as reflected by their pK_a* values (Table 6.1). This counterintuitive phenomenon is similar to the Marcus inverted region where the electron-transfer rates slow down as the reaction exergonicity increases.[42] It essentially correlates with an increased activation energy when the driving force is greater than the solvent reorganization energy. A similar theory could be applied to proton transfer as an appreciable amount of work has been performed through quantum treatment of a proton.[43-46] However, theoretical efforts on the photoinduced proton transfer remain scarce with respect to the thermally driven proton transfer.[47] We expect that future advances in computational chemistry could provide more insights into the ESPT dynamics for these contrasting GFP chromophore derivatives in this work. Moreover, isotopic labeling of these superphotoacids could shed more light.[19] From a classical perspective, we speculate that the structural difference between unlocked and locked compounds may result in intrinsically different H-bonding geometries near the chromophore where the solvent reorientation barrier is smaller for 2F and 2Br than for L2F and L2Br upon photoexcitation; hence, ultrafast ESPT on the ~100 fs time scale is only observed in 2F and 2Br. More importantly, structural restraints in the locked compounds effectively limit their phase space and conformational flexibilities. As a result, so after A* relaxation or I* formation within ~400 fs (Figure 6.8), two distinct solvent reorientation phases are

resolved on the ~1.5 ps and 7 ps time scales involving the first solvation shell and beyond, which substantiate a multi-staged dynamic portrait of locked superphotoacids (with A* subpopulations) undergoing ESPT surrounded by labile water molecules.
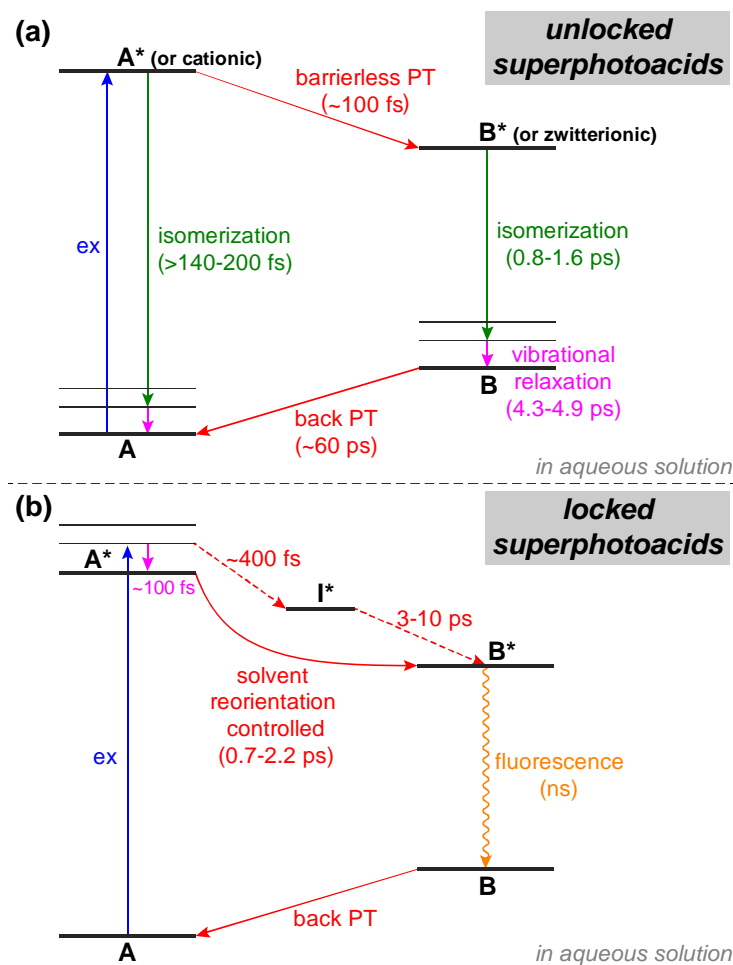
Figure 6.8. Schematic of ESPT pathways of the (a) unlocked and (b) locked superphotoacids in aqueous solutions. Pertinent electronic states and major internal conversion processes are color-coded with the characteristic time constants listed in panels (a) and (b) from Figure 6.4 and 6.5, respectively. Reproduced with permission from Cheng Chen et al., *J. Chem. Phys.* **2020**, 152, 021101. Copyright 2020 AIP Publishing.

6.3.4 Halogenation effect on ESPT and FQY

Furthermore, the difference between difluorination and dibromination is manifold in the context of ESPT and excited-state energy dissipation. First, bromination leads to lower pK_a and pK_a^* values than fluorination (Table 6.1), opposite to the ordering of their electron-withdrawing abilities (i.e., $-F > -Br$). This is usually considered as a consequence of the interplay between the electron-withdrawing effect and intramolecular H-bonding that connects $-OH$ to halogens in the ortho-substituted phenols.[48,49] Regarding ESPT dynamics, the unlocked compounds exhibit "inverted" kinetic behavior (2F is faster than 2Br), while the locked compounds show "normal" behavior (L2Br is faster than L2F), which could be a result of the interplay between the electronic distribution and nuclear motions. Second, bulkier halogens exert opposite effects on energy-dissipating pathways in the unlocked and locked compounds. In the unlocked case, bromination slows down the isomerization process (840 fs in 2F vs 1.2 ps in 2Br, Figure 6.4) and hence leads to a higher FQY than fluorination (Table 6.1). In contrast, bromination causes a tiny FQY drop in reference to fluorination in the locked case, which could be due to an increase in the size-dependent nonradiative decay pathways such as collision or thermal cooling.[25,50,51]

6.4 Conclusions

In conclusion, we investigated the ESPT dynamics of superphotoacids engineered from the GFP chromophore *p*-HBDI in aqueous solution. By strategic modification and systematic ultrafast characterization of the excited-state decay pathways via chemical synthesis and fs-TA spectroscopy, our results show that (1) the ESPT reaction rates display an inverted relationship between thermodynamics and kinetics, and (2) the conformationally locked fluorescent superphotoacids undergo two ESPT pathways with active solvent engagement, whereas the unlocked nonfluorescent superphotoacids exhibit essentially barrierless and more homogeneous ESPT dynamics with little solvent participation. Further details could be provided by advanced modeling and excited-state FSRS, which are currently underway in our laboratory. Since these rationally designed and engineered dihalogenated GFP chromophore derivatives retain a small size and are hydrophilic, they can be used in living systems. Moreover, their photoacidity and ESPT properties elucidated in this work could enable their optogenetic applications such as opening acid-sensitive ion channels (ASICs)[52] in live cells under light irradiation.

6.5 References

[1]   Shimomura, O.; Johnson, F. H.; Saiga, Y. Extraction, Purification and Properties of Aequorin, a Bioluminescent Protein from the Luminous Hydromedusan, Aequorea. *J. Cell. Comp. Physiol.* **1962**, *59*, 223-239.

[2]   Chalfie, M.; Tu, Y.; Euskirchen, G.; Ward, W.; Prasher, D. Green fluorescent protein as a marker for gene expression. *Science* **1994**, *263*, 802-805.

[3]   Tsien, R. Y. THE GREEN FLUORESCENT PROTEIN. *Annu. Rev. Biochem* **1998**, *67*, 509-544.

[4]   Zimmer, M. Green Fluorescent Protein (GFP): Applications, Structure, and Related Photophysical Behavior. *Chem. Rev.* **2002**, *102*, 759-782.

[5]   Chudakov, D. M.; Matz, M. V.; Lukyanov, S.; Lukyanov, K. A. Fluorescent Proteins and Their Applications in Imaging Living Cells and Tissues. *Physiol. Rev.* **2010**, *90*, 1103-1163.

[6]   Chattoraj, M.; King, B. A.; Bublitz, G. U.; Boxer, S. G. Ultra-fast excited state dynamics in green fluorescent protein: multiple states and proton transfer. *Proc. Natl. Acad. Sci. U.S.A.* **1996**, *93*, 8362-8367.

[7]   Fang, C.; Frontiera, R. R.; Tran, R.; Mathies, R. A. Mapping GFP Structure Evolution During Proton Transfer with Femtosecond Raman Spectroscopy. *Nature* **2009**, *462*, 200-204.

[8]   Weber, W.; Helms, V.; McCammon, J. A.; Langhoff, P. W. Shedding light on the dark and weakly fluorescent states of green fluorescent proteins. *Proc. Natl. Acad. Sci. U.S.A.* **1999**, *96*, 6177-6182.

[9]   Kummer, A. D.; Kompa, C.; Niwa, H.; Hirano, T.; Kojima, S.; Michel-Beyerle, M. E. Viscosity-Dependent Fluorescence Decay of the GFP Chromophore in Solution Due to Fast Internal Conversion. *J. Phys. Chem. B* **2002**, *106*, 7554-7559.

[10]   Litvinenko, K. L.; Webber, N. M.; Meech, S. R. Internal Conversion in the Chromophore of the Green Fluorescent Protein: Temperature Dependence and Isoviscosity Analysis. *J. Phys. Chem. A* **2003**, *107*, 2616-2623.

[11]   Yang, J.-S.; Huang, G.-J.; Liu, Y.-H.; Peng, S.-M. Photoisomerization of the green fluorescence protein chromophore and the meta- and para-amino analogues. *Chem. Commun.* **2008**, 1344-1346.

[12]   Bell, A. F.; He, X.; Wachter, R. M.; Tonge, P. J. Probing the Ground State Structure of the Green Fluorescent Protein Chromophore Using Raman Spectroscopy. *Biochemistry* **2000**, *39*, 4423-4431.

[13] Simkovitch, R.; Shomer, S.; Gepshtein, R.; Huppert, D. How Fast Can a Proton-Transfer Reaction Be beyond the Solvent-Control Limit? *J. Phys. Chem. B* **2015**, *119*, 2253-2262.

[14] Baranov, M. S.; Lukyanov, K. A.; Borissova, A. O.; Shamir, J.; Kosenkov, D.; Slipchenko, L. V.; Tolbert, L. M.; Yampolsky, I. V.; Solntsev, K. M. Conformationally Locked Chromophores as Models of Excited-State Proton Transfer in Fluorescent Proteins. *J. Am. Chem. Soc.* **2012**, *134*, 6025-6032.

[15] Hsu, Y.-H.; Chen, Y.-A.; Tseng, H.-W.; Zhang, Z.; Shen, J.-Y.; Chuang, W.-T.; Lin, T.-C.; Lee, C.-S.; Hung, W.-Y.; Hong, B.-C.; Liu, S.-H.; Chou, P.-T. Locked ortho- and para-Core Chromophores of Green Fluorescent Protein; Dramatic Emission Enhancement via Structural Constraint. *J. Am. Chem. Soc.* **2014**, *136*, 11805-11812.

[16] Solntsev, K. M.; Poizat, O.; Dong, J.; Rehault, J.; Lou, Y.; Burda, C.; Tolbert, L. M. Meta and Para Effects in the Ultrafast Excited-State Dynamics of the Green Fluorescent Protein Chromophores. *J. Phys. Chem. B* **2008**, *112*, 2700-2711.

[17] Scharnagl, C.; Raupp-Kossmann, R. A. Solution pK_a Values of the Green Fluorescent Protein Chromophore from Hybrid Quantum-Classical Calculations. *J. Phys. Chem. B* **2004**, *108*, 477-489.

[18] Chen, C.; Zhu, L.; Baranov, M. S.; Tang, L.; Baleeva, N. S.; Smirnov, A. Y.; Yampolsky, I. V.; Solntsev, K. M.; Fang, C. Photoinduced Proton Transfer of GFP-Inspired Fluorescent Superphotoacids: Principles and Design. *J. Phys. Chem. B* **2019**, *123*, 3804-3821.

[19] Chen, C.; Liu, W.; Baranov, M. S.; Baleeva, N. S.; Yampolsky, I. V.; Zhu, L.; Wang, Y.; Shamir, A.; Solntsev, K. M.; Fang, C. Unveiling Structural Motions of a Highly Fluorescent Superphotoacid by Locking and Fluorinating the GFP Chromophore in Solution. *J. Phys. Chem. Lett.* **2017**, *8*, 5921-5928.

[20] Meyers, A. I.; Lawson, J. P.; Walker, D. G.; Linderman, R. J. Synthetic studies on the streptogramin antibiotics. Enantioselective synthesis of the oxazole dienyl amine moiety. *J. Org. Chem.* **1986**, *51*, 5111-5123.

[21] Song, W.; Strack, R. L.; Svensen, N.; Jaffrey, S. R. Plug-and-Play Fluorophores Extend the Spectral Properties of Spinach. *J. Am. Chem. Soc.* **2014**, *136*, 1198-1201.

[22] Chen, C.; Baranov, M. S.; Zhu, L.; Baleeva, N. S.; Smirnov, A. Y.; Zaitseva, S. O.; Yampolsky, I. V.; Solntsev, K. M.; Fang, C. Designing redder and brighter fluorophores by synergistic tuning of ground and excited states. *Chem. Commun.* **2019**, *55*, 2537-2540.

[23] Driscoll, E. W.; Hunt, J. R.; Dawlaty, J. M. Photobasicity in Quinolines: Origin and Tunability via the Substituents' Hammett Parameters. *J. Phys. Chem. Lett.* **2016**, *7*, 2093-2099.

[24]   Berera, R.; van Grondelle, R.; Kennis, J. T. M. Ultrafast transient absorption spectroscopy: principles and application to photosynthetic systems. *Photosynth. Res.* **2009**, *101*, 105-118.

[25]   Liu, W.; Wang, Y.; Tang, L.; Oscar, B. G.; Zhu, L.; Fang, C. Panoramic portrait of primary molecular events preceding excited state proton transfer in water. *Chem. Sci.* **2016**, *7*, 5484-5494.

[26]   Tang, L.; Fang, C. Nitration of Tyrosine Channels Photoenergy through a Conical Intersection in Water. *J. Phys. Chem. B* **2019**, *123*, 4915-4928.

[27]   Taylor, M. A.; Zhu, L.; Rozanov, N. D.; Stout, K. T.; Chen, C.; Fang, C. Delayed vibrational modulation of the solvated GFP chromophore into a conical intersection. *Phys. Chem. Chem. Phys.* **2019**, *21*, 9728-9739.

[28]   Rini, M.; Magnes, B.-Z.; Pines, E.; Nibbering, E. T. J. Real-Time Observation of Bimodal Proton Transfer in Acid-Base Pairs in Water. *Science* **2003**, *301*, 349-352.

[29]   Laptenok, S. P.; Conyard, J.; Page, P. C. B.; Chan, Y.; You, M.; Jaffrey, S. R.; Meech, S. R. Photoacid behaviour in a fluorinated green fluorescent protein chromophore: ultrafast formation of anion and zwitterion states. *Chem. Sci.* **2016**, *7*, 5747-5752.

[30]   Chatterjee, T.; Lacombat, F.; Yadav, D.; Mandal, M.; Plaza, P.; Espagne, A.; Mandal, P. K. Ultrafast Dynamics of a Green Fluorescent Protein Chromophore Analogue: Competition between Excited-State Proton Transfer and Torsional Relaxation. *J. Phys. Chem. B* **2016**, *120*, 9716-9722.

[31]   Malhado, J. P.; Hynes, J. T. Photoisomerization for a model protonated Schiff base in solution: Sloped/peaked conical intersection perspective. *J. Chem. Phys.* **2012**, *137*, 22A543.

[32]   Frisch, M. J.; Trucks, G. W.; Schlegel, H. B.; Scuseria, G. E.; Robb, M. A.; Cheeseman, J. R.; Scalmani, G.; Barone, V.; Petersson, G. A.; Nakatsuji, H.; Li, X.; Caricato, M.; Marenich, A. V.; Bloino, J.; Janesko, B. G.; Gomperts, R.; Mennucci, B.; Hratchian, H. P.; Ortiz, J. V.; Izmaylov, A. F.; Sonnenberg, J. L.; Williams; Ding, F.; Lipparini, F.; Egidi, F.; Goings, J.; Peng, B.; Petrone, A.; Henderson, T.; Ranasinghe, D.; Zakrzewski, V. G.; Gao, J.; Rega, N.; Zheng, G.; Liang, W.; Hada, M.; Ehara, M.; Toyota, K.; Fukuda, R.; Hasegawa, J.; Ishida, M.; Nakajima, T.; Honda, Y.; Kitao, O.; Nakai, H.; Vreven, T.; Throssell, K.; Montgomery Jr., J. A.; Peralta, J. E.; Ogliaro, F.; Bearpark, M. J.; Heyd, J. J.; Brothers, E. N.; Kudin, K. N.; Staroverov, V. N.; Keith, T. A.; Kobayashi, R.; Normand, J.; Raghavachari, K.; Rendell, A. P.; Burant, J. C.; Iyengar, S. S.; Tomasi, J.; Cossi, M.; Millam, J. M.; Klene, M.; Adamo, C.; Cammi, R.; Ochterski, J. W.; Martin, R. L.; Morokuma, K.; Farkas, O.; Foresman, J. B.; Fox, D. J. *Gaussian 16*, Wallingford, CT, 2016.

[33] Fang, C.; Tang, L.; Oscar, B. G.; Chen, C. Capturing Structural Snapshots during Photochemical Reactions with Ultrafast Raman Spectroscopy: From Materials Transformation to Biosensor Responses. *J. Phys. Chem. Lett.* **2018**, *9*, 3253-3263.

[34] Mohammed, O. F.; Pines, D.; Dreyer, J.; Pines, E.; Nibbering, E. T. J. Sequential Proton Transfer Through Water Bridges in Acid-Base Reactions. *Science* **2005**, *310*, 83-86.

[35] Levine, B. G.; Martínez, T. J. Isomerization Through Conical Intersections. *Annu. Rev. Phys. Chem.* **2007**, *58*, 613-634.

[36] Pines, E.; Huppert, D.; Agmon, N. Geminate recombination in excited-state proton-transfer reactions: Numerical solution of the Debye–Smoluchowski equation with backreaction and comparison with experimental results. *J. Chem. Phys.* **1988**, *88*, 5620-5630.

[37] Simkovitch, R.; Rozenman, G. G.; Huppert, D. A fresh look into the time-resolved fluorescence of 8-hydroxy-1,3,6-pyrenetrisulfonate with the use of the fluorescence up-conversion technique. *J. Photochem. Photobiol. A* **2017**, *344*, 15-27.

[38] Pérez-Lustres, J. L.; Rodriguez-Prieto, F.; Mosquera, M.; Senyushkina, T. A.; Ernsting, N. P.; Kovalenko, S. A. Ultrafast Proton Transfer to Solvent: Molecularity and Intermediates from Solvation- and Diffusion-Controlled Regimes. *J. Am. Chem. Soc.* **2007**, *129*, 5408-5418.

[39] MARONCELLI, M.; MACINNIS, J.; FLEMING, G. R. Polar Solvent Dynamics and Electron-Transfer Reactions. *Science* **1989**, *243*, 1674-1681.

[40] Agmon, N. Elementary Steps in Excited-State Proton Transfer. *J. Phys. Chem. A* **2005**, *109*, 13-35.

[41] Tang, L.; Zhu, L.; Wang, Y.; Fang, C. Uncovering the Hidden Excited State toward Fluorescence of an Intracellular pH Indicator. *J. Phys. Chem. Lett.* **2018**, *9*, 4969-4975.

[42] Marcus, R. A.; Sutin, N. Electron transfers in chemistry and biology. *Biochim. Biophys. Acta, Rev. Bioenerg.* **1985**, *811*, 265-322.

[43] Kiefer, P. M.; Hynes, J. T. Nonlinear Free Energy Relations for Adiabatic Proton Transfer Reactions in a Polar Environment. II. Inclusion of the Hydrogen Bond Vibration. *J. Phys. Chem. A* **2002**, *106*, 1850-1861.

[44] Kiefer, P. M.; Hynes, J. T. Adiabatic and nonadiabatic proton transfer rate constants in solution. *Solid State Ion.* **2004**, *168*, 219-224.

[45] Hammes-Schiffer, S.; Soudackov, A. V. Proton-Coupled Electron Transfer in Solution, Proteins, and Electrochemistry. *J. Phys. Chem. B* **2008**, *112*, 14108-14123.

[46]   Hammes-Schiffer, S.; Stuchebrukhov, A. A. Theory of Coupled Electron and Proton Transfer Reactions. *Chem. Rev.* **2010**, *110*, 6939-6960.

[47]   Goyal, P.; Hammes-Schiffer, S. Tuning the Ultrafast Dynamics of Photoinduced Proton-Coupled Electron Transfer in Energy Conversion Processes. *ACS Energy Lett.* **2017**, *2*, 512-519.

[48]   Kovács, A.; Macsári, I.; Hargittai, I. Intramolecular Hydrogen Bonding in Fluorophenol Derivatives: 2-Fluorophenol, 2,6-Difluorophenol, and 2,3,5,6-Tetrafluorohydroquinone. *J. Phys. Chem. A* **1999**, *103*, 3110-3114.

[49]   Abraham, M. H.; Abraham, R. J.; Aliev, A. E.; Tormena, C. F. Is there an intramolecular hydrogen bond in 2-halophenols? A theoretical and spectroscopic investigation. *Phys. Chem. Chem. Phys.* **2015**, *17*, 25151-25159.

[50]   Kovalenko, S. A.; Schanz, R.; Hennig, H.; Ernsting, N. P. Cooling dynamics of an optically excited molecular probe in solution from femtosecond broadband transient absorption spectroscopy. *J. Chem. Phys.* **2001**, *115*, 3256-3273.

[51]   Liu, W.; Tang, L.; Oscar, B. G.; Wang, Y.; Chen, C.; Fang, C. Tracking Ultrafast Vibrational Cooling during Excited-State Proton Transfer Reaction with Anti-Stokes and Stokes Femtosecond Stimulated Raman Spectroscopy. *J. Phys. Chem. Lett.* **2017**, *8*, 997-1003.

[52]   Wemmie, J. A.; Price, M. P.; Welsh, M. J. Acid-sensing ion channels: advances, questions and therapeutic opportunities. *Trends Neurosci.* **2006**, *29*, 578-586.

Chapter 7 "Double-Donor-One-Acceptor": A New Strategy for Rational Design of Redder Fluorophores[f]

7.1 Introduction

Fluorescence imaging has been one of the most prevalent biological imaging methods with significant developments in recent decades.[1,2] Organic fluorophores are advantageous in this endeavor as it provides great tailorability in the aspects of sensitivity, selectivity, and synthesis, etc., while being metal-free, low-cost, green and sustainable and thus have drawn tremendous interest.[3] To improve these properties for practical applications, especially for *in vivo* imaging, several photophysical factors of the fluorophores such as long emission wavelengths, high fluorescence quantum yields (FQYs) and large Stokes shifts are desirable for high signal-to-noise ratios by mitigating tissue autofluorescence and improving the penetration depth. Along this line, extensive efforts have been devoted to designing fluorescent probes bearing these superior qualities, particularly red/near-infrared (NIR) emission wavelengths.

Promoting intramolecular charge transfer (ICT) in the excited electronic manifolds represents one of the most adopted strategies to red-shift emission wavelength.[4-9] These

---

[f]This chapter is based on the publications: (1) Chen, C.; Baranov, M. S.; Zhu, L.; Baleeva, N. S.; Smirnov, A. Y.; Zaitseva, S. O.; Yampolsky, I. V.; Solntsev, K. M.; Fang, C. Designing redder and brighter fluorophores by synergistic tuning of ground and excited states. *Chem. Commun.* **2019**, *55*, 2537-2540. (2) Chen, C.; Fang, C. Devising Efficient Red-Shifting Strategies for Bioimaging: A Generalizable Donor-Acceptor Fluorophore Prototype. *Chem. Asian. J.* **2020**, *15*, 1514-1523.

molecules contain at least one electron donor and one acceptor moiety such that ICT can occur upon photoexcitation to disperse electron density and generate a more stable electronic state with respect to the locally excited (LE) state. Notably, the LE electron density stays localized at the same moiety as the ground state molecular orbital (MO, usually HOMO) during vertical electronic excitation (Figure 7.1a).[10-12] To achieve red or NIR emission, extending the π-conjugation based on donor-acceptor frameworks to lower the energy of the ICT state (usually LUMO) remains the common strategy but as a result, most of the reported and commercial NIR dyes are quite large in size. This might be detrimental to brightness. For example, many red and NIR dyes have been built on the well-known fluorophore scaffolds (GFP,[13] rhodamine,[14] cyanine,[15] coumarin,[8] BODIPY[7] featured in Figure 7.1b) to take advantage of their appealing properties such as high FQY. The push-pull structure is usually established by incorporating the electron-donating groups (EDGs) and electron-withdrawing groups (EWGs) on the opposite ends of the parent backbone. The conjugated fluorophore core could then act as the π-linker to effectively promote ICT in the excited state.[11,16]

Despite this understanding, the current development of many fluorescent probes remains largely trial-and-error and lacks efficiency. The large sizes of organic fluorophores might not pose a severe issue for practical imaging applications because they are still smaller than dye-loaded polymer nanoparticles[17] and fluorescent proteins. However, many red/NIR dyes are designed with long-chain or bridge fragments.[5] These structures usually lead to drastic decreases in FQY due to other facile electronic or nuclear motions that depopulate the ICT state. For instance, the photoinduced electron

transfer in the donor-bridge-acceptor dyes might induce rapid fluorescence quenching of the ICT state by charge recombination.[18] The π-conjugated linker moiety could also undergo the photoinduced isomerization reaction as a main competing pathway to diminish fluorescence.[5]

(a)

(b)

$\lambda_{em} = 705$ nm (EtOH)

GFP dye

$\lambda_{em} = 712$ nm (H$_2$O)

rhodamine dye

$\lambda_{em} = 830$ nm (H$_2$O)

cyanine dye

$\lambda_{em} = 599$ nm (CH$_3$CN)

coumarin dye

$\lambda_{em} = 760$ nm (DMSO)

BODIPY dye
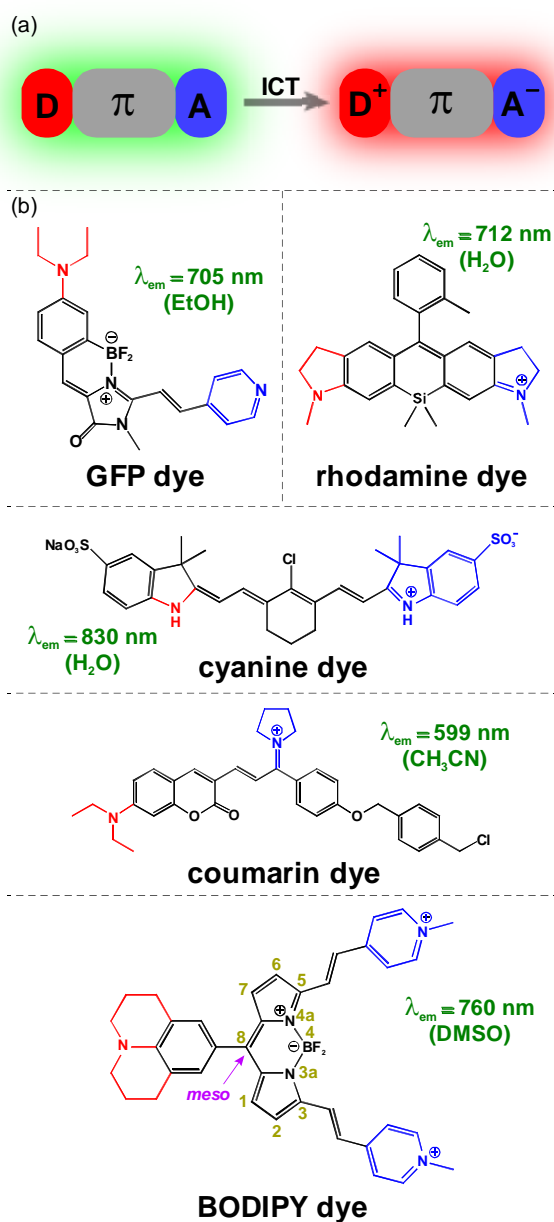
Figure 7.1. Conceptual illustration of the red-shifting mechanism for donor (D)-π-bridge-acceptor (A) dyes and representative red and NIR dyes adopting ICT strategy based on several classical fluorophore scaffolds. The D and A moieties are colored in red and blue, respectively, with the formal charges indicated. Main fluorescence peak positions in solutions are taken from the associated literature reports (see main text). Reproduced with permission from Cheng Chen, Chong Fang, *Chem. Asian. J.* **2020**, 15, 1514-1523. Copyright 2020 Wiley-VCH Verlag GmbH & Co. KGaA, Weinheim.

Herein, we present an effective red-shifting strategy from an integrated spectroscopic and computational characterization of two series of fluorophores, MnF and PnF, derived from the GFP model chromophore *p*-HBDI (Figure 7.2, also see Chapter 5) with a benzylidene imidazolones (BDIs) core.[19,20] As biomimetics, the locked *p*-HBDI derivatives were synthesized by a coordination-assisted borylation reaction that is effective in synthesizing various fixed BDIs' analogs.[13,20,21] These compounds are brightly colored and readily soluble in water and other polar solvents, making them versatile fluorescent or fluorogenic sensors. Similar BF_2 coupling strategy has also been applied and achieved successes in other molecular systems such as BODIPY-based dyes.[22] We show that strategic substitutions at phenolate (donor) and imidazolinone (acceptor) rings can enable a separate tuning of HOMO and LUMO energy to redshift emission of the locked GFP core in a synergistic manner, in contrast to the conventional ICT strategy that is mostly LUMO-centric.[5,6,9] This principle can help develop red/near-IR fluorophores without significant extension of π-conjugation.

Besides, excited-state proton transfer (ESPT) results in large Stokes shifts up to 150 nm between the neutral form absorption and anionic form emission. Conformational locking and addition of a sidechain phenyl group can also benchmark effects of the backbone and sidechain flexibility on FQY, corroborated in part by previous studies on the aggregation-induced emission and a series of modified fluorescent molecular rotors.[23,24] In addition, we provided perspectives on generalizing this strategy to fluorescent proteins with noncanonical amino acids and other fluorescent organic scaffolds.
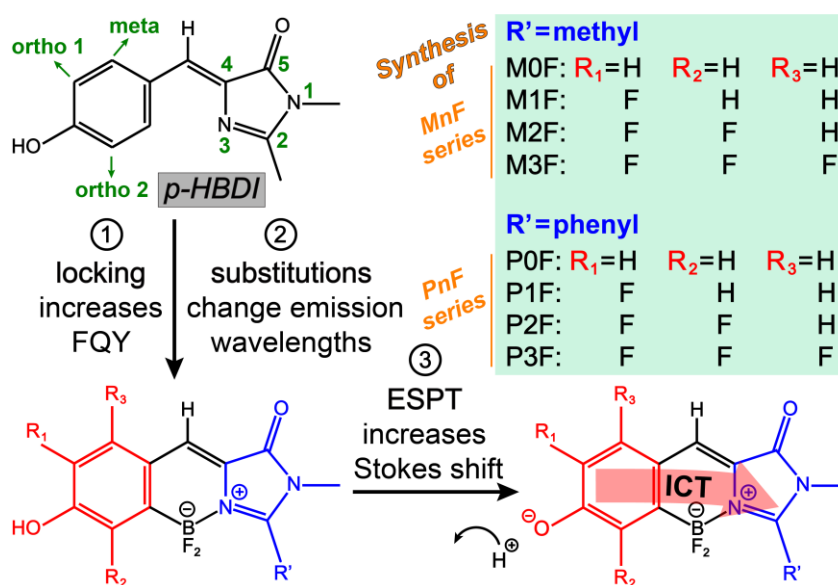
Figure 7.2. Design routes for GFP-chromophore derivatives with redder emission, higher fluorescence quantum yield, and larger Stokes shift. Adapted with permission from Cheng Chen et al., *Chem. Commun.* **2019**, 55, 2537-2540. Copyright 2019 The Royal Society of Chemistry.

7.2 Experimental

7.2.1 Synthesis

(1) Synthesis methods and procedures for the locked MnF and PnF compounds.

The detailed synthesis procedures can be referred to Section 5.2 in Chapter 5.

(2) Synthesis methods and procedures for the unlocked compounds with various substitutions.

Part 1: The general method for the preparation of the **(Z)-3-R-4-hydroxybenzylidene-1-methyl-2-R'-1H-imidazol-5(4H)-ones** (**1a-d,f, 2a-d,f**; Figure 7.3) is described in detail as follows. The corresponding aromatic aldehyde (10 mmol) was dissolved in 50 mL of $CHCl_3$ and mixed with 3.3 mL of methylamine solution (40% aqueous, 37 mmol) and anhydrous Na_2SO_4 (5 g). In case of substantially precipitation, methanol can be used for the complete dissolution. The mixture was stirred for 48 h at room temperature, filtered and dried over the additional Na_2SO_4. The solvent was evaporated, the corresponding ethyl 2-((methoxymethylene)amino)acetate (20 mmol) was added and the mixture was stirred for 24 h at room temperature. Then it was dried in vacuum and the product was purified by column chromatography (CH_2Cl_2-EtOH 100:1-5).
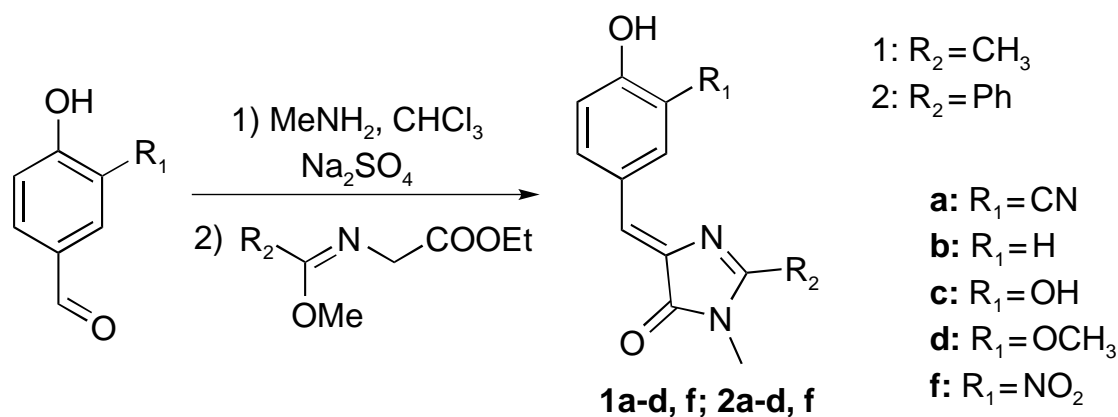
Figure 7.3. Synthesis of the unlocked compounds (Part 1) in this work. Reproduced with permission from Cheng Chen et al., *Chem. Commun.* **2019**, 55, 2537-2540. Copyright 2019 The Royal Society of Chemistry.

(*Z*)-4-(3-cyano-4-hydroxybenzylidene)-1,2-dimethyl-1*H*-imidazol-5(4*H*)-one (1a)

Pale yellow solid (385 mg, 16%); m. p. ~260 °C with decomposition; ^{1}H NMR (700 MHz, 303 K, DMSO-d_6) δ ppm: 11.71 (br. s., 1H), 8.48 (d, *J*=1.7 Hz, 1H), 8.35 (dd, *J*=8.9, 1.7 Hz, 1H), 7.08 (d, *J*=8.9 Hz, 1H), 6.92 (s, 1H), 3.09 (s, 3H), 2.35 (s, 3H); ^{13}C NMR (176 MHz, 303 K, DMSO-d_6) δ ppm: 169.6, 164.1, 161.1, 138.0, 137.9, 136.8, 126.0, 122.7, 116.5, 116.5, 99.5, 26.2, 15.3; HRMS (ESI) m/z: 242.0922 found (calculated for $C_{13}H_{12}N_3O_2^+$, [M+H]$^+$ 242.0924).

(*Z*)-4-(4-hydroxybenzylidene)-1,2-dimethyl-1*H*-imidazol-5(4*H*)-one (1b)[25]

(*Z*)-4-(3,4-dihydroxybenzylidene)-1,2-dimethyl-1*H*-imidazol-5(4*H*)-one (1c)

Brown solid (1.02 g, 44%); m. p. = 209−211 °C; ^{1}H NMR (700 MHz, 303 K, DMSO-d_6) δ ppm 9.57 (br. s., 1H), 9.17 (br. s., 1H), 7.84 (d, *J*=1.6 Hz, 1H), 7.36 (dd, *J*=8.2,

1.6 Hz, 1H), 6.79 (s, 1H), 6.77 (d, J=8.2 Hz, 1H), 3.08 (s, 3H), 2.33 (s, 3H); ^{13}C NMR (75 MHz, 293 K, DMSO-d_6) δ ppm 169.9, 162.0, 148.5, 145.3, 136.1, 126.1, 125.7 (2C), 118.5, 115.6, 26.2, 15.3; HRMS (ESI) m/z: 233.0918 found (calculated for $C_{12}H_{13}N_2O_3^+$, [M+H]$^+$ 233.0921).

(Z)-4-(4-hydroxy-3-methoxybenzylidene)-1,2-dimethyl-1H-imidazol-5(4H)-one (1d)[26]

(Z)-4-(4-hydroxy-3-cyano-benzylidene)-1-methyl-2-phenyl-1H-imidazol-5(4H)-one (2a)

Brown solid (1.03 g, 34%); m. p. ~ 285 °C with decomposition; ^{1}H NMR (300 MHz, 293 K, DMSO-d_6) δ ppm 8.57-8.45 (m, 2H), 7.94 (d, J=7.5 Hz, 2H), 7.66-7.60 (m, 3H), 7.14 (s, 1H), 7.09 (d, J=9.3 Hz, 1H), 3.26 (s, 3H); ^{13}C NMR (176 MHz, 303 K, DMSO-d_6) δ ppm 170.4, 162.3, 161.9, 138.2, 137.6, 137.4, 131.5, 128.9, 128.8, 128.6, 125.8, 125.0, 116.8, 116.5, 99.7, 28.6; HRMS (ESI) m/z: 304.1081 found (calculated for $C_{18}H_{14}N_3O_2^+$, [M+H]$^+$ 304.1081).

(Z)-4-(4-hydroxybenzylidene)-1-methyl-2-phenyl-1H-imidazol-5(4H)-one (2b)[27]

(Z)-4-(3,4-dihydroxybenzylidene)-1-methyl-2-phenyl-1H-imidazol-5(4H)-one (2c)

Brown solid (650 mg, 22%); m. p. = 214−217 °C; ^{1}H NMR (700 MHz, 303 K, DMSO-d_6) δ ppm 9.44 (br. s., 2H), 7.98 (s, 1H), 7.93 (d, J=7.2 Hz, 2H), 7.64-7.58 (m, 3H), 7.44 (d, J=8.0 Hz, 1H), 7.01 (s, 1H), 6.81 (d, J=8.2 Hz, 1H), 3.26 (s, 3H); ^{13}C NMR

(176 MHz, 303 K, DMSO-d_6) δ ppm 170.5, 160.6, 149.0, 145.4, 136.0, 131.2, 129.3, 128.7, 128.6, 128.3, 126.3, 125.8, 118.7, 115.7, 28.5; HRMS (ESI) m/z: 295.1076 found (calculated for $C_{17}H_{15}N_2O_3^+$, [M+H]$^+$ 295.1077).

(Z)-4-(4-hydroxy-3-methoxybenzylidene)-1-methyl-2-phenyl-1H-imidazol-5(4H)-one (2d)

Dark red solid (1.69 g, 55%); m. p. = 188−190 °C; ^{1}H NMR (700 MHz, 303 K, DMSO-d_6) δ ppm 8.10 (br. s., 1H), 7.94 (d, J=6.9 Hz, 2H), 7.71 (d, J=7.8 Hz, 1H), 7.64-7.58 (m, 3H), 7.10 (s, 1H), 6.86 (d, J=8.2 Hz, 1H), 3.82 (s, 3H), 3.28 (s, 3H); ^{13}C NMR (176 MHz, 303 K, DMSO-d_6) δ ppm 170.5, 160.7, 149.9, 147.6, 136.2, 131.2, 129.2, 128.8, 128.5, 128.0, 127.3, 125.8, 115.8, 115.7, 55.5, 28.6; HRMS (ESI) m/z: 309.1235 found (calculated for $C_{18}H_{17}N_2O_3^+$, [M+H]$^+$ 309.1234).

(Z)-4-(4-hydroxy-3-nitrobenzylidene)-1-methyl-2-phenyl-1H-imidazol-5(4H)-one (2f)

Orange solid (1.58 g, 49%); m. p. = 190−193 °C; ^{1}H NMR (700 MHz, 303 K, DMSO-d_6) δ ppm 8.85 (d, J=1.3 Hz, 1H), 8.42 (dd, J=8.7, 1.3 Hz, 1H), 7.93 (d, J=7.2 Hz, 2H), 7.65 (t, J=7.3 Hz, 1H), 7.61 (t, J=7.3 Hz, 2H), 7.17 (s, 1H), 7.12 (d, J=8.8 Hz, 1H), 3.27 (s, 3H); ^{13}C NMR (176 MHz, 303 K, DMSO-d_6) δ ppm 170.3, 162.0, 138.0, 137.5, 137.4, 131.5, 129.4, 129.0, 128.9, 128.8, 128.6, 128.1, 125.3, 120.4, 28.6; HRMS (ESI) m/z: 324.0977 found (calculated for $C_{17}H_{14}N_3O_4^+$, [M+H]$^+$ 324.0979).

Part 2: The general method for the preparation of **(Z)-4-benzylidene-1-methyl-2-((E)-styryl/pyridin-4-yl)vinyl)-1H-imidazol-5(4H)-ones (3b-d, 4b-d)** is described below. A solution of the corresponding (Z)-4-benzylidene-1,2-dimethyl-1H- imidazol-5(4H)-one (compound **1**, 1 mmol), aromatic aldehyde (5 mmol), and piperidine (40 μL) in pyridine (Py, 10 mL) were stirred for 24−72 h at 115 °C (Figure 7.4). The mixture was evaporated and the crude solid product was purified by column chromatography (CHCl₃-EtOH 50:1).
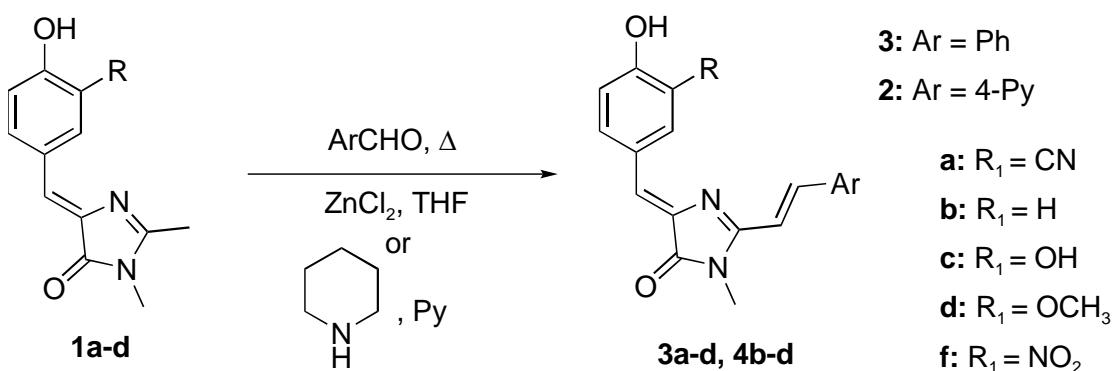
Figure 7.4. Synthesis of the unlocked compounds (Part 2) in this work. Reproduced with permission from Cheng Chen et al., *Chem. Commun.* **2019**, 55, 2537-2540. Copyright 2019 The Royal Society of Chemistry.

For **(Z)-4-(3-cyano-4 hydroxybenzylidene)-1-methyl-2-((E)-styryl)-1H-imidazol-5(4H)-one (3a)** and of **(Z)-4-(3-nitro-4-hydroxybenzylidene)-1-methyl-2-((E)-styryl/pyridin-4-yl)vinyl)-1H-imidazol 5(4H)-ones (3f and 4f),** to the solution of corresponding compound **1** (1 mmol) in THF (5 mL), the anhydrous zinc chloride (30 mg, 0.22 mmol) and corresponding aldehyde (1.2 mmol) were added. The mixture was

refluxed for 2–5 h and the solvent was removed in vacuum. The mixture was dissolved in EtOAc (50 mL) and washed by EDTA solution (0.5%, 10 mL), water (3×10 mL) and brine (1×10 mL). The mixture was dried over anhydrous Na_2SO_4. The solvent was then evaporated and the product was purified by column chromatography (CHCl$_3$-EtOH 9:1).

(*Z*)-4-(4-hydroxy-3-cyano-benzylidene)-1-methyl-2-((*E*)-styryl)-1*H*-imidazol-5(4*H*)-one (3a)

Orange solid (161 mg, 49%); m. p. ~ 254 °C with decomposition; ^{1}H NMR (700 MHz, 303 K, DMSO-*d$_6$*) δ ppm 11.77 (br. s., 1H), 8.62 (dd, *J*=8.8, 1.4 Hz, 1H), 8.44 (d, *J*=1.5 Hz, 1H), 8.03 (d, *J*=15.8 Hz, 1H), 7.87 (d, *J*=7.4 Hz, 2H), 7.48 (t, *J*=7.4 Hz, 2H), 7.46-7.43 (m, 1H), 7.25 (d, *J*=15.8 Hz, 1H), 7.14 (d, *J*=8.8 Hz, 1H), 7.00 (s, 1H), 3.29 (s, 3H); ^{13}C NMR (176 MHz, 303 K, DMSO-*d$_6$*) δ ppm 169.8, 161.3, 160.2, 140.4, 138.4, 138.1, 137.2, 135.0, 130.2, 128.9, 128.3, 126.4, 123.1, 116.7, 116.5, 114.0, 99.6, 26.4; HRMS (ESI) m/z: 330.1237 found (calculated for $C_{20}H_{16}N_3O_2^+$, [M+H]$^+$ 330.1237).

(*Z*)-4-(4-hydroxybenzylidene)-1-methyl-2-((*E*)-styryl)-1*H*-imidazol-5(4*H*)-one (3b)[28]

(*Z*)-4-(3,4-dihydroxybenzylidene)-1-methyl-2-((*E*)-styryl)-1*H*-imidazol-5(4*H*)-one (3c)

Dark red solid (109 mg, 34%); m. p. ~ 224 °C with decomposition; ^{1}H NMR (700 MHz, 303 K, DMSO-*d$_6$*) δ ppm 8.03 (s, 1H), 7.99 (d, *J*=15.9 Hz, 1H), 7.84 (d, *J*=7.2 Hz, 2H),

7.50-7.43 (m, 4H), 7.23 (d, J=15.9 Hz, 1H), 6.88 (s, 1H), 6.81 (d, J=8.2 Hz, 1H), 3.27 (s, 3H); ^{13}C NMR (176 MHz, 303 K, DMSO-d_6) δ ppm 169.9, 158.4, 148.7, 145.3, 139.2, 136.7, 135.2, 129.9, 128.9, 128.1, 126.4, 126.2, 126.1, 118.8, 115.7, 114.2, 26.3; HRMS (ESI) m/z: 321.1233 found (calculated for $C_{19}H_{17}N_2O_3^+$, [M+H]$^+$ 321.1234).

(*Z*)-4-(4-hydroxy-3-methoxy-benzylidene)-1-methyl-2-((*E*)-styryl)-1*H*-imidazol-5(4*H*)-one (3d)

Orange solid (177 mg, 53%); m. p. = 170−173 °C; ^{1}H NMR (700 MHz, 303 K, DMSO-d_6) δ ppm 9.78 (br. s., 1H), 8.15 (s, 1H), 7.97 (d, J=15.9 Hz, 1H), 7.83 (d, J=7.2 Hz, 2H), 7.70 (d, J=8.4 Hz, 1H), 7.53-7.38 (m, 3H), 7.24 (d, J=15.9 Hz, 1H), 6.98 (s, 1H), 6.87 (d, J=8.2 Hz, 1H), 3.89 (s, 3H), 3.28 (br. s., 3H); ^{13}C NMR (176 MHz, 303 K, DMSO-d_6) δ ppm 169.9, 158.6, 149.4, 147.6, 139.4, 136.9, 135.1, 130.0, 128.9, 128.2, 127.1, 126.3, 126.1, 115.7, 115.5, 114.1, 55.4, 26.3; HRMS (ESI) m/z: 335.1390 found (calculated for $C_{20}H_{18}N_2O_3^+$, [M+H]$^+$ 335.1391).

(*Z*)-4-(4-hydroxy-3-nitro-benzylidene)-1-methyl-2-((*E*)-styryl)-1*H*-imidazol-5(4*H*)-one (3f)

Red solid (195 mg, 56%); m. p. = 225−228 °C; ^{1}H NMR (700 MHz, 303 K, DMSO-d_6) δ ppm 11.61 (br. s., 1H), 8.87 (d, J=1.5 Hz, 1H), 8.54 (dd, J=8.6, 1.6 Hz, 1H), 8.03 (d, J=15.8 Hz, 1H), 7.86 (d, J=7.2 Hz, 2H), 7.49 (t, J=7.2 Hz, 2H), 7.47-7.44 (m, 1H), 7.26 (d, J=15.8 Hz, 1H), 7.23 (d, J=8.6 Hz, 1H), 7.06 (s, 1H), 3.29 (s, 3H); ^{13}C NMR (176 MHz, 303 K, DMSO-d_6) δ ppm 169.8, 160.5, 153.1, 140.5, 138.9, 138.1, 137.2, 135.0,

130.2, 128.9, 128.7, 128.3, 126.0, 122.7, 119.4, 113.9, 26.4; HRMS (ESI) m/z: 350.1134 found (calculated for $C_{19}H_{16}N_3O_4^+$, [M+H]$^+$ 350.1135).

(Z)-4-(4-hydroxybenzylidene)-1-methyl-2-((E)-2-(pyridin-4-yl)vinyl)-1H-imidazol-5(4H)-one (4b)

(Z)-4-(3,4-dihydroxybenzylidene)-1-methyl-2-((E)-2-(pyridin-4-yl)vinyl)-1H-imidazol-5(4H)-one (4c)

Brown solid (83 mg, 26%); m. p. ~ 273 °C with decomposition; ^{1}H NMR (700 MHz, 303 K, DMSO-d_6) δ ppm 8.67 (d, J=5.9 Hz, 2H), 8.01 (s, 1H), 7.91 (d, J=16.0 Hz, 1H), 7.79 (d, J=5.9 Hz, 2H), 7.50-7.48 (m, 2H), 6.95 (s, 1H), 6.82 (d, J=8.2 Hz, 1H), 3.28 (s, 3H); ^{13}C NMR (176 MHz, 303 K, DMSO-d_6) δ ppm 169.8, 157.7, 150.3, 149.1, 145.4, 142.2, 136.6, 136.2, 127.8, 126.4, 126.0, 121.9, 118.9, 118.9, 115.8, 26.4; HRMS (ESI) m/z: 322.1185 found (calculated for $C_{18}H_{16}N_3O_3^+$, [M+H]$^+$ 322.1186).

(Z)-4-(4-hydroxy-3-methoxy-benzylidene)-1-methyl-2-((E)-2-(pyridin-4-yl)vinyl)-1H-imidazol-5(4H)-one (4d)

Dark red solid (151 mg, 45%); m. p. = 238−241 °C; ^{1}H NMR (600 MHz, 303 K, DMSO-d_6) δ ppm 9.86 (br. s., 1H), 8.66 (d, J=5.9 Hz, 2H), 8.12 (d, J=1.4 Hz, 1H), 7.90 (d, J=15.9 Hz, 1H), 7.79 (d, J=5.9 Hz, 2H), 7.74 (dd, J=7.9, 1.3 Hz, 1H), 7.50 (d, J=15.9 Hz, 1H), 7.05 (s, 1H), 6.88 (d, J=8.2 Hz, 1H), 3.88 (s, 3H), 3.29 (s, 3H); ^{13}C NMR (176 MHz, 303 K, DMSO-d_6) δ ppm 169.7, 157.9, 150.3, 149.7, 147.7, 142.1, 136.8, 136.4,

127.5, 127.4, 126.1, 121.9, 118.8, 115.8, 115.7, 55.5, 26.4; HRMS (ESI) m/z: 336.1343 found (calculated for $C_{19}H_{18}N_3O_3^+$, $[M+H]^+$ 336.1343).

(Z)-4-(4-hydroxy-3-nitro-benzylidene)-1-methyl-2-((E)-2-(pyridin-4-yl)vinyl)-1H-imidazol-5(4H)-one (4f)

Dark red solid (52 mg, 15%); m. p. ~ 243 °C with decomposition; ^{1}H NMR (700 MHz, 303 K, DMSO-d_6) δ ppm 11.68 (br. s., 1H), 8.82 (d, J=1.3 Hz, 1H), 8.68 (br. d., J=4.8 Hz, 2H) 8.57 (dd, J=8.7, 1.3 Hz, 1H), 7.95 (d, J=15.9 Hz, 1H), 7.80 (d, J=5.5 Hz, 2H), 7.51 (d, J=15.9 Hz, 1H), 7.22 (d, J=8.8 Hz, 1H), 7.13 (s, 1H), 3.30 (br. s., 3H); ^{13}C NMR was not recorded due to the extremely low solubility of the compound; HRMS (ESI) m/z: 351.1088 found (calculated for $C_{18}H_{15}N_4O_4^+$, $[M+H]^+$ 351.1088).

Part 3: The general procedure for the reduction of NO_2 group in obtained chromophores (e.g., **2f**, **3f** and **4f**) involves the following steps. The corresponding chromophore (0.55 g, 2 mmol) and tin (II) chloride dihydrate (3.53 g, 17 mmol) were suspended in 10 mL of THF (Figure 7.5). The mixture was refluxed for 3 h. Afterwards it was neutralized with 10% Na_2CO_3 solution, filtered, extracted with dichloromethane (4×75 mL) and dried over Na_2SO_4. The solvent was evaporated and the crude product was purified by column chromatography (CHCl$_3$-EtOH 32:1).
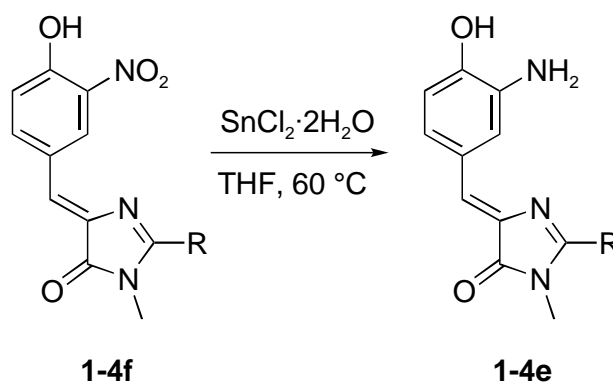
Figure 7.5. Synthesis of the unlocked compounds (Part 3) in this work. Reproduced with permission from Cheng Chen et al., *Chem. Commun.* **2019**, 55, 2537-2540. Copyright 2019 The Royal Society of Chemistry.

(Z)-4-(3-amino-4-hydroxybenzylidene)-1,2-dimethyl-1H-imidazol-5(4H)-one (1e)

Orange solid (378 mg, 82%); m. p. ~ 225 °C with decomposition; ^{1}H NMR (700 MHz, 303 K, DMSO-d_6) δ ppm 7.58 (d, J=1.9 Hz, 1H), 7.21 (dd, J=8.1, 1.8 Hz, 1H), 6.73 (s, 1H), 6.70 (d, J=8.1 Hz, 1H), 3.08 (s, 3H) 2.32 (s, 3H); ^{13}C NMR (176 MHz, 303 K, DMSO-d_6) δ ppm 169.8, 161.4, 147.0, 136.7, 135.7, 126.7, 125.7, 123.0, 116.9, 114.2, 26.1, 15.1; HRMS (ESI) m/z: 232.1079 found (calculated for $C_{12}H_{14}N_3O_2^+$, $[M+H]^+$ 232.1081).

(Z)-4-(3-amino-4-hydroxybenzylidene)-1-methyl-2-phenyl-1H-imidazol-5(4H)-one (2e)

Orange solid (193 mg, 33%); m. p. ~ 223 °C with decomposition; ^{1}H NMR (700 MHz, 303 K, DMSO-d_6) δ ppm 7.93 (d, J=7.1 Hz, 2H), 7.71 (d, J=1.3 Hz, 1H), 7.62 (t, J=7.1 Hz, 1H), 7.59 (t, J=7.2 Hz, 2H), 7.29 (dd, J=8.2, 1.3 Hz, 1H), 6.95 (s, 1H), 6.74 (d, J=8.2 Hz, 1H) 3.25 (s, 3H); ^{13}C NMR (176 MHz, 303 K, DMSO-d_6) δ ppm 170.5,

160.2, 147.6, 136.9, 135.7, 131.1, 129.3, 129.0, 128.7, 128.6, 125.9, 123.8, 117.1, 114.3, 28.5; HRMS (ESI) m/z: 294.1237 found (calculated for $C_{17}H_{16}N_3O_2^+$, [M+H]$^+$ 294.1237).

(Z)-4-(3-amino-4-hydroxybenzylidene)-1-methyl-2-((E)-styryl)-1H-imidazol-5(4H)-one (3e)

Red solid (305 mg, 48%); m. p. ~ 146 °C with decomposition; ^{1}H NMR (700 MHz, 303 K, DMSO-d_6) δ ppm 8.04 (d, J=15.8 Hz, 1H), 7.90-7.82 (m, 3H), 7.48 (t, J=7.4 Hz, 2H), 7.43 (t, J=7.4 Hz, 1H), 7.25-7.20 (m, 2H), 6.82 (s, 1H), 6.74 (d, J=8.2 Hz, 1H), 3.27 (s, 3H); ^{13}C NMR (176 MHz, 303 K, DMSO-d_6) δ ppm 170.0, 157.9, 147.4, 139.2, 136.8, 136.4, 135.3, 129.8, 128.9, 128.1, 127.1, 126.3, 123.7, 117.1, 114.3, 114.0, 26.3; HRMS (ESI) m/z: 320.1393 found (calculated for $C_{19}H_{18}N_3O_2^+$, [M+H]$^+$ 320.1394).

(Z)-4-(3-amino-4-hydroxybenzylidene)-1-methyl-2-((E)-2-(pyridin-4-yl)vinyl)-1H-imidazol-5(4H)-one (4e)

Dark red solid (173 mg, 27%); m. p. ~ 214 °C with decomposition; ^{1}H NMR (700 MHz, 303 K, DMSO-d_6) δ ppm 8.67 (br. s., 2H), 7.97 (d, J=15.8 Hz, 1H), 7.87 (s, 1H), 7.79 (d, J=4.8 Hz, 2H), 7.48 (d, J=15.8 Hz, 1H), 7.27 (d, J=7.8 Hz, 1H), 6.89 (s, 1H), 6.75 (d, J=8.2 Hz, 1H), 3.28 (s, 3H); ^{13}C NMR (176 MHz, 303 K, DMSO-d_6) δ ppm 169.8, 157.3, 150.3, 147.7, 142.3, 136.9, 136.2, 136.2, 128.4, 126.2, 124.1, 121.9, 118.8, 117.2, 114.3, 26.3; HRMS (ESI) m/z: 321.1345 found (calculated for $C_{18}H_{17}N_4O_2^+$, [M+H]$^+$ 321.1346)

7.2.2 Spectroscopic measurement and DFT calculations

The detailed description of our FSRS setup can be found elsewhere. See Chapter 5 for the brief description for the generation of FSRS beams including actinic pump, Raman pump and Raman probe pulses. For the ground-state Stokes FSRS measurement, (1) the Raman pump wavelength for the anionic MnF and PnF in water is at 560 nm; (2) the Raman pump wavelength for the anionic M3F and P3F in methanol is at 560 and 590 nm, respectively. For the excited-state Stokes FSRS measurement, (1) the Raman pump wavelength for the neutral M3F and P3F in water is at 520 and 560 nm, respectively; (2) the Raman pump wavelength for the neutral M3F and P3F in methanol is at 500 nm. Due to superphotoacidity of M3F and P3F, both neutral M3F and P3F undergo ESPT in water and methanol (Chapter 4 to 6) and therefore the spectrum at 900-ps time delay is dominated by the modes of the anionic form.

The HOMO and LUMO energies were obtained by geometric optimization calculations at the TD-DFT RB3LYP level with 6-311G (d, p) basis sets in Gaussian 09 program.[29] The ground- and excited-state vibrational frequencies with water as IEFPCM solvent were calculated at the DFT and TD-DFT RB3LYP level with 6-311G(d, p) basis sets. The same calculations with methanol as solvent were performed at the same level but with 6-311G+(d, p) basis sets.

7.3 Results and discussion

7.3.1 Site-specificity from experimental observations

We first examined the emission properties of MnF and PnF (Table 7.1). Cumulative

fluorination leads to an emission redshift from 0F → 2F but a blueshift from 2F → 3F

in both series. This turning point suggests that the *ortho-* and *meta-*site fluorination

exert different effects on the energetics of the ground or excited state, which highlights

the site specificity at the phenol moiety of the locked *p*-HBDI.

Table 7.1. Photophysical Properties of MnF and PnF in water.

Compd.	neutral		anionic		$\Phi_F{}^b$	$\Phi_F'{}^c$	$\Phi_{PT}{}^d$
	$\lambda_{abs}{}^a$	$\lambda_{em}{}^a$	$\lambda_{abs}{}^a$	$\lambda_{em}{}^a$			
M0F	404	485	485	520	0.28	0.77	0.36
M1F	401	$-^e$	485	528	0.41	0.64	0.64
M2F	394	$-^e$	479	532	0.51	0.66	0.77
M3F	393	$-^e$	474	520	0.55	0.66	0.83
P0F	422	503	512	545	0.12	0.34	0.35
P1F	416	$-^e$	511	555	0.25	0.36	0.69
P2F	409	$-^e$	508	558	0.27	0.38	0.71
P3F	406	$-^e$	499	545	0.33	0.45	0.73

[a]Peak maximum in nm.

[b]Anionic FQY upon excitation of the neutral form.

[c]Anionic FQY upon excitation of the anionic form.

[d]ESPT quantum yield, calculated as the ratio of Φ_F/Φ_F'.

[e]Not detected due to the highly efficient ESPT in water.

7.3.2 Electron density analysis of the parent fluorophore

We performed the time-dependent density functional theory (TD-DFT) calculations at the RB3LYP/6-311G(d, p) level and unveiled the correlations between the radiative emission and electronic structures. Since TD-DFT optimization produces a relaxed excited-state geometry, the HOMO-LUMO energy gap could be used to estimate the emission peak wavelength.[30] The emission turning point upon cumulative fluorination is reproduced by our calculations. Figure 7.6a and 7.6b show the electron density distribution of HOMO and LUMO for the locked HBDI scaffolds with no fluorination (M0F, P0F). The largest oscillator strength indicates that HOMO-LUMO transition constitutes the primary ICT excitation/emission.

Both HOMO and LUMO are delocalized across the phenolate-bridge-imidazolinone-ring plane except that the LUMO is delocalized more evenly than HOMO. Notably, electron density at the phenolate ring (P-ring) decreases from HOMO to LUMO while that at the C-2 position (as well as the methyl group) of the imidazolinone ring (I-ring) increases. It indicates a dominant charge flow from the P-ring to the C-2 site of the I-ring, which provides a basis for conventional ICT design, i. e., incorporating EWGs at the C-2 site to enhance ICT and achieve a more stable ICT state for redder emission.[31]

Another series termed as PnF was synthesized to incorporate a phenyl group at the C-2 site in place of a methyl group as the acceptor moiety so we could confirm the ICT flow to the C-2 site. Notably, a choice of unsuitable sites may give rise to an insignificant enhancement of ICT and consequently a marginal redshift.[32-34] For *p-*

HBDI, the incorporation of EWGs at N-1 site barely red-shifts the emission, in contrast to those with the same EWGs at C-2 site.[35] The unsubstituted compound in PnF series, i. e., P0F, shows a delocalized LUMO over both HBDI backbone and the phenyl group (Figure 7.6b), confirming ICT to the C-2 site. Meanwhile, the HOMO remains mostly localized at the P- and I-rings, almost identical to that of M0F. Key results are manifested in the MO energies: The HOMOs are isoenergetic for MnF and PnF with the same fluorination while the LUMO energy of PnF are consistently lower than the MnF counterparts (Figure 7.6c). It can be qualitatively understood by the quantum box theory for which the more delocalized LUMOs of PnF represent larger boxes than the MnF compounds and hence lie lower in energy. The HOMOs of both series, on the other hand, are largely the same in box size. This finding is also in accord with previous views that in donor-acceptor systems HOMO is localized at the donor moiety and LUMO is localized at the acceptor moiety[36,37] or delocalized over both donor and acceptor moieties.[38] The *p*-HBDI framework showcases the latter and is characteristic of a globally delocalized LUMO.

Notably, two *ortho* sites to the phenolic hydroxyl are electron rich whereas the *meta* site is deficient in HOMO. This is because the phenolate $-O^-$ is a strong electron-donating group (EDG), thereby increasing and decreasing the electron density at its *ortho* and *meta* sites, respectively, on a ''push–pull'' π-conjugated system. The LUMO, however, shows similar electron densities at these sites after charge redistribution. Since electrophilic substitutions at nucleophilic sites lower HOMO and LUMO energy (Fig. 7.6c),[32,39] the emission redshift from 0F to 2F arises from better stabilization of

LUMO than HOMO by fluorination. The *meta*-site fluorination seems to grant more stability to HOMO than LUMO despite its electron deficiency in S_0, leading to a blue-shifted emission in 3F.
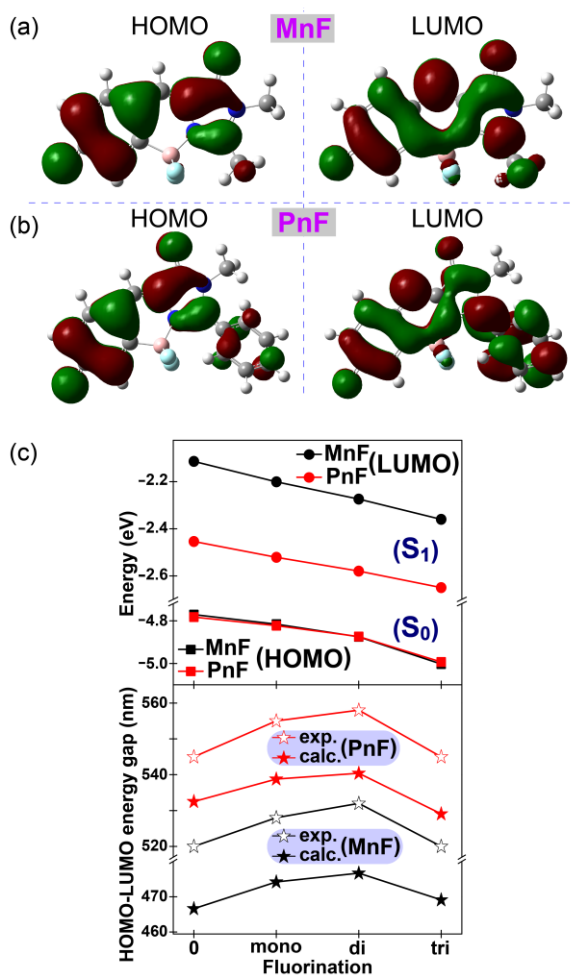
Figure 7.6. Theoretical energetics analysis of the locked and fluorinated *p*-HBDI derivatives. Electron density distribution of HOMO and LUMO for (a) M0F and (b) P0F. (c) Calculated HOMO, LUMO energies and their gaps for the MnF and PnF series. Experimental emission wavelengths are shown for comparison. Adapted with permission from Cheng Chen et al., *Chem. Commun.* **2019**, 55, 2537-2540. Copyright 2019 The Royal Society of Chemistry.

7.3.3 Substitution effects on the LUMO/excited state

To red-shift the emission wavelengths, the most used strategy has been the stabilization of ICT state by introducing a donor and acceptor with suitable electron donating/withdrawing strengths at specific molecular sites.[40,41] Considering the delocalized nature of LUMO, it is expected that a large conjugated acceptor structure would lower LUMO energy more than small groups with similar electron-pulling abilities (upper panel, Figure 7.6c). Note that this difference arises from the modification of acceptor moiety. On the other hand, modifications at the donor moiety (e. g., fluorination) lead to the stabilization of LUMO as well but to a smaller extent. Moreover, the energy lowering is almost linearly correlated with the accumulative fluorination. It is likely due to the similarity in electron density at these three sites in LUMO, because of which the electrophilic substitutions are energetically favored.[42,43]

To explore the substituent and site dependence, TD-DFT calculations at the same level were performed on the *p*-HBDI derivatives with single substitutions at different P-ring sites (two *ortho* and one *meta* sites to $-O^-$). The $-CN$ and $-NH_2$ groups are used to demonstrate the EWG and EDG effects, respectively. The strong EWG $-CN$ stabilizes LUMO more than $-F$ while $-NH_2$ slightly destabilizes LUMO (right panel, Figure 7.7). The relatively weak stabilization effect by $-F$ is attributable to the partial cancellation of the halogen's electron-donating resonance (+Re) and electron-withdrawing inductive ($-I$) effects. In addition, no significant site dependence is observed for LUMO because it is stabilized/destabilized by EWG/EDG to a similar extent (left panel,

Figure 7.7), consistent with similar electron densities at these sites in LUMO. Furthermore, the phenyl group at C-2 position leads to a stabilization effect regardless of substitutions at P-ring, indicating that LUMO is mainly affected by the acceptor moiety.
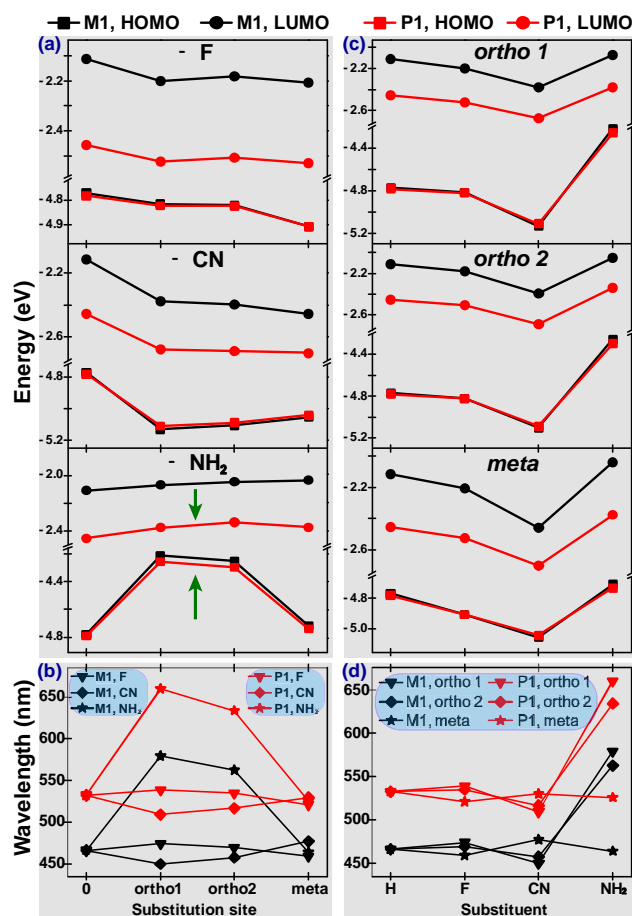
Figure 7.7. P-ring single-site substitution effects on the HOMO/LUMO energies of the locked *p*-HBDI derivatives. Calculated site-dependent (a) HOMO/ LUMO energies and (b) gaps, as well as the substituent-dependent (c) HOMO/LUMO energies and (d) gaps. Green arrows denote the smallest HOMO-LUMO gap achieved by an adjacent EDG substitution. Reproduced with permission from Cheng Chen et al., *Chem. Commun.* **2019**, 55, 2537-2540. Copyright 2019 The Royal Society of Chemistry.

7.3.4 Substitution effects on the HOMO/ground state

With respect to LUMO/excited state, tuning HOMO/ground state has traditionally drawn much less attention or been overlooked in the realm of fluorophore design. Previous works in dye-sensitized solar cells show that the HOMO/LUMO energy levels of the organic dyes can be upshifted/downshifted by increasing the donor/acceptor strengths, respectively, and the HOMO upshift could be a dominant factor for the red-shifted ICT excitation.[40,41] In these dyes, a donor group containing one strong donating atom is typically used such as arylamines. For *p*-HBDI, we found that a small-group substitution in the proximity of the conserved donor (i. e., $-O^-$ in the anionic form) could significantly change chromophore electrostatics particularly in the ground state.

First, the incorporation of an EWG/EDG at P-ring next to the $-O^-$ group leads to the stabilization/destabilization of HOMO, in accord with the *para* Hammett parameter (σ_p) ordering [$-CN$ (+0.66) > $-F$ (+0.062) > $-NH_2$ (−0.66)] due to nucleophilicity of the ortho site to the $-O^-$ group (Figure 7.6a and 7.6b).[44-46] As a result, the $-NH_2$ and $-CN$ greatly increases and decreases the HOMO energy by strong electron donating and withdrawing abilities, respectively, while halogen effect is moderate (Figure 7.7). In contrast, the EDG-substitution at the electron-deficient *meta* site appears to cause much less effect than EWGs (Figure 7.7a), which remains in good agreement with the *meta* Hammett parameters [$-CN$ (+0.56) > $-F$ (+0.337) > $-NH_2$ (−0.161)]. It implies that the HOMO/ground-state energy upon additional substitutions can be dictated by Hammett parameters in the presence of a pre-existing donor group.

In this context, the substitution effects on LUMO/excited state can be understood in a similar manner by analyzing the electron density at the substitution sites. Different from HOMO ruled by the ground-state push-pull mechanism, LUMO exhibits the evenly distributed electron density at these three sites (Figure 7.6a and 7.6b). The substitution effects can be estimated by Hammett parameters at the *para* site (used for *ortho* sites assuming no or little steric effect with small substituents),[46] evinced by a similar stabilization or destabilization effect by an EWG or EDG at these sites in LUMO. Notably, both ortho-site effects for LUMO are weaker than those for HOMO due to the ICT-induced electron density reduction at P-ring, which accounts for the emission wavelength blueshift and redshift by EWGs and EDGs, respectively (Figure 7.7b).

Second, the incorporation of a large conjugated group as the electron acceptor at C-2 position barely affects the HOMO energy, irrespective of the P-ring substitutions (see methyl series versus phenyl series, Figure 7.7). This is because the electron density map in HOMO is largely conserved and distributed across the P-ring, methine bridge and I-ring in the p-HBDI backbone, without much contribution from the C-2 substitutions (Figure 7.6a and 7.6b).

In aggregate, an effective red-shifting strategy can be realized by incorporating EDGs at the *ortho* site (electron rich) to the pre-existing donor group to mainly destabilize HOMO/ground state, while introducing EWGs at the acceptor end to primarily stabilize LUMO/excited ICT state. The molecular prototype is illustrated in the context of anionic *p*-HBDI chromophore in Figure 7.8.
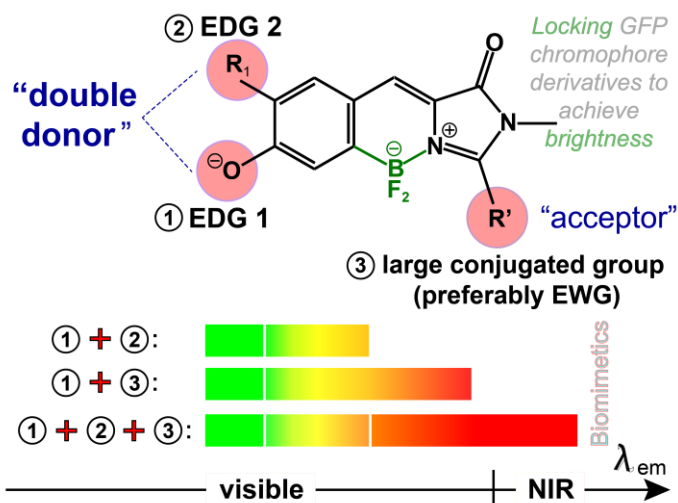
Figure 7.8. Molecular prototype for color tuning based on the anionic GFP chromophore. Strategic substitutions promote redder emission (aided by the light-induced ICT), and conformational locking can improve FQY. Reproduced with permission from Cheng Chen et al., *Chem. Commun.* **2019**, 55, 2537-2540. Copyright 2019 The Royal Society of Chemistry.

7.3.5 Solvatochromism

Solvatochromism is a strong indicator for ICT, since the electronic ground and excited states of the chromophore have different polarities and therefore are stabilized by polar solvents to different extents.[47] We used Kamlet-Taft analysis to quantitatively characterize the solvatochromism of locked *p*-HBDI derivatives, i.e., MnF and PnF. The pertinent analysis correlates the solute spectral shift (Tables 7.2 and 7.3) with solvent parameters including the H-bond donating (α or acidity) and H-bond accepting (β or basicity) abilities, as well as dipolarity (π^* or polar solvating property):[48,49]

$$\nu = \nu_0 + a\alpha + b\beta + p\pi^*$$

Table 7.4 summarizes the Kamlet-Taft analysis results for the emission of the anionic MnF and PnF. For both series, especially PnF, solvent acidity α plays a major role in the solvatochromic shift. The notable positive coefficient a indicates a decrease in anion basicity in the relaxed excited state due to the charge migration from P-ring to I-ring that reduces the electron density on $-O^-$ (i. e., the donor end). Meanwhile, a weak dependence on solvent basicity β is likely due to the absence of H-bond donating sites in the anionic form. The consistently negative correlation between solvent dipolarity π^* and spectral shift suggests that the electric dipole moment of the anion in the relaxed excited state (e. g., the emissive state) increases due to the ICT with respect to the electronic ground state.[42,49,50]

Table 7.2. Absorption and emission maxima (nm) of anionic MnF in various solvents.

Solvent	solvent parameters			M0F		M1F		M2F		M3F	
	π^*	β	α	λ_{abs}	λ_{em}	λ_{abs}	λ_{em}	λ_{abs}	λ_{em}	λ_{abs}	λ_{em}
Water	1.09	0.4	1.17	485	520	485	528	479	532	474	520
MeOH	0.6	0.62	0.93	498	531	498	535	493	536	490	520
EtOH	0.54	0.77	0.83	512	532	514.5	536	511	537	500	529
Dioxane	0.49	0.37	0	529	541	506	530	504	531	504	529
EtOAc	0.45	0.45	0	533	543	507	530.5	505	533	498	529
CH₂Cl₂	0.73	0	0.3	536	551	514	540	510	540	509	540
Et₂O	0.24	0.47	0	539	543	502	531	507	530	455	533
ACN	0.66	0.31	0.19	533	540	537	545	533	545	501	535
THF	0.55	0.55	0	536	544	512	543.5	509	534.5	509	535
Toluene	0.49	0.11	0	535	543	511	530.5	511	531.5	509	530
DMSO	1.0	0.76	0	538	545	542	549.5	539	548	528	540
Acetone	0.62	0.48	0.08	531	552	543	547.5	540	548	505	537
DMF	0.88	0.69	0	543	550	548	552	545	546	531	539
Pyridine	0.87	0.64	0	543	551	548	553	547	554	536	544

Table 7.3. Absorption and emission maxima (nm) of anionic PnF in various solvents.

Solvent	solvent parameters			M0F		M1F		M2F		M3F	
	π^*	β	α	λ_{abs}	λ_{em}	λ_{abs}	λ_{em}	λ_{abs}	λ_{em}	λ_{abs}	λ_{em}
Water	1.09	0.4	1.17	512	545	511	555	508	558	499	545
MeOH	0.6	0.62	0.93	526	565	527	572	521	568	516	563
EtOH	0.54	0.77	0.83	534	570	537	572	537	576	530	566
Dioxane	0.49	0.37	0	497	–	535	591	535	591	526	580
EtOAc	0.45	0.45	0	537	590	528	594	537	590	528	580
CH$_2$Cl$_2$	0.73	0	0.3	543	591	548	594	543	593	530	585
Et$_2$O	0.24	0.47	0	540	593	543	598	540	594	532	583
ACN	0.66	0.31	0.19	545	584	551	600	535	591	535	583
THF	0.55	0.55	0	–	588	545	600	541	597	532	584
Toluene	0.49	0.11	0	541	594	545	600	543	592	533	585
DMSO	1.0	0.76	0	551	604	557	604	554	602	545	587
Acetone	0.62	0.48	0.08	547	600	554	604	553	601	533	586
DMF	0.88	0.69	0	549	599	555	606	553	603	546	587
Pyridine	0.87	0.64	0	553	605	547	608	543	604	538	594

Table 7.4. Kamlet-Taft analysis for emission of anionic MnF and PnF in solution.

compound	a	b	p	$\nu_0{}^a$	R^b
M0F	0.7	0	−0.2	18.4	0.86
M1F	0.4	−0.5	−0.7	19.1	0.79
M2F	0.3	−0.3	−0.7	19.1	0.75
M3F	0.5	−0.1	−0.5	19.0	0.82
P0F	1.2	−0.2	−0.2	16.9	0.94
P1F	1.1	−0.1	−0.2	16.8	0.95
P2F	1.0	−0.2	−0.3	17.0	0.96
P3F	0.9	0	−0.1	17.1	0.93

^{a}Spectral shift in the unit of 10^3 cm^{-1}.

^{b}Linear correlation coefficient for the multivariable regression fits.

7.3.6 Validation of ICT by FSRS with site precision

Though ICT can be intuitively speculated by identifying the donor and acceptor moieties, site-specific differences may still exist and cause an inefficient use of molecular structure "footprint" and insignificant redshifts, especially when the correct functional site is not chosen, e. g., C-2 versus N-1 (Figure 7.2). Solvatochromism provides evidence for ICT, but there is limited information about how charge flows within the fluorophore upon photoexcitation. To gain more experimental insights into ICT, femtosecond stimulated Raman spectroscopy (FSRS) was used to track the charge migration events using local vibrational marker bands as the electron density probes.[51-53] By analyzing the frequency shift from ground state to excited state, one could acquire the information concerning the directional ICT in the excited state. In case of locked p-HBDI, local stretch modes at P-ring and I-ring should be red- and blue-shifted from S_0 to S_1, respectively, due to the ICT from P-ring to I-ring (Figure 7.9).
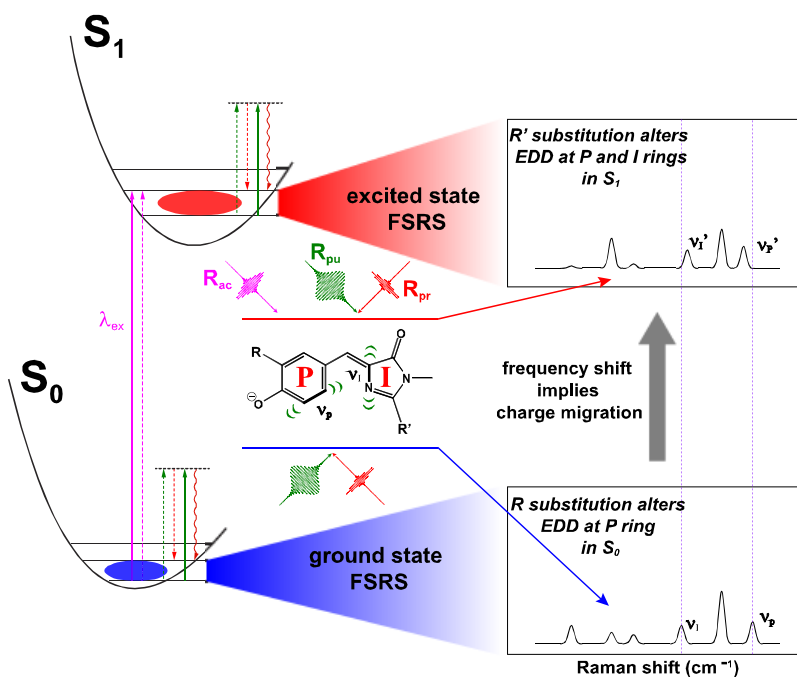
Figure 7.9. Illustration of the ground- and excited-state FSRS to track vibrational signature bands indicative of charge migration from the P-ring to I-ring. Representative energy level diagrams and light-matter interactions are shown in S_0 and S_1 states. EDD: electron density distribution. Adapted with permission from Cheng Chen, Chong Fang, *Chem. Asian. J.* **2020**, 15, 1514-1523. Copyright 2020 Wiley-VCH Verlag GmbH & Co. KGaA, Weinheim.

The ground- and excited-state FSRS spectra on the anionic M3F and P3F in water revealed that the photoinduced ICT occurs from P-ring to I-ring, indicated by the blueshift of a local I-ring C$-$N stretching mode (i. e., 1350 to 1373 cm^{-1} for M3F and 1343 to 1356 cm^{-1} for P3F, Figure 7.10a).[42] To examine the site-specificity of C-2 position for ICT, a direct observation of C-2 substituent localized modes would be more supportive such as the phenyl ring vibrations in P3F. In water, the signal-to-noise ratio of excited-state FSRS is greatly limited by the solubility of P3F and subject to the resonance conditions[54-57] (Raman pump of 560 nm for P3F) in FSRS and intrinsic electric polarizabilities associated with the vibrational motions. Notably for P3F, two excited-state phenyl-ring vibrational marker bands at 1184 (ring-H scissoring) and 1414 cm^{-1} (ring-H rocking, in-plane ring deformation) become dominant with a different resonance condition (Raman pump of 500 nm) in methanol. The corresponding ground-state modes, on the other hand, are largely absent.[50] This observation could be attributed to the polarizability increase of these two modes in the excited state, in accord with the electron density increase at phenyl ring. Meanwhile,

the P-ring mode (phenolate C=C stretch with bridge C=C stretch) of M3F under the same resonance condition redshifts from 1649 cm^{-1} in the ground state to 1566 cm^{-1} in the excited state, indicative of the electron density decrease at P-ring. These correlated spectral patterns imply that substitutions at C-2 position could promote an efficient excited-state ICT from P-ring to I-ring (specifically toward C-2 position) such that a stabilized excited state can be reached for a smaller emission gap. Such structural dynamics insights are crucial to dissect photochemistry of fluorophores in solution, because only the comparative studies of related samples (Figure 7.10) can validate the underlying ICT.

Interestingly, the ground-state I-ring C−N stretching at ~1340 cm^{-1} is insensitive to P-ring (e. g., fluorination) and I-ring (methyl to phenyl group at C-2) substitutions (Figure 7.10b), confirming no dramatic charge migration or redistribution from P-ring to I-ring in the electronic ground state. This spectral finding agrees with the isoenergetic HOMOs of MnF and PnF with same fluorination due to their relatively localized and similar HOMO electron density distribution (Figure 7.6). The characteristic mode frequency shifts from $S_0 \rightarrow S_1$ (Figure 7.10) thus show that the ground- and excited-state energies can be tuned in a largely "separate" manner.
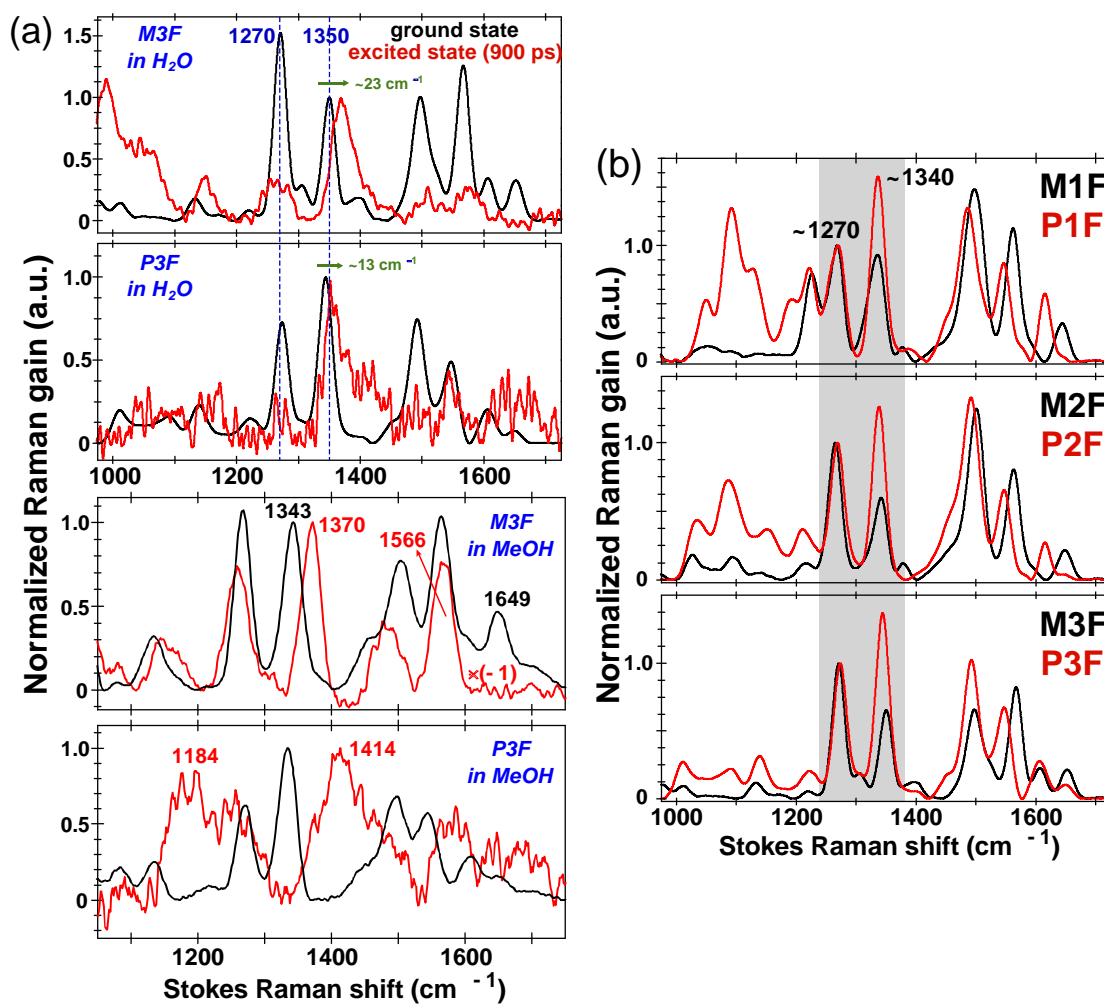
Figure 7.10. Tunable FSRS for characterization of substitution effects and site selectivity during ICT. (a) Comparison of ground- and excited-state Stokes FSRS for the anionic M3F and P3F in water (upper two panels, Raman pump for excited-state FSRS at 520 and 560 nm, respectively) and methanol (lower two panels, Raman pump for excited-state FSRS at 500 nm) at 900 ps following 400 nm femtosecond photoexcitation. (c) Comparison of ground-state Stokes FSRS for the anionic MnF and PnF series with Raman pump at 560 nm. Adapted with permission from Cheng Chen, Chong Fang, *Chem. Asian. J.* **2020**, 15, 1514-1523. Copyright 2020 Wiley-VCH Verlag GmbH & Co. KGaA, Weinheim.
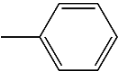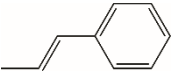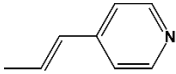
7.3.7 Proof-of-concept synthesis and characterization

To validate our color-tuning strategy from computations and spectroscopy, several series of unlocked GFP fluorophores with different substituents were synthesized due to current challenges in synthesizing the locked compounds with certain functional groups.[21] The P-ring substitutions of cyano, methoxy, hydroxy, amino groups and I-ring substitutions of methyl, phenyl, styryl, vinylpyridine groups are used to demonstrate the effects of donor and acceptor modifications on the emission color, respectively (Figure 7.11a). The steady-state absorption and emission as well as FQY data are tabulated in Table 7.5. The additive tuning strategy is well substantiated by the observed emission wavelengths of synthesized fluorophores. In particular, the mostly volume-conserving substitution by $-NH_2$ could red-shift the emission by up to 100 nm with respect to the unsubstituted molecule in case of GFP chromophore scaffolds.

Interestingly, other groups have designed and synthesized fluorescent small-molecule scaffolds that lend support to the color-tuning scheme for D-π-A systems.[31,32,58,59] In Figure 7.11b, a relatively small fluorescent core skeleton via a concise and practical one-pot synthetic route shows the emission redshift as the donor and acceptor get stronger at the electron-rich sites in HOMO and LUMO, respectively,[32] in accord with the destabilization of HOMO and stabilization of LUMO by the strategic substituents (Figure 7.7a). In Figure 7.11c, a more compact dimethylamino quinoline "core" scaffold also demonstrates a red-shifting trend of emission wavelength as the EWG gets stronger (i. e., larger σ_p values or the Hammett constants, see above) at the acceptor site as excited-state ICT occurs from the EDG (dimethylamino group) on one end to

the C-2 site on the other end (aryl R group as the acceptor) of the fluorophore.[31] The underlying electron distribution and structural dynamics basis for the photophysics and/or photochemistry (ultimately leading to the fluorescence properties) can be elucidated by an integrated and powerful experimental platform of ultrafast electronic and vibrational spectroscopies, theoretical calculations, and organic synthesis.

Table 7.5. Photophysical properties of the synthesized unlocked fluorophores in water.

R_1	R'	CH_3		phenyl		styryl		pyridyl	
		HA	A^-	HA	A^-	HA	A^-	HA	A^-
CN	Abs.	371	408	382	434	426	465	$-^b$	$-^b$
	Em.^{a}	481	485	475	520	535	570	$-^b$	$-^b$
	FQY(%)	0.2	0.2	0.2	0.08	0.1	0.1	$-^b$	$-^b$
H	Abs.	367	425	390	454	424	490	430	511
	Em.^{a}	453	491	479	526	528	585	545	630
	FQY(%)	0.03	0.06	0.04	0.08	0.2	0.2	0.03	0.03
OH	Abs.	379	442	401	474	437	511	446	529
	Em.^{a}	475	518	500	555	542	617	575	657
	FQY(%)	0.06	0.06	0.04	0.06	0.1	0.05	0.06	0.03
OCH₃	Abs.	378	448	402	480	370	408	442	536
	Em.^{a}	471	515	495	552	465	488^c	581	660
	FQY(%)	0.06	0.1	0.08	0.1	0.05	0.09	0.2	0.1
NH₂	Abs.	388	454	412	486	448	523	450	543
	Em.^{a}	474	~600	$-^d$	~620	$-^d$	~620	~582	~650
	FQY(%)	0.04	0.05	$-^d$	0.02	$-^d$	0.03	0.07	0.02

^{a}The highlighted anionic emission wavelengths by red color were used for Figure 7.11a.

^{b}This compound cannot be purified due to the decomposition especially upon heating.

^{c}Spectral anomaly.

^{d}Unavailable due to the extremely efficient ESPT and low quantum yield.
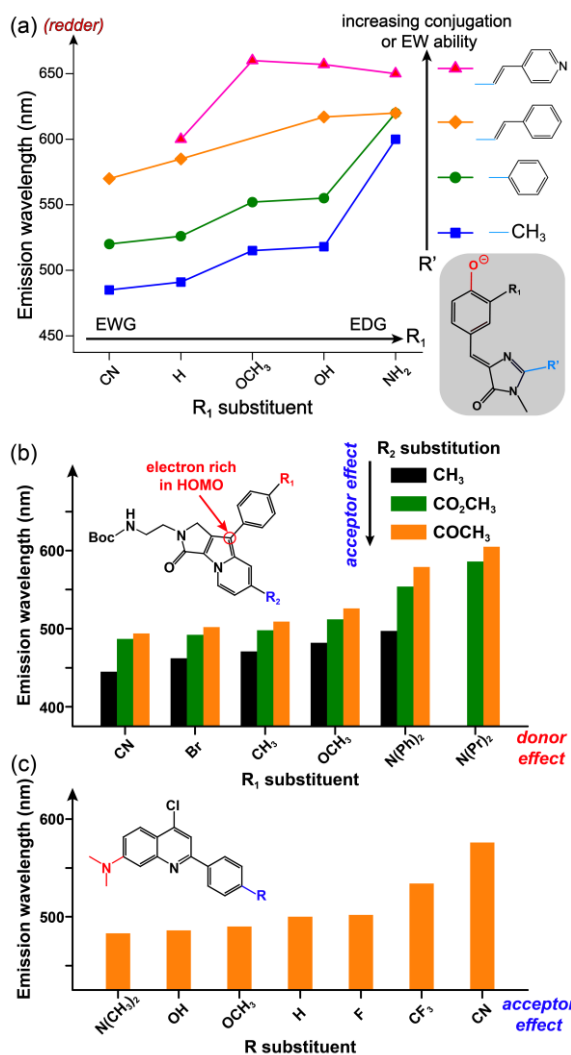
Figure 7.11. Rational design of the synthetic fluorophores with broad tunability. (a) Effects of P-ring and I-ring substitutions on emission wavelengths of the anionic *p*-HBDI fluorophores in aqueous solutions. (b) Effects of various donors and acceptors on the emission wavelength of 9-Aryl-1,2-dihydropyrrolo[3,4-*b*]indolizin-3-one-based dyes. (c) Effects of various acceptors on the emission wavelength of the synthesized quinoline-based dyes. Reproduced with permission from Cheng Chen, Chong Fang, *Chem. Asian. J.* **2020**, 15, 1514-1523. Copyright 2020 Wiley-VCH Verlag GmbH & Co. KGaA, Weinheim.

7.4 Conclusions

In conclusion, we have devised a unique red-shifting strategy by synthesizing two new series of GFP chromophore derivatives in aqueous solution, aided by quantum calculations of frontier molecular orbitals, electronic and vibrational spectroscopies in S_0 and S_1, and systematic synthesis of the substituted (at both the donor and acceptor sites) unlocked HBDIs. We reveal that the electronic ground and excited-state energetics can be separately and synergistically tuned for a single-core molecular framework with specific substituents, as validated by direct comparison between the predicted emission wavelengths and the observed spectral values (Figure 7.6) as well as the newly synthesized fluorophores with various FQYs (Figure 7.11). In conjunction with ESPT capabilities enabled by photoacidity and further conformational locking of the backbone, these newly revealed foundational design routes for redder and brighter fluorophores in solution will inspire chemical synthesis methods and advance a broad range of imaging applications with effectiveness and efficiency.

7.5 Perspectives on generalization of the red-shifting strategy

As an iconic system, the GFP chromophore and its synthetic analogues have been extensively studied in chemistry and biology,[60] providing an excellent platform to study and develop advanced properties for various imaging applications concerning color, FQY, Stokes shift with rich prior knowledge. The "double-donor-one-acceptor" approach presented in this chapter can be viewed as a shortcut for achieving redder fluorophores with respect to the conventional ICT strategy. We foresee that such an effective broadening of EDG space in conjunction with a suitable EWG on the opposite end could impact fluorescence imaging fields in a significant manner.

7.5.1 Applications on non-canonical amino acids in fluorescent proteins

One direct impact of the "double-donor-one-acceptor" red-shifting strategy lies in the chromophore modifications of fluorescent proteins (FPs). By introducing noncanonical amino acids into the autocatalytically matured chromophore, the FPs' properties such as color and FQY can be tuned. For the GFP family and its derivatives, the readily changeable chromophore moiety is the P-ring from the tyrosine residue, and some recent works demonstrated the potential in red-shifting GFP emission[46,61] without significantly enlarging the conjugated chromophore. In terms of color, the redder GFP chromophore structure is in line with the "double donor" (an EDG next to $-OH/-O^-$) structure (Figure 7.8). The I-ring, however, has limited options and is rather challenging to modify because the two contributing amino acids are anchoring points to the β-barrel enclosing the protein pocket. Nevertheless, most photoconvertible red FPs[62,63] entail either a strong electron-withdrawing group (e. g., asFP595, −COR) or a

large conjugated group (e. g., Kaede-like FPs, 4-vinylimidazole),[64] or both (e. g., far-red PSmOrange) in the converted red form, which substantiates that the "one acceptor" at C-2 position red-shifts the FP emission by promoting a further delocalized and stabilized ICT state of the protein chromophore. Encouraged by these existing RFPs with an engineerable residue sidechain at the C-2 site, we expect that the combination of double donor and one acceptor could further red-shift FPs while retaining the photoconvertibility to benefit bioimaging applications.

7.5.2 Applications on other fluorophore scaffolds

This red-shifting strategy should be generalizable to other fluorophore scaffolds, which provide more opportunities for designing new bioprobes. Though the modified *p*-HBDI derivatives by the double-donor-one-acceptor approach may be non-fluorescent due to facile rotational motions of the backbone, conformational restraint can improve FQY. Another promising route is to design and build new fluorophores on a fluorescent backbone.[65-67] For example, indole (the amino acid tryptophan sidechain) is a fluorescent two-ring system consisting of a benzene ring fused to a pyrrole ring. Some reports showed that EWG substitutions at the benzene sites (e.g., C-4) lead to a redshift in emission due to the enhanced ICT from pyrrole to benzene ring while a high FQY is maintained.[68,69] Based on the push-pull analysis and our double-donor-one-acceptor concept, an EDG can be incorporated at C-3 site of the pyrrole ring (nearby N-1 is the first donor) to destabilize the ground state, while an EWG substitution at the benzene ring (e. g., C-4 site) is expected to stabilize the excited state. Therefore, a further red-shifted fluorophore with a compact size and high brightness in solution is within reach.

Another fitting example is BODIPY, one of the most studied classes of fluorescent probes, which is highly fluorescent due to a rigid backbone also with the BF_2 locking (Figure 7.1b). Despite extensive synthetic efforts, many current modifications make it quite bulky and consequently quench the fluorescence due to the increased structure flexibility caused by large substituents.[59] We expect that the general double-donor-one-acceptor strategy could red-shift emission color while mitigating the fluorescence loss of BODIPY derivatives because it does not require large-group substitutions. Besides inviting bioorganic chemists to synthesize new redder fluorophores, we provide preliminary insights into the basis of electron density analysis from ab initio calculations. The meso site is found to undergo an electron density increase from HOMO to LUMO while the C-2 and C-6, C-3 and C-5 sites exhibit electron density decrease to different extents (see Figure 7.1b bottom panel for the atomic numbering). The EWG substitution at the meso site could then stabilize LUMO while two adjacent EDGs at C-2 and C-3 (and/or symmetric modifications at C-6 and C-5) sites destabilize HOMO. In fact, this kind of modification has been confirmed in literature to be more effective than other substitutions for redder emission while preserving high FQYs due to the small-size substituents (dye 74–76 in ref. [58]). We envision that advanced computations and ultrafast spectroscopy will continue to elucidate and validate fluorescence mechanisms with clear electronic and vibrational signatures of a wide range of functionalizable molecular scaffolds, and enable more rational design strategies for redder, brighter, and versatile fluorescent probes to power the next-generation imaging and optogenetic applications across the science and engineering disciplines.

7.6 References

[1] Chudakov, D. M.; Matz, M. V.; Lukyanov, S.; Lukyanov, K. A. Fluorescent Proteins and Their Applications in Imaging Living Cells and Tissues. *Physiol. Rev.* **2010**, *90*, 1103-1163.

[2] Yuan, L.; Lin, W.; Zheng, K.; He, L.; Huang, W. Far-red to near infrared analyte-responsive fluorescent probes based on organic fluorophore platforms for fluorescence imaging. *Chem. Soc. Rev.* **2013**, *42*, 622-661.

[3] Gonçalves, M. S. T. Fluorescent Labeling of Biomolecules with Organic Probes. *Chem. Rev.* **2009**, *109*, 190-212.

[4] Peng, X.; Song, F.; Lu, E.; Wang, Y.; Zhou, W.; Fan, J.; Gao, Y. Heptamethine Cyanine Dyes with a Large Stokes Shift and Strong Fluorescence: A Paradigm for Excited-State Intramolecular Charge Transfer. *J. Am. Chem. Soc.* **2005**, *127*, 4170-4171.

[5] Karton-Lifshin, N.; Albertazzi, L.; Bendikov, M.; Baran, P. S.; Shabat, D. "Donor–Two-Acceptor" Dye Design: A Distinct Gateway to NIR Fluorescence. *J. Am. Chem. Soc.* **2012**, *134*, 20412-20420.

[6] Chai, X.; Cui, X.; Wang, B.; Yang, F.; Cai, Y.; Wu, Q.; Wang, T. Near-Infrared Phosphorus-Substituted Rhodamine with Emission Wavelength above 700 nm for Bioimaging. *Chem. Eur. J.* **2015**, *21*, 16754-16758.

[7] Sirbu, D.; Butcher, J. B.; Waddell, P. G.; Andras, P.; Benniston, A. C. Locally Excited State–Charge Transfer State Coupled Dyes as Optically Responsive Neuron Firing Probes. *Chem. Eur. J.* **2017**, *23*, 14639-14649.

[8] Long, L.; Huang, M.; Wang, N.; Wu, Y.; Wang, K.; Gong, A.; Zhang, Z.; Sessler, J. L. A Mitochondria-Specific Fluorescent Probe for Visualizing Endogenous Hydrogen Cyanide Fluctuations in Neurons. *J. Am. Chem. Soc.* **2018**, *140*, 1870-1875.

[9] Shen, P.; Zhuang, Z.; Jiang, X.-F.; Li, J.; Yao, S.; Zhao, Z.; Tang, B. Z. Through-Space Conjugation: An Effective Strategy for Stabilizing Intramolecular Charge-Transfer States. *J. Phys. Chem. Lett.* **2019**, *10*, 2648-2656.

[10] Olsen, S. Locally-Excited (LE) versus Charge-Transfer (CT) Excited State Competition in a Series of Para-Substituted Neutral Green Fluorescent Protein (GFP) Chromophore Models. *J. Phys. Chem. B* **2015**, *119*, 2566-2575.

[11] Kim, S.-Y.; Cho, Y.-J.; Lee, A.-R.; Son, H.-j.; Han, W.-S.; Cho, D. W.; Kang, S. O. Influence of π-conjugation structural changes on intramolecular charge transfer and photoinduced electron transfer in donor–π–acceptor dyads. *Phys. Chem. Chem. Phys.* **2017**, *19*, 426-435.

[12] Buck, J. T.; Wilson, R. W.; Mani, T. Intramolecular Long-Range Charge-Transfer Emission in Donor–Bridge–Acceptor Systems. *J. Phys. Chem. Lett.* **2019**, *10*, 3080-3086.

[13] Baleeva, N. S.; Myannik, K. A.; Yampolsky, I. V.; Baranov, M. S. Bioinspired Fluorescent Dyes Based on a Conformationally Locked Chromophore of the Fluorescent Protein Kaede. *Eur. J. Org. Chem.* **2015**, *2015*, 5716-5721.

[14] Koide, Y.; Urano, Y.; Hanaoka, K.; Piao, W.; Kusakabe, M.; Saito, N.; Terai, T.; Okabe, T.; Nagano, T. Development of NIR Fluorescent Dyes Based on Si–rhodamine for in Vivo Imaging. *J. Am. Chem. Soc.* **2012**, *134*, 5029-5031.

[15] Lee, H.; Akers, W.; Bhushan, K.; Bloch, S.; Sudlow, G.; Tang, R.; Achilefu, S. Near-Infrared pH-Activatable Fluorescent Probes for Imaging Primary and Metastatic Breast Tumors. *Bioconjugate Chem.* **2011**, *22*, 777-784.

[16] Piontkowski, Z.; McCamant, D. W. Excited-State Planarization in Donor–Bridge Dye Sensitizers: Phenylene versus Thiophene Bridges. *J. Am. Chem. Soc.* **2018**, *140*, 11046-11057.

[17] Reisch, A.; Klymchenko, A. S. Fluorescent Polymer Nanoparticles Based on Dyes: Seeking Brighter Tools for Bioimaging. *Small* **2016**, *12*, 1968-1992.

[18] Escudero, D. Revising Intramolecular Photoinduced Electron Transfer (PET) from First-Principles. *Acc. Chem. Res.* **2016**, *49*, 1816-1824.

[19] Bell, A. F.; He, X.; Wachter, R. M.; Tonge, P. J. Probing the Ground State Structure of the Green Fluorescent Protein Chromophore using Raman Spectroscopy. *Biochemistry* **2000**, *39*, 4423-4431.

[20] Baranov, M. S.; Lukyanov, K. A.; Borissova, A. O.; Shamir, J.; Kosenkov, D.; Slipchenko, L. V.; Tolbert, L. M.; Yampolsky, I. V.; Solntsev, K. M. Conformationally Locked Chromophores as Models of Excited-State Proton Transfer in Fluorescent Proteins. *J. Am. Chem. Soc.* **2012**, *134*, 6025-6032.

[21] Baranov, M. S.; Solntsev, K. M.; Baleeva, N. S.; Mishin, A. S.; Lukyanov, S. A.; Lukyanov, K. A.; Yampolsky, I. V. Red-Shifted Fluorescent Aminated Derivatives of a Conformationally Locked GFP Chromophore. *Chem. Eur. J.* **2014**, *20*, 13234-13241.

[22] Ulrich, G.; Ziessel, R.; Harriman, A. The Chemistry of Fluorescent Bodipy Dyes: Versatility Unsurpassed. *Angew. Chem. Int. Ed.* **2008**, *47*, 1184-1201.

[23] Hong, Y.; Lam, J. W. Y.; Tang, B. Z. Aggregation-Induced Emission. *Chem. Soc. Rev.* **2011**, *40*, 5361-5388.

[24] Qian, H.; Cousins, M. E.; Horak, E. H.; Wakefield, A.; Liptak, M. D.; Aprahamian, I. Suppression of Kasha's Rule as a Mechanism for Fluorescent Molecular Rotors and Aggregation-Induced Emission. *Nat. Chem.* **2017**, *9*, 83-87.

[25] Kojima, S.; Ohkawa, H.; Hirano, T.; Maki, S.; Niwa, H.; Ohashi, M.; Inouye, S.; Tsuji, F. I. Fluorescent Properties of Model Chromophores of Tyrosine-66 Substituted Mutants of *Aequorea* Green Fluorescent Protein (GFP). *Tetra. Lett.* **1998**, *39*, 5239-5242.

[26] Lee, C.-Y.; Chen, Y.-C.; Lin, H.-C.; Jhong, Y.; Chang, C.-W.; Tsai, C.-H.; Kao, C.-L.; Chien, T.-C. Facile Synthesis of 4-arylidene-5-imidazolinones as Synthetic Analogs of Fluorescent Protein Chromophore. *Tetrahedron* **2012**, *68*, 5898-5907.

[27] Chatterjee, S.; Karuso, P. An Efficient and Concise Method to Synthesize Locked GFP Chromophore Analogues. *Tetra. Lett.* **2016**, *57*, 5197-5200.

[28] Yampolsky, I. V.; Kislukhin, A. A.; Amatov, T. T.; Shcherbo, D.; Potapov, V. K.; Lukyanov, S.; Lukyanov, K. A. Synthesis and Properties of the Red Chromophore of the Green-to-Red Photoconvertible Fluorescent Protein Kaede and Its Analogs. *Bioorg. Chem.* **2008**, *36*, 96-104.

[29] Frisch, M. J.; Trucks, G. W.; Schlegel, H. B.; Scuseria, G. E.; Robb, M. A.; Cheeseman, J. R.; Scalmani, G.; Barone, V.; Mennucci, B.; Petersson, G. A.; Nakatsuji, H.; Caricato, M.; Li, X.; Hratchian, H. P.; Izmaylov, A. F.; Bloino, J.; Zheng, G.; Sonnenberg, J. L.; Hada, M.; Ehara, M.; Toyota, K.; Fukuda, R.; Hasegawa, J.; Ishida, M.; Nakajima, T.; Honda, Y.; Kitao, O.; Nakai, H.; Vreven, T.; J. A. Montgomery, J.; Peralta, J. E.; Ogliaro, F.; Bearpark, M.; Heyd, J. J.; Brothers, E.; Kudin, K. N.; Staroverov, V. N.; Kobayashi, R.; Normand, J.; Raghavachari, K.; Rendell, A.; Burant, J. C.; Iyengar, S. S.; Tomasi, J.; Cossi, M.; Rega, N.; Millam, J. M.; Klene, M.; Knox, J. E.; Cross, J. B.; Bakken, V.; Adamo, C.; Jaramillo, J.; Gomperts, R.; Stratmann, R. E.; Yazyev, O.; Austin, A. J.; Cammi, R.; Pomelli, C.; Ochterski, J. W.; Martin, R. L.; Morokuma, K.; Zakrzewski, V. G.; Voth, G. A.; Salvador, P.; Dannenberg, J. J.; Dapprich, S.; Daniels, A. D.; Farkas, Ö.; Foresman, J. B.; Ortiz, J. V.; Cioslowski, J.; Fox, D. J. *Gaussian 09*, Gaussian, Inc.: Wallingford, CT, 2009.

[30] Adamo, C.; Jacquemin, D. The Calculations of Excited-State Properties with Time-Dependent Density Functional Theory. *Chem. Soc. Rev.* **2013**, *42*, 845-856.

[31] Jun, J. V.; Petersson, E. J.; Chenoweth, D. M. Rational Design and Facile Synthesis of a Highly Tunable Quinoline-Based Fluorescent Small-Molecule Scaffold for Live Cell Imaging. *J. Am. Chem. Soc.* **2018**, *140*, 9486-9493.

[32] Kim, E.; Koh, M.; Lim, B. J.; Park, S. B. Emission Wavelength Prediction of a Full-Color-Tunable Fluorescent Core Skeleton, 9-Aryl-1,2-dihydropyrrolo[3,4-b]indolizin-3-one. *J. Am. Chem. Soc.* **2011**, *133*, 6642-6649.

[33] Niko, Y.; Sasaki, S.; Narushima, K.; Sharma, D. K.; Vacha, M.; Konishi, G.-i. 1-, 3-, 6-, and 8-Tetrasubstituted Asymmetric Pyrene Derivatives with Electron Donors and Acceptors: High Photostability and Regioisomer-Specific Photophysical Properties. *J. Org. Chem.* **2015**, *80*, 10794-10805.

[34] Liu, X.; Cole, J. M.; Xu, Z. Substantial Intramolecular Charge Transfer Induces Long Emission Wavelengths and Mega Stokes Shifts in 6-Aminocoumarins. *J. Phys. Chem. C* **2017**, *121*, 13274-13279.

[35] Song, W.; Strack, R. L.; Svensen, N.; Jaffrey, S. R. Plug-and-Play Fluorophores Extend the Spectral Properties of Spinach. *J. Am. Chem. Soc.* **2014**, *136*, 1198-1201.

[36] Ooyama, Y.; Inoue, S.; Nagano, T.; Kushimoto, K.; Ohshita, J.; Imae, I.; Komaguchi, K.; Harima, Y. Dye-Sensitized Solar Cells Based On Donor–Acceptor π-Conjugated Fluorescent Dyes with a Pyridine Ring as an Electron-Withdrawing Anchoring Group. *Angew. Chem. Int. Ed.* **2011**, *50*, 7429-7433.

[37] Congrave, D. G.; Drummond, B. H.; Conaghan, P. J.; Francis, H.; Jones, S. T. E.; Grey, C. P.; Greenham, N. C.; Credgington, D.; Bronstein, H. A Simple Molecular Design Strategy for Delayed Fluorescence toward 1000 nm. *J. Am. Chem. Soc.* **2019**, *141*, 18390-18394.

[38] Barnsley, J. E.; Pelet, W.; McAdam, J.; Wagner, K.; Hayes, P.; Officer, D. L.; Wagner, P.; Gordon, K. C. When "Donor–Acceptor" Dyes Delocalize: A Spectroscopic and Computational Study of D–A Dyes Using "Michler's Base". *J. Phys. Chem. A* **2019**, *123*, 5957-5968.

[39] Hashimoto, N.; Umano, R.; Ochi, Y.; Shimahara, K.; Nakamura, J.; Mori, S.; Ohta, H.; Watanabe, Y.; Hayashi, M. Synthesis and Photophysical Properties of λ5-Phosphinines as a Tunable Fluorophore. *J. Am. Chem. Soc.* **2018**, *140*, 2046-2049.

[40] Wu, Y.; Zhu, W. Organic sensitizers from D–π–A to D–A–π–A: effect of the internal electron-withdrawing units on molecular absorption, energy levels and photovoltaic performances. *Chem. Soc. Rev.* **2013**, *42*, 2039-2058.

[41] Ji, J.-M.; Zhou, H.; Kim, H. K. Rational design criteria for D–π–A structured organic and porphyrin sensitizers for highly efficient dye-sensitized solar cells. *J. Mater. Chem. A* **2018**, *6*, 14518-14545.

[42] Chen, C.; Baranov, M. S.; Zhu, L.; Baleeva, N. S.; Smirnov, A. Y.; Zaitseva, S. O.; Yampolsky, I. V.; Solntsev, K. M.; Fang, C. Designing redder and brighter fluorophores by synergistic tuning of ground and excited states. *Chem. Commun.* **2019**, *55*, 2537-2540.

[43] Chen, C.; Zhu, L.; Boulanger, S. A.; Baleeva, N. S.; Myasnyanko, I. N.; Baranov, M. S.; Fang, C. Ultrafast excited-state proton transfer dynamics in dihalogenated non-fluorescent and fluorescent GFP chromophores. *J. Chem. Phys.* **2020**, *152*, 021101.

[44] Hansch, C.; Leo, A.; Taft, R. W. A survey of Hammett substituent constants and resonance and field parameters. *Chem. Rev.* **1991**, *91*, 165-195.

[45] Driscoll, E. W.; Hunt, J. R.; Dawlaty, J. M. Photobasicity in Quinolines: Origin and Tunability via the Substituents' Hammett Parameters. *J. Phys. Chem. Lett.* **2016**, *7*, 2093-2099.

[46] Romei, M. G.; Lin, C.-Y.; Mathews, I. I.; Boxer, S. G. Electrostatic control of photoisomerization pathways in proteins. *Science* **2020**, *367*, 76-79.

[47] Reichardt, C. Solvatochromic Dyes as Solvent Polarity Indicators. *Chem. Rev.* **1994**, *94*, 2319-2358.

[48] Kamlet, M. J.; Abboud, J.-L. M.; Abraham, M. H.; Taft, R. W. Linear Solvation Energy Relationships. 23. A Comprehensive Collection of the Solvatochromic Parameters, π*, α, and β, and Some Methods for Simplifying the Generalized Solvatochromic Equation. *J. Org. Chem.* **1983**, *48*, 2877-2887.

[49] Reichardt, C.; Welton, T. *Solvents and Solvent Effects in Organic Chemistry*; 4th ed.; Wiley-VCH Verlag GmbH & Co. KGaA: Weinheim, Germany, 2011.

[50] Chen, C.; Zhu, L.; Baranov, M. S.; Tang, L.; Baleeva, N. S.; Smirnov, A. Y.; Yampolsky, I. V.; Solntsev, K. M.; Fang, C. Photoinduced Proton Transfer of GFP-Inspired Fluorescent Superphotoacids: Principles and Design. *J. Phys. Chem. B* **2019**, *123*, 3804-3821.

[51] Kukura, P.; McCamant, D. W.; Mathies, R. A. Femtosecond Stimulated Raman Spectroscopy. *Annu. Rev. Phys. Chem.* **2007**, *58*, 461-488.

[52] Fang, C.; Frontiera, R. R.; Tran, R.; Mathies, R. A. Mapping GFP structure evolution during proton transfer with femtosecond Raman spectroscopy. *Nature* **2009**, *462*, 200-204.

[53] Chen, C.; Zhu, L.; Baranov, M. S.; Tang, L.; Baleeva, N. S.; Smirnov, A. Y.; Yampolsky, I. V.; Solntsev, K. M.; Fang, C. Photoinduced Proton Transfer of GFP-Inspired Fluorescent Superphotoacids: Principles and Design. *J. Phys. Chem. B* **2019**, *123*, 3804-3821.

[54] Niu, K.; Zhao, B.; Sun, Z.; Lee, S.-Y. Analysis of femtosecond stimulated Raman spectroscopy of excited-state evolution in bacteriorhodopsin. *J. Chem. Phys.* **2010**, *132*, 084510.

[55] Chen, C.; Liu, W.; Baranov, M. S.; Baleeva, N. S.; Yampolsky, I. V.; Zhu, L.; Wang, Y.; Shamir, A.; Solntsev, K. M.; Fang, C. Unveiling Structural Motions of a Highly Fluorescent Superphotoacid by Locking and Fluorinating the GFP Chromophore in Solution. *J. Phys. Chem. Lett.* **2017**, *8*, 5921-5928.

[56] Oscar, B. G.; Chen, C.; Liu, W.; Zhu, L.; Fang, C. Dynamic Raman Line Shapes on an Evolving Excited-State Landscape: Insights from Tunable Femtosecond Stimulated Raman Spectroscopy. *J. Phys. Chem. A* **2017**, *121*, 5428-5441.

[57] Fang, C.; Tang, L.; Oscar, B. G.; Chen, C. Capturing Structural Snapshots during Photochemical Reactions with Ultrafast Raman Spectroscopy: From Materials Transformation to Biosensor Responses. *J. Phys. Chem. Lett.* **2018**, *9*, 3253-3263.

[58] Loudet, A.; Burgess, K. BODIPY Dyes and Their Derivatives: Syntheses and Spectroscopic Properties. *Chem. Rev.* **2007**, *107*, 4891-4932.

[59] Boens, N.; Leen, V.; Dehaen, W. Fluorescent indicators based on BODIPY. *Chem. Soc. Rev.* **2012**, *41*, 1130-1172.

[60] Zimmer, M. Green Fluorescent Protein (GFP): Applications, Structure, and Related Photophysical Behavior. *Chem. Rev.* **2002**, *102*, 759-782.

[61] Augustine, G.; Raghavan, S.; NumbiRamudu, K.; Easwaramoorthi, S.; Shanmugam, G.; Seetharani Murugaiyan, J.; Gunasekaran, K.; Govind, C.; Karunakaran, V.; Ayyadurai, N. Excited State Electronic Interconversion and Structural Transformation of Engineered Red-Emitting Green Fluorescent Protein Mutant. *J. Phys. Chem. B* **2019**, *123*, 2316-2324.

[62] Subach, F. V.; Verkhusha, V. V. Chromophore Transformations in Red Fluorescent Proteins. *Chem. Rev.* **2012**, *112*, 4308-4327.

[63] Acharya, A.; Bogdanov, A. M.; Grigorenko, B. L.; Bravaya, K. B.; Nemukhin, A. V.; Lukyanov, K. A.; Krylov, A. I. Photoinduced Chemistry in Fluorescent Proteins: Curse or Blessing? *Chem. Rev.* **2017**, *117*, 758-795.

[64] Krueger, T. D.; Tang, L.; Zhu, L.; Breen, I. L.; Wachter, R. M.; Fang, C. Dual Illumination Enhances Transformation of an Engineered Green-to-Red Photoconvertible Fluorescent Protein. *Angew. Chem. Int. Ed.* **2020**, *59*, 1644-1652.

[65] Chen, W.; Xu, S.; Day, J. J.; Wang, D.; Xian, M. A General Strategy for Development of Near-Infrared Fluorescent Probes for Bioimaging. *Angew. Chem. Int. Ed.* **2017**, *56*, 16611-16615.

[66] Ren, T.-B.; Xu, W.; Zhang, W.; Zhang, X.-X.; Wang, Z.-Y.; Xiang, Z.; Yuan, L.; Zhang, X.-B. A General Method To Increase Stokes Shift by Introducing Alternating Vibronic Structures. *J. Am. Chem. Soc.* **2018**, *140*, 7716-7722.

[67] Ren, X.; Zhang, F.; Luo, H.; Liao, L.; Song, X.; Chen, W. Red-emitting boron difluoride complexes with a mega-large Stokes shift and unexpectedly high fluorescence quantum yield. *Chem. Commun.* **2020**, *56*, 2159-2162.

[68] Hilaire, M. R.; Ahmed, I. A.; Lin, C.-W.; Jo, H.; DeGrado, W. F.; Gai, F. Blue fluorescent amino acid for biological spectroscopy and microscopy. *Proc. Natl. Acad. Sci. USA* **2017**, *114*, 6005-6009.

[69] You, M.; Fan, H.; Wang, Y.; Zhang, W. Aldehyde-derivatized indoles as fluorescent probes for hydration environments. *Chem. Phys.* **2019**, *526*, 110438.

Chapter 8 Concluding Remarks

In this dissertation, a state-of-the-art vibrational spectroscopic technique, femtosecond stimulated Raman spectroscopy (FSRS), assisted by femtosecond transient absorption spectroscopy (fs-TA), was employed to study two scientific problems that could benefit a range of chemical and biological applications. First, the ultrafast dynamics of excited-state proton transfer (ESPT) events for series of superphotoacids in different solvents were investigated. The superphotoacids were derived from the synthetic green fluorescent protein (GFP) chromophore core through halogenation and conformational locking on the parent molecule (i.e., p-HBDI) and named as MnF and PnF (n=2, 3). The ESPT dynamics for superphotoacids were found to be dominated and rate-limited by solvent reorientation motions, which are further complicated in organic solvents like alcohols. In methanol, three ESPT pathways are revealed: direct ESPT pathway (tens to hundreds of fs timescale) that is ultrafast and does not require H-bonding reorganization; solvent reorientation-controlled ESPT pathway (ps timescale); and rotational diffusion-controlled ESPT pathway (hundreds of ps timescale). Meanwhile, the role of other competing decay pathways such as photoisomerization during the course of ESPT has been revealed by comparing halogenated locked and unlocked p-HBDI derivatives, both of which remain superphotoacids. We found that the ESPT process prevails within the excited-state lifetime with respect to the facile nonradiative photoisomerization in case of the unlocked superphotoacids due to its relatively slower rate, and the ESPT for the locked superphotoacids exhibits a higher degree of inhomogeneity in terms of ESPT pathways. On the basis of these studies, we proposed

new design principles of tuning photoacidity in a synergistic manner: incorporating electron-withdrawing groups into the proximal (often as "donor") and distal (often as "acceptor") ring moieties to the dissociative hydroxyl group to lower the ground-state pK_a and increase the ΔpK_a, respectively.

Second, we devised a novel red-shifting strategy for fluorescence wavelengths with physical chemistry insights gained from quantum calculations and FSRS spectral shifts. We built the molecular prototype on the anionic GFP chromophore, i.e., p-HBDI, where an EDG and EWG are incorporated into the *ortho* site to the electron-donating phenolate $-O^-$ (hence two EDGs) and site C-2 of the electron-withdrawing imidazolinone ring, respectively. We termed this framework as "double-donor-one-acceptor". The quantum calculations suggest that, in reference to the parent fluorophore, the "double-donor" and "one-acceptor" structures increases and decreases the HOMO and LUMO energies, respectively, in a largely separate manner. This approach provides a shortcut toward redder emission in comparison to the conventional ICT strategy that mostly focuses on the stabilization of the excited state/LUMO. The spectral shifts from ground- to excited-state FSRS marker bands offer further mechanistic insights into the optimal site selection in promoting ICT. We envision that this synergistic spectroscopy and computations-guided strategy could advance the noncanonical fluorescent protein design and be generalized to various fluorophore scaffolds for redder emission while preserving other superior properties such as high FQYs.

Chapter 9 Future Perspectives

9.1 ESPT in solution

Despite the intensive efforts on ESPT, there remain questions insufficiently addressed concerning the role of solvent for photoacids of different strengths. For instance, it has not been systematically explored how the solvent orientation motions, as the rate-limiting step for superphotoacids, influence the ESPT process by competing with other nonradiative decay pathways if the superphotoacid is not fluorescent. This line of inquiry is important in that it could be foundational to the design of relevant chemical or biological systems by controlling reactivity of the proton transfer process. For example, in photosystem II of photosynthesis, the proton acceptor is the side chain of Histidine 190 (His190) which is a Lewis base.[1] By removing His190, the crucial water oxidation no longer occurs, which highlights the importance of proton acceptor in the electron-proton transfer reaction.[2,3] The pertinent studies in chemical systems mimicking this proton transfer process have also been actively ongoing.[4,5] Meanwhile, some extremely strong photoacids such as QCy9 exhibit ultrafast ESPT rate regardless of the solvents used.[6] This remains unresolved and deserves more investigations. Besides photoacids, photobases are another interesting class of molecules that undergo ESPT as well and have drawn increasing interest recently.[7] Notably, photoacids and photobases undergo intermolecular ESPT to solvent. Excited-state intramolecular proton transfer (ESIPT) represents another category of ESPT that has broad applications in bio-imaging and optoelectronics[8] and will be studied as well.

9.1.1 Further investigation of the solvent role in ESPT dynamics

As shown in Chapters 4 and 5, the fluorescent superphotoacids exhibit inhomogeneous ESPT ways and are mainly rate-limited by the solvent orientation.[9] This is because solvents molecules have to reorganize themselves to adapt to the change in dipole moment of the photoacid upon photoexcitation and rebuild the H-bonding chain to favor proton transfer.[10] In Chapter 6, fluorescent and non-fluorescent superphotoacids were compared in their ESPT behaviors in aqueous solution.[11] The former shows clear engagement of solvent motions during ESPT while the latter does not. It is obvious that the solvent motions play an important role in governing the ESPT dynamics. However, it remains unclear how solvent molecules act in competition with other nonradiative decay pathways for non-fluorescent photoacids (i.e., the excited-state lifetime is short) in the presence of ESPT. Because the solvent orientation rate is relatively constant, this question can be explored by studying superphotoacids of different excited-state lifetimes. It is also noted that protic solvents have been investigated the most while basic organic aprotic solvents in which ESPT can also occur have received much less attention.[12] However, this line of inquiry deserves more attention as the basic molecules (i.e., Lewis base) such as the side chain of some amino acids are the direct or indirect proton acceptors for the ESPT relay in many biological systems.[1,13,14] Another interesting system is the superphotoacid QCy9 in Regime IV (Figure 1.2d) which is the strongest photoacid to date. The ESPT rate of QCy9 is independent of the solvents, i.e., water and alcohols, but the origin remains elusive.[15] This represents a unique scenario where the ESPT is not rate-limited by solvent orientation.

9.1.2 Photobases

In contrast to photoacids that transfer a proton to the solvent upon photoexcitation, photobases are molecules that undergoes intermolecular ESPT in the opposite direction, i.e., proton abstraction from solvent, and therefore the solvent has to be protic. Similar to photoacids, the intramolecular charge transfer (ICT) underpins the photoinduced basicity increase (i.e., pK_a increase from ground- to excited-state). The photobasicity can thus be tuned by enhancing or weakening ICT. Photobases such as quinoline (or quinoline derivatives) and Schiff bases has been increasingly reported in recent years.[16,17] Strong photobases can abstract the proton from protic organic solvents such as alcohols which is similar to strong photoacids that undergo ESPT to alcohols. However, a systematic study of correlations between ESPT dynamics in solvents and photobasicity is still lacking. We plan to employ fs-TA and FSRS to shed more light on it by studying the ESPT dynamics of photobases of different strengths in water and alcohols.

9.1.3 Excited-state intramolecular proton transfer (ESIPT)

This class of molecules involves the relocation of the proton due to intramolecular ESPT which is therefore often referred as tautomerization as well. Compared to photoacids and photobases, ESIPT molecules yield a tautomer (i.e., zwitterionic form) with a larger Stokes-shifted emission because of the photobase nature of the proton-accepting site.[18] Thus, ESIPT has wide applications in bio-imaging and optoelectronics because of the unique photophysical properties.[19,20] Notably, ESIPT is not significantly

affected by the solvent in many cases although some works reported that protic solvent may rupture the intramolecular H-bonding and hence complicate the proton transfer dynamics. For example, the *ortho* substituted GFP core chromophore (*o*-HBDI, Figure 9.1) is capable of ESIPT in both protic and aprotic solvents.[21,22] The ESIPT rate is usually ultrafast (<100 fs) due to strong intramolecular H-bonding between the proton donating and accepting sites. It has been suggested by some reports that low-frequency skeletal vibrations impulsively modulate the O−H distance and adiabatically lead to ultrafast proton transfer.[22] This agrees well with previous reports on the role of low-frequency vibrational motions in modulating the intermolecular ESPT reaction.[13,23] FSRS fits this inquiry as it provides the capability to track coherent vibrational motions and retrieve vibrational couplings starting from the Franck-Condon region of actinic photoexcitation.[24]
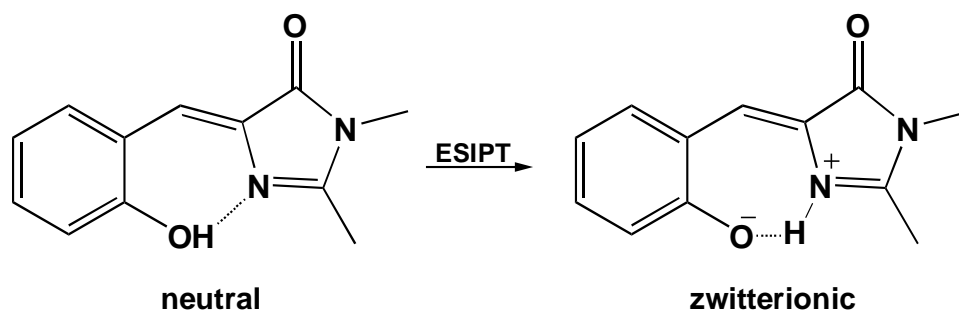

Figure 9.1. Excited-state intramolecular proton transfer for *o*-HBDI.

9.2 Design of advanced bio-imaging probes

Encouraged by our new discovery of "double-donor-one-acceptor" red-shifting strategy (Chapter 7), further efforts can be devoted to characterizing the mechanism in a systematic manner, combining other desired properties into design such as high FQY and large Stokes shift, and developing fluorogenic dyes as an alternative for bright probes. Besides, non-canonical fluorescent proteins (FPs) and the pertinent FP-based biosensors bearing the "double-donor-one-acceptor" structure can be developed.

9.2.1 Characterization of the "double-donor-one-acceptor" strategy

With quantum calculations and vibrational analysis, we demonstrated the synergistic tuning of both ground- and excited-state energetics by electrostatic modifications at the electron donating and accepting moieties, respectively. These results were based on the characterization of two series of locked *p*-HBDI derivatives (Chapter 7).[25,26] To better characterize the "double-donor-one-acceptor" mechanism, *p*-HBDI derivatives with more variations in substitutions at the donor (phenol ring) and acceptor (imidazolinone ring) moieties have been synthesized (Figure 9.2). Quantitative modeling could be performed for the correlation between substitutions (e.g., Hammett parameters) and the ground-/excited-state energies (which can be determined by cyclic voltammetry in conjunction with steady-state absorption and emission measurements). FSRS and quantum calculations can provide the highly desirable insights into the electron distributions in the ground and excited states that account for the electronic energetics.
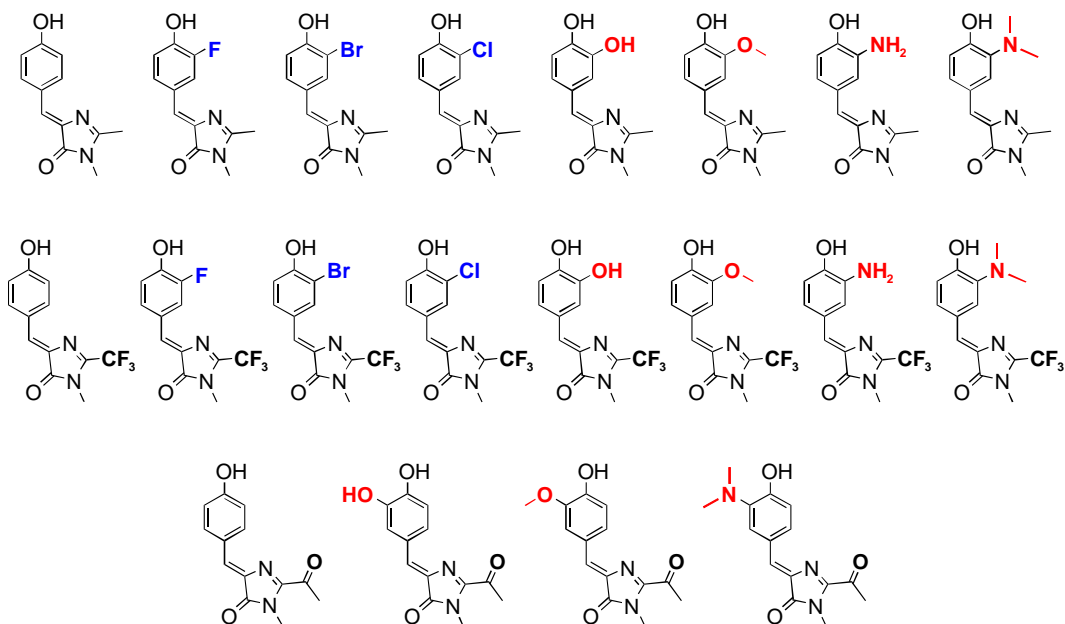
Figure 9.2. Structural analogues of *p*-HBDI for "double-donor-one-acceptor" strategy.

9.2.2 Design of dyes with large Stokes shifts

A large Stokes shift (i.e., the energy difference between absorption and emission) is a desirable property of bio-imaging probes. From the definition, a large Stokes shift requires significant modifications of the ground- and excited-state potential energy surfaces such that the emission gap is much smaller than the absorption gap based on the Franck-Condon principle. This is a nontrivial task and to date most relevant works have been trial-and-error. A few recent works in which dyes with similar "double-donor" structures were built on common fluorophore backbones have shown that the "double-donor" structure produces large Stokes shifts.[27-29] Whether it applies to *p*-HBDI as well remains unknown and merits further investigation. ESPT is another approach to achieve large Stokes shift because of the lower-energy deprotonated emission upon excitation of the protonated form. Likewise, ESIPT is a good strategy to achieve huge

Stokes shifts. For intermolecular ESPT, the ground-state pK_a value has to be rationally designed considering the common physiological pH of 7.4. Our work on tuning photoacidity has provided solid foundation for this issue (Chapter 5). Interestingly, the "two-donor" structure (one is −OH) does not significantly change the pK_a with respect to the parent molecules (i.e., only −OH). For example, the *m*-NH$_2$-*p*-HBDI compound (−NH$_2$ is *ortho* to −OH, Figure 9.2) has a pK_a of 8.1 for −OH/−O⁻ and would support a considerable population of the protonated form in bio-imaging experiments.

9.2.3 Design of dyes with high FQY or brightness

Besides long emission wavelengths and large Stokes shifts, the fluorescence imaging also requires a high FQY or brightness (defined as the product of molar extinction coefficient and FQY)[30] for better sensitivity and signal-to-noise ratio. An empirical understanding of improving FQY is to increase the structural rigidity of fluorophore such that the nonradiative decay pathways induced by twisting motions such as isomerization could be inhibited.[31] However, this is far from adequate in understanding the FQY-structure relationships because of the neglection of other quenching processes such as photoinduced electron transfer.[32] Regardless, the generalizability of the "double-donor-one-acceptor" strategy offers new and exciting opportunities to red-shift the emission wavelength while retaining a high FQY by applying it to a fluorescent molecular backbone. Several well-known fluorophore scaffolds such as BODIPY,[33] rhodamine, indole,[34,35] etc. would fit this purpose, which have been supported by some recent works.[28,29]

9.2.4 Design of fluorogenic dyes

The unlocked *p*-HBDI derivatives are non-fluorescent due to the facile twisting motions around the methine bridge. Therefore, locked *p*-HBDI are desired for bio-imaging probe designs. However, some proposed "double-donor-one-acceptor" derivatives cannot be synthesized due to the current challenges in incorporating a second donor *ortho* to the original donor. For example, the $-NH_2$ does not survive the borylation method we use to lock the *p*-HBDI. One way to overcome this issue is to develop fluorogenic property for the chromophore. The FQY of a fluorogenic dye is environment-sensitive and can be boosted in a restrictive bio-environment.[36-38] We found that a "double-donor-one-acceptor"-like compound m2738d (Figure 9.3) shows more than 500-fold fluorescence enhancement (FE) upon binding with a fluorogen-activating protein FAST (fluorescence-activating and absorption-shifting tag).[39] Its control compound with $-CF_3$ replaced by $-CH_3$ at C-2 site (Figure 9.3) only exhibits a few tens of times FE from the free to bound state. It is interesting that one single small substitution ($-CF_3$) can cause such a large difference in fluorogenicity. The exact origin, on the other hand, remains elusive and will be investigated by examining the excited-state relaxation pathways using fs-TA and FSRS (manuscript in preparation).
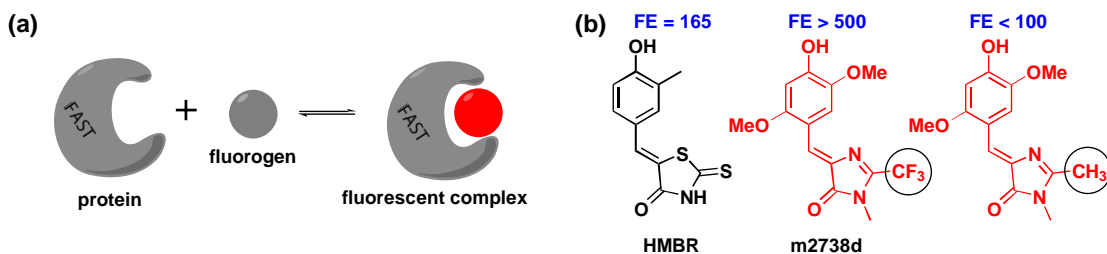

Figure 9.3. Fluorogens from "double-donor-one-acceptor" strategy. (a) Illustration of FAST protein mechanism. (B) Structures of fluorogens derived from *p*-HBDI.

9.2.5 Non-canonical fluorescent proteins

Most fluorescent proteins (FPs) and FP-based biosensors share the same chromophore core, i.e., *p*-HBDI, and therefore can directly benefit from the "double-donor-one-acceptor" strategy for redder emission. Since the tyrosine constitutes the phenol moiety in the protein chromophore, non-canonical tyrosine bearing another strong EDG *ortho* to −OH can be incorporated into the protein through mutagenesis. This line of efforts has emerged in recent years such as non-canonical GFP with amino-tyrosine introduced into the chromophore.[40-42] The resultant FP shows significantly red-shifted absorption and emission. Furthermore, non-canonical FP-based biosensors have also been developed. These FPs and biosensors all adopted the "double-donor" structure for tyrosine as part of the chromophore. It is noteworthy that the protein environment may also play a role in the redshift as suggested by some reports. More interestingly, these modified FPs and biosensors are fluorescent in the protein matrix, in contrast to the synthetic chromophore in solutions (i.e., *m*-NH_2-*p*-HBDI, Figure 9.2).[43] It is likely due to the inhibition of the chromophore twisting motions by the restrictive protein environment which still demands further investigation.

9.3 References

[1] Gagliardi, C. J.; Westlake, B. C.; Kent, C. A.; Paul, J. J.; Papanikolas, J. M.; Meyer, T. J. Integrating proton coupled electron transfer (PCET) and excited states. *Coord. Chem. Rev.* **2010**, *254*, 2459-2471.

[2] Svensson, B.; Etchebest, C.; Tuffery, P.; van Kan, P.; Smith, J.; Styring, S. A Model for the Photosystem II Reaction Center Core Including the Structure of the Primary Donor P$_{680}$. *Biochemistry* **1996**, *35*, 14486-14502.

[3] Mamedov, F.; Sayre, R. T.; Styring, S. Involvement of Histidine 190 on the D1 Protein in Electron/Proton Transfer Reactions on the Donor Side of Photosystem II. *Biochemistry* **1998**, *37*, 14245-14256.

[4] Westlake, B. C.; Brennaman, M. K.; Concepcion, J. J.; Paul, J. J.; Bettis, S. E.; Hampton, S. D.; Miller, S. A.; Lebedeva, N. V.; Forbes, M. D. E.; Moran, A. M.; Meyer, T. J.; Papanikolas, J. M. Concerted electron-proton transfer in the optical excitation of hydrogen-bonded dyes. *Proc. Natl. Acad. Sci. U.S.A.* **2011**, *108*, 8554-8558.

[5] Ko, C.; Solis, B. H.; Soudackov, A. V.; Hammes-Schiffer, S. Photoinduced Proton-Coupled Electron Transfer of Hydrogen-Bonded *p*-Nitrophenylphenol–Methylamine Complex in Solution. *J. Phys. Chem. B* **2013**, *117*, 316-325.

[6] Simkovitch, R.; Karton-Lifshin, N.; Shomer, S.; Shabat, D.; Huppert, D. Ultrafast Excited-State Proton Transfer to the Solvent Occurs on a Hundred-Femtosecond Time-Scale. *J. Phys. Chem. A* **2013**, *117*, 3405-3413.

[7] Driscoll, E. W.; Hunt, J. R.; Dawlaty, J. M. Photobasicity in Quinolines: Origin and Tunability via the Substituents' Hammett Parameters. *J. Phys. Chem. Lett.* **2016**, *7*, 2093-2099.

[8] Padalkar, V. S.; Seki, S. Excited-state intramolecular proton-transfer (ESIPT)-inspired solid state emitters. *Chem. Soc. Rev.* **2016**, *45*, 169-202.

[9] Chen, C.; Zhu, L.; Baranov, M. S.; Tang, L.; Baleeva, N. S.; Smirnov, A. Y.; Yampolsky, I. V.; Solntsev, K. M.; Fang, C. Photoinduced Proton Transfer of GFP-Inspired Fluorescent Superphotoacids: Principles and Design. *J. Phys. Chem. B* **2019**, *123*, 3804-3821.

[10] Simkovitch, R.; Shomer, S.; Gepshtein, R.; Huppert, D. How Fast Can a Proton-Transfer Reaction Be beyond the Solvent-Control Limit? *J. Phys. Chem. B* **2015**, *119*, 2253-2262.

[11] Chen, C.; Zhu, L.; Boulanger, S. A.; Baleeva, N. S.; Myasnyanko, I. N.; Baranov, M. S.; Fang, C. Ultrafast excited-state proton transfer dynamics in dihalogenated non-fluorescent and fluorescent GFP chromophores. *J. Chem. Phys.* **2020**, *152*, 021101.

[12] Kumpulainen, T.; Rosspeintner, A.; Dereka, B.; Vauthey, E. Influence of Solvent Relaxation on Ultrafast Excited-State Proton Transfer to Solvent. *J. Phys. Chem. Lett.* **2017**, *8*, 4516-4521.

[13] Fang, C.; Frontiera, R. R.; Tran, R.; Mathies, R. A. Mapping GFP Structure Evolution During Proton Transfer with Femtosecond Raman Spectroscopy. *Nature* **2009**, *462*, 200-204.

[14] Tang, L.; Wang, Y.; Zhu, L.; Kallio, K.; Remington, S. J.; Fang, C. Photoinduced proton transfer inside an engineered green fluorescent protein: a stepwise–concerted-hybrid reaction. *Phys. Chem. Chem. Phys.* **2018**, *20*, 12517-12526.

[15] Simkovitch, R.; Akulov, K.; Shomer, S.; Roth, M. E.; Shabat, D.; Schwartz, T.; Huppert, D. Comprehensive Study of Ultrafast Excited-State Proton Transfer in Water and D2O Providing the Missing $RO^-\cdots H^+$ Ion-Pair Fingerprint. *J. Phys. Chem. A* **2014**, *118*, 4425-4443.

[16] Driscoll, E. W.; Hunt, J. R.; Dawlaty, J. M. Proton Capture Dynamics in Quinoline Photobases: Substituent Effect and Involvement of Triplet States. *J. Phys. Chem. A* **2017**, *121*, 7099-7107.

[17] Sheng, W.; Nairat, M.; Pawlaczyk, P. D.; Mroczka, E.; Farris, B.; Pines, E.; Geiger, J. H.; Borhan, B.; Dantus, M. Ultrafast Dynamics of a "Super" Photobase. *Angew. Chem. Int. Ed.* **2018**, *57*, 14742-14746.

[18] Hsieh, C.-C.; Jiang, C.-M.; Chou, P.-T. Recent Experimental Advances on Excited-State Intramolecular Proton Coupled Electron Transfer Reaction. *Acc. Chem. Res.* **2010**, *43*, 1364-1374.

[19] Hsu, Y.-H.; Chen, Y.-A.; Tseng, H.-W.; Zhang, Z.; Shen, J.-Y.; Chuang, W.-T.; Lin, T.-C.; Lee, C.-S.; Hung, W.-Y.; Hong, B.-C.; Liu, S.-H.; Chou, P.-T. Locked ortho- and para-Core Chromophores of Green Fluorescent Protein; Dramatic Emission Enhancement via Structural Constraint. *J. Am. Chem. Soc.* **2014**, *136*, 11805-11812.

[20] Chatterjee, S.; Ahire, K.; Karuso, P. Room-Temperature Dual Fluorescence of a Locked Green Fluorescent Protein Chromophore Analogue. *J. Am. Chem. Soc.* **2020**, *142*, 738-749.

[21] Chen, K.-Y.; Cheng, Y.-M.; Lai, C.-H.; Hsu, C.-C.; Ho, M.-L.; Lee, G.-H.; Chou, P.-T. Ortho Green Fluorescence Protein Synthetic Chromophore; Excited-State Intramolecular Proton Transfer via a Seven-Membered-Ring Hydrogen-Bonding System. *J. Am. Chem. Soc.* **2007**, *129*, 4534-4535.

[22] Hsieh, C.-C.; Chou, P.-T.; Shih, C.-W.; Chuang, W.-T.; Chung, M.-W.; Lee, J.; Joo, T. Comprehensive Studies on an Overall Proton Transfer Cycle of the ortho-Green Fluorescent Protein Chromophore. *J. Am. Chem. Soc.* **2011**, *133*, 2932-2943.

[23] Liu, W.; Wang, Y.; Tang, L.; Oscar, B. G.; Zhu, L.; Fang, C. Panoramic portrait of primary molecular events preceding excited state proton transfer in water. *Chem. Sci.* **2016**, *7*, 5484-5494.

[24] Hoffman, D. P.; Mathies, R. A. Femtosecond Stimulated Raman Exposes the Role of Vibrational Coherence in Condensed-Phase Photoreactivity. *Acc. Chem. Res.* **2016**, *49*, 616-625.

[25] Chen, C.; Baranov, M. S.; Zhu, L.; Baleeva, N. S.; Smirnov, A. Y.; Zaitseva, S. O.; Yampolsky, I. V.; Solntsev, K. M.; Fang, C. Designing redder and brighter fluorophores by synergistic tuning of ground and excited states. *Chem. Commun.* **2019**, *55*, 2537-2540.

[26] Chen, C.; Fang, C. Devising Efficient Red-Shifting Strategies for Bioimaging: A Generalizable Donor-Acceptor Fluorophore Prototype. *Chem. Asian. J.* **2020**, *15*, 1514-1523.

[27] Chen, W.; Xu, S.; Day, J. J.; Wang, D.; Xian, M. A General Strategy for Development of Near-Infrared Fluorescent Probes for Bioimaging. *Angew. Chem. Int. Ed.* **2017**, *56*, 16611-16615.

[28] Ren, T.-B.; Xu, W.; Zhang, W.; Zhang, X.-X.; Wang, Z.-Y.; Xiang, Z.; Yuan, L.; Zhang, X.-B. A General Method To Increase Stokes Shift by Introducing Alternating Vibronic Structures. *J. Am. Chem. Soc.* **2018**, *140*, 7716-7722.

[29] Ren, X.; Zhang, F.; Luo, H.; Liao, L.; Song, X.; Chen, W. Red-emitting boron difluoride complexes with a mega-large Stokes shift and unexpectedly high fluorescence quantum yield. *Chem. Commun.* **2020**, *56*, 2159-2162.

[30] Chudakov, D. M.; Matz, M. V.; Lukyanov, S.; Lukyanov, K. A. Fluorescent Proteins and Their Applications in Imaging Living Cells and Tissues. *Physiol. Rev.* **2010**, *90*, 1103-1163.

[31] Baranov, M. S.; Lukyanov, K. A.; Borissova, A. O.; Shamir, J.; Kosenkov, D.; Slipchenko, L. V.; Tolbert, L. M.; Yampolsky, I. V.; Solntsev, K. M. Conformationally Locked Chromophores as Models of Excited-State Proton Transfer in Fluorescent Proteins. *J. Am. Chem. Soc.* **2012**, *134*, 6025-6032.

[32] Escudero, D. Revising Intramolecular Photoinduced Electron Transfer (PET) from First-Principles. *Acc. Chem. Res.* **2016**, *49*, 1816-1824.

[33] Boens, N.; Leen, V.; Dehaen, W. Fluorescent indicators based on BODIPY. *Chem. Soc. Rev.* **2012**, *41*, 1130-1172.

[34] Hilaire, M. R.; Ahmed, I. A.; Lin, C.-W.; Jo, H.; DeGrado, W. F.; Gai, F. Blue fluorescent amino acid for biological spectroscopy and microscopy. *Proc. Natl. Acad. Sci. U.S.A.* **2017**, *114*, 6005-6009.

[35]   You, M.; Fan, H.; Wang, Y.; Zhang, W. Aldehyde-derivatized indoles as fluorescent probes for hydration environments. *Chem. Phys.* **2019**, *526*, 110438.

[36] Chen, H.-J.; Chew, C. Y.; Chang, E.-H.; Tu, Y.-W.; Wei, L.-Y.; Wu, B.-H.; Chen, C.-H.; Yang, Y.-T.; Huang, S.-C.; Chen, J.-K.; Chen, I. C.; Tan, K.-T. *S-Cis* Diene Conformation: A New Bathochromic Shift Strategy for Near-Infrared Fluorescence Switchable Dye and the Imaging Applications. *J. Am. Chem. Soc.* **2018**, *140*, 5224-5234.

[37]   Ermakova, Y. G.; Sen, T.; Bogdanova, Y. A.; Smirnov, A. Y.; Baleeva, N. S.; Krylov, A. I.; Baranov, M. S. Pyridinium Analogues of Green Fluorescent Protein Chromophore: Fluorogenic Dyes with Large Solvent-Dependent Stokes Shift. *J. Phys. Chem. Lett.* **2018**, *9*, 1958-1963.

[38]   Hoche, J.; Schulz, A.; Dietrich, L. M.; Humeniuk, A.; Stolte, M.; Schmidt, D.; Brixner, T.; Würthner, F.; Mitric, R. The origin of the solvent dependence of fluorescence quantum yields in dipolar merocyanine dyes. *Chem. Sci.* **2019**, *10*, 11013-11022.

[39]   Povarova, N. V.; Zaitseva, S. O.; Baleeva, N. S.; Smirnov, A. Y.; Myasnyanko, I. N.; Zagudaylova, M. B.; Bozhanova, N. G.; Gorbachev, D. A.; Malyshevskaya, K. K.; Gavrikov, A. S.; Mishin, A. S.; Baranov, M. S. Red-Shifted Substrates for FAST Fluorogen-Activating Protein Based on the GFP-Like Chromophores. *Chem. Eur. J.* **2019**, *25*, 9592-9596.

[40]   Augustine, G.; Raghavan, S.; NumbiRamudu, K.; Easwaramoorthi, S.; Shanmugam, G.; Seetharani Murugaiyan, J.; Gunasekaran, K.; Govind, C.; Karunakaran, V.; Ayyadurai, N. Excited State Electronic Interconversion and Structural Transformation of Engineered Red-Emitting Green Fluorescent Protein Mutant. *J. Phys. Chem. B* **2019**, *123*, 2316-2324.

[41] Lin, C.-Y.; Romei, M. G.; Oltrogge, L. M.; Mathews, I. I.; Boxer, S. G. Unified Model for Photophysical and Electro-Optical Properties of Green Fluorescent Proteins. *J. Am. Chem. Soc.* **2019**, *141*, 15250-15265.

[42]   Zhang, S.; Ai, H.-w. A general strategy to red-shift green fluorescent protein based biosensors. *bioRxiv* **2020**, 2020.2004.2009.034561.

[43] Oscar, B. G.; Zhu, L.; Wolfendeen, H.; Rozanov, N. D.; Chang, A.; Stout, K. T.; Sandwisch, J. W.; Porter, J. J.; Mehl, R. A.; Fang, C. Dissecting Optical Response and Molecular Structure of Fluorescent Proteins With Non-canonical Chromophores. *Front. Mol. Biosci.* **2020**, *7*, 131.